

The Properties of Electrical Steels and Their Coatings

Victoria Louise Bemmer

Department of Chemistry

Cardiff University

2013



DECLARATION

This work has not been submitted in substance for any other degree or award at this or any other university or place of learning, nor is being submitted concurrently in candidature for any degree or other award.

Signed (candidate) Date

STATEMENT 1

This thesis is being submitted in partial fulfilment of the requirements for the degree of PhD

Signed (candidate) Date

STATEMENT 2

This thesis is the result of my own independent work/investigation, except where otherwise stated.

Other sources are acknowledged by explicit references. The views expressed are my own.

Signed (candidate) Date

STATEMENT 3

I hereby give consent for my thesis, if accepted, to be available for photocopying and for inter-library loan, and for the title and summary to be made available to outside organisations.

Signed (candidate) Date

ACKNOWLEDGEMENTS

As with any extended study I could not have completed this piece of work without the support of many people throughout the last three and a half years and would like to take this opportunity to thank each of them.

Firstly I would like to thank my supervisors Prof Michael Bowker and Dr Philip Davies for their excellent guidance and support throughout the project, I could not have wished for better supervisors.

I would like to thank Cogent Power Ltd and in particular Andrew Nolan and Keith Jenkins for not only funding this project but also for the constant advice and support provided throughout.

I would like to take the opportunity to thank Dr David Morgan and Dr Albert Carley for all their helpful advice- particularly with regards to all things XPS and machine breakdowns!

I would like to thank the Surface Science Group within the school of chemistry past and present Jon, Jen, Lee, Kareem, Liza, Hatem, Ryan, Charlie, Ibrahim, Julia, Cat, Matt and Jonas for the warm welcome and continued friendship I have found there.

I must also thank the people who I shared the mezzanine office space in particular Clare, James, Chris, Emily, Mark and Lee for providing friendship and some light-hearted relief both in the office and outside, I couldn't have done it without you!

I would also like to thank the Cogent sponsored group within the School of Engineering for the insights they often provided from another perspective and for aiding in my understanding to the background of the project.

I would like to thank my parents for their constant love and support throughout my life, I truly could not have gotten to this point without it and appreciate everything you do for me.

Finally I would like to thank my partner Rob for his continued love and support. From practical advice and fixing broken machines to listening to me whine throughout the write up process (which I did often) you have been a consistent support for which I am eternally grateful.

ABSTRACT

Grain oriented steels containing 3 % silicon are widely used as stacks of thin laminations in transformers and other electrical devices. Phosphate coatings are applied to these laminations in order to insulate between the sheets and hold them under tension, reducing the electrical energy losses and making the transformers more efficient. This thesis explores the properties of aluminium and magnesium phosphate, two commonly used coating materials. Using model phosphate coatings it has been shown that an excess of phosphoric acid is required to cause the condensation reaction that produces the metaphosphate, thought to be the cause of the increased tension imparted on the steel.

The addition of chromium oxide was found to prevent this transformation by reacting with the excess acid to form chromium pyrophosphate, which leads to a more stable coating which imparts a greater tension upon the steel substrate.

XPS has been shown to be a useful technique for the characterisation of model phosphate coatings, however it cannot be used to quantitatively analyse the systems (unlike other phosphate systems) possibly due to the higher number of phases present within the samples.

CONTENTS

Chapter 1 Introduction	1
Chapter 2 Experimental.....	23
Chapter 3 The Stability Of Model Phosphate Coatings	50
Chapter 4 XPS studies of Model Phosphate Coatings.....	113
Chapter 5 Conclusions and Future Work.....	198
Appendix 1 Additional Characterisation Data	204

Chapter sections and their associated page numbers are described on the contents page at the beginning of each chapter

LIST OF ABBREVIATIONS AND SYMBOLS

<i>ATR</i>	<i>Attenuated Total Reflectance</i>
<i>B</i>	<i>Flux Density</i>
<i>BO</i>	<i>Bridging Oxygen</i>
<i>BCC</i>	<i>Body Centred Cubic</i>
<i>CGO</i>	<i>Conventional Grain Oriented</i>
<i>FCC</i>	<i>Face Centred Cubic</i>
<i>FT</i>	<i>Fourier Transform</i>
<i>GO</i>	<i>Grain Oriented</i>
<i>H</i>	<i>Magnetic Field Strength</i>
<i>HiB</i>	<i>High Permeability</i>
<i>HTCA</i>	<i>High Temperature Coil Anneal</i>
<i>IR</i>	<i>Infrared</i>
<i>LEED</i>	<i>Low Energy Electron Diffraction</i>
<i>NBO</i>	<i>Non Bridging Oxygen</i>
<i>NGO</i>	<i>Non Grain Oriented</i>
<i>QMS</i>	<i>Quadrupole Mass Spectrometry</i>
<i>STM</i>	<i>Scanning Tunnelling Microscopy</i>
<i>TGA</i>	<i>Thermogravimetric Analysis</i>
<i>UHV</i>	<i>Ultra High Vacuum</i>
<i>XPS</i>	<i>X-Ray Photoelectron Spectroscopy</i>
<i>XRD</i>	<i>X-Ray Diffraction</i>
β	<i>asymmetry parameter</i>
θ	<i>Sticking Probability</i>
λ	<i>Mean Free Path</i>

CHAPTER 1 INTRODUCTION

1.1 Overview	2
1.2 Electrical Steels	2
1.2.1 Definitions of Key Magnetic Terms	2
1.2.2 The development of electrical steels and their coatings	4
1.3 Steel Processing at Cogent Power Ltd.	8
1.4 An Introduction to Surface Science.....	11
1.5 Crystal and Surface Structures	12
1.5.1 Miller Indices	12
1.5.2 Real Surfaces.....	15
1.5.2.1 The Role of Defects	15
1.5.2.2 Surface Relaxation and Reconstruction	16
1.6 Reactions on Surfaces.....	17
1.6.1 Adsorption on surfaces.....	17
1.6.2 Adsorption kinetics.....	19
1.7 Thesis Synopsis	20
1.8 References.....	21

1.1 OVERVIEW

The purpose of this chapter is to provide an overview of the technical importance of electrical steels. An introduction to the properties of electrical steel is given, along with a brief outline of the history of its development. The processing route at Cogent Power Ltd is discussed along with details of the current on-line coatings. The surface coatings of these materials are the focus of this research and so an introduction to both the fundamentals of surface science is given and the importance of surfaces with regards to the overall properties of a material. Finally a brief synopsis of the thesis is given with a brief outline of each chapter.

1.2 ELECTRICAL STEELS

Electrical steel is a term that refers to a variety of steels generally containing 3-6% silicon. These steels are also known as lamination steels, silicon electron steels, silicon steels or transformer steels.¹ The percentage of silicon within the steel is of vital importance; the higher the percentage of silicon present the better the magnetic properties. However if it is taken much above 6% the steel becomes too brittle to work with.

Electrical steels can be split into two main categories, oriented and non-oriented (NGO) steels. Oriented steels can be further divided in grain oriented (GO) and High- permeability (HiB) steels.

1.2.1 DEFINITIONS OF KEY MAGNETIC TERMS

In order to fully describe the background and history of electrical steels it is useful to define a few key magnetic terms here.

Hysteresis refers to magnetic dependence of a system on its past environment as well as its present². Within ferromagnetic materials the magnetic field strength (H) can be systematically varied and flux density (B) measured to produce a hysteresis curve similar to that seen in Figure 1.1.

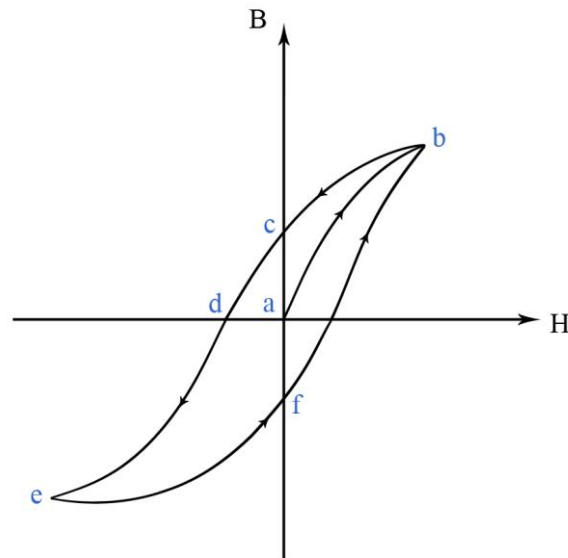


Figure 1.1 A typical hysteresis curve for a ferromagnetic materials (taken from reference (3))

The intercepts of the B axis are a measure of flux where the field strength is 0 and are termed the remanence B_r .⁴ 'Soft' magnetic materials such as those used in transformer cores will have a small remanence and will therefore magnetise and demagnetise easily, 'hard' materials will have a large remanence and will remain magnetised for longer (and in extreme cases will remain permanently magnetised).

The shape of the hysteresis curve indicates the flux density increasing due to alignment of magnetic domains (areas within a magnetic material with uniform magnetisation⁵) and when the domains are all aligned the curve plateaus, indicating that magnetic saturation has been reached. After this point when the field strength is reduced flux density is also reduced, however the resulting curve will not match the original one observed during the increase in field strength.

Domains arise in materials as a method of minimising internal energy⁴. If a material were to consist of a single domain (as in Figure 1.2a) a large magnetic field would extend into the space outside of the material, with a large amount of energy being stored in the field. This energy is reduced when the domain splits into two with oppositely aligned poles (Figure 1.2b) and the size of the field outside the material (and therefore the energy requirements) is reduced. Figure 1.2c represents the lowest energy arrangement where additional small horizontal domains form. During domain formation some energy is lost in the formation of 'domain walls' high energy areas where opposing dipoles meet. Domain formation will continue until the field

energy saved is equal to the energy lost in domain wall formation (a typical domain size is around $20 \mu\text{m}^4$).

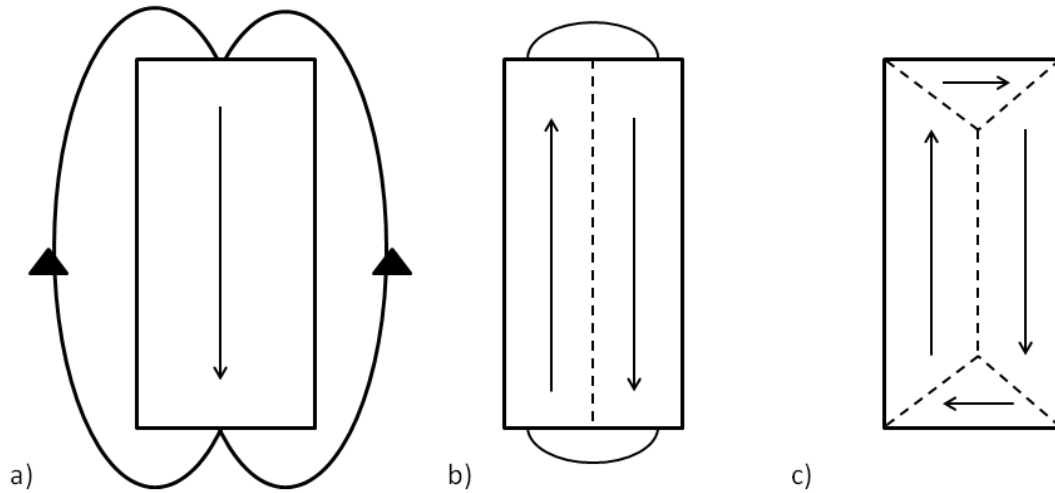


Figure 1.2 a) a single domain b) a two domain system c) a multi domain system. Arrows represent the alignment of the magnetic poles.

The formation of domains at an angle to other domains has additional energy costs in the form of magnetic anisotropy. Magnetic anisotropy refers to the ‘easy’ direction of magnetisation typically parallel to a crystal axis, and the changing of the direction of magnetisation will require energy.

Magnetostriction is the change in shape of a material during magnetisation, caused by the alignment of magnetic dipoles ‘stretching’ the material slightly. This causes the loss of energy as frictional heat and as the buzzing sound heard near electrical transformers.

Permeability refers to how readily a material will magnetise and support a magnetic field within itself. Permeability is often given the symbol μ and is measured in henrys per metre (Hm^{-1}). The permeability constant (μ_0) is the resistance to forming a magnetic field in a vacuum and has the value $1.2566 \times 10^{-6} \text{ Hm}^{-1}$.¹

1.2.2 THE DEVELOPMENT OF ELECTRICAL STEELS AND THEIR COATINGS

The development of electrical steels first really began when Hadfield published work showing the introduction of silicon or aluminium to steels reduced energy losses by up to four times.⁶

Grain oriented steels were invented by N. P. Goss in 1934,⁷ and the process was commercialised by ARMCO, with the first strips being produced in 1939.⁶

Through a series of hot and cold rollings, Goss produced steel where a large number of crystal grains were oriented with the [001] direction close to the rolling direction and the (110) planes close to the sheet plane. During the Goss process the strip is heated to around 1200 °C, stimulating the secondary recrystallisation of these [001](110) grains, whilst the additive manganese sulphide prevents the growth of other grains.⁶ This orientation is often referred to as 'cube-on-edge'⁸ (see Figure 1.3). Steel developed following this process is often referred to as conventional grain oriented (CGO) steel. By keeping the grains within the steel regularly orientated the magnetic properties of the steel are improved and therefore energy losses are reduced.

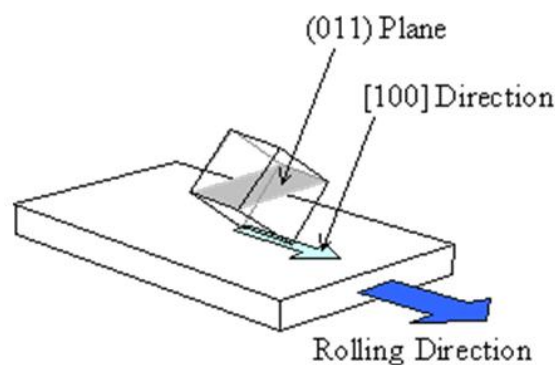


Figure 1.3 the Cube-On-Edge texture of grain oriented steel (adapted from reference (9))

The magnetic properties of CGO steel were improved over the following years by refinement of the steel production process improving the purity of the resulting product. In 1965 Nippon Steel introduced the production of high permeability (HiB) steels.⁶ This process removed one of the cold-rolling stages used in the Goss method and saw the addition of aluminium nitride as a growth inhibitor. This process saw a better alignment of the grains to the Goss orientation. However, the grains were much larger than those in CGO steels. The reduction in losses in these steels arises from a reduction of 30-40 % in hysteresis.^{6,10}

The phosphate coating applied to the steel was first studied in the 1970's⁶ with early work indicating that magnetostriction was reduced by the coating holding the steel under tension.¹¹ The amount of tension on the steel has been measured as 1.2 MPa¹², and it has been shown that tension coatings are more effective on better oriented steels.^{6,13}

Armco first developed phosphate based coatings for electrical steels in the late 1940s.^{14, 15} Gifford developed a coating containing phosphoric acid (the free acid forming around 7.5- 50% of the coatings) and the optional addition of magnesia.¹⁴ A later patent saw the addition of muscovite (a phyllosilicate $(\text{KF})_2(\text{Al}_2\text{O}_3)_2(\text{SiO}_2)_6$).¹⁵ Previous coatings used on electrical steels had fused upon heating (generally done on coils to reduce stress) and caused adjacent laminations to stick together. It was believed that the addition of muscovite prevented this due to its crystal structure being plate-like and sliding over each other. The coating could be applied to the steel using a roller and dried at 760 °C to completely stop adhesion between laminations, however this made the sheets very hard and greatly reduced die life used in the production of cut sheets.

Steinherz added aluminium hydrate to phosphate coatings with at least 4.5 phosphoric acid to 1 aluminium hydrate.¹⁶ The resulting coating was less damaging to dies used in punch and die production methods, and reduced the amount of 'burr' on the edges of steel sheets.

Throughout the 1970s ARMCO developed a series of coatings consisting of magnesium oxide, alumina and phosphoric acid in varying ratios.^{8, 17, 18} The oxides react within the solution to form aluminium and magnesium phosphates. Colloidal silica was also added to the solution but kept below 40% of the total volume to permit formation of a good glass⁸ and chromium oxide was also added. Later coatings also saw the addition of boric acid to the coating.⁸ The coatings consisted of at least 45% water.

The ratio of silica to phosphate within the coating has been shown to have an important effect on the magnetic losses of the final steel with the optimal ratio of silica/phosphate being approximately 0.7(see Figure 1.4).^{19, 20} FT-IR spectroscopy has been shown to be an effective tool for use in industry to measure the relative concentrations of the components in the final coating, particularly as it is a non-destructive technique which can be used while the coating is still on the sheet.¹⁹

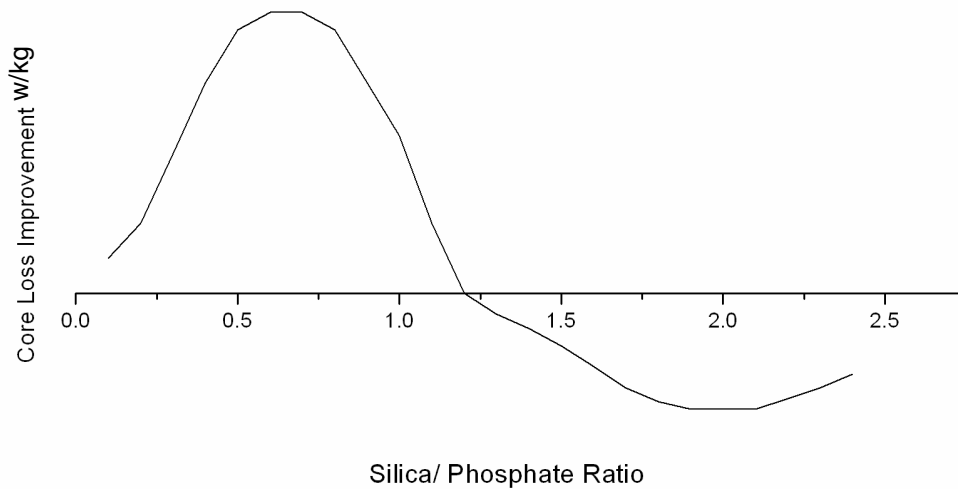


Figure 1.4 The relationship between silica/phosphate ratio and core loss of transformer steels ^{19, 20}

Magnesium phosphate based coatings have been shown to induce greater tension in the steel sheets than aluminium phosphate coatings; however they are much less stable towards hydration than aluminium phosphate (see sections 3.2.1 and 3.2.2 for a fuller discussion on the curing and stability of aluminium and magnesium phosphates).

The addition of chromium oxide was shown to improve the wettability of the coating and the resistivity between sheets after the stress relief anneal.⁸ It has also been shown to increase the solubility of the magnesium oxide within the solution and improve the moisture resistance of the final coating. This is seen in Figure 1.5 where the presence of chromium oxide in the coating formulation is observed to prevent a percentage mass increase of up to 3.5 % over a month.

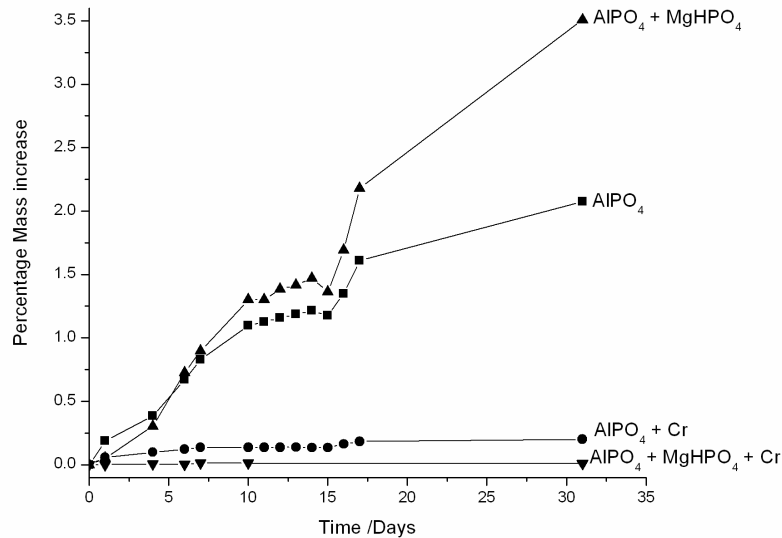


Figure 1.5 Variation in mass of coatings over time under humid conditions (estimated 65 % humidity at 333 K) (data collected by A. Nolan, Cogent Ltd.)

Recent EU directives such as The Restriction of the Use of Certain Hazardous Substances in Electrical and Electronic Equipment (RoHS)²¹ and Waste Electronic and Electrical Equipment Regulations (WEEE)²² have called for the removal of hexavalent chromium from all new electrical products. This has led to the search for either a new coating material or a new coating additive that will stabilise phosphate coatings in the same way as chromium oxide. The key points on which the suitability of a coating can be assessed on are

- Coating stability (no stickiness at high humidity)
- Magnetic loss reduction
- Is the curing temperature low enough to ensure curing occurs during production?
- Ease of mixing
- Coating appearance.

1.3 STEEL PROCESSING AT COGENT POWER LTD.

An overall schematic of steel process at Cogent Power is shown in Figure 1.6. The incoming steel arrives as large coils weighing 20 tons, with a sheet thickness of around 2.5 mm. These coils are trimmed and passed through the annealing and de-scaling line, where acid and process known as 'shot-blasting' removes dirt and scale from the surface. After this cleaning process the steel

undergoes a final cold reduction, where the steel is reduced to its final thickness (0.23-0.3 mm depending on customer requirements).

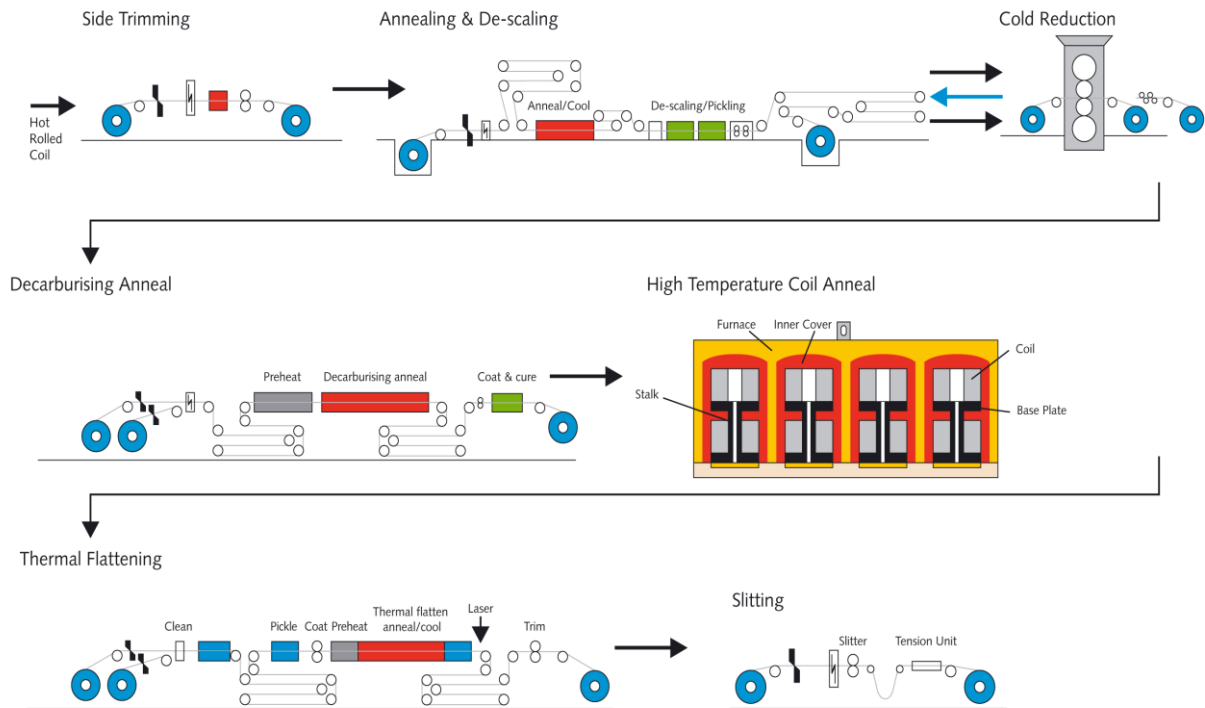


Figure 1.6 The Steel preparation process at Cogent Power Ltd (taken from reference (23))

After this final reduction the steel passes through the decarburising anneal. This process mainly aims to reduce the amount of carbon within the steel to less than 0.003 % by heating in a mixture of hydrogen, nitrogen and water vapour.⁶ Other contaminants present at much lower concentrations (such as sulphur) are also removed during this process, reducing the brittleness of the resulting product. At the end of the anneal the steel is coated in a magnesium oxide slurry.

After this the coil passes through to the high temperature coil anneal (HTCA). The rolls are heated to 1100 ° C in hydrogen for five days. During this anneal the grains ‘grow’ to give the typical magnetic properties observed for grain oriented steels. During this anneal the magnesium slurry reacts with fayalite (Fe_2SiO_4) on the steel surface to form forsterite (Mg_2SiO_4) (see Figure 1.7).

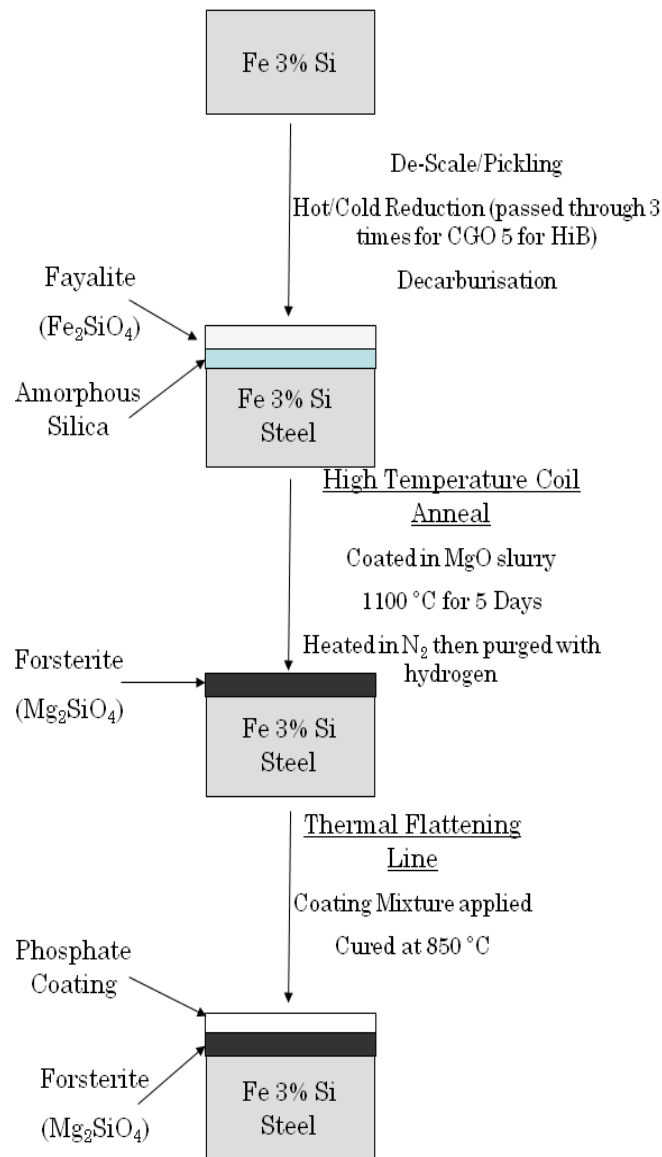


Figure 1.7 The coatings formed on grain oriented steel during processing a Cogent Power Ltd.

After the HTCA, the steel sheets pass to the Thermal Flattening line. This is where the final phosphate coating is applied (Figure 1.7) and the steel is heated to 850 °C. This has the effect to flattening the steel and also holding it under tension in order to improve its magnetic properties. After the coating has been applied and cured, the steel may be scribed by a laser if required, in order to further improve the magnetic properties by reducing domain size. After this the steel goes through a final trim and is ready to be sent to the customer.

1.4 AN INTRODUCTION TO SURFACE SCIENCE

Much of the work of this thesis involves analysis of the surfaces of the materials involved in transformer steels. Surface science can be defined as the study of processes that occur at interfaces between phases (generally between gases and solids). The surface can be viewed as the termination of a bulk structure²⁴, and therefore will be comprised of atoms which are in a low co-ordination state. This makes the surfaces atoms much more reactive than bulk atoms, as they will readily interact with other atoms.

Surface science has been employed in many fields including semiconductors (molecular beam epitaxy was initially used a method of growing high purity compound semiconductors), self-assembled monolayers and the development of fuel-cells; however its major applications have been in the field of heterogeneous catalysis. Surface science is of vital importance to catalysis as it is the surface of the catalysis that is involved in reactions and therefore it is this that must be understood in order to develop a greater understanding of the catalytic process.

Langmuir is often credited as the founder of modern surface science²⁵, due to his development of the Langmuir isotherm relating the surface coverage of an absorbant with gas pressure²⁶ (see section 1.6.1 for a fuller discussion of absorption isotherms) and the definition of dissociative chemisorption.²⁷

Since these early developments there was a large development from the 1960s onwards²⁸ with many more techniques being developed including STM in 1981^{29, 30} and XPS in 1967³¹. In 1974 Ertl used low energy electron diffraction (LEED) to study the adsorption of hydrogen on palladium,³² a vital hydrogenation catalyst. This increase in the uses of surface science was caused by the arrival of ultra-high vacuum (UHV, pressures lower than 1×10^{-9} mbar) and the increased availability of single crystal samples.

A combination of surface sensitive techniques is used to fully characterise a surface by answering the following questions

- What atoms are present at the surface and in what concentrations?
- Where are the molecules on the surface and what are the related bond lengths and angles
- How strong is the bonding of absorbate atoms and how does the surface influence reactivity?²⁴

1.5 CRYSTAL AND SURFACE STRUCTURES

The structure of a surface is defined by the structure of the bulk. Metals generally have one of two bulk structures, either body centered cubic (b.c.c. Figure 1.8a) or face centered cubic (f.c.c. Figure 1.8b). Iron is an example of a b.c.c. metal, whereas palladium is an example of an f.c.c. metal.

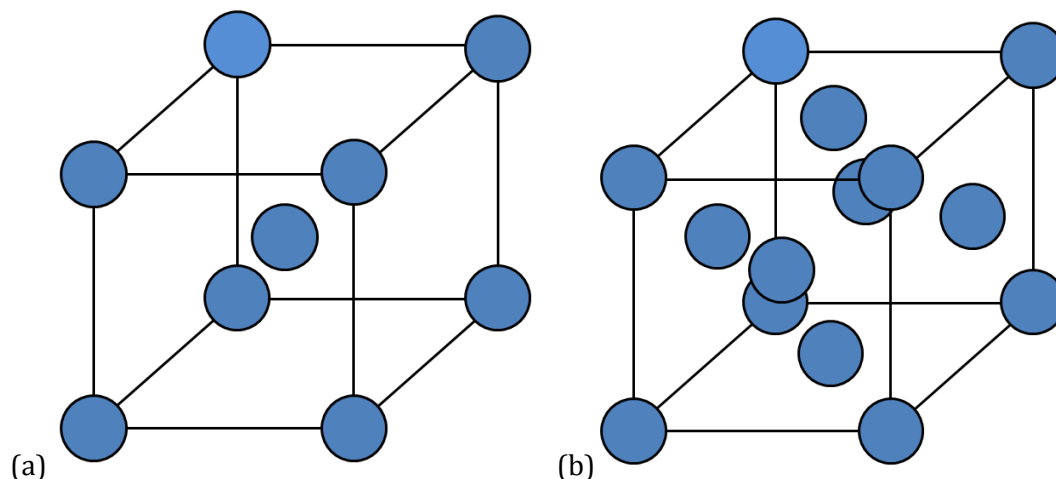


Figure 1.8 the structure of (a) b.c.c and (b) f.c.c. metals

In order for experiments to be performed on well-defined surface a single crystal is often used as a reaction substrate. A single crystal is defined as 'a material in which the crystal lattice of the entire sample is continuous and unbroken to the edges of the sample with no grain boundaries'.³³ This means that cutting through the sample on a given plane will reveal a limited number of atoms in a well-defined arrangement. The arrangement of the atoms exposed at the surface can be controlled by varying the angle the plane is cut at.

1.5.1 MILLER INDICES

The surface obtained from a crystal is determined by the plane chosen to cut through it. These are defined by Miller indices, which consist of three integers (h,k,l). The indices are determined by taking the reciprocal of the point at which a plane intersects the three main axis of the crystal (x,y,z Figure 1.9). the three simplest planes are the (1 0 0), (1 1 0) and (1 1 1) planes (Figure 1.10, Figure 1.11 and Figure 1.12 respectively). These planes are also more stable than other higher index planes (e.g. 2 1 0) as they have a higher co-ordination and are therefore lower energy.

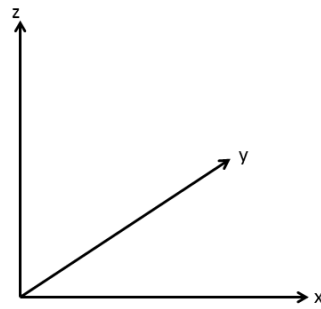


Figure 1.9 axes for Miller Indices notation

The $(1\ 0\ 0)$ plane is shown in Figure 1.10. The plane intersects the x axis at distance a (the unit cell) and never intercepts the y and z axis. These intercepts can be written as $(a\ \infty\ \infty)$. If the intercepts a are re-written in terms of a the term becomes $(1\ \infty\ \infty)$. Finally the reciprocals of these values are taken to give the miller index of $(1\ 0\ 0)$.

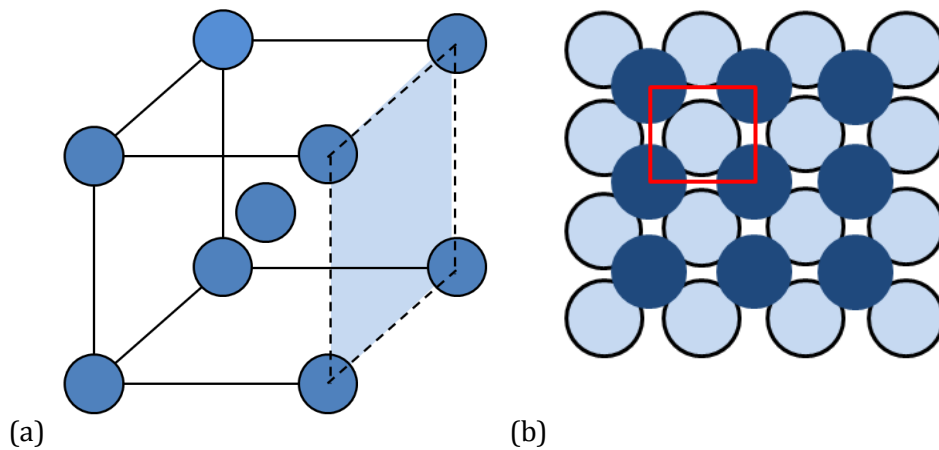


Figure 1.10 (a) the $(1\ 0\ 0)$ plane and (b) the resulting surface of a b.c.c. metal. The unit cell is shown in red.

Following a similar procedure for the $(1\ 1\ 0)$ plane (Figure 1.11) the plane intersects at $(a\ a\ \infty)$ or $(1\ 1\ \infty)$. The reciprocals of these values gives the index of $(1\ 1\ 0)$. If this is done for the $(1\ 1\ 1)$ (Figure 1.12) plane the intercepts are $(a\ a\ a)$ or $(1\ 1\ 1)$. Reciprocals give the miller index of $(1\ 1\ 1)$.

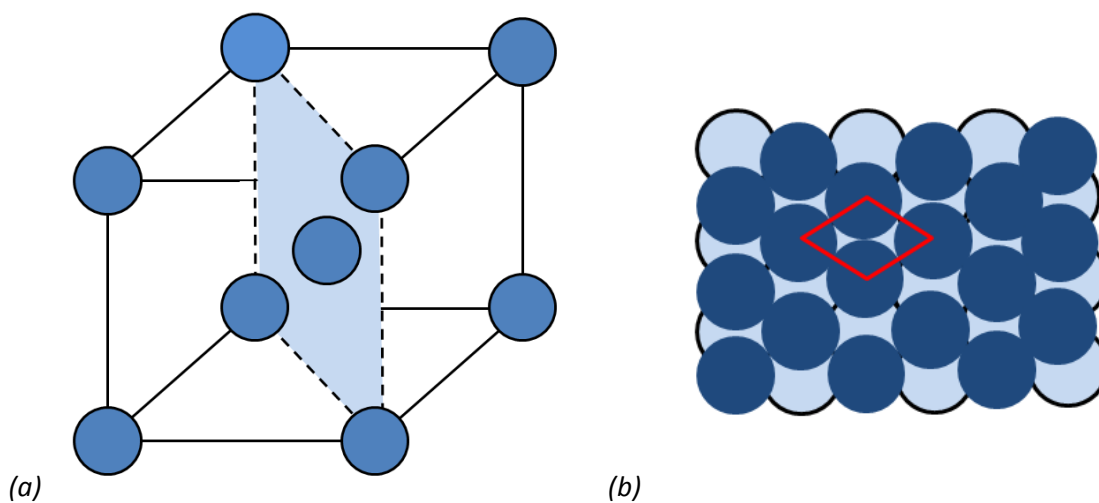


Figure 1.11(a) the $(1\ 1\ 0)$ plane and (b) the resulting surface of a b.c.c. metal The unit cell is shown in red.

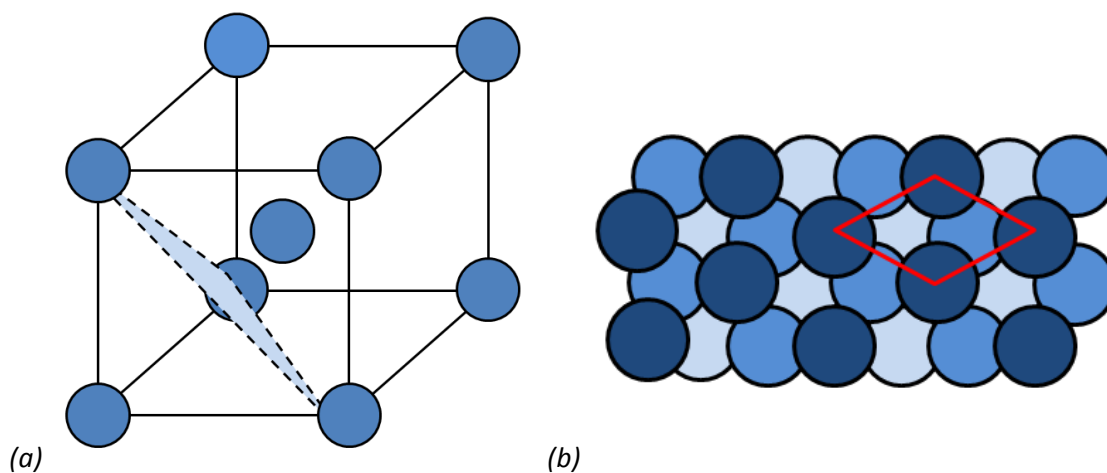


Figure 1.12(a) the $(1\ 1\ 1)$ plane and (b) the resulting surface of a b.c.c. metal The unit cell is shown in red.

The resulting surfaces are shown in Figure 1.10b, Figure 1.11b and Figure 1.12b with the unit cells shown in red. The co-ordination number of the surface atoms is the number of atoms at its nearest neighbour distance. The co-ordination numbers for the $(1\ 0\ 0)$, $(1\ 1\ 0)$ and $(1\ 1\ 1)$ surfaces are 4, 6 and 3 respectively. This means that the $(1\ 1\ 1)$ is the most open surface and therefore the most reactive. $(1\ 1\ 0)$ is the most densely packed surface and therefore the more stable of the three.

The unit cell of a surface is the smallest arrangement of atoms that can be repeated in order to form a pattern of atoms on the surface. The primitive unit cell is the simplest unit cell and contains just one atom.

1.5.2 REAL SURFACES

1.5.2.1 THE ROLE OF DEFECTS

Once a single crystal has been cut to expose the desired plane it is polished to a mirror shine. This polishing masks atomic scale defects present on the surface. Examples of surface defects include step edges from incomplete layers of atoms, terrace vacancies due to missing atoms, kinks in step edges due to missing atoms and adsorbed adatoms. These defects are depicted in Figure 1.13.

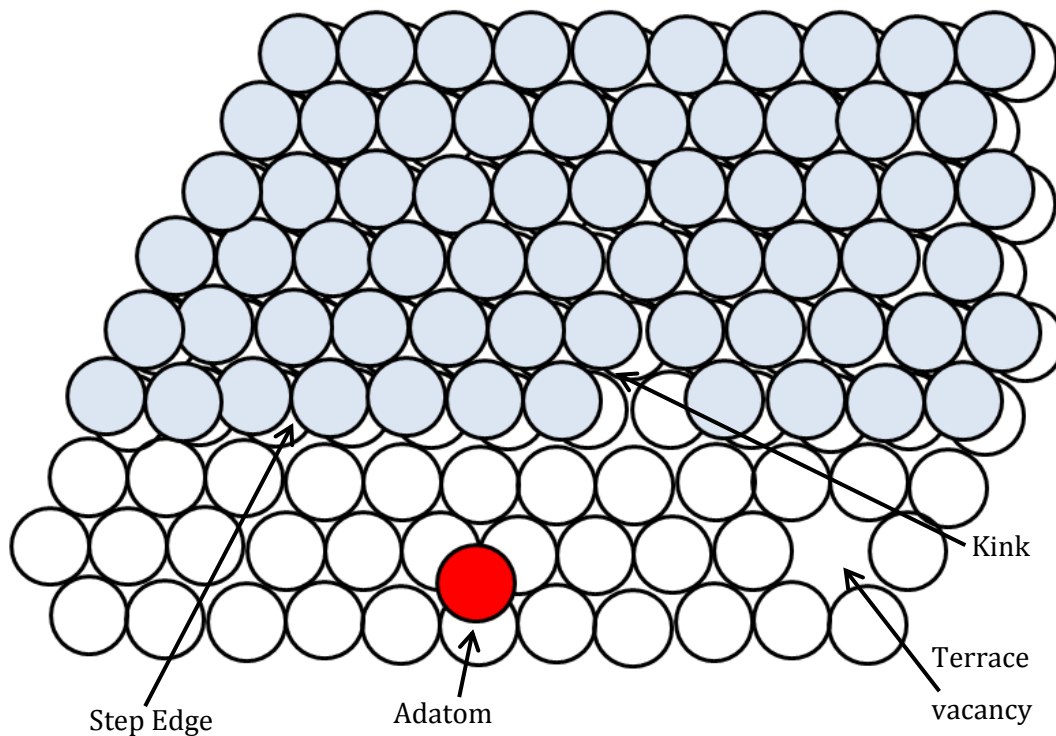


Figure 1.13 Schematic representation of typical surface defects

Defects are of interest to surface scientists as they are often the sites of reactions, due to their lower coordination than non-defective sites. This is because the lower coordination gives these sites a higher surface free energy, making the formation of bonds with adsorbates more likely, and also increasing the strength of bonds formed.

1.5.2.2 SURFACE RELAXATION AND RECONSTRUCTION

As previously mentioned surfaces are high energy due to the low coordination of the surface atoms. This means that energy is required to form a surface and that once formed a surface is energetically unfavourable. Surfaces can be stabilized in several ways, the first of which is surface relaxation. During this process the layer spacing's perpendicular to the surface contract, effectively pulling the surface atoms closer to the bulk. This slightly increases the coordination of the surface atoms by pulling them a little closer to the atoms underneath.

If the surface energy is much higher than the energy of atoms within the bulk surface reconstruction will occur. This is where the arrangement of atoms on a surface is altered in order to reduce the total surface energy. A classic example of the this is the rearrangement of the Gold (1 1 0) surface from a (1 x 1) to a (1 x 2) structure (Figure 1.14²⁴). Surface rearrangement is also commonly observed in semi-conductors.²⁴

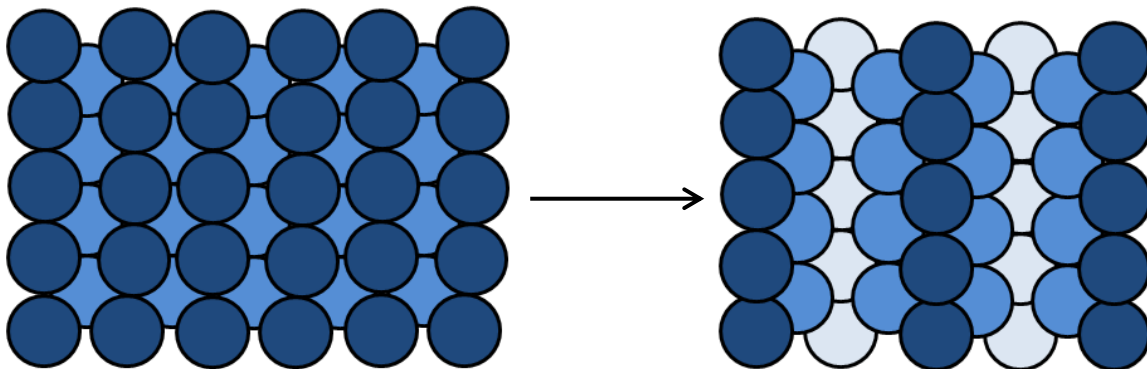


Figure 1.14 The surface reconstruction of Au (1 1 0) from a (1 x 1) to (1 x 2) structure.

The simplest method for a surface to reduce its free energy is the adsorption of a gas atom or molecule. This leads to the formation of bonds between the adsorbate and surface atoms, increasing the coordination of the surface atoms.

1.6 REACTIONS ON SURFACES

1.6.1 ADSORPTION ON SURFACES

When an atom collides with a surface it may either rebound off the surface (either elastically or inelastically) or be absorbed in one of two ways. Physisorption refers to the weak absorption of atoms or molecules based on Van der Waals interactions where there is no interaction of electron density. Chemisorption refers to the much stronger adsorption of atoms and molecules leading to bond formation. The fractional coverage of an adsorbate (θ) is given in Equation 1.1. When this value is one then all the available sites on a surface are occupied (known as a monolayer).

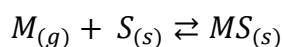
$$\theta = \frac{\text{Number of surface sites occupied by adsorbate}}{\text{Total number of available adsorption sites}}$$

Equation 1.1 Determining of fractional coverage of a surface.

Langmuir related the number of atoms absorbed at a given temperature to the gas pressure, P, and developed an isotherm for the determination of absorption given the following assumptions:

- The surface is uniform and all surface sites are equivalent and may only be occupied by one molecule of adsorbate
- At constant temperature the gas and adsorbed atoms are in dynamic equilibrium
- Adsorbate molecules are continually colliding with the surface and if they encounter a vacant site they will stick
- if a molecule encounters a filled site it will not diffuse to a vacant site but remains in the gas phase
- Once adsorbed a molecule will not move to a neighbouring site

For a gas in dynamic equilibrium with adsorbed atoms the following holds true:



Equation 1.2 dynamic equilibrium between a gas and a surface

Adsorption (the 'forward' reaction) will have a rate constant k_a and desorption (the 'back' reaction) k_d . The equilibrium constant (K) for this reaction is given by Equation 1.3

$$K = \frac{k_a}{k_d}$$

Equation 1.3 the equilibrium constant for the reaction given in Equation 1.2

At pressure P and fractional surface coverage θ the rate of adsorption is given by Equation 1.4 and the rate of desorption by Equation 1.5.

$$r_a = k_a P(1 - \theta)$$

Equation 1.4 rate of adsorption of gas molecules on a solid surface, where $(1-\theta)$ is the fraction of vacant sites present on the surface

$$r_d = k_d \theta$$

Equation 1.5 rate of desorption of gas molecules from a solid surface

At equilibrium the rates of these two processes are equal, as shown in Equation 1.6. This can then be rearranged to give the Langmuir Isotherm in its usual form (Equation 1.7).

$$k_a P(1 - \theta) = k_d \theta$$

Equation 1.6

$$\theta = \frac{KP}{1 + KP}$$

Equation 1.7 The Langmuir Isotherm. (θ = surface coverage, K = equilibrium constant, P = pressure)

The main drawback of the Langmuir Isotherm is that it does not allow for the formation of multilayers during adsorption. The heat of adsorption for a multilayer will be different to that of monolayer formation due to the differences in adsorbate-surface and adsorbate-adsorbate bond strengths.²⁴ Brunauer, Emmett and Teller applied the following additional assumptions to the Langmuir Isotherm

- The first adsorbate layer forms on a uniform surface with identical surface sites (as with the Langmuir isotherm)

- Adsorption of a second layer can take place on top of a first, third on top of second etc.
- When $P=P_0$ (the saturated vapour pressure of the adsorbate) an infinite number of layers will form
- The rates of condensation and desorption are the same for each layer at equilibrium
- In a multilayer system all thermodynamic equilibrium constants for adsorption (K^0) are equal for each layer

Application of these assumptions gives the BET isotherm (shown in its linear form, Equation 1.8).³⁴ The BET adsorption isotherm is also routinely used to measure the surface area of powdered materials.

$$\frac{P}{N_s(P_0 - P)} = \frac{1}{NC} + \frac{(C - 1)}{NC} \times \frac{P}{P_0}$$

Equation 1.8 The BET isotherm (P = pressure, N = total number of adsorption sites, N_s = number of occupied surface sites, C = BET constant ($\approx e^{(\Delta H^{\circ}_{des} - \Delta H^{\circ}_{vap})/RT}$)

1.6.2 ADSORPTION KINETICS

The sticking probability (S) is a measure of the likelihood of the collision of a gas molecule on the surface resulting in adsorption. Equation 1.9 shows the relationship between sticking probability and the coverage for Langmuir adsorption. However, this dependence is not linear in practice and generally sticking probability remains high as coverage increases, before dropping rapidly as θ approaches 1.

$$S = S_0(1 - \theta)$$

Equation 1.9 the relationship between sticking probability (S) and the coverage of a surface

This observation can be explained as the formation of a precursor state where the incoming molecule approaches a filled adsorption site and forms a weak interaction with the surface before diffusing to a vacant site. The adsorption of this precursor state is then dependent on the lifetime of the interaction with the surface (τ_0) and the enthalpy of adsorption (ΔH°_{ads}). The time this precursor is present on the surface (or residence time, τ) is given by Equation 1.10

$$\tau = \tau_0 e^{\Delta H^{\circ} ads/RT}$$

Equation 1.10 the Frenckel equation giving the residence time of a precursor state on a surface before adsorption

The longer the precursor is on the surface (i.e. the greater τ) the more likely adsorption is to occur.

1.7 THESIS SYNOPSIS

The experiments in this thesis can be split into two categories. The first set deals with the synthesis, curing and aging of phosphates and the effects of different additives to their stability. The aim of these experiments is to provide an insight into the properties of both test and on-line coatings developed at Cogent Power Ltd. This can be done by characterising the phosphates using a variety of techniques (including vibrational, spectroscopic and thermal methods). The second set of experiments aims to characterise the steel substrate and the first forsterite coating using surface science methods.

This chapter has provided an overview of surface science and electrical steels and their coatings. A brief description of the main properties of electrical steels has also been given, along with a history of coatings used.

Chapter two provides a description of all the techniques used, including relevant background theory and limitations to the techniques. A full description of the UHV chamber used in this investigation is given, as well as the reasons for the need for these conditions.

Chapter three examines the properties of model phosphate coatings, such as the effects of the curing process and the addition of different chromium oxides. The stability of the phosphates in humid environments is also probed through the use of a humidity chamber.

Chapter four covers XPS studies of phosphate coatings as powdered coatings, powdered model coatings and coatings on steel. The forsterite coating and bare steel substrate are also studied.

Chapter five summarises the main findings of the previous results chapters and gives the main conclusions taken from this work, along with a discussion of possible future work.

1.8 REFERENCES

1. http://en.wikipedia.org/wiki/Electrical_steel,
2. <http://en.wikipedia.org/wiki/Hysteresis>,
3. <http://www.codecogs.com/library/physics/magnetism/index.php>,
4. W. J. Duffin, *Electricity and Magnetism*, 4th edn., McGraw- Hill, 1997.
5. http://en.wikipedia.org/wiki/Magnetic_domain,
6. A. J. Moses, *Iee Proceedings-a-Science Measurement and Technology*, 1990, **137**, 233.
7. *US Pat.*, 1965559, 1934.
8. *US Pat.*, 4347085, 1982.
9. http://www.softmagneticalloy.com/soft_magnetic_materials.htm,
10. B. Fukuda, K. Sato, T. Sugiyama, A. Honda and Y. Ito, ASM Conf. Hard and soft magnetic materials symp 8710-008, Cincinnati, 1987.
11. A. J. Moses, J. E. Thompson and S. M. Pegler, *Proceedings of the Institution of Electrical Engineers-London*, 1972, **119**, 1222.
12. S. Szymura and B. Wyslocki, *Acta Physica Polonica A*, 1976, **49**, 627.
13. S. D. Washko and E. G. Choby, *Ieee Transactions on Magnetics*, 1979, **15**, 1586.
14. *US Pat.*, 2501846, 1950.
15. *US Pat.*, 2492095, 1949.
16. *US Pat.*, 2743203, 1956.
17. *US Pat.*, 3996073, 1976.
18. *US Pat.*, 3948786, 1976.
19. D. Poultney and D. Snell, *Journal of Magnetism and Magnetic Materials*, 2008, **320**, e649.

20. O. Tanaka, H. Kobayashi and E. Minematsu, *Journal of Materials Engineering*, 1991, **13**, 161.
21. Directive 2002/95/EC of the European Parliament and of the Council of 27 January 2003 on the restriction of the use of certain hazardous substances in electrical and electronic equipment Organization
22. Directive 2012/19/EU of the European Parliament and of the Council of 4 July 2012 on waste electrical and electronic equipment (WEEE) Organization
23. <http://www.cogent-power.com/downloads/Process-Diagram.pdf>
24. G. Attard and C. Barnes, *Surfaces*, Oxford Science Publications, Oxford, 1998.
25. G. Tricot, D. Coillot, E. Creton and L. Montagne, *Journal of the European Ceramic Society*, 2008, **28**, 1135.
26. I. Langmuir, *J. Chem Soc.*, 1916, **38**, 2221.
27. I. Langmuir, *J. Chem Soc.*, 1912, **34**, 1310.
28. G. A. Somorjai, *Introduction to Surface Chemistry and Catalysis*, John Wiley & Sons, Inc., 1994.
29. G. Binnig, H. Rohrer, C. Gerber and E. Weibel, *Surface Science*, 1983, **131**, L379.
30. G. Binnig and H. Rohrer, *IBM Journal of Research and Development*, 1986, **30**, 355.
31. K. Siegbahn, *ESCA; atomic, molecular and solid state structure studied by means of electron spectroscopy*, Almqvist & Wiksells, Uppsala, 1967.
32. H. Conrad, G. Ertl and E. E. Latta, *Surface Science*, 1974, **41**, 435.
33. http://en.wikipedia.org/wiki/Single_crystal,
34. S. Brunauer, P. H. Emmett and E. Teller, *Journal of the American Chemical Society*, 1938, **60**, 309.

CHAPTER 2 EXPERIMENTAL

2.1 Introduction	24
2.2 Sample Preparation.....	24
2.2.1 Steel Sheet samples and High Purity Gases.....	24
2.2.2 Powdered Industrial Samples.....	24
2.2.3 Phosphate preparation and humidity treatment	25
2.3 The Ultra High Vacuum System.....	26
2.4 Quadrupole Mass Spectrometer (QMS)	31
2.5 X-Ray Photoelectron spectroscopy (XPS)	32
2.5.1 Theory	32
2.5.2 Experimental.	37
2.5.3 XPS interpretation and quantification	38
2.5.4 Data Analysis	40
2.6 Attenuated total reflectance Infrared spectroscopy (ATR-IR).....	40
2.6.1 Introduction to Infrared Spectroscopy.....	40
2.6.2 Experimental	41
2.7 Raman Spectroscopy.....	42
2.7.1 Introduction to Raman Spectroscopy.....	42
2.7.2 Experimental	44
2.8 Powder X-Ray Diffraction (XRD).....	44
2.8.1 Introduction to XRD.....	44
2.8.2 Experimental	46
2.9 Thermo-gravimetric Analysis (TGA).....	46
2.9.1 Introduction to TGA.....	46
2.9.2 Experimental	48
2.10 References	48

2.1 INTRODUCTION

During these investigations a wide number of samples and techniques have been studied. This chapter aims to provide information on the samples used- single crystals, steel samples and powdered phosphate samples. This is followed by a description of basic theory behind the analytical techniques used, their practical application and describes the equipment used.

2.2 SAMPLE PREPARATION

2.2.1 STEEL SHEET SAMPLES AND HIGH PURITY GASES

Sheets of industrial steel samples were acquired from Cogent Power Ltd. Forsterite (MgSiO_4) coated and fully coated samples were obtained from the steel processing line and bare steel was produced by pickling forsterite coated samples in hydrogen fluoride (HF) at Cogent Power Ltd.

Before experimental work can be performed in the UHV chamber all samples must be cleaned in order to remove contaminants such as adventitious carbon. All cleaning was done in situ by sputtering and then annealing. Sputtering was performed using a PSP ISIS 3000 sputter gun. Ar^+ ions were used with ion energy of 2 kV for 30 minutes unless otherwise stated. XPS was used to confirm the surface was clean before experiments began.

Oxygen and argon (99.6% and 99.999% purity respectively) were present on the UHV gas line and were purchased from Argo International Ltd.

2.2.2 POWDERED INDUSTRIAL SAMPLES

Industrial coatings (typically consisting of aluminium orthophosphate and colloidal silica) were collected as liquids from the steel processing line (M2 line) and dried at 100 °C to produce a white powder. Additionally, a selection of powdered trial industrial coatings were received from Cogent Power Ltd. and used as received.

2.2.3 PHOSPHATE PREPARATION AND HUMIDITY TREATMENT

Aluminium orthophosphate ($\geq 95\%$ purity) and chromium orthophosphate (99.9% purity) were purchased from Sigma Aldrich Ltd. and used as received. All curing was performed by heating in air at the required temperature for 15 minutes.

Magnesium phosphate was synthesised by the addition of phosphoric acid solution in water (≥ 85 wt% Sigma Aldrich ACS reagent) to a slurry of magnesium oxide (Sigma Aldrich 98 % purity) in water with stirring at room temperature. This mimics the coating preparation route followed in industry.

Mixed model coatings were produced via the addition of chromium VI oxide (CrO_3 , $\geq 98\%$ purity Sigma Aldrich Ltd.) to a solution of the appropriate phosphate (typically 4.69 g) in water (50 cm^3) with stirring at room temperature.

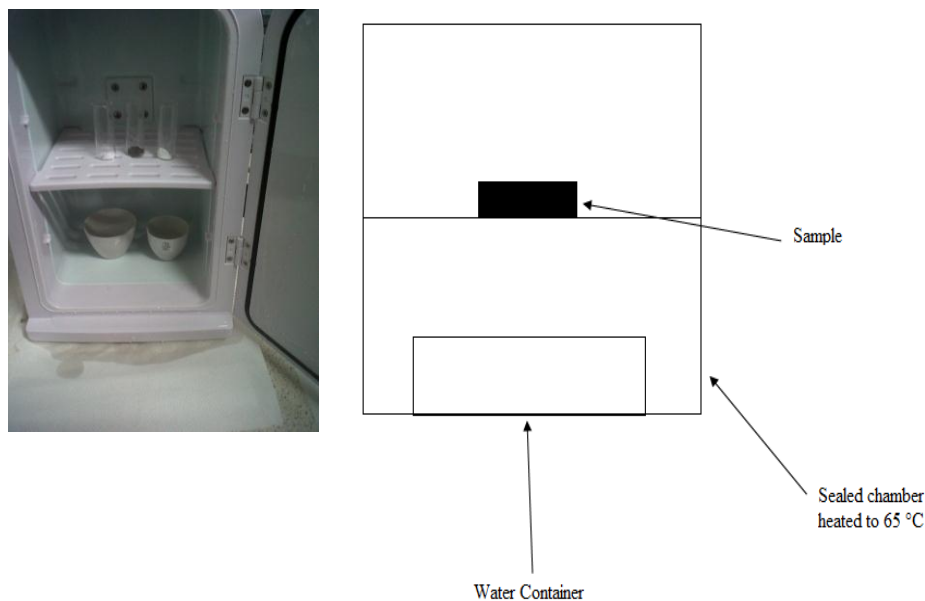


Figure 2.1 The Humidity Chamber used in this work

A humidity chamber was constructed for use during the PhD in order to investigate the effects of humidity on phosphates. A schematic of the chamber is shown in Figure 2.1.

The humidity and temperature inside the chamber was monitored for two week periods regularly using a RS 1364 digital humidity and temperature meter, in order to ensure they remained constant throughout. Example data from this process is shown in Figure 2.2. This testing showed the chamber to be stable provided that the water levels were kept constant.

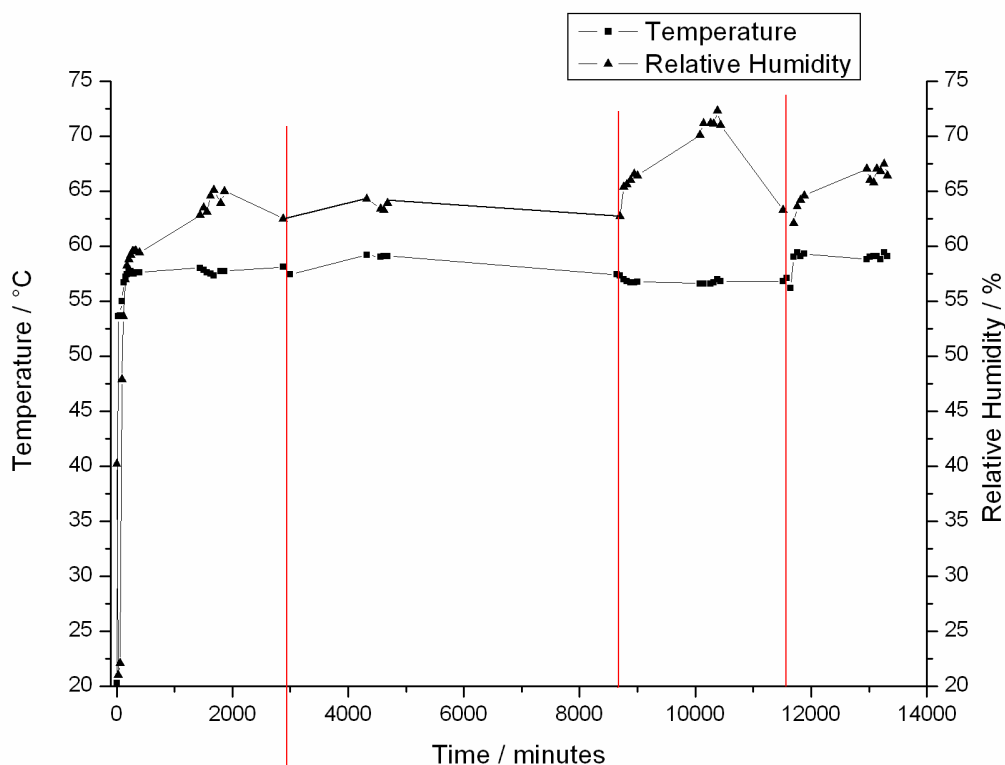


Figure 2.2 Temperature and humidity inside the chamber. The red lines indicate points where the chamber was opened for refilling

2.3 THE ULTRA HIGH VACUUM SYSTEM

Most surface science techniques are performed under vacuum for three main reasons. The first reason is to prevent scattering of electrons by gas molecules. This is important in techniques such as XPS which depend on the detection of electrons (see section 2.5). Prevention of this scattering requires pressures below 1×10^{-7} mbar.

A higher vacuum is required to prevent damage to the X-ray source and electron detector from discharges caused by the high voltages involved (up to 15 kV for the X-ray source). This requires pressures below 1×10^{-6} mbar.

The final reason a low background pressure is required is to prevent contamination of reactive sample surfaces by adsorption of background gases. The rate of surface bombardment by gas molecules is given by the Hertz-Knudsen equation (see Equation 2.1), derived from consideration of the kinetic theory of gases¹.

$$Z = \frac{p}{(2\pi mkT)^{1/2}}$$

Equation 2.1 the rate of surface bombardment by gas phase molecules. p = pressure, m = molecular mass, T = temperature, k = Boltzmann constant

The rate of contamination of the sample surface is then determined by the sticking probability (S , see Equation 2.2) which is a measure of how many gas molecules are absorbed when they collide with the surface.

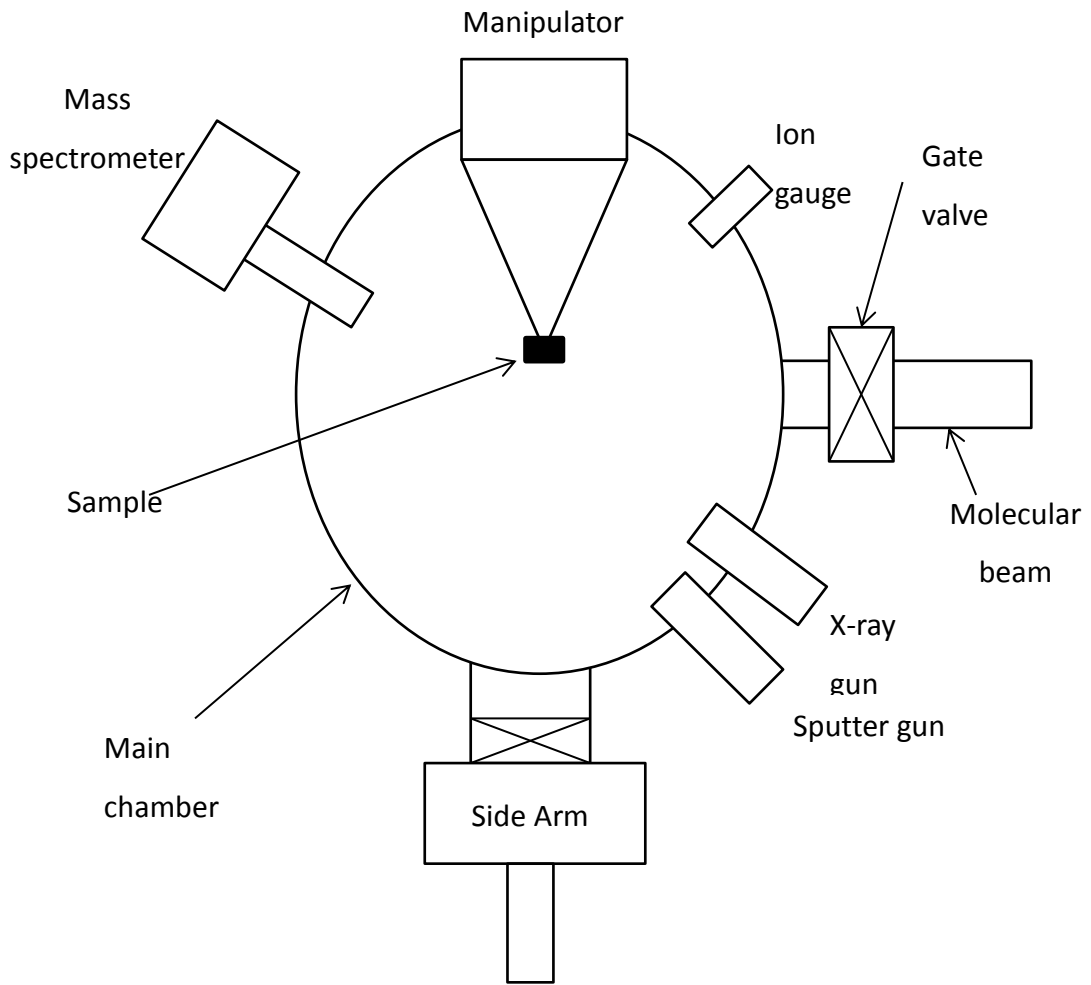
$$S = \frac{N_s}{N}$$

Equation 2.2 Measurement of sticking probability. S = sticking probability, N_s = number of surface sites occupied by adsorbate, N = total absorption sites

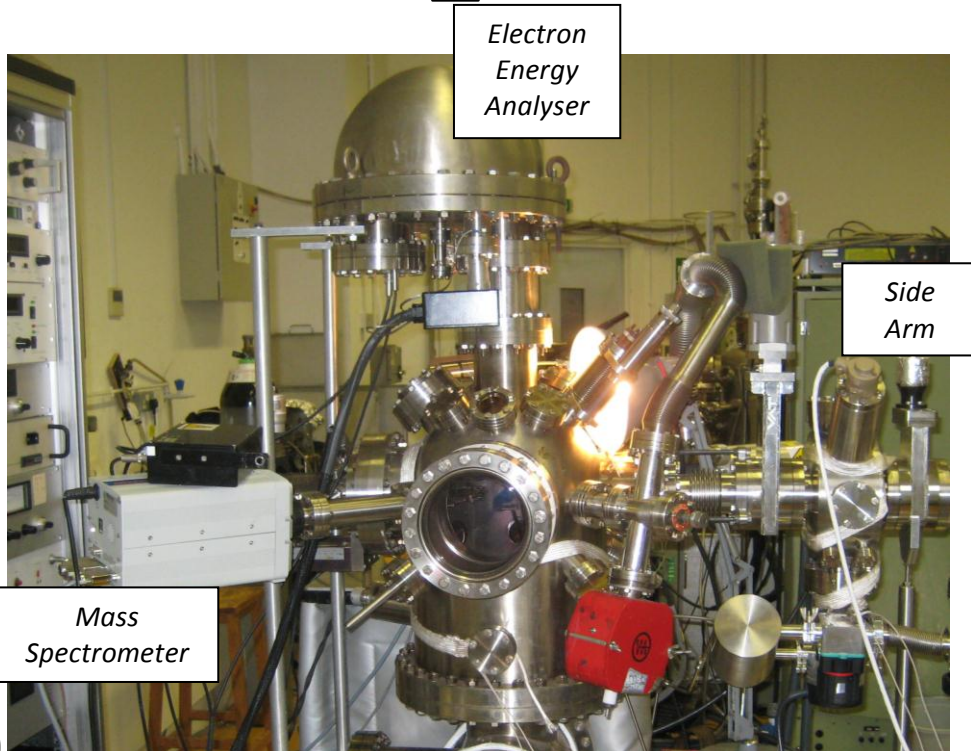
If carbon monoxide (a common gaseous contaminant) is used as an example, at a pressure of 1×10^{-6} mbar and room temperature (298 K) the bombardment rate is calculated to be $2.87 \times 10^{14} \text{ cm}^{-2}\text{s}^{-1}$. Using the assumption that the atomic density of the surface is $1 \times 10^{15} \text{ cm}^{-2}$, and the sticking probability is 1 (i.e. the surface is highly reactive and every collision results in absorption) the surface will be completely contaminated (i.e. a monolayer of carbon monoxide forms) after 3.48 seconds.

If the calculation is repeated for a pressure of 1×10^{-10} mbar the surface will be completely contaminated after 9.7 hours, which is an appropriate time frame for the majority of experiments. Pressures below 1×10^{-9} mbar are known as ultra-high vacuum (UHV).

The system used in this work is equipped with XPS, molecular beam, a mass spectrometer for molecular beam experiments and leak detection, a sputter gun for cleaning of samples, Pirani and Ionisation gauges for the measurement of pressure in the chamber and gas line. In addition to the experimental techniques a side chamber is also present, separated from the main chamber by a gate valve. This allows for a second sample to be inserted without the need to bring the entire system up to atmosphere. Schematics of the chamber are shown in Figure 2.3.



(a)



(b)

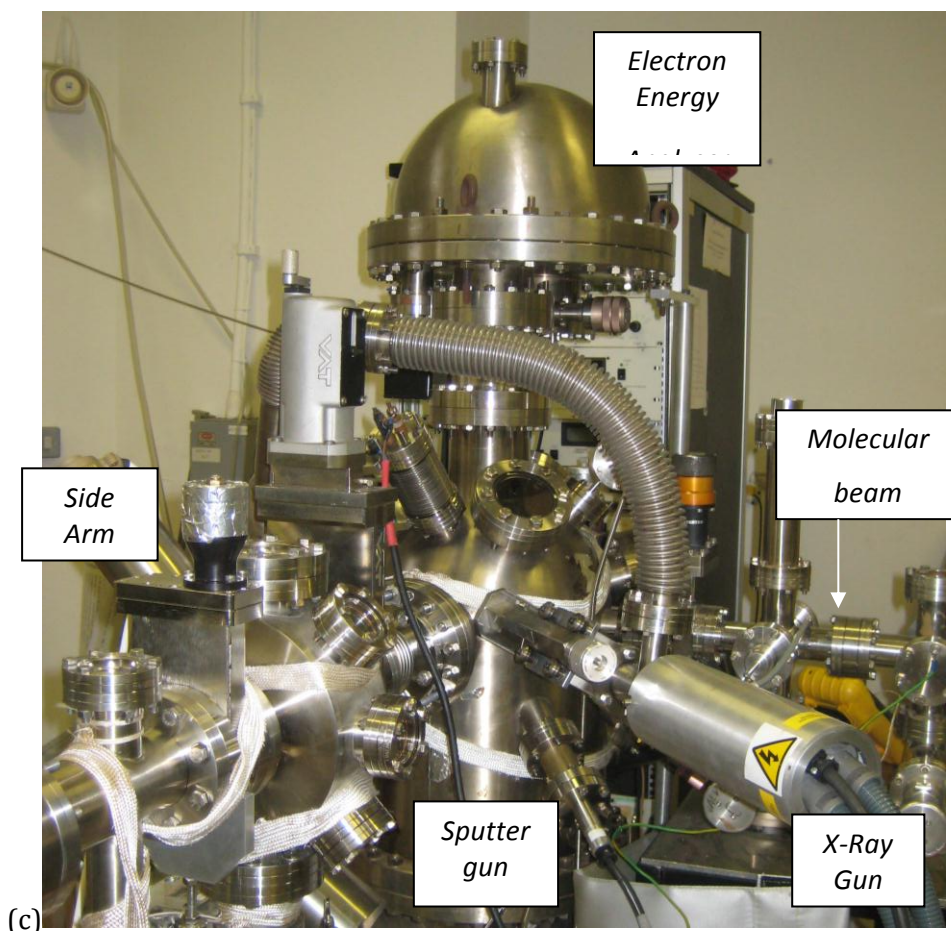


Figure 2.3 (a) Schematic, (b) and (c) photographs of the UHV Chamber used in this work

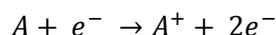
In order to achieve the low pressures required for experimental work the chamber is equipped with two types of pumps: turbo molecular and rotary vane. Rotary pumps are one of the most widely used types of pump and are a form of positive displacement pump. In the pump a slotted rotor turns inside a cylindrical stator driven by an electric motor, gas is drawn into the pump, compressed and expelled through the exhaust valve. The rotary pumps on the vacuum chamber are used to 'rough down' the system from atmosphere to around 1×10^{-2} mbar, after which the large turbo pump is started. The rotary pump then acts as a 'backing' pump for the main turbo. The turbo molecular pump is a form of molecular drag pump (a kinetic pump where gases molecules are given momentum through contact with the surface of the high speed motor directing the molecules towards the pump outlet) consisting of a rotor of slotted discs rotating between the discs of the stator.²

Once the turbo pump has reached pressures of around 1×10^{-7} mbar the system must be 'baked' to temperatures of up 140°C in order to achieve UHV conditions via desorption of background from the chamber walls and equipment.

Measurement of pressure inside the chamber is required in order to monitor the pumping down in the chamber (and checking for any possible leaks) as well as monitoring sputtering and the levels of gas the sample is exposed to during dosing. Due to the large range of pressures involved in the UHV chamber work (atmospheric to 1×10^{-10} mbar) the chamber is equipped with two types of gauges: the Pirani and ionisation gauges.

The Pirani gauge is a type of thermal conductivity gauge used to measure pressures between atmospheric and 1×10^{-4} mbar. The gauge works on the basis that the thermal conductivity of a gas is proportional to its pressure within this range. The gauge consists of a hot metal filament (typically platinum) suspended in a tube, and either the temperature or current of the filament is kept constant. At higher pressures gas molecules will collide more frequently with the filament and result in cooling. Therefore in a lower pressure the filament will be hotter (lower pressures result in fewer collisions and therefore less cooling). As the resistance of the wire is temperature dependent this allows for pressure in the chamber to be measured.² Pirani gauges are used on the gas line and during the initial pumping down of the UHV chamber.

The Ionisation gauge is used to measure pressures in the main chamber between 1×10^{-4} and 1×10^{-11} mbar. Ionisation gauges rely on the ionisation of molecules (A) in a low pressure gas by a beam of energetic electrons according to Equation 2.3²



Equation 2.3 ionic emission

The resulting ion current is given by Equation 2.4. The ions are collected by a negatively charged electrode called the collector and the current in the collector is proportional to the rate of ionisation which can be used to give a measurement of the pressure. The lower limit of the gauge is caused by the photoelectric effect as electrons produced will collide with the grid causing X-Ray emission. This emission causes photoelectric noise in the detector.

$$I^+ = nl\sigma I^-$$

Equation 2.4 ion current produced during thermionic emission. I^+ = ion current, n =molecular density, l = average electron path, σ = ionisation cross-section, I^- = electron current

The Ionisation gauge used on the UHV chamber is a form of hot cathode gauge known as the Bayard-Alpert hot cathode ionization gauge. This gauge consists of three electrodes (collector, filament and grid) with a small ion collector inside the grid. Electrons are emitted from the filament and move back and forth before entering the grid. During this process the electrons will collide with gas molecules to form ions.

2.4 QUADRUPOLE MASS SPECTROMETER (QMS)

The quadrupole mass spectrometer (QMS) is used in the ultra-high vacuum chamber in conjunction with the molecular beam, monitoring the composition of residual gases within the chamber, monitoring the purity of reactant gases as well as for leak detection. A schematic of a quadrupole mass spectrometer is shown in Figure 2.4.

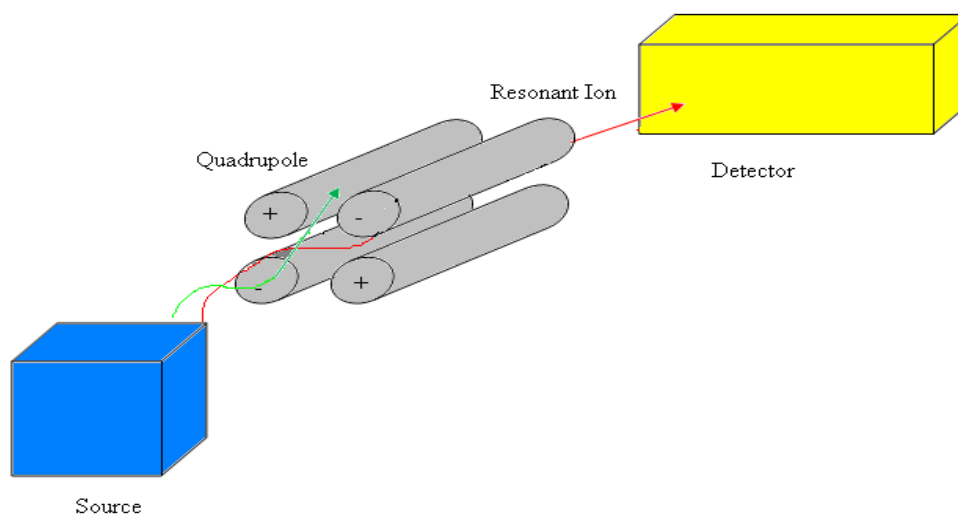


Figure 2.4 schematic of the quadrupole mass spectrometer

The analyser consists of four precisely matched metal poles set parallel to each other and separates ions based on their mass to charge (m/z) ratio. Opposing rods in the quadrupole are electronically connected and a radio frequency (RF) applied between the pairs with a direct current voltage superimposed. Two poles will have an applied potential of $(U + V\cos\omega t)$ and the others a potential of $-(U + V\cos\omega t)$ (U is dc voltage and $V\cos\omega t$ is the ac voltage where ω is the angular frequency). The ratio of these frequencies is varied and as the ions pass through the quadrupole only ions of a specific m/z (mass charge) ratio will reach the detector- all others will collide with the rods. Systematic variation of the ratio of frequencies (either through alteration of ω or U/V) produces a mass spectrum.

A ThermoVG QMS was used throughout this investigation in conjunction with the Gas Works Software suite. This mass spectrometer is capable of monitoring several masses simultaneously allowing for the study of initial beam reactivity, in addition to the products evolved in surface reactions during molecular beam experiments.

2.5 X-RAY PHOTOELECTRON SPECTROSCOPY (XPS)

2.5.1 THEORY

X-Ray Photoelectron spectroscopy (XPS) is one of the most widely used surface characterisation techniques due to its versatility and high surface sensitivity. XPS allows for not only the determination of elements present on a surface but can also provide information on chemical state of the elements.

XPS is reliant on the photoelectric effect first reported by Hertz in 1887³ where the bombardment of a metal with photons will cause the emission of electrons. Around ten years later Thomson identified the emission was caused by light⁴ and in 1915 Einstein provided a full description of the effect⁵ where discrete quanta of light are adsorbed causing electrons of specific energy to be emitted provided the photon energy ($h\nu$) is greater than the work function (the minimum energy required to remove an electron from the highest occupied energy level to the vacuum level, ϕ) (Equation 2.5).¹ Siegbahn utilised this photoelectric effect in the development of XPS (or ESCA (electron spectroscopy for chemical analysis)) during the 1960s.⁶

$$E_{KIN} = h\nu - E_B + \phi$$

Equation 2.5 the energy of electrons ejected during the photoelectric effect E_{KIN} = kinetic energy of ejected electron, h = Plancks constant, ν = wavelength, E_B = binding energy of electron, ϕ = work function

During an XPS experiment a monochromatic beam of X-rays is aimed at a solid surface causing the emission of core (electrons from the inner quantum shells which do not participate in bonding) and valence electrons (electrons from the weakly bound outer levels). Equation 2.5 shows that for a fixed photon energy photoemission from an atom with well-defined core-levels will produce photoelectrons with well-defined kinetic energies. The process of the X-ray excitation of a core shell electron is shown in Figure 2.5⁷. These core electrons are the key to

chemical identification using XPS, as they are relatively insensitive to chemical bonding and maintain consistent binding energies specific to the element.

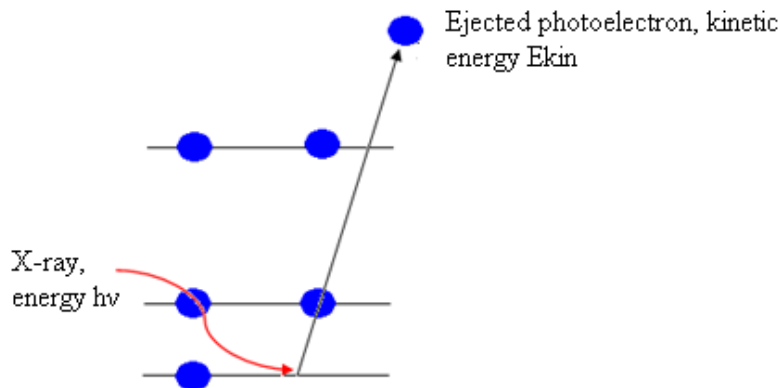


Figure 2.5 The X-ray excitation of a core shell electron during XPS

The energy of the photoelectron will be dependent on both the element and the oxidation state. The intensity of electrons ($N(E)$) is recorded as a function of kinetic energy and the resulting XP spectrum is usually plotted as $N(E)$ against binding energy.¹⁷

$$I(d) = I_0 \exp\left(\frac{-d}{\lambda(E)}\right)$$

Equation 2.6 The dependence of electron intensity on the distance travelled through the sample
 $I(d)$ is the intensity after travelling distance d through the solid, I_0 is the initial intensity and $\lambda(E)$ is the IMFP

The high surface sensitivity of XPS arises from the inelastic mean free path (IMFP λ) of the excited electrons generated during the experiment. The IMFP refers to the average distance the electron travels through the sample before it is inelastically scattered, and the intensity decays to $1/e$ of its initial value. The intensity of the electrons is dependent on the distance travelled through the solid and is known to obey Equation 2.6. The low IMFP of the electrons means that whilst the initial X-rays can travel several millimetres into the bulk of the sample the resulting photoelectrons will only be from the first few atomic layers.

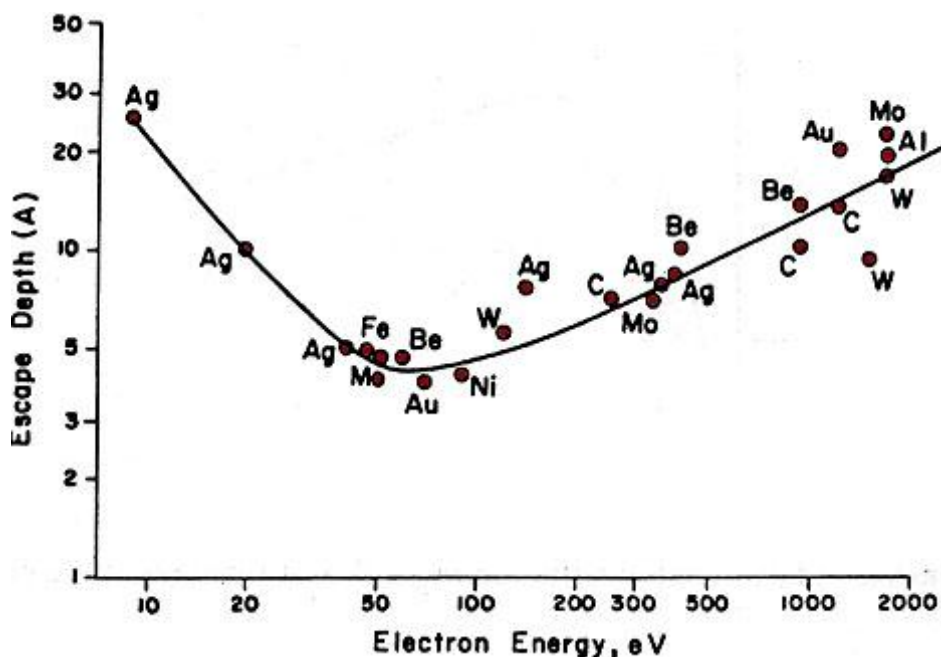


Figure 2.6 The 'Universal Curve' illustrating the relationship between the IMFP and Energy of the electron⁸

The IMFP is known to have a strong dependence on the kinetic energy of the electron. This relationship is shown in the 'universal curve' (Figure 2.6⁹) constructed from the measurement of IMFP for electrons generated from a range of metals. The figure clearly shows a minimum in IMFP when the electron has an energy of around 50 eV, and this is where the highest degree of surface sensitivity will occur. An empirical fit for the data was suggested by Seah (Equation 2.7⁸). When the kinetic energy is greater than 50 eV the IMFP increases as the IMFP is directly proportional to the square root of the energy and therefore velocity. This can be rationalised as the electron having a greater velocity, reducing the time taken to pass through the solid and therefore reducing the probability of a collision (and therefore inelastic scattering) occurring.

$$\frac{\lambda}{nm} = \frac{538a}{E^2} + 0.41a^{3/2}(E_{Kin})^{1/2}$$

Equation 2.7 The Dependence of an electron's mean free path on its energy where λ is the IMFP, E is the kinetic energy and a is the mean atomic diameter

Once photoemission has occurred during the XPS experiment there is a vacancy present in the core electron levels. This 'hole' is filled by the transition of an electron from a higher energy shell (known as the down electron). Once this transition has occurred the energy given off by

the electron is lost in one of two ways. The first is that the energy can be transferred to another electron, causing the emission of a second electron from the atom. This is known as the Auger process and is depicted in Figure 2.7. The emitted electron is known as the Auger electron.

The energy of the Auger electron is independent of the energy of the radiation used to cause the first excitation and therefore the electron may be used for elemental identification. All elements apart from hydrogen and helium (i.e. those with three or more electrons) will produce an Auger spectrum, with the complexity increasing with the number of electrons due to the greater number of transitions available.

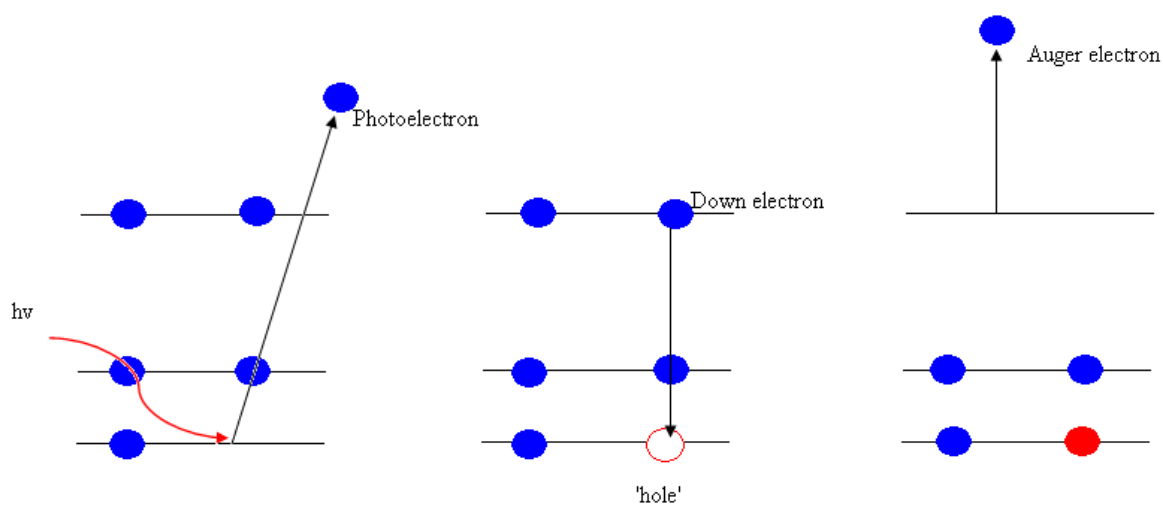


Figure 2.7 The Auger Process

The second process through which the atom can release the energy emitted by the down electron is to emit it as a photon of light. This process is known as X-ray fluorescence. The probability of Auger emission and X-ray fluorescence relative to atomic number is shown in Figure 2.8¹⁰. It is clear that Auger emission is favourable for elements with low atomic number whereas X-ray fluorescence becomes dominant for heavier elements.

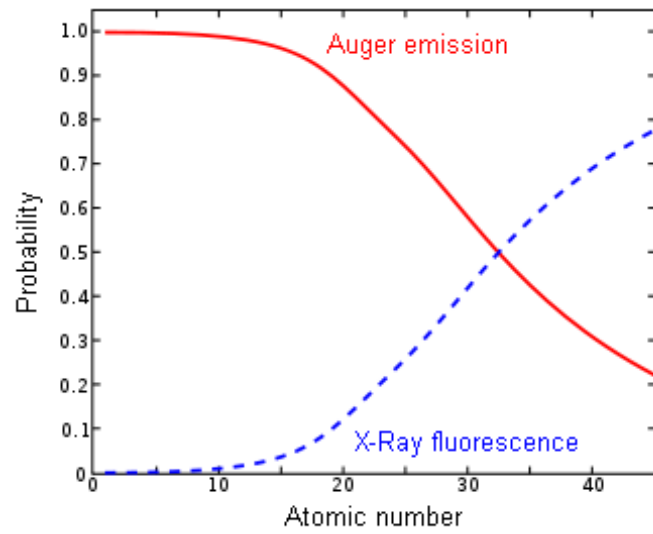


Figure 2.8 The probability of Auger emission and X-ray Fluorescence as a function of Atomic Number (taken from reference (11))

A typical wide scan of a clean Fe 3 % Si single crystal is shown in

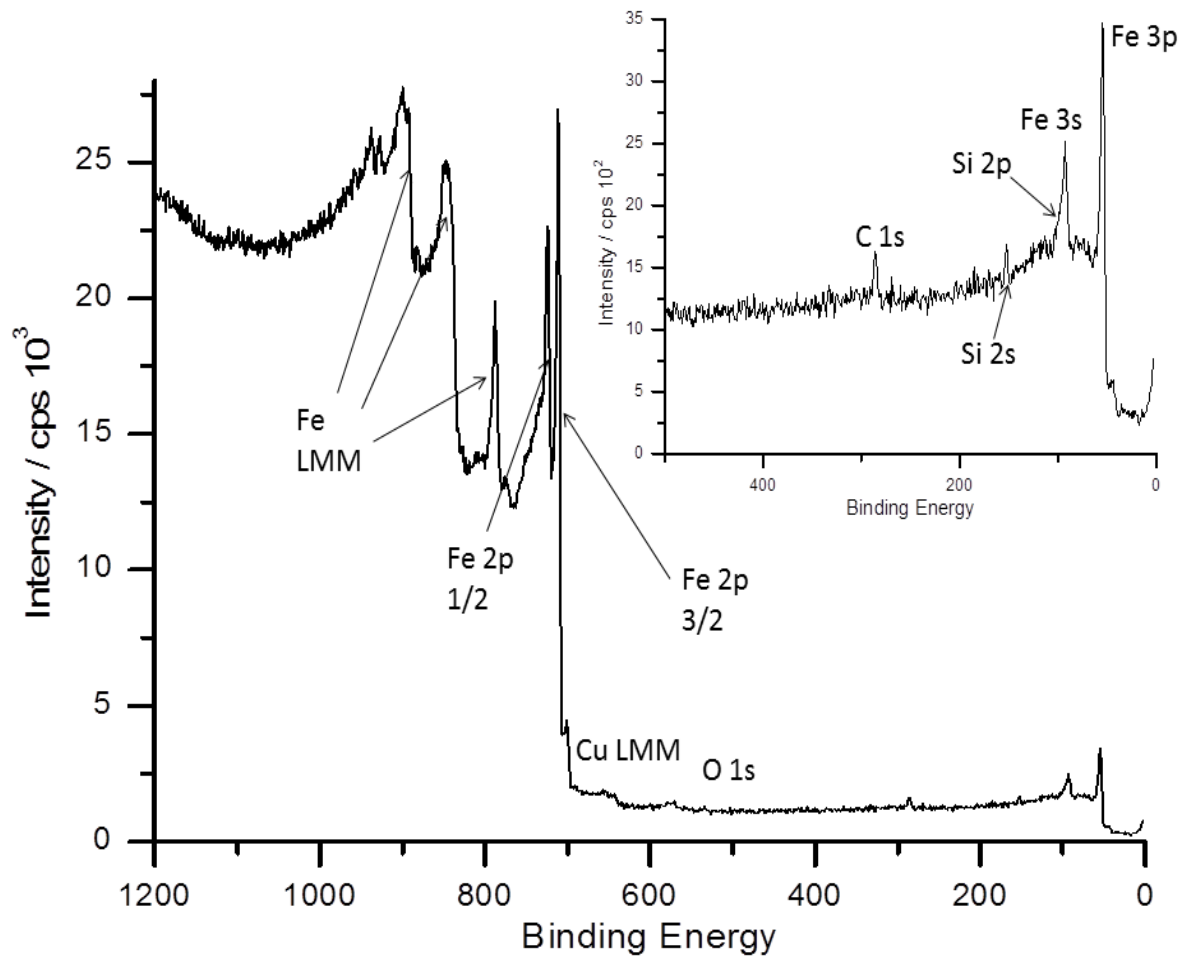


Figure 2.9. The spectrum consists of a series of peaks from XPS and Auger transitions over a background level of low energy electrons arising from inelastic scattering. The background is much larger at higher binding energy and consists of inelastically scattered electrons from XPS transitions and Bremsstrahlung radiation (produced by the deceleration of a charged particle when deflected by another charged particle, with a continuous spectrum) arising from X-ray generation.

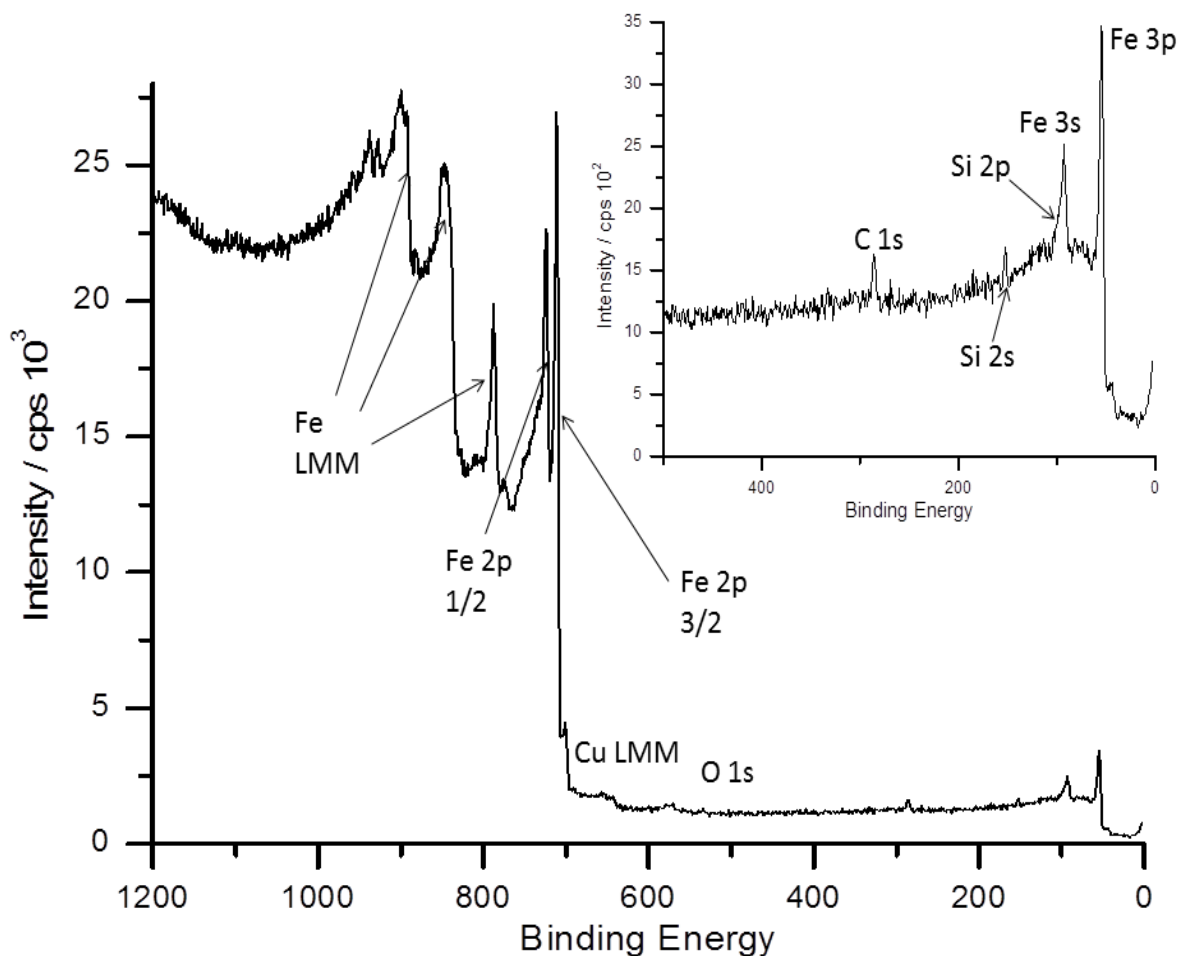


Figure 2.9 A typical XPS spectrum of a clean Fe 3% Si (100) surface

2.5.2 EXPERIMENTAL.

Two XPS systems were used to collect the spectra used in this study. All XPS spectra from the heating studies of the steel sheet samples were collected using a PSP TX400 X-ray source and resolve detector with a Spellman SL600 electronic supply. A pass energy of 100 eV was used for the wide scans and 50 eV for all regions.

The X-ray gun (Figure 2.10) consists of a twin anode source which produces both magnesium $K\alpha$ (1253.6 eV) and aluminium $K\alpha$ (1486.6 eV) radiation. The gun contains two filaments which produce electrons via thermionic emission. These electrons collide with the anode to produce the required emission- switching the filament used allows for a change in excitation source.

The X-rays produced leave the source through the aluminium window which has two roles in protecting the sample from heating effects, stop and reducing the amount of Bremsstrahlung radiation and secondary electrons to reach the sample.

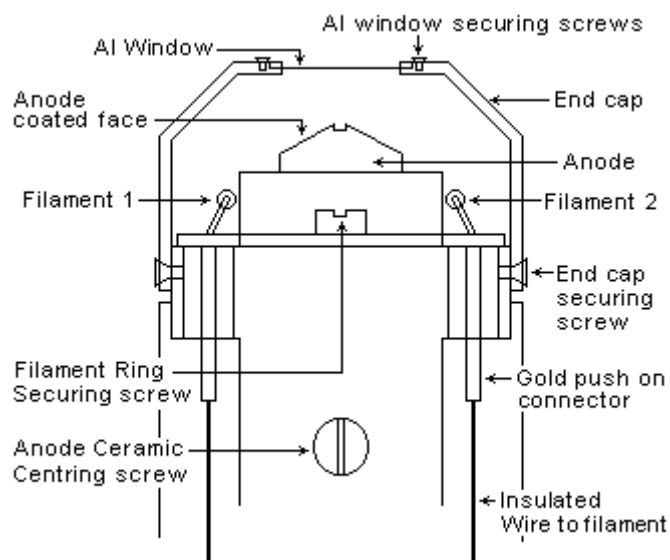


Figure 2.10 Schematic of the x-ray gun head, taken from the PSP vacuum technology x-ray source for XPS laboratory manual.

The detector used was a hemispherical analyser as developed by Siegbahn in 1967⁶. The detector consists of two concentric hemispheres with a potential difference between them. This electrostatic field only allows electrons of a specific energy (the pass energy) through the detector, higher energy electrons will hit the outer hemisphere, lower energy electron the inner one. Electrons are slowed by a negative electron known as the retard plate. By varying the voltage on this plate electrons of different kinetic energy can reach the detector at the end of the analyser and a spectrum can be recorded.

The XP spectra of all powdered samples and some steel sheet samples were collected on the Kratos AXIS ULTRA- DLD.

2.5.3 XPS INTERPRETATION AND QUANTIFICATION

One of the major advantages of XPS in surface science is it allows for the calculation of the concentration of atoms adsorbed onto the surface of the crystal of interest, as the area of an XPS peak is directly related to the surface abundance of an element. Madey first proposed an

equation relating the surface concentration of an adsorbate to its XPS signal in 1973¹². This was modified by Carley and Roberts in 1978 into the well-known Carley-Roberts equation (Equation 2.8¹³)

$$\frac{Ke_A}{Ke_S} \times \frac{I_A}{I_S} \times \frac{\mu_S N_A \lambda_s \rho_s \cos \theta}{\mu_A m_S}$$

Equation 2.8 The Carley- Roberts equation for the quantification of an adsorbate on a surface.

Where σ = surface coverage, A= adsorbate, S= substrate, Ke= kinetic energy, I= Intensity, μ = ionisation cross section, N_A = Avagadros Constant, λ = mean free path of substrate electrons through substrate, ρ = density of substrate

Data for determination of the asymmetry constant have been published by Reilman et al.¹⁴ The ionisation cross section of XPS peaks (μ) were tabulated for each element at 1254 and 1487 eV ($K\alpha$ emissions of magnesium and aluminium respectively) by J Scofield.¹⁵ Unfortunately these values do not allow for variation caused by the angle between the analyser and x-ray source. The corrected ionisation cross section is given by Equation 2.9

$$\mu' = \mu \left(1 - \frac{\beta}{2} P_z(\cos \theta) \right)$$

Equation 2.9 Corrected ionisation cross-section μ = ionisation cross section, β = asymmetry constant,

$$\theta = \text{angle between x-ray source and analyser, } P_z(x) = \frac{3x^2-1}{2}$$

Many of the terms within the Carley-Roberts equation remain constant for a particular adsorbate-substrate system and therefore the equation can be simplified as shown in Equation 2.10.

$$\sigma_A = A(I_A/I_S)$$

Equation 2.10 Simplification of the Carley-Roberts Equation

A major weakness of the Carley- Roberts equation is that it will only hold true for coverages less than one monolayer. For higher coverages Equation 2.11 must be used as it takes into account the attenuation of the substrate XPS signal by the adsorbate.

$$d = \frac{\lambda(\ln I - \ln I_0)}{-\cos\theta}$$

Equation 2.11 Calculating the Depth of a surface absorbate where d= film thickness, I= intensity of substrate, I₀= intensity of clean substrate λ= IMFP of substrate electrons through absorbate

2.5.4 DATA ANALYSIS

All XPS analysis was performed using the CasaXPS software.¹⁶ Regions were created around each elemental transition and a Shirley background was applied. The expected number of components was inserted under the curve and adjusted until a reasonable fit was achieved. In general the full-width half maximum values were restricted to remain below 2 when fitted data collected using the Kratos spectrometer, slightly wider components were allowed when fitting data collected with the PSP spectrometer.

When Spin-Orbit splitting was observed (for example in the Fe 2p spectrum) components were fitted in pairs with the intensity and full width half maximum values constrained relative to each other. In the Fe 2p this would mean the component within the 1/2 transition would be constrained to have the same full width half maximum value as the 3/2 transition. The area of the 1/2 component would be constrained to be half that of the 3/2 transition.

2.6 ATTENUATED TOTAL REFLECTANCE INFRARED SPECTROSCOPY (ATR-IR)

2.6.1 INTRODUCTION TO INFRARED SPECTROSCOPY

Infrared Spectroscopy (IR) is a powerful technique for the probing of molecular bonds. The technique is an absorption technique and uses light in the range 10-4000 cm⁻¹ depending on the information required, however commonly the range of 400-4000 cm⁻¹ is used (mid-infrared).

An in depth discussion of the interaction of molecules with IR radiation can be found in any book covering basic spectroscopy for example 'Fundamentals of Molecular Spectroscopy' by Banwell and McCash¹⁷

2.6.2 EXPERIMENTAL

The infrared spectrometer used in this study is the Varian 600 UMA FT-IR microscope. It is a Fourier transform infrared (FT-IR) spectrometer and is capable of attenuated total reflectance (ATR) spectrometry. During an IR experiment Infrared light is passed through the sample and then an interferometer with a mirror. This results in an 'interferogram' which is processed using a Fourier Transform to produce the required spectrum. FTIR is favoured over other IR methods as data from all frequencies is collected simultaneously, improving both the speed of collection and the signal to noise. The resulting output is the absorbance as a function of wavenumber.

In this study the ATR method was used to collect the IR spectrum. The main benefits of using this method are the increase in surface sensitivity, the reduction in sample preparation time and the increase in signal. In ATR-IR the sample is pressed against a crystal with a high refractive index (in this case germanium). The Infrared beam passes through the crystal and is internally refracted. The internal refraction causes the formation of an evanescent wave which extends out of the crystal slightly and into the sample. Some of this wave is absorbed by the sample and alters the wave. These alterations are detected and are used to produce the infrared spectrum of the sample as summarised in the Figure 2.11.

In order for the technique to be effective good contact must be between the sample and germanium crystal as the evanescent wave only travels a few microns outside of the crystal. Additionally the refractive index of the crystal must be higher than that of the sample or internal reflectance will not occur.

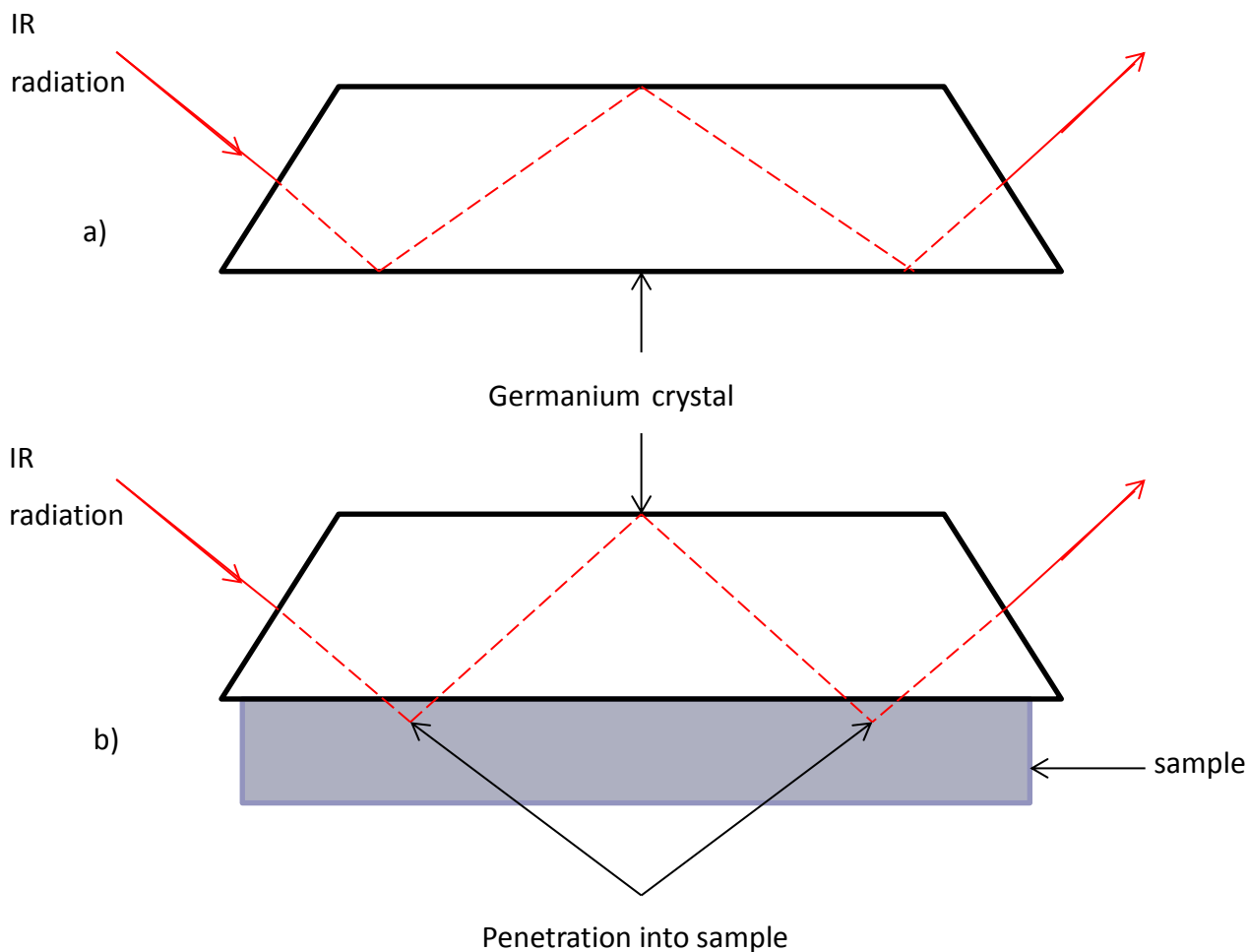


Figure 2.11 Schematic of ATR a) internal reflection within the germanium crystal b) penetration into the sample pressed against the crystal. Adapted from Banwell and McCash¹⁷

2.7 RAMAN SPECTROSCOPY

2.7.1 INTRODUCTION TO RAMAN SPECTROSCOPY

As with infrared spectroscopy (IR) Raman spectroscopy is a vibration technique which probes bonds present in molecules. Raman spectroscopy is often used as a complimentary technique to IR as the techniques have different selection rules and therefore probe different bonds. In IR spectroscopy a permanent electric dipole is required for a molecule to be spectroscopically active however in Raman spectroscopy a change in polarisability is required.

During Raman spectroscopy a beam of monochromatic light (typically from a laser) is scattered by a sample. This beam of light is viewed as a stream of photons with energy $h\nu$. If the light is directed at a molecule it can interact with it in several ways. If the light is scattered elastically (no change in energy of the incident photon) as the majority of photons are the scattering is known as Rayleigh scattering. A very small percentage of the photons are inelastically scattered (energy is lost or gained)-this is known as Raman scattering (see figure 1). Raman scattering can be further divided into Stokes (where energy is lost) and anti-Stokes (where energy is gained) scattering.

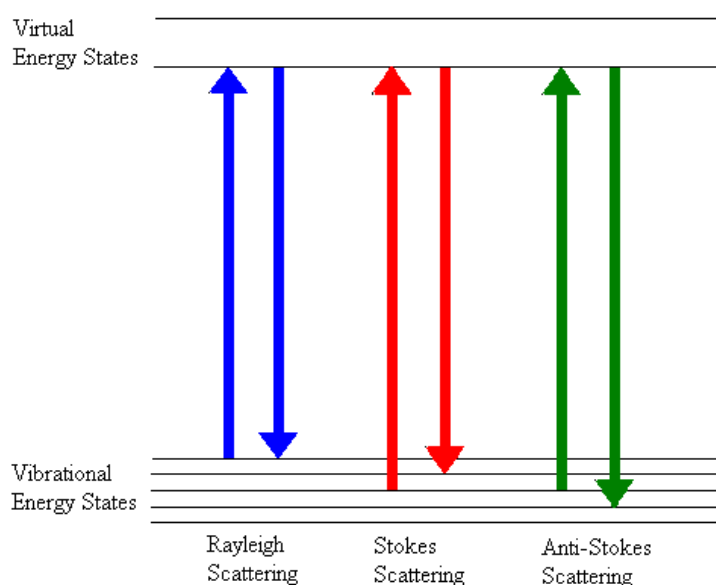


Figure 2.12 Rayleigh and Raman Scattering

Energy is lost or gained by the photon through the following process. The incident photon exposes the molecule to an oscillating electric field inducing a time-dependent electric dipole moment in the molecule. This dipole itself emits electromagnetic radiation which is seen as the lower or higher energy photon.

As the internal energy of the molecule is quantised (can only have specific values) the energy of the scattered light will only be altered by specific amounts. As the energy of light is related to its frequency the frequency components of the scattered light will be shifted from the incident frequency by discrete values (giving the observed bands in the Raman spectrum).

2.7.2 EXPERIMENTAL

In a typical modern Raman spectrometer monochromatic light from a laser is focused on a sample. The scattered light is viewed at a right angle to the incident radiation and is resolved into its component wavelengths with a high resolution instrument such as a monochromator or interferometer. This instrument set up is summarised below in Figure 2.13.

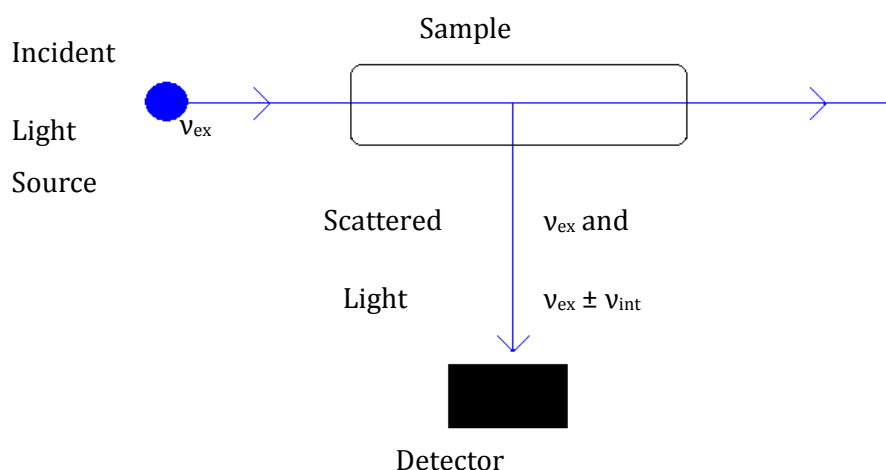


Figure 2.13 typical experiment set-up of a modern Raman spectrometer

The Raman spectrometer available in the School of Chemistry is a Renishaw microscope with two lasers- one with a wavelength of 514 nm (visible light) and one with a wavelength of 785 nm (near IR). The spectrometer uses a CCD (charged couple device) detector. All spectra reported in this investigation were recorded by placing a small amount of sample on a clean aluminium slide and focusing the laser using a camera within the Raman enclosure. All spectra were recorded using the argon (Ar+) laser ($\lambda = 514$ nm) and the spectrometer was calibrated daily using a silicon standard.

2.8 POWDER X-RAY DIFFRACTION (XRD)

2.8.1 INTRODUCTION TO XRD

XRD is one of the oldest and most widely used characterisation techniques¹⁰ developed by the Braggs at the turn of the century. The technique can be used to probe both the phases present in

a sample and the particle size. The wavelength of an X-ray is generally around a few angstroms (i.e. comparable to atom spacing within a solid) meaning it will be diffracted by a well ordered solid. The diffraction angle of the scattered X-rays can be predicted using the Bragg equation (Equation 2.12)

$$n\lambda = 2d\sin\theta$$

Equation 2.12 The Bragg Equation predicting Diffraction angle of X-rays diffracted by a well ordered solid n = an integer, λ = wavelength of X-rays, d = lattice spacing, ϑ = diffraction angle

This equation assumes that the lattice planes of the crystal are stacked and each reflect the incident radiation as shown in Figure 2.14. The net difference in path length between the waves is $AB + BC$ which equates to $2d\sin\theta$. If this distance is equal to integral number of wavelengths (i.e. $n\lambda = 2d\sin\theta$) the waves will be in-phase and constructive interference will occur, allowing the spacing between atoms to be calculated using the Bragg equation (Equation 2.12). If $AB + BC$ is not equal to $n\lambda$ than the interference will be destructive and no signal will be detected.

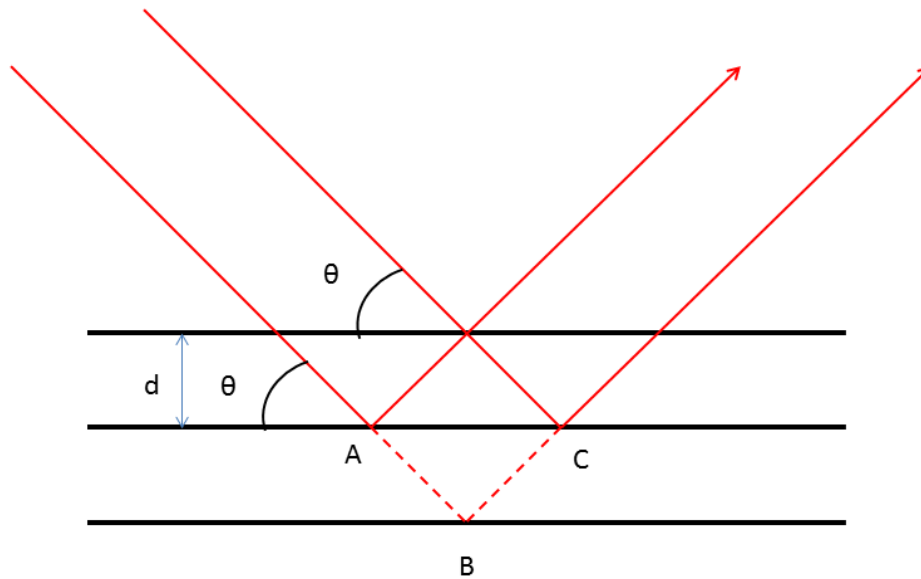


Figure 2.14 X-ray diffraction within a solid

Powdered samples were used in this investigation and therefore a powder diffractometer was used to measure the bulk composition. A powder consists of many randomly oriented crystals, within which several will satisfy the Bragg equation.

2.8.2 EXPERIMENTAL

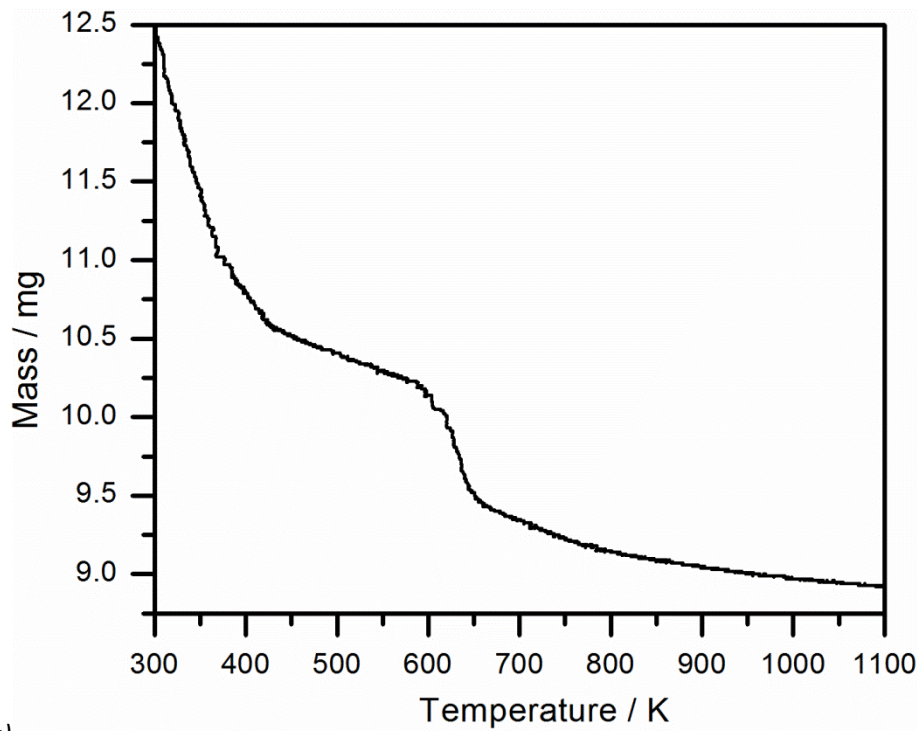
The XRD used in this investigation was the Panalytical X-pert pro spectrometer. The copper K α radiation was used with a voltage of 40 kV and current of 40 mA. The spectra were analysed using the High Score Plus database.

2.9 THERMO-GRAVIMETRIC ANALYSIS (TGA)

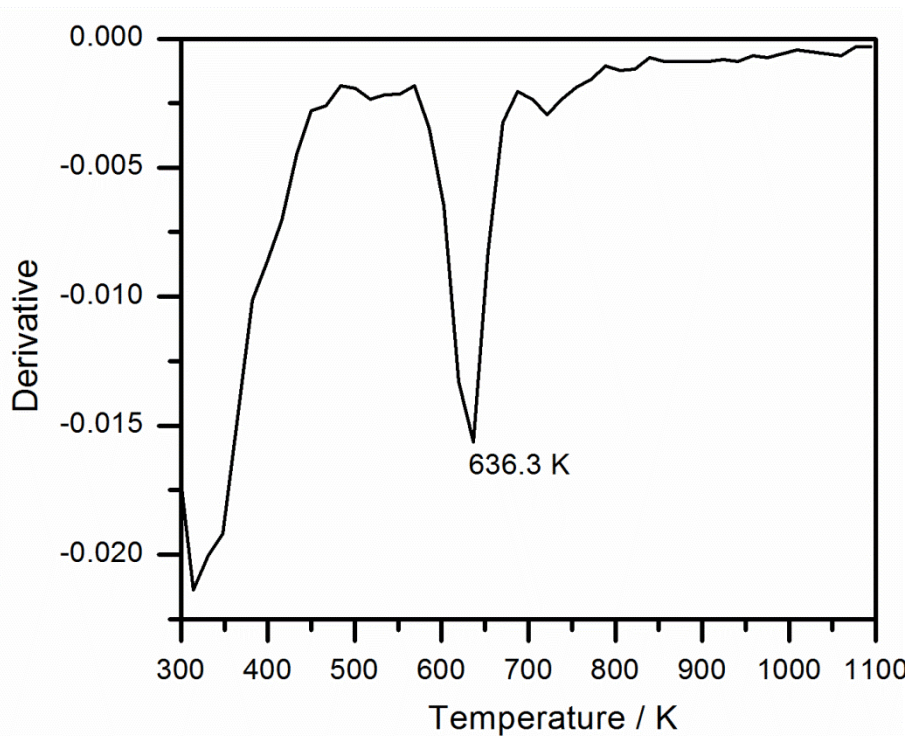
2.9.1 INTRODUCTION TO TGA

Thermal gravimetric analysis (TGA) is a form of analysis where changes in weight are monitored relative to temperature. The analysis requires a high degree of precision in monitoring both the weight and temperature of a sample. During thermogravimetric analysis the sample is heated to a high enough temperature to cause the decomposition of components of a sample, which are then lost from the sample as a gas. If the components of the mixture are known then percentage weight losses from the sample can be used to determine what is evolved.

TGA is often used in conjunction with differential thermal analysis (DTA) or differential scanning calorimetry (DSC). These techniques are used to determine if the degradation seen in the TGA is endothermic or exothermic, and also provide information on processes with no associated weight loss (i.e. melting and crystallisation). As many weight loss curves are unclear the information is often plotted in a differential weight curve in order to identify the points with the highest weight loss.



(a)



(b)

2.15(a) A weight vs. temperature curve and (b) a differential weight curve from a typical TG analysis of magnesium phosphate

2.9.2 EXPERIMENTAL

The TGA used in this investigation was the Stanton-Redcroft STA-780. A ramp rate of 10 °C min⁻¹ was used for all experiments and the sample heated from room temperature to approximately 800 °C.

2.10 REFERENCES

1. G. Attard and C. Barnes, *Surfaces*, Oxford University Press, 1998.
2. A. Chambers, R. K. Fitch and B. S. Halliday, *Basic Vacuum Technology*, 1 edn., Adam Hilger, IOP Publishing Ltd, 1989.
3. H. Hertz, *Annalen der Physik und Chemie*, 1887, **267**, 983.
4. J. J. Thomson, *Philosophical Magazine*, 1899, **48**, 547.
5. A. Einstein, *Annalen der Physik*, 1905, **322**, 132.
6. K. Siegbahn, *ESCA; atomic, molecular and solid state structure studied by means of electron spectroscopy*, Almqvist & Wiksells, Uppsala, 1967.
7. <http://www.ifw-dresden.de/institutes/ikm/organisation/dep-31/methods/x-ray-photoelectron-spectroscopy-xps>,
8. M. P. Seah and W. A. Dench, *Surface and Interface Analysis*, 1979, **1**, 2.
9. http://www.virginia.edu/ep/SurfaceScience/electron_interactions.htm,
10. J. W. Niemantsverdriet, *Spectroscopy in Catalysis*, Wiley-VCH, Weinheim, 2007.
11. http://en.wikipedia.org/wiki/Auger_electron_spectroscopy,
12. T. E. Madey, J. T. Yates and N. E. Erickson, *Chemical Physics Letters*, 1973, **19**, 487.
13. A. F. Carley and M. W. Roberts, *Proceedings of the Royal Society of London Series a-Mathematical Physical and Engineering Sciences*, 1978, **363**, 403.
14. R. F. Reilman, A. Msezane and S. T. Manson, *Journal of Electron Spectroscopy and Related Phenomena*, 1976, **8**, 389.

15. J. H. Scofield, *Journal of Electron Spectroscopy and Related Phenomena*, 1976, **8**, 129.
16. www.casaxps.com,
17. C. N. Banwell and E. M. McCash, *Fundamentals Of Molecular Spectroscopy*, 4th edn., McGraw-Hill, 1994.

CHAPTER 3 THE STABILITY OF MODEL PHOSPHATE COATINGS

3.1 Introduction.....	51
3.2 Background.....	52
3.2.1 The Structure and Stability of Aluminium Phosphates.....	52
3.2.2 The Synthesis and Stability of Magnesium Phosphates.....	55
3.3 The Synthesis and Curing of Model Phosphate Coatings.....	57
3.3.1 Curing of Model Aluminium Phosphate Coatings.....	57
3.3.2 The Synthesis and Curing of Model Magnesium Phosphate Coatings.....	60
3.3.2.1 The Effects of Magnesium Oxide: Phosphoric Acid Ratio.....	65
3.4 Aging of Model Phosphate Coatings.....	74
3.5 The Effects of Chromium Addition on Model Phosphate Coatings.....	76
3.5.1 The Curing of Chromium Oxide.....	77
3.5.2 The Effects of Chromium Addition to Model Magnesium Phosphate Coatings.....	81
3.5.2.1 The Role of Chromium Oxide Concentration.....	81
3.5.2.2 The Role of Temperature.....	90
3.5.3.3 Probing The Active Chromium Species.....	98
3.5.3 The Effects of Chromium Addition to Model Aluminium Phosphate Coatings.....	100
3.6 Summary.....	107
3.7 References.....	108

3.1 INTRODUCTION

In this chapter the structure and stability of model phosphate coatings are studied. The final phosphate coating is important for reducing the energy losses (caused by magnetostriction- the expansion and contraction of steel when a current is applied) by holding the sheet under tension. The application of a phosphate based coating has been shown to reduce losses by 10-15 % when compared to uncoated steel when evaluated via the loss separation method¹. "Stress coatings" were introduced by Nippon Steel in 1965 and phosphates were studied extensively from the early 70's.²

There are several structural forms of phosphate- the main ones of relevance for this work are orthophosphates (PO_4) pyrophosphates (P_2O_7) and metaphosphates (PO_3), the structures of which are shown in Figure 3.1. The aim of this work is to build an understanding of the changes that occur in the phosphates during the curing process used in production (see chapter 1) and during usage of the electrical steels. A full understanding of these processes is vital to the development and optimisation of new coating materials. The structures will be studied using spectroscopic (ATR-IR and Raman) and diffraction (XRD) techniques and their stability under humid conditions will be probed.

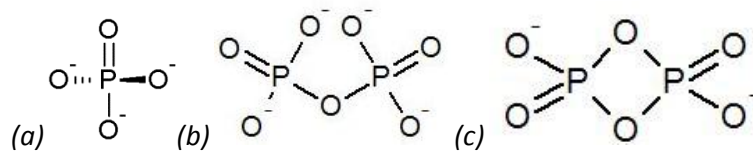


Figure 3.1 The structures of (a) orthophosphates (PO_4) (b) pyrophosphates (P_2O_7) and (c) metaphosphates (PO_3)

The addition of chromium (VI) oxide (CrO_3) is known to improve the stability of electrical steel coatings and therefore the effects of its addition to the model coating will be investigated in this chapter.

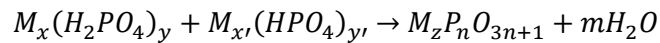
Full characterisation data was collected for all samples (ATR-IR, Raman, TGA, XRD and XPS where relevant); however only the data central to the discussion is included within this chapter. All other data can be found in appendix one (page 196).

3.2 BACKGROUND

3.2.1 THE STRUCTURE AND STABILITY OF ALUMINIUM PHOSPHATES

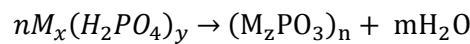
Aluminium phosphate is the primary constituent of the coatings currently used on electrical steels at Cogent Power Ltd. It has been extensively studied in the literature, primarily in its uses as a binder³⁻⁹ but also as a corrosion resistant coating for metals.¹⁰⁻¹⁴

Aluminium phosphate binders are typically synthesized from a mixture of aluminium hydroxide and phosphoric acid, and are cured by heating in air⁶. During this curing process the hydrated orthophosphate undergoes dehydrolytic condensation to form polymeric phosphates containing P-O-P bonds^{3, 7, 15-18} (Equation 3.1).



Equation 3.1 The dehydrolytic condensation of orthophosphates to form polyphosphates³

This reaction is known to continue as further curing occurs (generally above 773 K⁵), causing the formation of metaphosphates³ (Equation 3.2). The curing process produces a mixture of phosphates with end, chain and branched functionalities (sometimes referred to as Q¹, Q² and Q³ polymerisation respectively^{19, 20}), and it is believed that increasing the amount of branched functionality within a chain increases its stability.



Equation 3.2 Metaphosphate formation during the curing of orthophosphates³

Tricot et al⁴ have used a combination of NMR and XRD to study the phase changes that occur during the curing of two aluminium phosphate binders synthesized from a mixture of aluminium hydroxide and phosphoric acid. The main phases observed are shown in Table 3.1; however not all diffraction peaks were assigned indicating that additional phases were present within the binder. Binders with a P/Al ratio greater than 3 are much more chemically stable than those between 2-3 (solutions of which are known to precipitate after a few weeks at room temperature²¹) and XRD indicated that the more stable binder formed the metaphosphate phase and was completely cured at 623 K (150 K lower than the less stable binder). Increasing aluminium to phosphorus ratio further to 1:4.2 caused the formation of the cyclic metaphosphate Al₂P₆O₁₈ (Figure 3.2).⁶

Temperature / K	Phases	Phases
	P/Al= 3	P/Al= 3.5
423	$Al(H_2PO_4)_3$	$Al(H_2PO_4)_3$
473	$Al(H_2PO_4)_3$	-
623	$AlH_2P_3O_{10} \cdot xH_2O$ + $Al(PO_3)_3[B]$	$Al(PO_3)_3[A]$
773	$Al(PO_3)_3[A]$	$Al(PO_3)_3[A]$
873	$Al(PO_3)_3[A]$	$Al(PO_3)_3[A]$
1123	$Al(PO_3)_3[A]$	$Al(PO_3)_3[A]$
1273	$Al(PO_3)_3[A]$	$Al(PO_3)_3[A]$
1473	$Al(PO_3)_3[A]$	$Al(PO_3)_3[A]$

Table 3.1 phases observed in aluminium phosphate binders during curing⁴ ($Al(PO_3)_3 [A]$ is a cubic crystal structure whereas $Al(PO_3)_3 [B]$ is monoclinic)

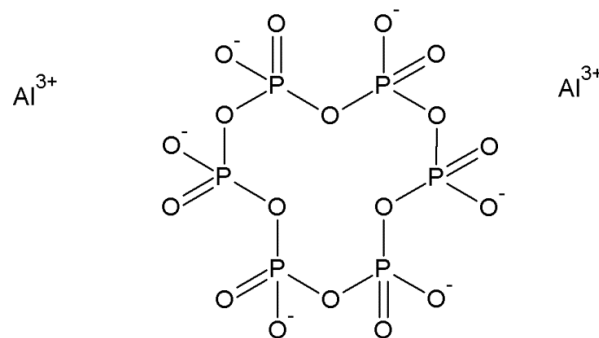


Figure 3.2 The structure of cyclohexaphosphate ($Al_2P_6O_{18}$)

Kobayashi studied the hydration of phosphate glasses and concluded the reaction depicted in Figure 3.3 and argued that the P=O group destabilized the glass towards hydration as the π -bond is weaker than the σ -bond in P-O group due to a poor atomic orbital overlap²².

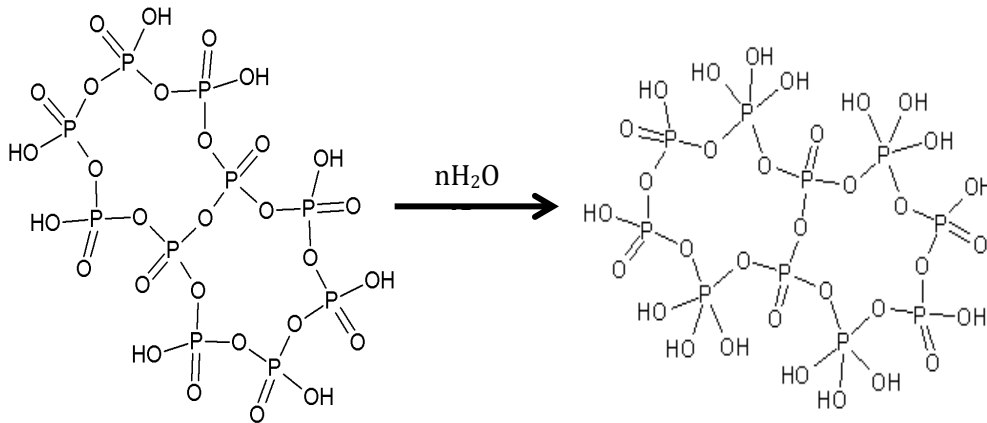


Figure 3.3 The hydration of aluminium phosphate glasses (adapted from reference (22))

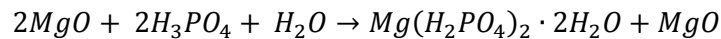
It is believed that additives can increase the stability of aluminium phosphate binders by increasing the amount of branching within the phosphate network. It is also thought that these additives can promote the curing reaction at a lower temperature (possibly by the substitution of hydrogen within phosphoric acid with a metal ion causing an irregular structure).^{5, 9, 23, 24}

Chromium (VI) oxide (CrO_3) has been widely studied as an additive to aluminium phosphate^{3, 9}. Addition of chromium oxide was found to promote the dehydrolytic condensation reaction and formation of an amorphous phase at lower temperatures. This suppression of crystallisation was found to increase with chromium concentration, and it was argued chromium's small cation size increased the disorder in the phosphate chain.⁹ Curing temperature was found to be important for stability of chromium containing binders; all binders cured below 423 K were very unstable towards hydration³. Curing in an autoclave at high pressures (for example 10 atm) was also found to improve the stability of the binders.³

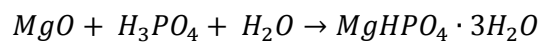
Other additives to aluminium phosphate have been investigated, including AlN ⁵, MgO ⁵, Cu_2O ⁵, ZrO_2 ^{5, 8}, Al_2O_3 ^{8, 25} and TiO_2 ⁸. Hong et al studied aluminium nitride, magnesium oxide and hydrated zirconia as replacements for chromium oxide as an additive as the materials had previously been shown to lower the hardening temperature and improve rehydration resistance of aluminium phosphate binders.^{5, 7, 26} All of the additives were found to promote the curing reaction with increasing amounts of additives. Aluminium nitride was found to be significantly better than the other additives with zirconia being the worst promoter. Aluminium nitride was also found to be the best additive at preventing rehydration of the phosphate. Singh et al compared the use of aluminium phosphate as binder for a variety of steel corrosion resistant coatings with ivory-400 (a commercially available binder).⁸ The alumina coatings were found to be the most stable of the aluminium phosphate containing coatings; however the ivory-400 binder was found to be more effective in all cases.

3.2.2 THE SYNTHESIS AND STABILITY OF MAGNESIUM PHOSPHATES

Whilst the synthesis and thermal treatment of magnesium phosphate has been studied²⁷⁻³⁶ (mainly as phosphate cements) it has been done so less broadly than aluminium phosphate. It has been shown that when a one to one ratio of magnesia to phosphoric acid is reacted a violent exothermic reaction occurs^{23, 27} following the pathway shown in Equation 3.3 as opposed to the expected route described in Equation 3.4. The phases present were identified using XRD.



Equation 3.3 The 1:1 reaction between magnesia and phosphoric acid



Equation 3.4 the expected reaction between a 1:1 mixture of magnesia and phosphoric acid

Higashi and Taguchi showed that heating the product in Equation 3.3 to 333 K whilst maintaining a pH of 2.5-3.5 would result in the formation of the hydrogen free phosphate ($Mg_3(PO_4)_2$).³⁷ A 1:1 mixture of magnesium hydroxide and phosphoric acid has been shown to react via Equation 3.4, and the resulting product formed a pyrophosphate (α - $Mg_2P_2O_7$) after curing at 773 K.³²

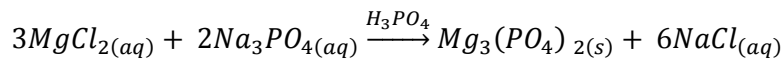
Dudenhoefer et al³⁰ synthesised the other hydrates of monomagnesium phosphate ($Mg(H_2PO_4)_2 \cdot 3H_2O$ and $Mg(H_2PO_4)_2 \cdot 4H_2O$) using magnesium carbonate as a precursor instead of magnesium oxide. The authors showed the tetrahydrate was only stable under acidic conditions, and therefore ethyl acetate was required as a solvent in order to perform purification of the sample (standard washing drying techniques caused decomposition to the trihydrate).

Magnesium phosphate ($Mg_3(PO_4)_2$) syntheses have been reported since the 60's^{31, 37, 38}. Synthetic routes include the treatment of metal salts with phosphoric acid (either as oxides or hydroxides)³⁷, or the heating of magnesium diphosphate and magnesium oxide in platinum tubes³⁸. Both of these methods required heating to high temperatures (923 and 1373 K respectively) in order to produce pure anhydrous phosphates.

Baykal et al³¹ synthesised the phosphate at room temperature from sodium phosphate and magnesium chloride in phosphoric acid by maintaining a pH of 5.1. The resulting phosphate was characterised using IR, SEM, XRD and DTA. SEM showed the phosphate was microporous with an open framework structure. The authors related this structure to the catalytic activity that has been observed for magnesium phosphates in various reactions including the conversion of 2-

Chapter 3 The Structure and Stability Of Model Phosphate Coatings

hexanol to hexanes or hexones depending on structure,³² the dehydration of 2-propanol³⁹ and oxidative coupling of methane.⁴⁰

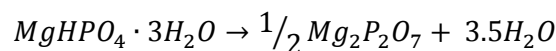


Equation 3.5 the synthesis of magnesium phosphate from magnesium chloride and sodium phosphate³¹

It has been shown that the molar ratio between the phosphoric acid and magnesium oxide is important to the final phosphate formed, with water soluble products forming when the acid content is too low.³⁶ In addition the sources of magnesium and phosphorus have an important effect on the phosphate formed.^{32, 35}

Mousa³⁵ showed a 1:1 Mg/P ratio generally formed $MgHPO_4 \cdot 3H_2O$, which they author observed formed the pyrophosphate $Mg_2P_2O_7$ upon calcination (1123 K for 6 hours) when magnesium hydroxide and phosphoric acid were used. Increasing the magnesium content was found to produce $Mg_3(PO_4)_2 \cdot 22H_2O$ with calcination under the same conditions leading to the loss of the waters of hydration.

The thermal transformations of magnesium phosphates has been studied by Boonchom;^{33, 34} however this work was mainly restricted to temperatures below ?? K (compared to the 1123 K temperature reached during the coating curing at Cogent Power Ltd) and studied the loss of waters of hydration. It was found that $MgHPO_4 \cdot 3H_2O$ lost both the waters of crystallisation and underwent dehydrolytic condensation in one well defined step between 400-623 K. The author stated “waters of crystallization cannot usually be removed without destruction of the anion structure” and gave the overall reaction for this one step as shown in Equation 3.6



Equation 3.6 The one step decomposition of $MgHPO_4 \cdot 3H_2O$

Abdelrazig and Sharp studied the phase changes that occur when heating ammonium dihydrogen phosphate (ADP) with an excess of magnesium oxide. The key phase changes are given in Table 3.2. Magnesium phosphate formed at 498 K, and reacted to form the pyrophosphate ($Mg_2P_2O_7$) and metaphosphate ($Mg(PO_3)_2$) at 723 K.

<i>Temperature</i> / K	<i>Phases Observed</i>
413	<i>MgO and ADP</i>
498	<i>MgO and amorphous phase (H₃PO₄ or NH₄H₂PO₄)</i>
603	<i>MgO, amorphous phase, MgNH₄(PO₃)₃</i>
723	<i>MgO, amorphous phase, MgNH₄(PO₃)₃ Mg(PO₃)₂</i>
973	<i>Mg₂P₂O₇ Mg(PO₃)₂</i>
1158	<i>Mg₂P₂O₇ Mg(PO₃)₂ Mg₃(PO₄)₂</i>

Table 3.2 the phases observed during the heating of magnesium phosphate and ADP

Aramendía et al followed the curing process of some commercially available magnesium phosphates³² and showed the resulting products were dependent on the starting phosphate. Curing of the orthophosphate Mg₃(PO₄)₂·8H₂O caused on the loss of water up to 700 °C (with an amorphous phase forming between 393- 773 K).

3.3 THE SYNTHESIS AND CURING OF MODEL PHOSPHATE COATINGS

3.3.1 CURING OF MODEL ALUMINIUM PHOSPHATE COATINGS

Coatings used on electrical steels at Cogent Power typically consist of aluminium orthophosphate, colloidal silica and water. The colloidal silica is use in the coating both as a bulking agent and in order to improve the wettability of the coating. It is believed that aluminium phosphate is responsible for the major properties of the coating and therefore is the component of interest. Model coatings consisting of just the phosphate were produced in order to simplify the data collected, allowing for an easier interpretation.

A portion of aluminium orthophosphate (Sigma Aldrich reagent grade) was cured at 1123 K in air for 15 minutes. The ATR-IR spectra before and after curing are shown in Figure 3.4. The bands observed in both the Raman and IR spectra and their assignments^{9, 41, 42} are given in Table 3.3. It is clear there is no change in the IR spectrum after curing, indicating that the phosphate in

unchanged by this process. This is also observed in the Raman spectra of the aluminium phosphate samples (Figure 3.5).

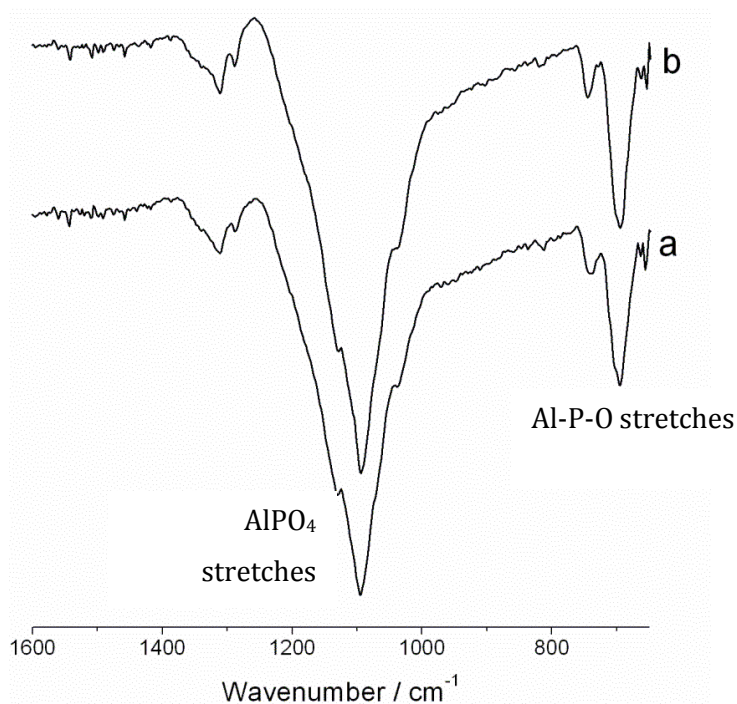


Figure 3.4 The ATR-IR spectra of aluminium orthophosphate (a) before and (b) after heating at 1123 K for 15 minutes in Air.

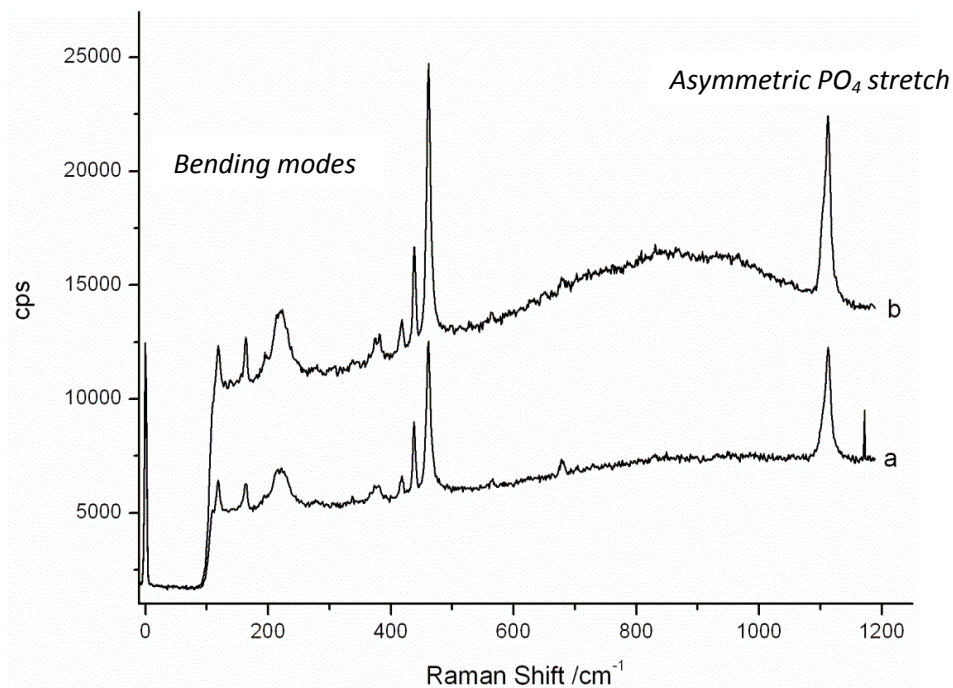


Figure 3.5 The Raman spectra of aluminium orthophosphate (a) before and (b) after heating at 1123 K for 15 minutes in Air.

<i>IR bands</i> <i>/cm⁻¹</i>	<i>Raman Bands</i> <i>/cm⁻¹</i>	<i>Assignment</i>	<i>Reference</i>
1311.59 (w)	1112.9	Asymmetric PO ₄ stretch	[⁴¹]
1130.28 (sh)		Asymmetric PO ₄ stretch	[⁴¹]
1095.56 (vs)		Symmetric PO ₄ stretch	[⁴¹]
740.66 (w)		Asymmetric Al-O-P	[⁴²]
694.37 (m)		Asymmetric Al-O-P	[⁴²]
	461.3	Symmetric bend	[⁴¹]
	437.4	Symmetric bend	[⁴¹]
	417.6	Symmetric bend	[⁴¹]

Table 3.3 The main bands observed in the ATR-IR and Raman spectra of aluminium orthophosphate (w= weak, m= medium, s= strong, v= very, sh= shoulder)

During curing it is expected the aluminium orthophosphate would undergo dehydrolytic condensation to form either meta- or pyrophosphate. If this was to occur we would expect to see the broad band 1095 cm⁻¹ become sharper and shift to a higher wavenumber. Additionally we would expect to see a new band(s) appear due to the formation of P-O-P bonds. These bands are expected either between 950 and 1000 cm⁻¹ if a linear metaphosphate is formed or two bands at around 800 and 1050 cm⁻¹ if a ring metaphosphate is formed.⁹

TGA (see appendix one) confirmed there was no phase change during the heating process. The lack of change observed in these spectra is in sharp contrast to results previously seen from the curing of aluminium phosphate binders.^{4, 5} For example Tricot et al⁴ observed dehydrolytic condensation at 773 K and 623 K, depending on the starting aluminium phosphate binder. The phosphates studied by Tricot et al⁴ contained hydrogen whereas the aluminium orthophosphate studied here does not, indicating that the presence of hydrogen may destabilise the orthophosphate and make P-O-P bond formation more favourable. In addition, the literature samples were synthesised from an excess of phosphoric acid, which was present during curing. The sample investigated here was a purified phosphate with no acid present, which may also have an impact on the curing process.

3.3.2 THE SYNTHESIS AND CURING OF MODEL MAGNESIUM PHOSPHATE COATINGS

The model magnesium phosphate coatings are based on a test coating trialled at Cogent Power Ltd. The coating consists of aluminium phosphate, magnesium oxide, phosphoric acid, colloidal silica and water. As the presence of magnesium oxide and phosphoric acid are the only differences between the test coating and the current on-line coating modelled in section 3.3.1 this coating was modelled by the mixture of phosphoric acid and magnesium oxide known to produce a magnesium phosphate.²⁷

The procedure followed for the synthesis of model magnesium phosphate coatings is outlined in chapter 2 (section 2.2.2). A portion of the resulting powder was heated in air for 15 minutes at 1073 K and the ATR-IR and Raman spectra were collected before and after heating (Figure 3.6 and Figure 3.7 respectively). This sample will be referred to as phosphate 2. As a clear change was observed in both sets of spectra the powder was cured in 100 K intervals and spectra collected at each stage.

Absorption in the region of $\sim 1050\text{ cm}^{-1}$ is typical of a metal oxygen double bond (see for example references (41) and (43)) In the spectra of the samples cured at 573 and 673 K the absorption bands between 950 and 1087 cm^{-1} can be assigned to the P=O stretch, and vibrations at lower energy than this to the phosphorus oxygen single bonds. These assignments provide strong evidence for the formation of the phosphate in the solution as observed by others.^{27, 31, 35, 37} As these are the only absorption bands present in the spectra it is likely that a magnesium orthophosphate is formed.

Curing above 673 K saw the shift of the centre of the P=O absorption band to a slightly lower wavenumber (from 1047.3 to 1030.0 cm^{-1}) and the formation of new bands at 1294.2 and 1317.4 cm^{-1} . These higher energy bands can be assigned to symmetric stretches of the P-O-P bond and indicate that the phosphate undergoes dehydrolytic condensation to form either a pyro- (P_2O_7) or metaphosphate (PO_3). This differs from the aluminium orthophosphate which did not undergo any changes during curing. This is interesting when compared to observations made in industry where coatings containing magnesium phosphate have been shown to impart a greater tension on the steel sheets than those consisting solely of aluminium phosphate.

Inspection of the Raman spectra from the same samples (Figure 3.7) showed a similar change in the spectra between 673 and 773 K. Assignments of the absorption bands are given in Table 3.5 and there is some indication of P-O-P bonds being present in the sample. This indicates that a pyrophosphate is present in the sample. ATR-IR probes the surface of the powder whereas

Chapter 3 The Structure and Stability Of Model Phosphate Coatings

Raman is a bulk technique, so more orthophosphate being present on the surface of the powder may be the cause of the differences in the spectra from the two techniques.

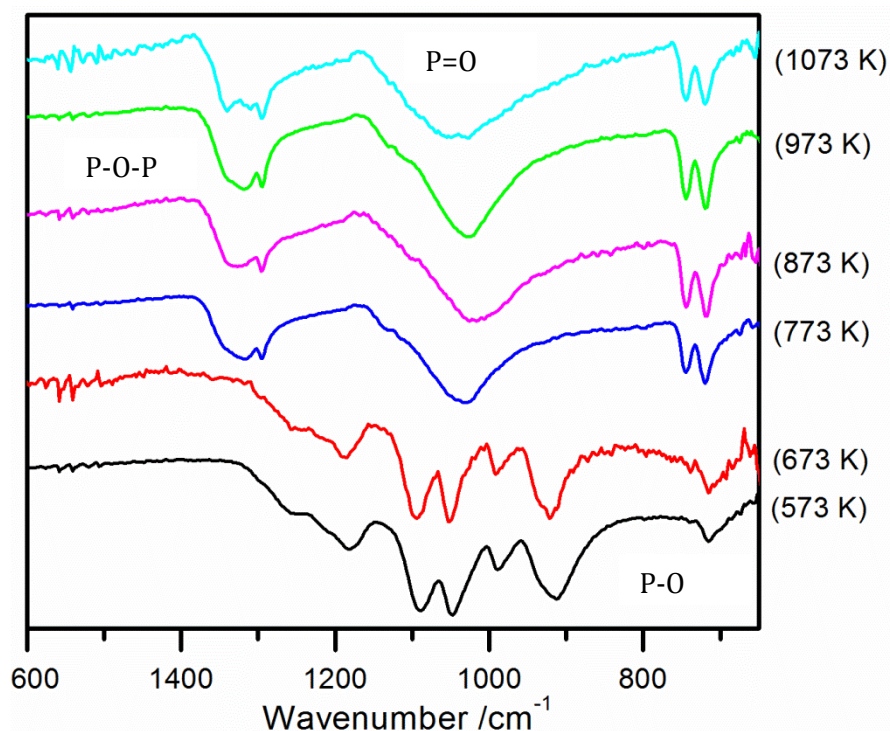


Figure 3.6 The ATR-IR spectra of phosphate 2 after heating for 15 minutes in Air.

IR Adsorption bands		Assignment	Reference
573-673 K	773-1073 K		
713.66	719.47	P-O	
	744.52	P-O	
912.33		P-O	
989.48		P=O	
1047.34	1029.99	P=O	
1087.85		P=O	
1180.43			
	1294.23	P-O-P	
	1317.38	P-O-P	

Table 3.4 The major absorption bands observed in the ATR-IR Spectra of magnesium phosphates and their assignments

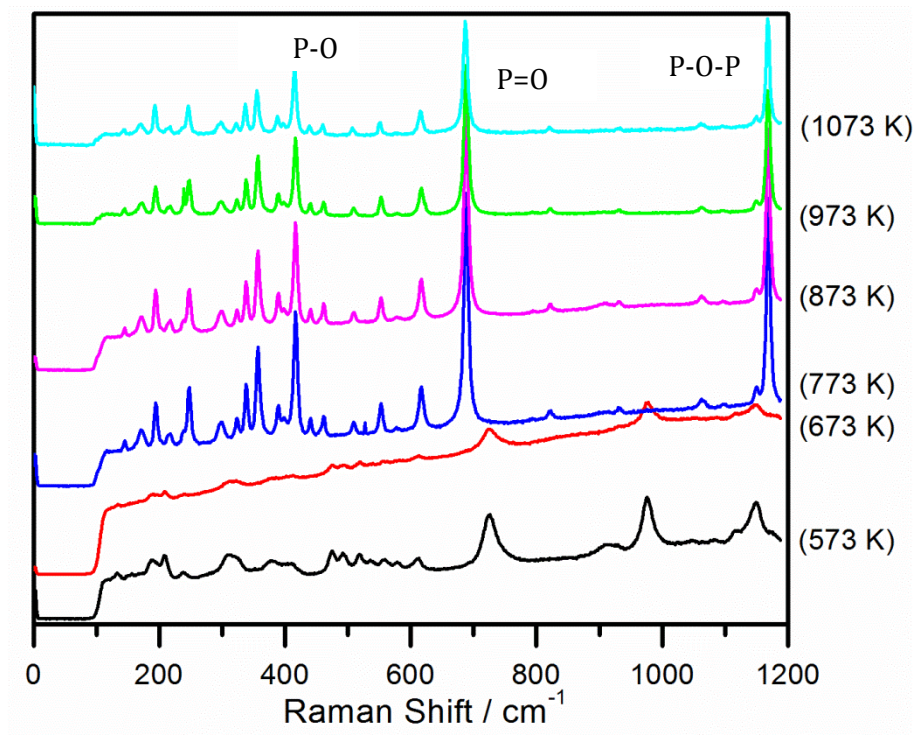


Figure 3.7 The Raman spectra of phosphate 2 after heating for 15 minutes in Air.

Raman Adsorption Bands / Raman			
Shift cm^{-1}		Assignment	Reference
573-673 K	773-1073 K		
	380.9		
	387.97		
410.62	414.86	P-O	
	438.82	P-O	
	459.90	P-O	
473.91		P-O	
518.59			
612.66	615.41		
	686.54		
724.56		P=O	
909.22		P=O	
975.05	930.35	P=O	
1148.81	1168.03	P-O-P	

Table 3.5 The Absorption bands observed in the Raman Spectra of phosphate 2 and their assignments

Inspection of the X-ray diffraction patterns of the magnesium phosphate after heating at 573 and 1073 K (Figure 3.8) confirmed the assignments of trimagnesium orthophosphate ($\text{Mg}_3(\text{PO}_4)_2 \cdot x\text{H}_2\text{O}$) and a magnesium metaphosphate which was identified as magnesium cyclo-tetraphosphate ($\text{Mg}_2(\text{PO}_3)_4$, Figure 3.8c). In addition the sample heated to 573 K was found to contain the pyrophosphate MgHP_2O_7 . This pyrophosphate has previously been observed when heating magnesium orthophosphate ($\text{Mg}(\text{H}_2\text{PO}_4)_2 \cdot 2\text{H}_2\text{O}$) above 523 K.⁴⁴ The presence of the pyrophosphate provides support for the band assignments in the Raman spectra.

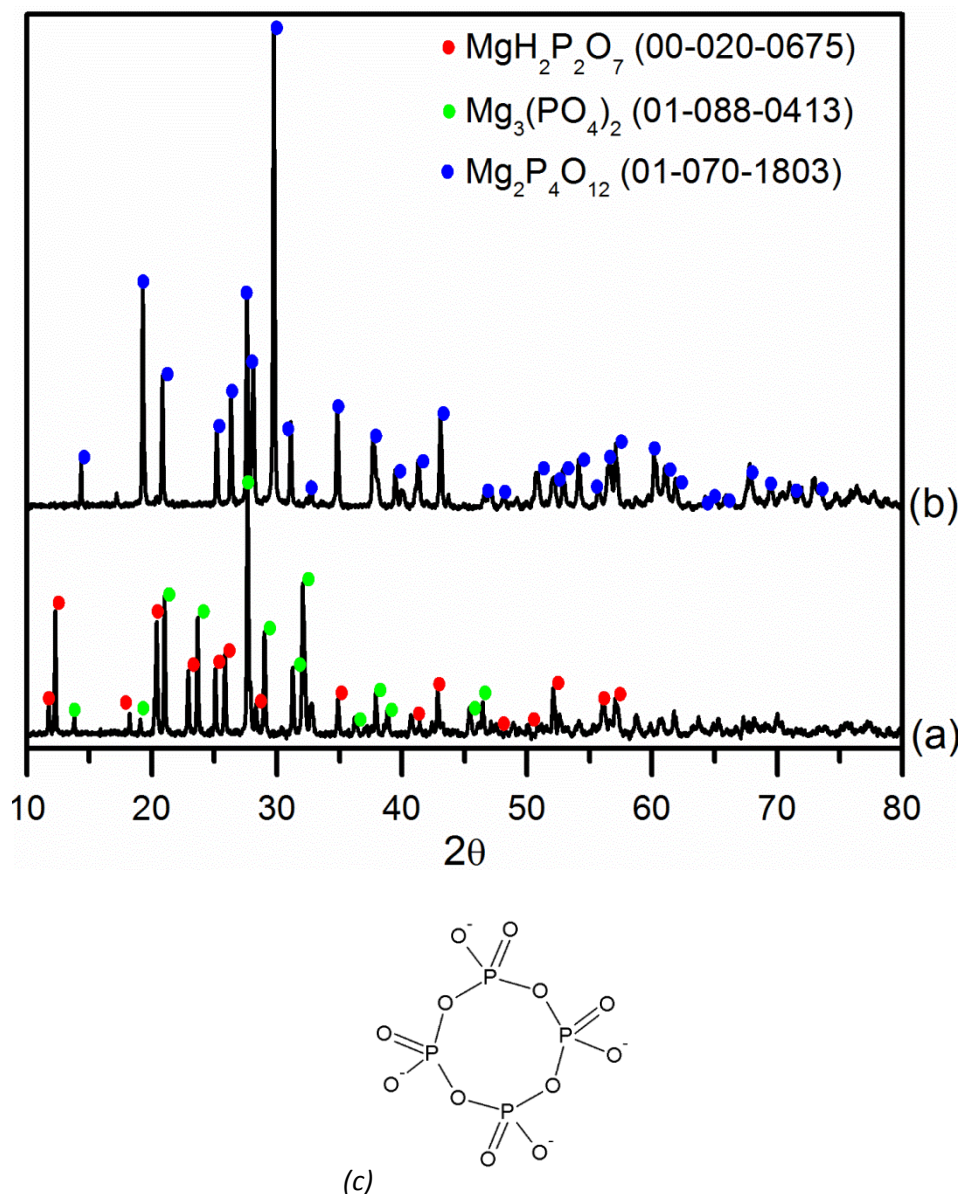
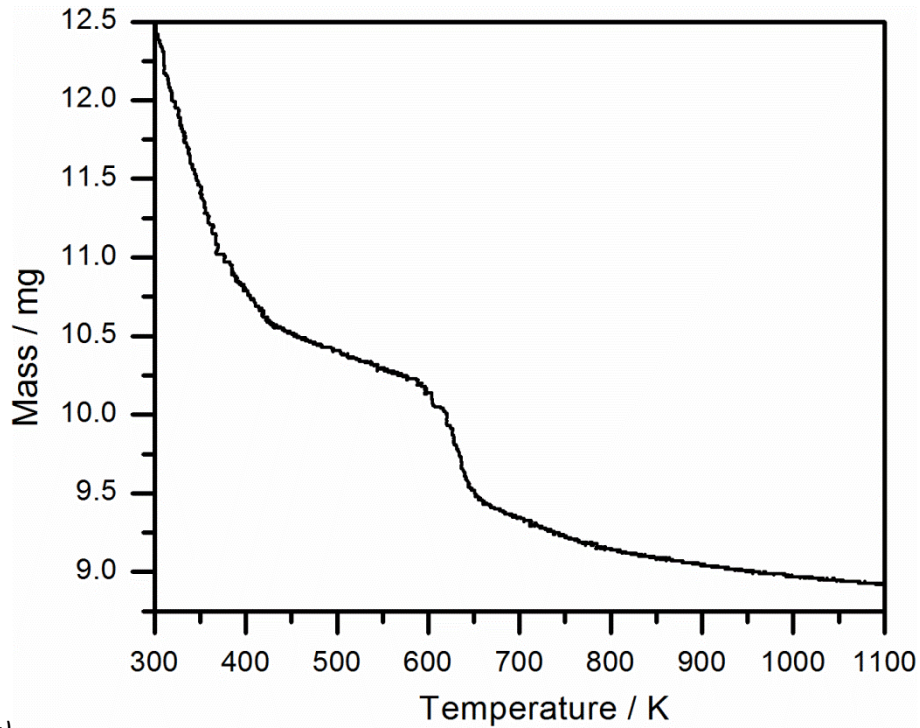
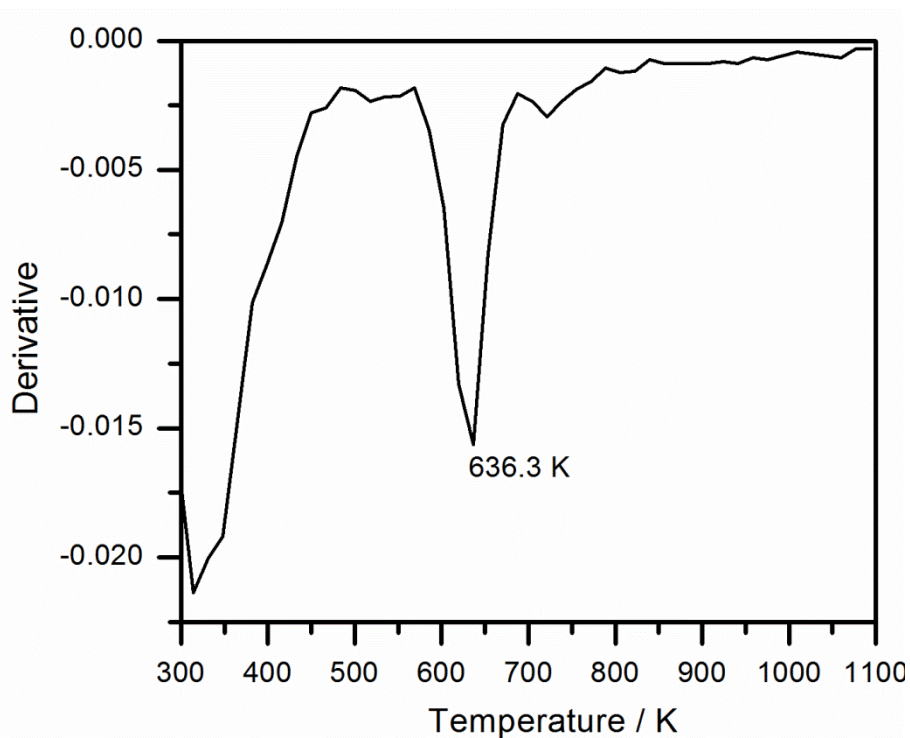


Figure 3.8 The XRD spectra of phosphate 2 after heating to (a) 573 and (b) 1073 K in air for 15 minutes and (c) the structure of the observed metaphosphate



(a)

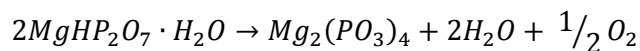


(b)

Figure 3.9 TGA of fresh magnesium phosphate dried at 573 K

The TGA of the dried magnesium phosphate is shown in Figure 3.9. It is clear there are two transitions within the TGA. The first gradual transition up to 373 K is associated with the loss of water adsorbed by the powder. The second sharper transition at 636 K was associated with a

10.9 % drop in sample mass. Equation 3.7 shows the proposed reaction occurring in this transition. The loss of water and oxygen within this reaction would account for a mass reduction of 12.5 %.



Equation 3.7 The proposed reaction observed in the TGA of magnesium phosphate

Attempts were made to synthesis a sample consisting of only magnesium orthophosphate (mainly by heating on a hot plate overnight), however all resulting powders were found to contain the pyrophosphate.

3.3.2.1 THE EFFECTS OF MAGNESIUM OXIDE: PHOSPHORIC ACID RATIO

In order to probe the effects of magnesium oxide: phosphoric acid ratio a series of samples were synthesised containing 25, 50 and 75 molar % magnesium oxide in order to produce samples with an excess of phosphoric acid or magnesium oxide. The sample studied in the previous section contained 40 % magnesium oxide. All samples were fully characterised using IR, Raman, XRD and TGA, however some data has been placed in appendix one (page 196) in order to improve the flow of the chapter. All samples were produced under the same conditions using the same method as described in chapter 2.

3.3.2.1.1 25 % MAGNESIUM OXIDE

Synthesis of magnesium phosphate from a 1:3 mixture of magnesium oxide and phosphoric acid produced a colourless gel, which formed a hard white powder when heated to 673 K. Attempts were made to dry the sample at 573 K (as with the previous sample) however no powder formed until 673 K. This sample is referred to as phosphate 3. The Raman spectra of the resulting powder are shown in Figure 3.10, and the key absorptions are listed in Table 3.6 and Table 3.7 along with the main IR bands (the IR spectra are shown in appendix one).

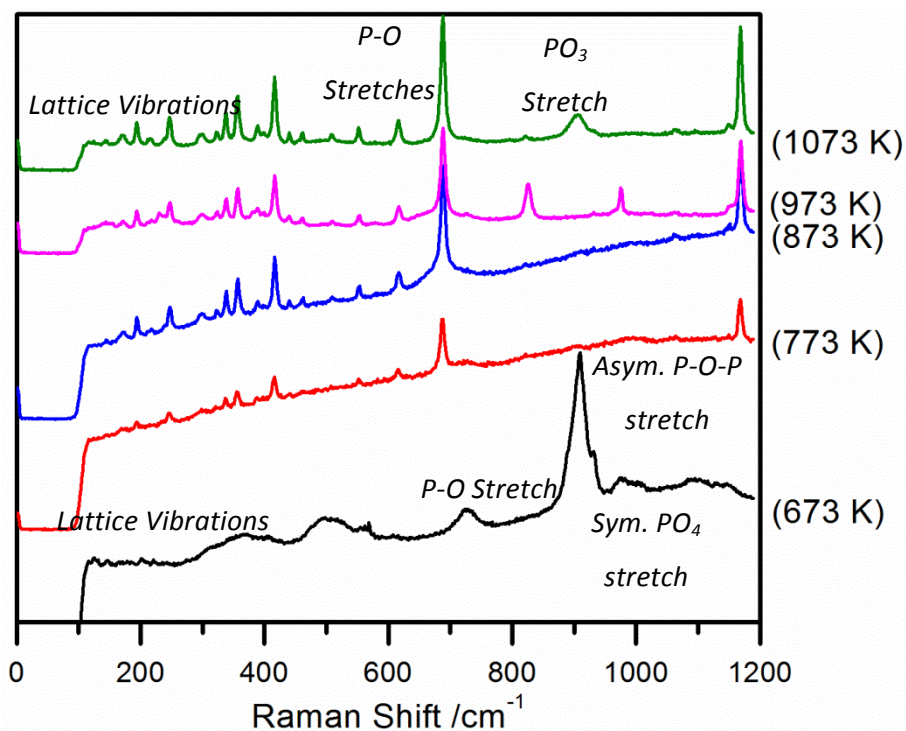


Figure 3.10 The Raman spectra taken from magnesium phosphate 2 after heating between 673 and 1073 K.

Raman Adsorption / cm^{-1}	IR adsorption / cm^{-1}	Assignment	References
362.4		Lattice Vibrations	
497.6		Lattice Vibrations	
	725.2	P-O-P bend	45
	916.2	P-O-P stretch	45
725.8	1003.0	P-O stretch	45, 46
909.2	1166.9	P-O stretch	46
981.5		Asymmetric P-O-P stretch	47
1093.4		Symmetric PO_3 stretch	47
	1261.4	P-O ionic stretch	45

Table 3.6 The major absorption bands in the IR and Raman spectra of phosphate 3 when dried at 673 K

Chapter 3 The Structure and Stability Of Model Phosphate Coatings

<i>Raman Adsorption / cm⁻¹</i>	<i>IR adsorption/ cm⁻¹</i>	<i>Assignment</i>	<i>References</i>
194.1		<i>Lattice Vibrations</i>	
244.9		<i>Lattice Vibrations</i>	
338.2		<i>Lattice Vibrations</i>	
355.3	713.7	<i>P-O-P bend</i>	45, 47
414.8			
615.3		<i>P-O stretch</i>	46
	922.0	<i>P-O-H bend</i>	45
687.8		<i>P-O stretch</i>	46
721.8	985.6	<i>P-O stretch</i>	45, 46
1166.7		<i>PO₃ symmetric stretch</i>	47
	1197.8	<i>P=O</i>	45
	1685.8 (<i>broad</i>)		

Table 3.7 The major absorption bands in the IR and Raman spectra of phosphate 3 when heated between 773 and 1073 K

It is clear from Figure 3.10 and the data collected in the tables that a phase change occurs between 673 and 773 K. The IR and Raman data indicates that the initial dried powder collected at 673 K is pyrophosphate, with good agreement to the assignments collected by Corbridge and Lowe in the IR spectra,⁴⁵ and the Raman absorptions observed by Popovic⁴⁶ and Sarr.⁴⁷ This assignment of magnesium pyrophosphate is also in good agreement with the assignment of phosphate 2 when dried, and the observations by Hinsch et al.⁴⁴

Inspection of the Raman and IR spectra of the sample after heating above 673 K shows there is a clear change in the sample, with the peak at 981.5 cm⁻¹ arising from the P-O-P stretch in magnesium pyrophosphate decreasing and the peaks at 721.8 and 1166.7 cm⁻¹ (characteristic of metaphosphate P-O symmetric stretch and PO₃ symmetric stretch respectively) increasing with temperature. Based on the spectra it appears that the sample is a metaphosphate chain. It is most likely to be a straight linear chain than a ringed phosphate, due to the lack of absorptions associated with ring bending and breathing (typically around 370 and 380 cm⁻¹⁴⁸). Three absorption bands were observed in the region 650-800 cm⁻¹ of the Raman spectrum, and the number of bands present here has previously been shown to give a measure of the periodicity of the phosphate chain.^{46, 49}

When the sample was heated to 1073 K, an additional adsorption band appeared at 901.2 cm^{-1} , however it is unclear what this adsorption is associated with. Unfortunately the sample was too hard to achieve a good contact with the ATR crystal and the IR spectrum could not be collected, meaning this could not be probed further. As this was the only change observed in the Raman spectrum, it is likely that the sample is still a linear metaphosphate chain.

3.3.2.1.2 50 % MAGNESIUM OXIDE

A sample was prepared containing equal amounts of magnesium oxide and phosphoric acid (referred to as phosphate 4). As with previous samples the sample was dried at 573 K and portions were heated in air for 15 minutes in 100 K intervals. The Raman spectra of the resulting powders are shown in Figure 3.11 and the IR spectra in Appendix 1. The main absorption bands from both sets of spectra are listed in Table 3.8 and 3.9.

Inspection of Figure 3.11 shows there is a clear change in the Raman spectrum between 673 and 773 K (as observed in phosphate 2). This change was also observed in the IR spectra. The position and relative intensities of the bands in the IR and Raman spectra showed good agreement with those observed by others for pyrophosphates⁴⁵⁻⁴⁷ however the two highest wavenumber IR absorbances (1089.8 and 1180.4 cm^{-1}) can also be assigned to orthophosphate P-O stretches, or pyrophosphate ionic P-O stretches⁴⁵. XRD (see Appendix 1) indicates both magnesium orthophosphate and pyrophosphate are present within the sample, supporting this assignment.

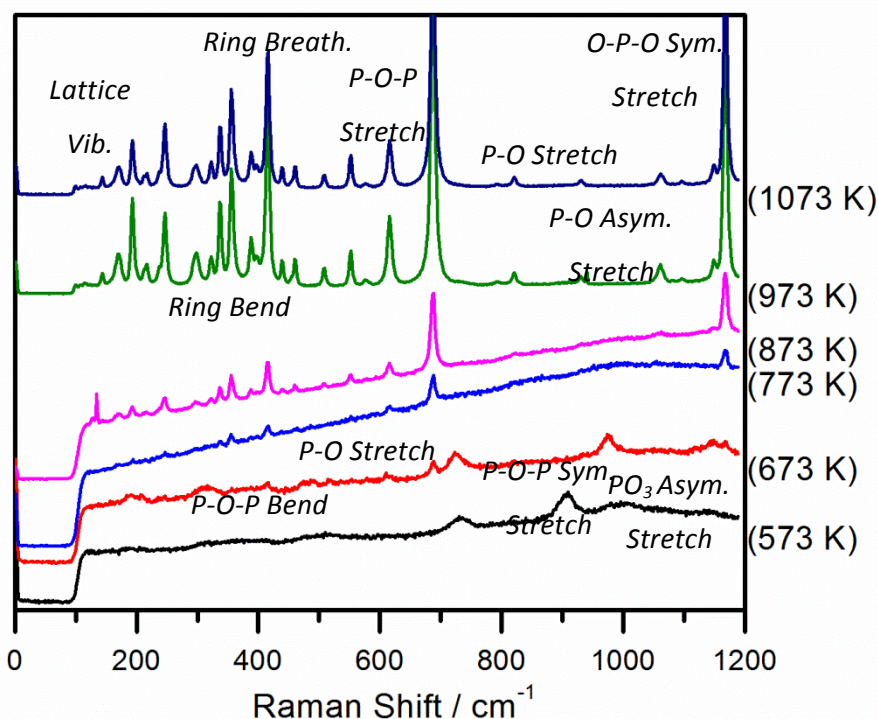


Figure 3.11 The Raman spectra taken from phosphate 4 after heating between 573 and 1073 K.

Raman Adsorption / cm^{-1}	IR adsorption/ cm^{-1}	Assignment	References
185.4		Lattice vibrations	
315.3	719.4	P-O-P bend	45, 46
412.0			
486.4			
	920.0	P-O-P stretch	45
609.8	991.4	P-O stretch	45, 46
727.2		P-O-P symmetric stretch	47
973.6		PO_3 asymmetric stretch	47
	1047.3	P-O stretch	45
	1089.8	P-O ionic stretch pyrophosphate or P-O stretch orthophosphate	45, 47
1144.9		PO_3 asymmetric stretch	47
	1180.4	P-O ionic stretch pyrophosphate or P-O stretch orthophosphate	45

Table 3.8 The major absorption bands in the IR and Raman spectra of phosphate 4 when heated to 573 and 673 K

Chapter 3 The Structure and Stability Of Model Phosphate Coatings

<i>Raman Adsorption / cm⁻¹</i>	<i>IR adsorption/ cm⁻¹</i>	<i>Assignment</i>	<i>References</i>
143.0		<i>Lattice vibrations</i>	
172.3		<i>Lattice vibrations</i>	48
192.7		<i>Lattice vibrations</i>	48
246.3		<i>Lattice vibrations</i>	
293.8		<i>Lattice vibrations</i>	
336.7		<i>Lattice vibrations</i>	48
355.3		<i>Ring bending</i>	48
389.3 (shoulder)			
416.2		<i>Ring breathing</i>	48
459.8			
507.4			
551.9			
616.7	721.4	<i>P-O-P stretch</i>	45, 48
687.8	744.5	<i>P-O-P stretch</i>	45, 48
	933.5*		
878.7	1037.7	<i>P-O stretch</i>	45, 46
931.6			
1059.7		<i>P-O asymmetric stretch</i>	46
1150.0 (shoulder)		<i>P-O symmetric stretch</i>	46
1168.0		<i>O-P-O symmetric stretch</i>	48
	1296.2	<i>P=O stretch</i>	45
	1321.2	<i>P=O stretch</i>	45

*Table 3.9 The major absorption bands in the IR and Raman spectra of phosphate 4 when heated between 773 and 1073 K. the adsorption labelled with a * was only observed in the IR spectrum after the sample has been heated to 873 K.*

A clear change is observed in both the IR and Raman spectra between 673 and 773 K. As the sample is heated further the absorption bands in the Raman spectra become sharper and more intense. The spectra indicated that the sample had undergone a condensation reaction and was now a cyclic metaphosphate. This was confirmed in the XRD which indicated the sample was cyclic tetrametaphosphate (the same result as phosphate 2).

3.3.2.1.3 75 % MAGNESIUM OXIDE

The final phosphate produced in this section was made using 75 % magnesium oxide (giving an excess of magnesium oxide, unlike all the previous samples where an excess of phosphoric acid was used). As with the previous samples portions were heated in air for 15 minutes in 100 K intervals and the Raman and IR spectra were collected. The Raman spectra are shown in Figure 3.12 and the IR spectra in appendix 1. All major absorbencies are listed in Table 3.10 and 3.11 along with their proposed assignments. Inspection of the Raman spectra shows that the changes are more gradual than in previous samples with the spectra collected from samples heated to 673 and 773 K appearing to be a mixture of the spectra produced at 573 K with ones produced at 873 K and above. The spectrum produced from the sample heated to 573 K indicated the sample was a mixture of magnesium pyrophosphate and unreacted magnesium oxide- in good agreement with the IR spectra and the X-ray diffraction patterns (see appendix one).

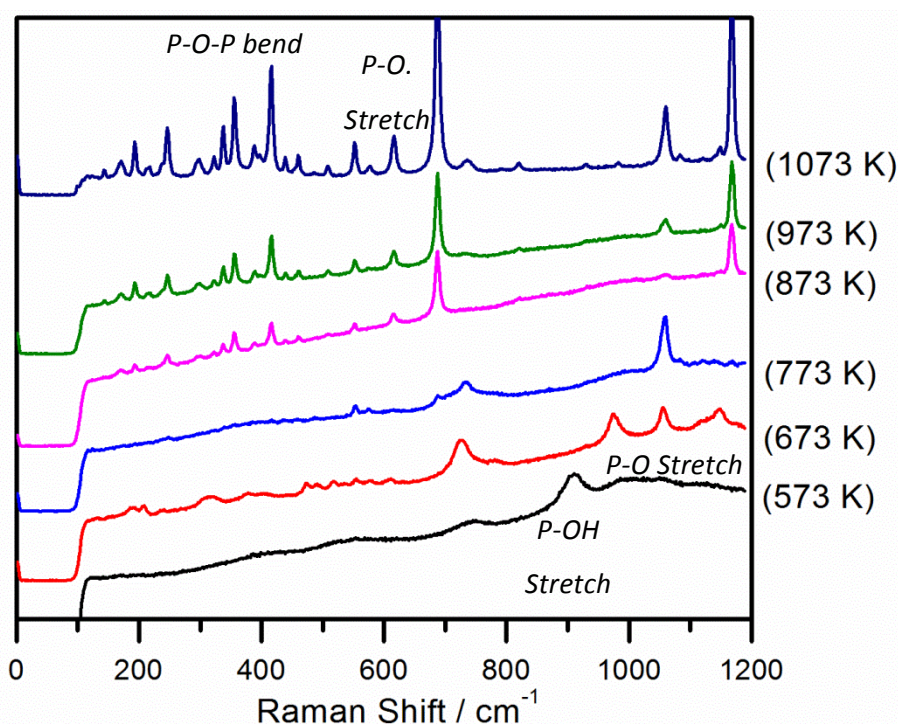


Figure 3.12 The Raman spectra taken from phosphate 5 after heating between 573 and 1073 K.

After heating to 873 K and above the absorption bands became much sharper and there was a clear change in the position and number of peaks. The assignment of these peaks indicates that either pyro- or metaphosphate is present in addition to the unreacted magnesium oxide. XRD indicated that a short chain metaphosphate had formed by 1073 K ($\text{Mg}(\text{PO}_3)_2$), but that pyrophosphate and magnesium oxide were still both present in the sample.

Chapter 3 The Structure and Stability Of Model Phosphate Coatings

Raman Adsorption / cm⁻¹	IR adsorption/ cm⁻¹	Assignment	References
550.5			
	734.9	<i>P-O-P bend</i>	45
739.4			
907.8		<i>P-OH asymmetric stretch</i>	50
	914.3	<i>P-O-P stretch</i>	45
1028.5 (v. broad)		<i>P-O stretch</i>	46
	1070.5	<i>MgO or P-O stretch</i>	45, 51

Table 3.10 The major absorption bands in the IR and Raman spectra of phosphate 5 when heated to 573 K

Raman Adsorption / cm⁻¹	IR adsorption/ cm⁻¹	Assignment	References
192.7		<i>Lattice vibration</i>	
244.9		<i>Lattice vibration</i>	
336.7		<i>P-O-P bend</i>	47
355.3			
416.2			
551.9			
616.7		<i>P-O stretch</i>	46
	721.4	<i>P-O-P stretch in ring or pyrophosphate</i>	45
	746.5	<i>P-O-P stretch in ring or pyrophosphate</i>	45
	964.4	<i>P-O-P stretch</i>	45
687.8	1045.4	<i>P-O stretch</i>	45, 46
1059.7			
	1078.2	<i>MgO</i>	51
1168.0			
	1207.4 (sh)		
	1294.2 (sh)	<i>P=O stretch</i>	45
	1319.3	<i>P=O stretch</i>	45

Table 3.11 The major absorption bands in the IR and Raman spectra of phosphate 5 when heated between 873 and 1073 K.

Chapter 3 The Structure and Stability Of Model Phosphate Coatings

Based on the Raman spectra it can be concluded that at 673 K and 773 K the sample is a mixture of pyro and metaphosphate with the metaphosphate concentration increasing as the sample is heated to higher temperatures.

3.3.2.4 SUMMARY

The main phases of all magnesium phosphate samples are shown in Table 3.12 as determined by XRD (the only exception is phosphate 3, where poor yields meant there was not enough sample available to run XRD). It is clear that all dried samples consisted of magnesium pyrophosphate, indicating it is highly likely that magnesium orthophosphate was formed in solution and reacted as the sample was heated during drying (as noted by others⁴⁴). The metaphosphate formed during curing was found to have some dependence on the amount of oxide present, as an excess of magnesium oxide produced small 2 membered rings as opposed to the larger 4 member rings seen in phosphates 2 and 4.

All samples containing an excess of phosphoric acid were found to completely react to form the metaphosphate, whereas the sample containing excess magnesium oxide (phosphate 5) only formed a pyrophosphate. This supports the proposition made in section 3.3.1 that an excess of phosphoric acid is required during curing for the formation of metaphosphate.

<i>Sample</i>	<i>Phosphate 3</i>	<i>Phosphate 2</i>	<i>Phosphate 4</i>	<i>Phosphate 5</i>
<i>Dried</i>	<i>Pyrophosphate</i>	$Mg_3(PO_4)_2 \cdot xH_2O,$ $MgHP_2O_7$	$Mg_3(PO_4)_2,$ $MgH_2P_2O_7$	$MgO, Mg_2P_2O_7$
<i>Cured</i>	<i>Linear Metaphosphate</i>	$Mg_2P_4O_{12}$	$Mg_2P_4O_{12}$	$Mg(PO_3)_2, MgO,$ $Mg_2P_2O_7$
<i>Temperature of phase transition /K</i>	673-773	636	673-773 K	573-773 K

Table 3.12 The phases present in all magnesium phosphate samples and the temperature of the phase transition

3.4 AGING OF MODEL PHOSPHATE COATINGS

Initial investigations by Cogent Power Ltd indicated that when aluminium phosphate and aluminium/ magnesium phosphate mixed coatings were left in humid atmospheres a steady increase in the mass of the coating was observed (Figure 3.13). It is clear from the figure that the mass of both coatings increased with time. This is thought to be due to the coating absorbing water from the atmosphere; however there is little other information on what is happening to the coatings during this process. The data indicates that for the first 15 days the rate of increase in coating mass is similar for both coatings, however after this point the coating containing magnesium phosphate begins to gain mass much more rapidly than the pure aluminium phosphate coating.

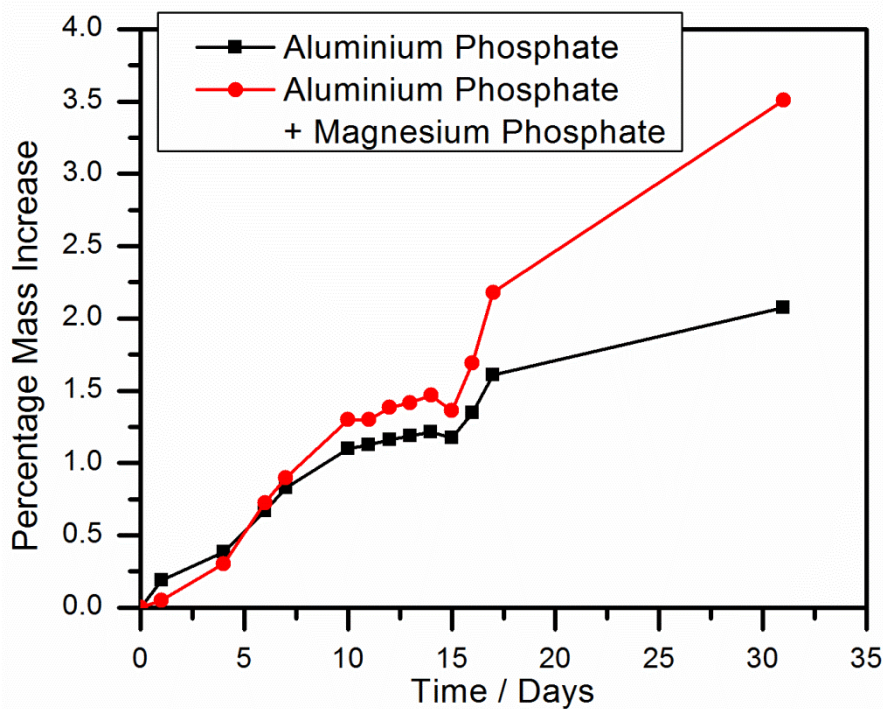


Figure 3.13 The changes in mass of industrial phosphate coatings when left in humid atmospheres (approximately 65 % humidity at 333 K) as monitored by A. Nolan at Cogent Power Ltd.

In order to monitor the chemical changes occurring in the phosphate coatings the model coatings discussed previously were placed in the humidity chamber described in Chapter two. Samples were taken from the chamber weekly and their ATR-IR spectra were collected. IR spectroscopy was chosen to monitor the samples as it was a fast technique that could quickly identify any changes in the sample.

Figure 3.14 shows that the model aluminium phosphate coating (phosphate 1) was unchanged after three weeks in the humidity chamber. This was expected as IR had previously indicated that curing had no effect on the phosphate (see Figure 3.4).

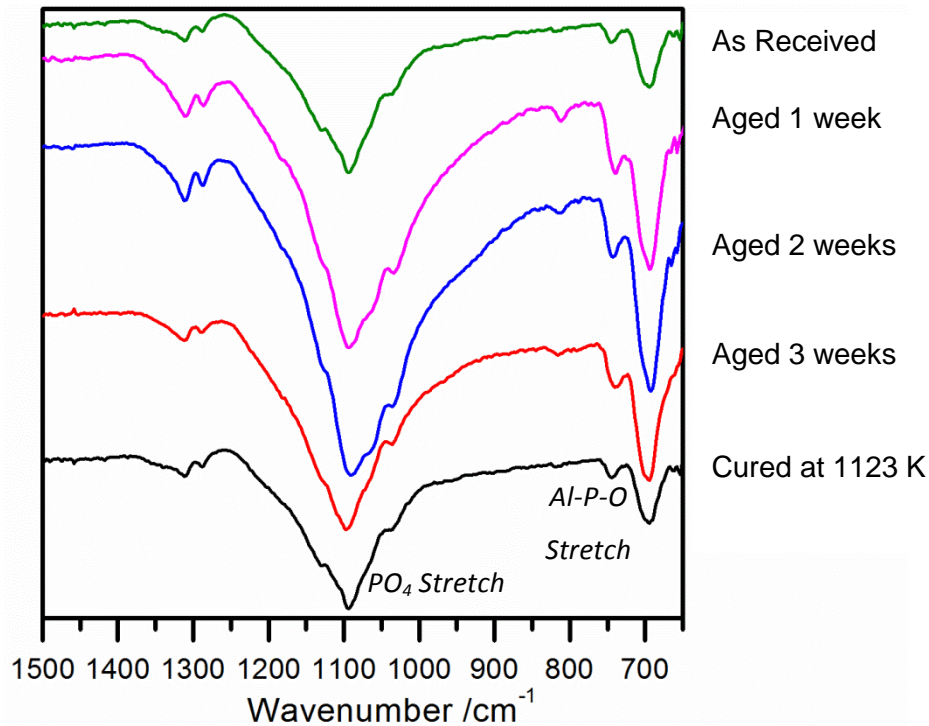


Figure 3.14 The effects of aging in a humidity chamber on the IR spectrum of a model aluminium phosphate steel coating. The IR spectra of the coating before aging (but after heating to 1173 K) and without any heat treatment are also shown for reference.

The effects of aging on the model magnesium phosphate coating (sample 2) are shown in Figure 3.15. It is clear from the data that as with the model aluminium phosphate coating the sample is unchanged after one week in the humidity chamber as the spectra of the aged and week old sample are identical. This is in good agreement with the data obtained by Cogent Power Ltd (Figure 3.13) which indicated aluminium and magnesium phosphate coatings had a similar percentage mass gain after aging for one week.

After aging for two weeks a shift was observed in the absorbance arising from P=O (from 1045.4 to 1097.5 cm^{-1}). This is thought to be due to the breakdown of the metaphosphate rings to either pyro or orthophosphate. The multiple band structure observed in the spectrum taken from the freshly dried sample (Figure 3.6, also shown in Figure 3.15 for reference) is not observed in the sample aged after two or three weeks, however the overall shape of the spectra and positions of the absorption bands in the aged samples are similar to those observed in the freshly dried sample, indicating that the rings formed during curing are broken down in humid atmospheres.

This change in structure at two weeks is again in good agreement with the data collected at Cogent Power Ltd (Figure 3.13) which indicated that the mass of the magnesium phosphate containing coating began to increase much more rapidly than the mass of the aluminium phosphate coating after ten days.

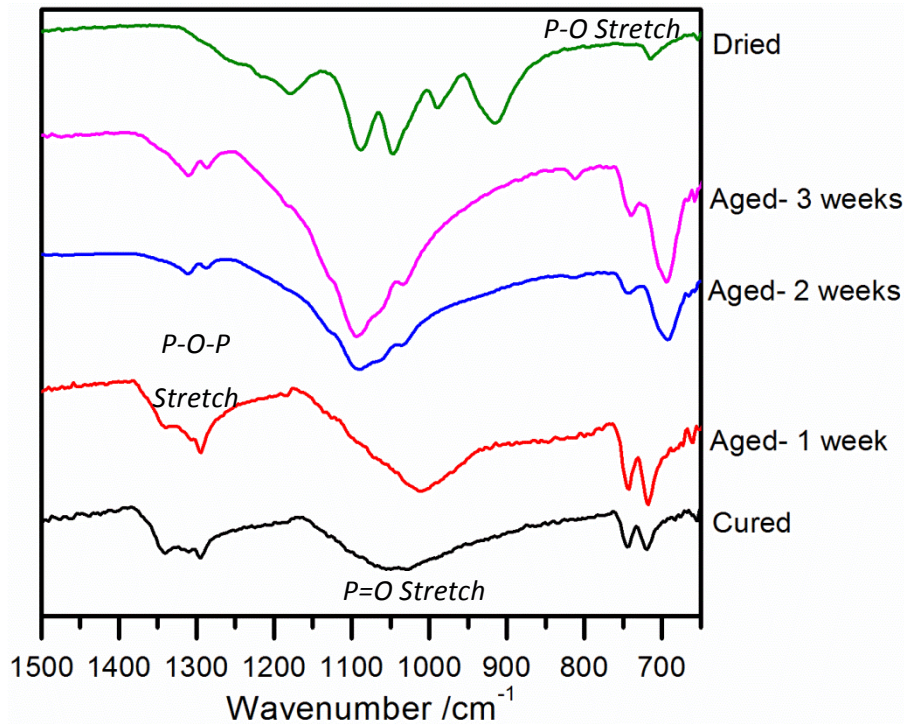


Figure 3.15 The effects of aging in a humidity chamber on the IR spectrum of a model magnesium phosphate steel coating. The IR spectra of the coating after heating to 673 K and 1073 K are also shown for reference.

3.5 THE EFFECTS OF CHROMIUM ADDITION ON MODEL PHOSPHATE COATINGS

The addition of chromium (VI) oxide to has been shown to dramatically increase the stability of both magnesium and aluminium phosphate coatings, with little change in mass over thirty one days within a humidity chamber (see Figure 3.16), however there is little understanding of the chemical effects of adding chromium oxide to the phosphate.

As it has been shown that the curing process has an important effect on the pure phosphate coatings (in particular the magnesium phosphate) the curing of the phosphate coatings will be studied again when different amounts of chromium oxide are added. The curing of the

chromium oxide by itself will also be studied, in order to determine what effect the phosphate has on the oxide during heating.

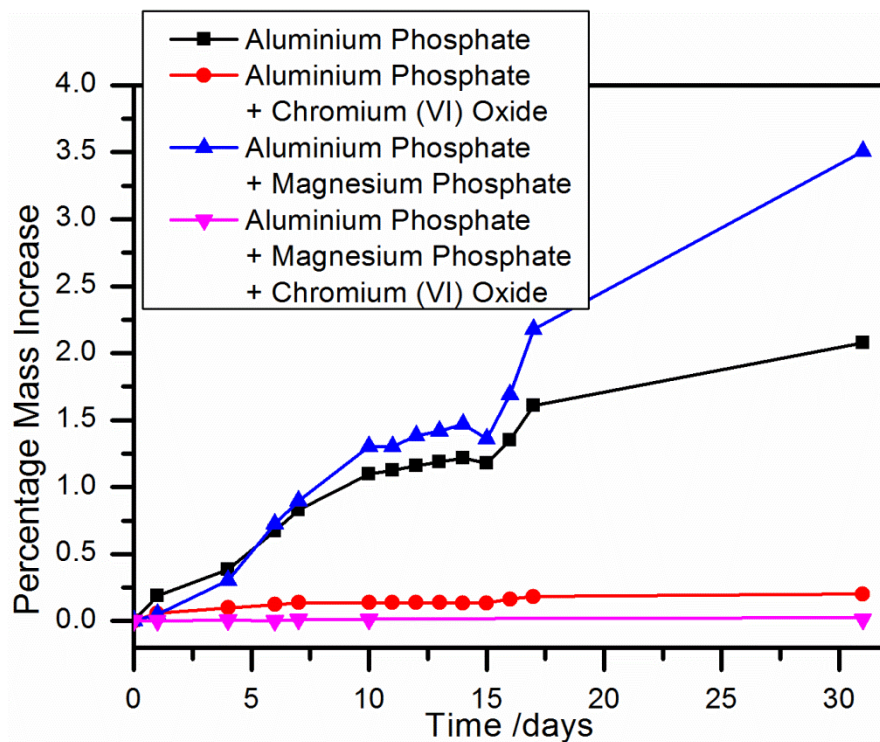
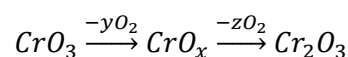


Figure 3.16 The mass changes of industrial phosphate coatings and the effects of chromium oxide on stability when left in humid atmospheres as monitored by A. Nolan at Cogent Power Ltd.

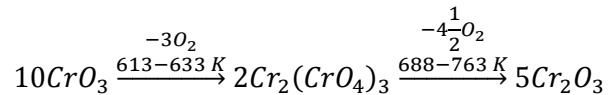
3.5.1 THE CURING OF CHROMIUM OXIDE

The thermal decomposition of chromium trioxide has previously been studied by others;⁵²⁻⁵⁴ however there is some disagreement on the route the thermal decomposition follows. Both authors agree that heating above 773 K leads to formation of the chromic oxide α -Cr₂O₃. Józwiak stated that the decomposition is a two or three stage process over a temperature range 543-773 K with the intermediate CrO_x.⁵² This intermediate was likely to be a mix of Cr₃O₈, Cr₅O₁₂, Cr₂O₅ and CrO₂, with the exact composition being determined by decomposition conditions. This decomposition route is summarised in Equation 3.8.



Equation 3.8 The thermal decomposition of chromium trioxide as proposed by Józwiak et al.⁵² An additional intermediate may be formed depending on reaction conditions.

Fouad observed a two-step decomposition process when the trioxide was heated in both oxidation (N₂/ Air) and reductive (H₂) atmospheres⁵³. The first stage occurred between 613-633 K and was associated with a 9.4 % drop in mass. This stage was attributed to the formation of chromium chromate (Cr₂(CrO₄)₃)⁵⁴ and was described by the author as a exothermic deoxygenation and polymerisation reaction. This chromate then decomposed between 688 and 763 K with a 24 % drop in mass to form α-Cr₂O₃. DSC analysis indicated that this step was endothermic. This reaction pathway is summarised in Equation 3.9.



Equation 3.9 The thermal decomposition of chromium trioxide as proposed by Fouad^{53, 54}

Due to the disputes in the literature it was decided to repeat thermogravimetic analysis on chromium trioxide before further study, in addition to full characterisation of the starting and ending materials and any intermediates. When the sample was heated in 100 K intervals it was observed to change from a purple powder to a black/brown powder between 573 and 673 K and to a green powder above 773 K, indicating the decomposition was most likely to be a two stage process. The ATR- IR spectra of the sample as it was heated (Figure 3.17) supported this observation as there were clear changes in the spectra between 573- 673 K and 773- 873 K. The spectra collected below 573 K were in good agreement with other spectra recorded from chromium trioxide in the literature and the ones recorded above 773 K were similar to those recorded from chromium (III) oxide,⁵⁵ however there is little data available for the intermediate oxides observed between 573- 773 K.

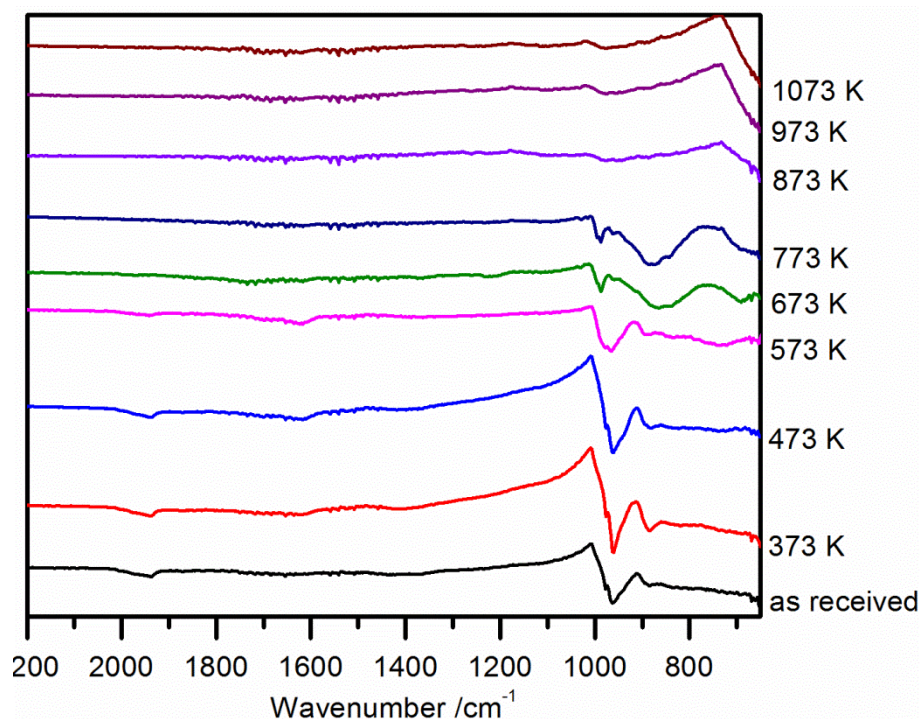
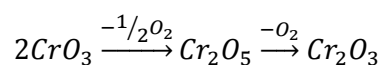


Figure 3.17 The effects of heating on the ATR-IR spectrum of chromium (VI) oxide

Thermogravimetric analysis of the chromium oxide as received from Sigma Aldrich (Figure 3.18) indicated that there were two transformations during the heating, one at 607 K and one at 758 K.

The phase transformation at 607 K is associated with a 20.7 % drop in mass. The temperature of this first mass loss is similar to the range recorded by Fouad,⁵³ however the mass decrease is much greater and does not allow for the assignment of chromium chromate as the intermediate. This percentage weight loss is equivalent to the loss of 1.3 oxygen atoms from the CrO_3 molecule; however the shape of the differentiated TGA graph (Figure 3.18) is very broad and there may be a second stage present. The best assignment that can be given to this mass loss is the formation of a mixed chromium oxide of the form CrO_x as described by Józwiak et al.⁵²

The second transition at 758 K is associated with a 14.9 % drop in mass. As this final product has already been identified using vibrational spectroscopies as chromium (III) oxide (Cr_2O_3) this mass loss is most likely to be associated with the reduction of Cr_2O_5 . Based on this deduction part of the thermal decomposition is summarised in Equation 3.10.



Equation 3.10 The proposed reaction observed in the TGA of Chromium (VI) oxide

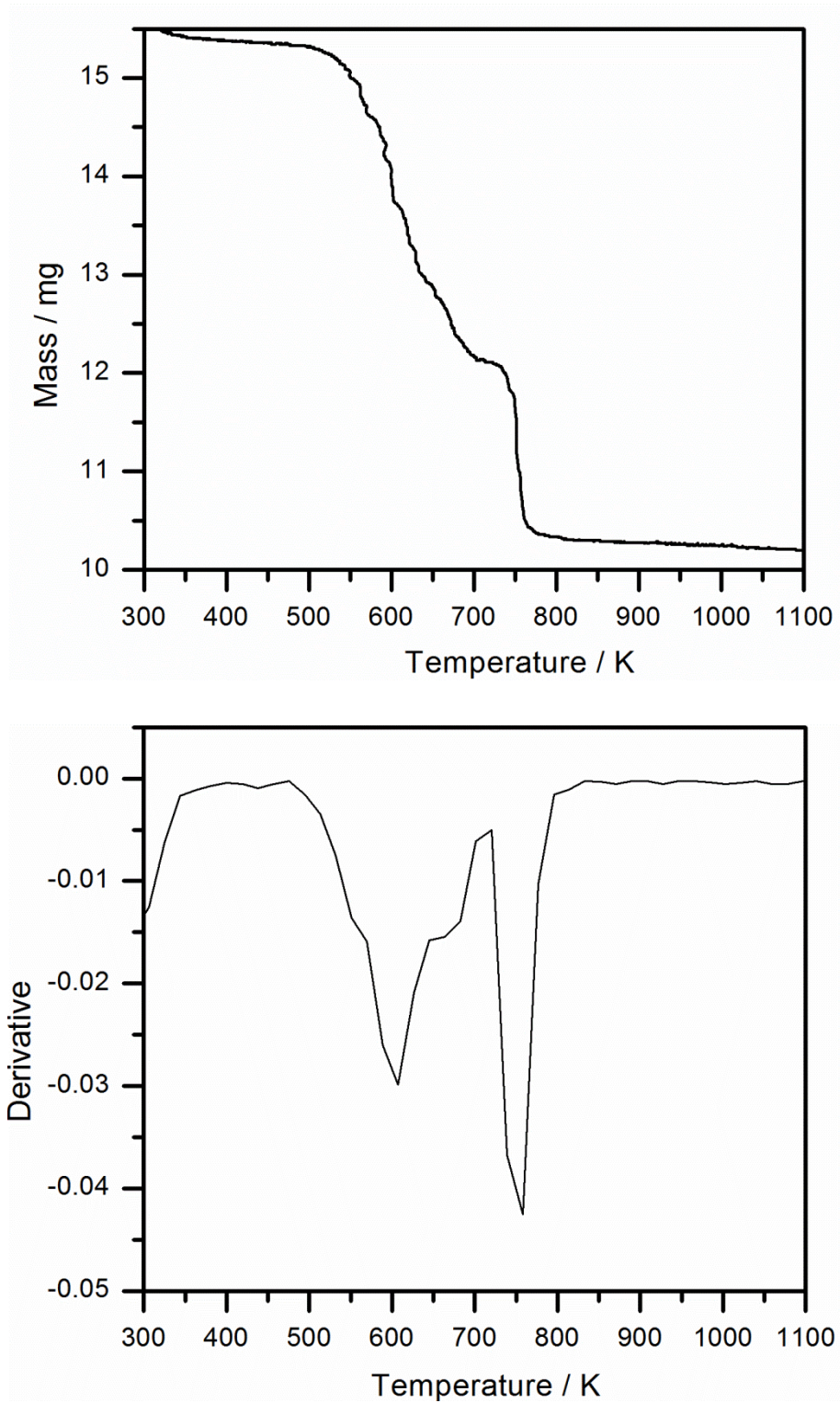


Figure 3.18 TGA of Chromium (VI) oxide (Sigma Aldrich, $\geq 98\%$ pur.)

3.5.2 THE EFFECTS OF CHROMIUM ADDITION TO MODEL MAGNESIUM PHOSPHATE COATINGS

Whilst aluminium phosphate is of more interest industrially as it is the currently used coating material online it was decided to investigate the effects of chromium oxide on magnesium oxide first. The two main reasons for this were that we had developed a greater understanding of magnesium phosphates behaviour during curing than aluminium phosphate and changes in magnesium phosphate were easily monitored using vibrational spectroscopies. Additionally it has previously been shown that chromium (VI) oxide has a greater effect on the magnesium phosphate.

3.5.2.1 THE ROLE OF CHROMIUM OXIDE CONCENTRATION

In order to probe the effects of chromium oxide on model magnesium phosphate coatings a range of samples were produced with differing concentrations of chromium VI oxide present. ATR-IR spectra from the resulting powders after drying and curing are shown in Figure 3.19 and Figure 3.20, and the Raman spectra are in Figure 3.21 and Figure 3.22.

Inspection of the ATR-IR spectra after drying (Figure 3.19) shows that they are a mixture of the spectra collected from the dried pure compounds (also shown in Figure 3.19 for clarity). The absorption bands observed in the ATR-IR spectra of the mixed coatings are listed in Table 3.13 along with their assignments. These mixed spectra indicate that the compounds within the coating are physically mixed; however at this point no chemical interaction has yet occurred.

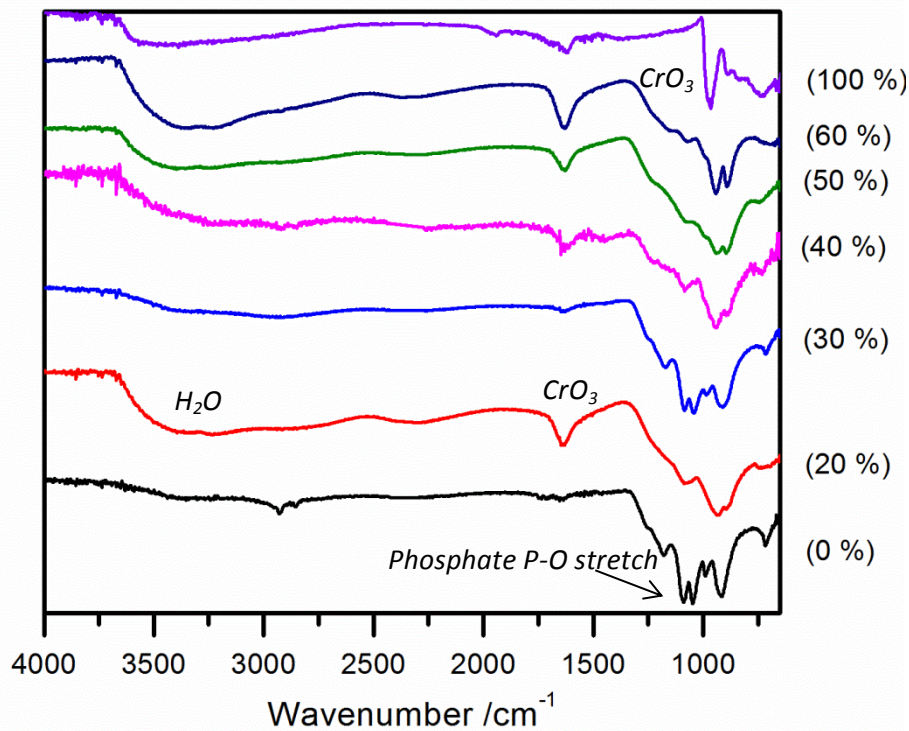


Figure 3.19 The ATR-IR spectra of magnesium phosphate/ chromium (VI) oxide model coatings after drying at 573 K. The percentage concentration of chromium (VI) oxide is given for each spectrum.

Absorbance/ cm^{-1}	Assignment
3394.7	Water
1629.8	Chromium Trioxide
1084.0	Magnesium Orthophosphate
941.3	Chromium Trioxide
896.9	Magnesium Orthophosphate
746.5	Chromium Trioxide

Table 3.13 The absorption bands in the ATR-IR spectra of mixed magnesium phosphate/ chromium oxide samples after drying at 573 K.

The addition of chromium trioxide to magnesium phosphate has a dramatic effect on the IR spectra even at low concentrations. As the concentration of chromium oxide increases the bands associated with absorption by chromium oxide become much more prominent- particularly those at 1629.8 and 941.3 cm^{-1} . By 60 % chromium oxide concentration the spectrum is dominated by oxide absorption bands. It is also clear from the spectra that the mixed coatings

have absorbed a large amount of water as indicated by the absorption at 3394.7 cm^{-1} (typical of a hydroxyl stretch) this was not observed in the IR spectrum collected from the pure magnesium phosphate sample.

Inspection of the ATR-IR spectra of the samples after curing (Figure 3.20) shows marked changes after the addition of chromium trioxide. At low concentrations of chromium oxide the absorption band at 1028.1 cm^{-1} associated with the P-O stretch appears to broaden and resolves into two separate peaks at 954.8 cm^{-1} and 1080.1 cm^{-1} as oxide concentration increases to 40%. As the concentration of chromium increases further the two bands begin to merge as the intensity of the lower wavenumber band increases and begins to dominate this region of the spectrum. This additional band cannot be assigned to either the magnesium metaphosphate or chromium (III) oxide and instead could be part of the magnesium orthophosphate spectrum, indicating the chromium oxide may be inhibiting the formation of metaphosphate previously observed in the pure magnesium phosphate samples.

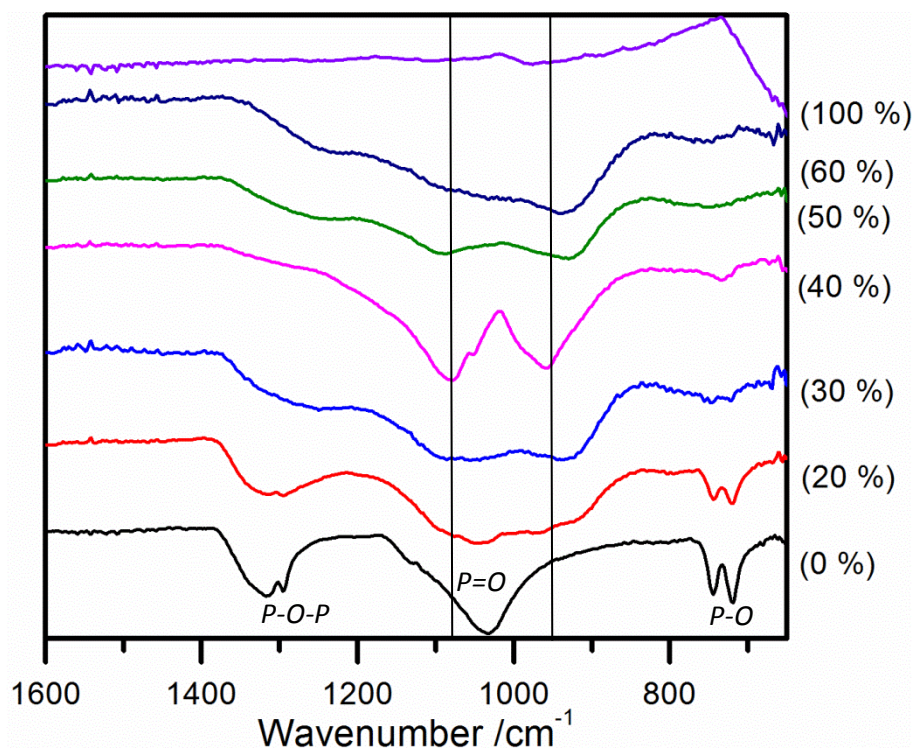


Figure 3.20 The ATR-IR spectra of magnesium phosphate/ chromium (VI) oxide model coatings after curing at 1073 K. The percentage concentration of chromium (VI) oxide is given for each spectrum.

The rest of the bands observed in the IR spectrum are part of the magnesium metaphosphate spectrum (also shown in Figure 3.20 for clarity). No absorptions from chromium (III) oxide

were recorded, which is most likely to be because the strongest absorptions associated with the oxide are outside the range of these spectra.

Inspection of the Raman spectra of the mixed model coating samples after drying (Figure 3.21) yielded similar results to those observed in the ATR-IR spectra. As with the ATR-IR data the observed absorption bands are listed in Table 3.14 with their assignments. The spectra indicated that both chromium trioxide and magnesium orthophosphate were present in the samples in good agreement with the IR spectroscopy. Mixing the compounds reduced the number of observed bands in the Raman spectra so that only the strongest absorptions for each compound were visible in the spectra.

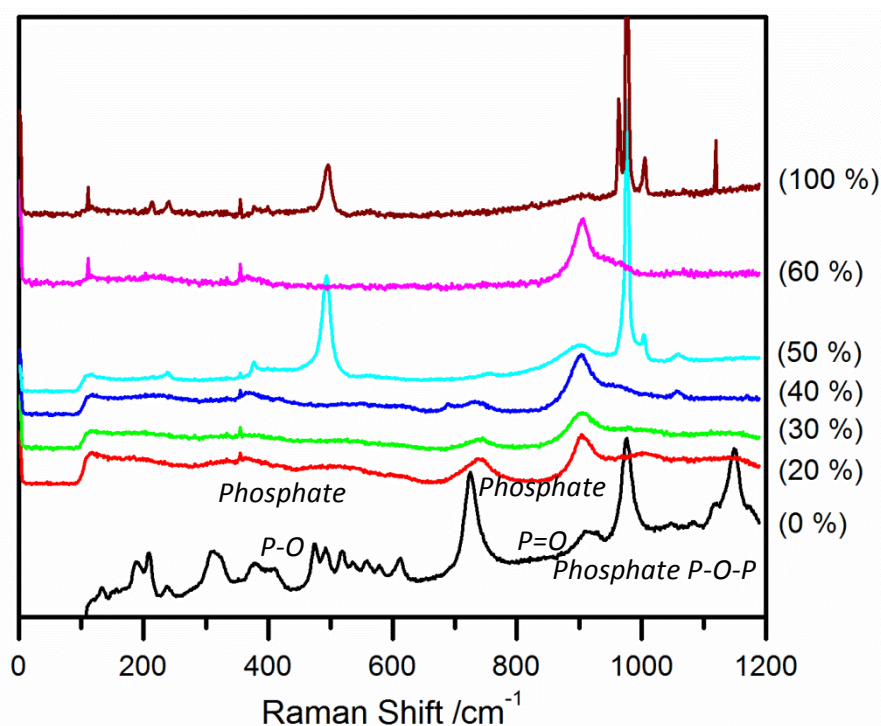


Figure 3.21 The Raman spectra of magnesium phosphate/ chromium (VI) oxide model coatings after drying at 573 K. The percentage concentration of chromium (VI) oxide is given for each spectrum.

<i>Absorbance/ cm⁻¹</i>	<i>Assignment</i>
115.2	
240.6	
378.1	
493.5	<i>Magnesium Phosphate</i>
757.0	
897.3	<i>Magnesium Phosphate</i>
976.4	<i>Magnesium Phosphate</i>
1003.8	
1058.5	<i>Magnesium Phosphate</i>

Table 3.14 The absorption bands in the Raman spectra of mixed magnesium phosphate/ chromium oxide samples after drying at 573 K.

The Raman spectra after curing (Figure 3.22) showed a similar reduction in the number of bands as the samples after drying. The spectra supported the conclusions drawn from the ATR-IR spectra and indicated the mixed samples were primarily chromium (III) oxide and magnesium metaphosphate.

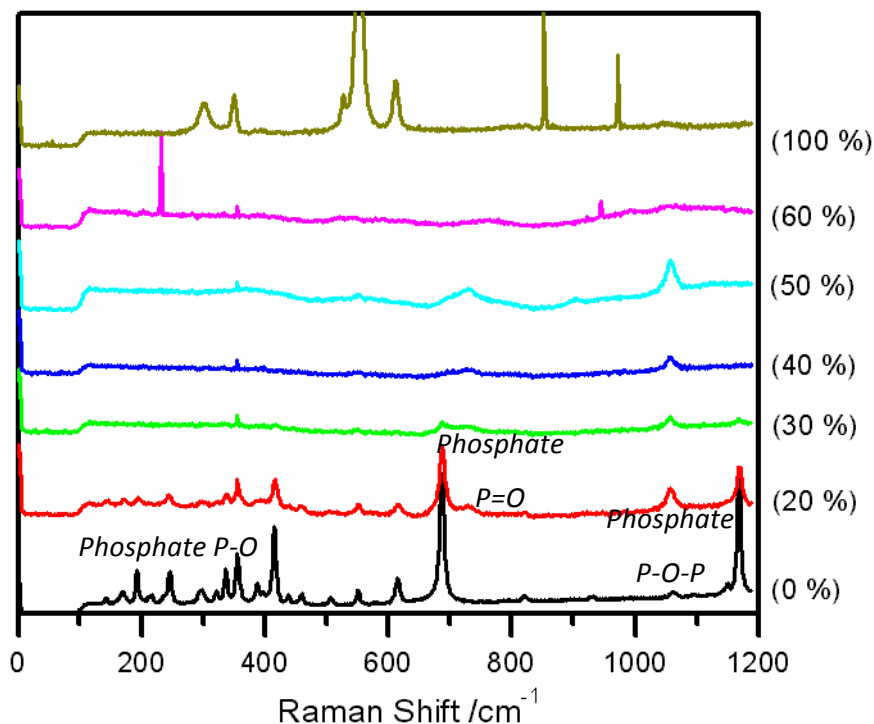


Figure 3.22 The Raman spectra of magnesium phosphate/ chromium (VI) oxide model coatings after curing at 1073 K. The percentage concentration of chromium (VI) oxide is given for each spectrum

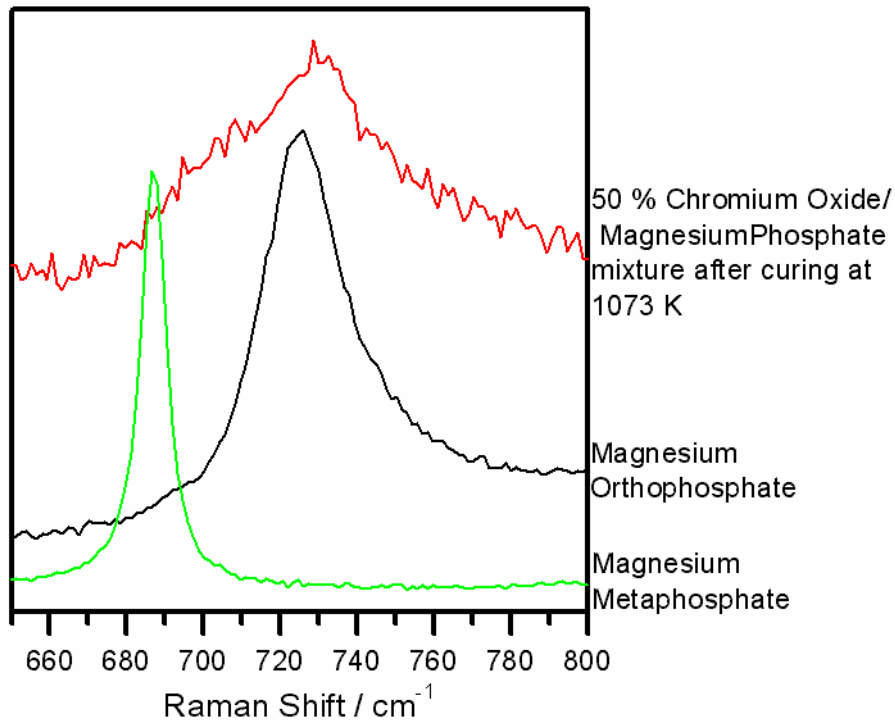


Figure 3.23 The broadening of the P=O stretch in the Raman spectrum of 50 % chromium oxide magnesium phosphate mixture after curing at 1073 K.

Inspection of the P=O stretch around 726 cm^{-1} in the mixed samples showed it was significantly broader than in the pure magnesium metaphosphate sample and at a higher Raman shift more typical of orthophosphate. A shoulder was present 697.5 cm^{-1} (see Figure 3.23). The Raman shift of this shoulder is similar to the shift recorded in pure magnesium metaphosphate samples (around 687 cm^{-1} , also shown in Figure 3.23), indicating that the samples are mixed phosphates as observed in the ATR-IR spectra.

<i>Absorbance/ cm⁻¹</i>	<i>Assignment</i>
372.4	<i>Magnesium Metaphosphate</i>
429.0	<i>Magnesium Metaphosphate</i>
554.7	<i>Chromium (III) Oxide or Magnesium Metaphosphate</i>
687.9	<i>Magnesium Metaphosphate</i>
728.7	<i>Magnesium Orthophosphate</i>
901.3	<i>Chromium (III) Oxide or Magnesium Metaphosphate</i>
1058.7	<i>Magnesium Metaphosphate</i>
1173.2	<i>Magnesium Metaphosphate</i>

Table 3.15 The absorption bands in the Raman spectra of mixed magnesium phosphate/ chromium oxide samples after curing at 1073 K.

XRD was used to confirm the identity of the phases present in the samples (see Figure 3.24 and Figure 3.25). It is clear from the diffraction patterns that chromium trioxide decreases the crystallinity of the model coatings, as indicated by the reduction in diffraction peaks and the prominent curve in the patterns typical of amorphous samples in good agreement with previous work by others.⁹ When patterns collected from the same sample before and after curing are compared it is clear that curing causes the sample to take on a more crystallised nature- particularly in samples containing less chromium.

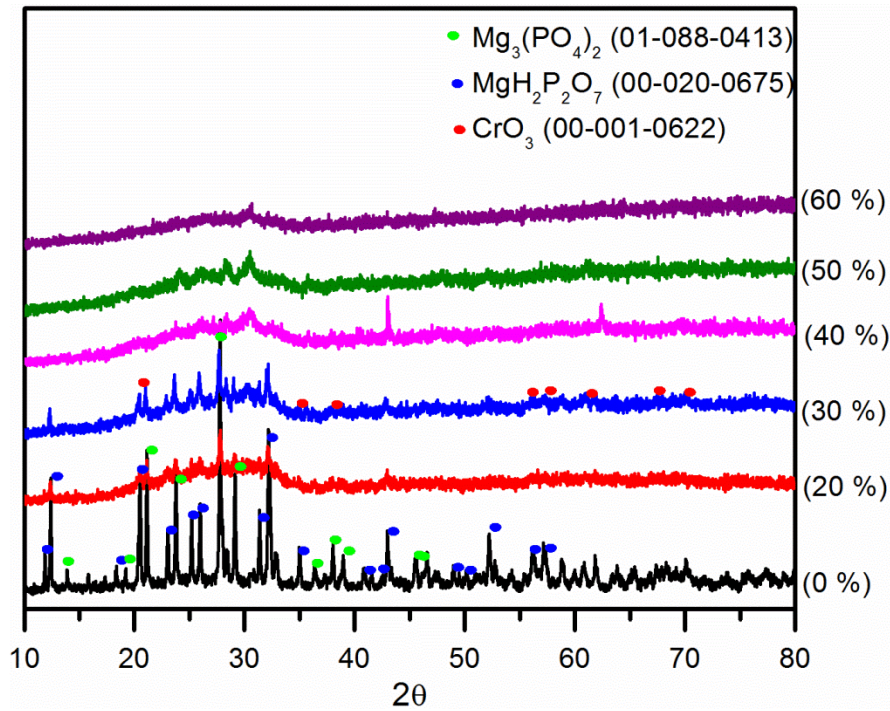


Figure 3.24 The X-ray diffraction patterns collected from magnesium phosphate/ chromium (VI) oxide model coatings after drying at 573 K. The concentration of chromium oxide is given for each spectrum.

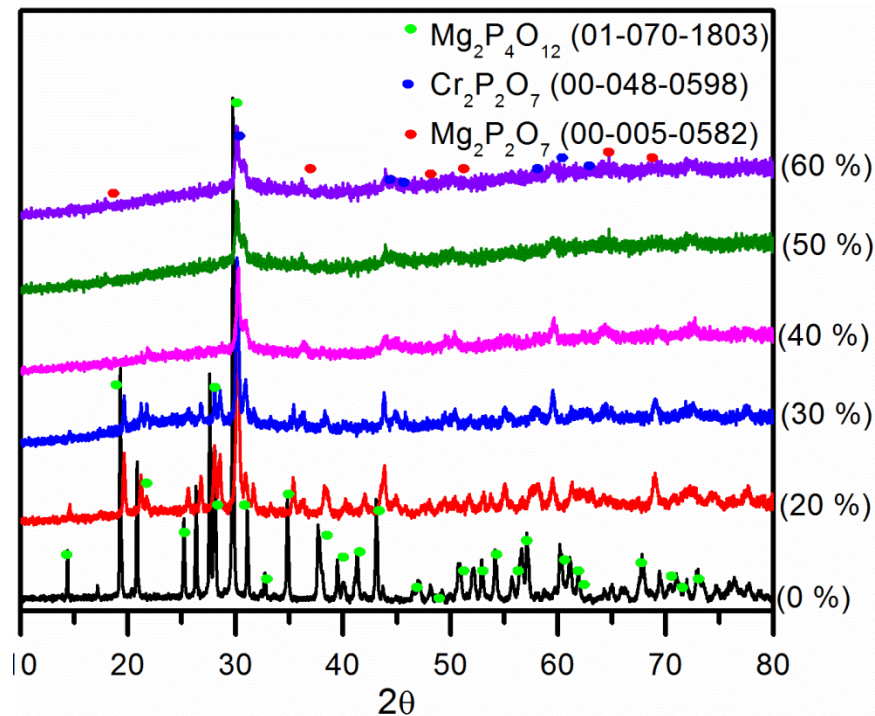


Figure 3.25 The X-ray diffraction patterns collected from magnesium phosphate/ chromium (VI) oxide model coatings after curing at 1073 K. The concentration of chromium oxide is given for each spectrum.

Chapter 3 The Structure and Stability Of Model Phosphate Coatings

The phases identified from the X-ray diffraction patterns taken from selected samples are listed in Table 3.16. The diffraction patterns support the conclusions drawn from the vibrational spectra that the dried samples are simply a physical mixture of magnesium phosphate and chromium trioxide. After curing the XRD indicated the presence of a chromium pyrophosphate ($\text{Cr}_2\text{P}_2\text{O}_7$), which was not observed in the vibrational spectroscopy. This is likely to be because magnesium and chromium pyrophosphate would have very bond energies making them difficult to distinguish via IR or Raman spectroscopy. Additionally the absorptions from chromium trioxide were off the scale in the IR spectra and the strongest transitions in the chromium (III) oxide Raman spectrum were at similar energies to ones in the magnesium phosphate spectrum, making them difficult to distinguish.

The mixtures used to produce the coatings contained a 2:3 ratio of magnesium oxide to phosphoric acid, which react in solution to form a phosphate before the chromium oxide was added. This ratio meant an excess of phosphoric acid was present in the solution which could have reacted when the sample was cured to form the observed chromium phosphate. Chromium pyrophosphate is likely to have similar tension and insulation properties to aluminium and magnesium phosphates and its formation is likely to be the cause of the increased tension observed when coatings with added chromium oxide are used on steel sheets.

XRD also indicates that the addition of chromium oxide prevents the formation of magnesium metaphosphate. This supports the earlier conclusion that excess phosphoric acid has a role in the formation of magnesium metaphosphate during curing and when it reacts to form the chromium pyrophosphate it makes the condensation reaction with the magnesium oxide (see Equation 3.7) much more difficult. As magnesium tetrametaphosphate is not formed during curing it cannot degrade as the coating is aged in humid atmospheres, therefore preventing the tackiness observed with pure magnesium phosphate samples. This data also indicates that the addition of phosphoric acid to aluminium orthophosphate coatings may aid the formation of aluminium metaphosphate and therefore cause an increase in the tension these coating impart on the steel sheets.

<i>Sample</i>	<i>Pure Magnesium Phosphate</i>	<i>30 % Chromium Oxide</i>	<i>50 % Chromium Oxide</i>	<i>70 % Chromium Oxide</i>
<i>Phases present after drying at 573 K</i>	$Mg_3(PO_4)_2 \cdot xH_2O$, $MgHP_2O_7$	<i>Periclase- Syn (MgO), Farringtonite (Mg₃(PO₄)₂), Chromium trioxide (CrO₃)</i>	<i>Farringtonite (Mg₃(PO₄)₂), α- Mg₂P₂O₇, Chromium trioxide (CrO₃)</i>	<i>Amorphous</i>
<i>Phases present after curing at 1073 K</i>	$Mg_2P_4O_{12}$	<i>Mg₂P₄O₁₂, β- Cr₂P₂O₇, Mg₂P₂O₇</i>	<i>Farringtonite (Mg₃(PO₄)₂), α- Mg₂P₂O₇, Cr₂P₂O₇ possible Mg₂P₄O₁₂</i>	<i>Mg₂P₂O₇</i>

Table 3.16 Summary of Phases observed in the X-ray diffraction patterns of selected model aluminium phosphate coatings

3.5.2.2 THE ROLE OF TEMPERATURE

In order to probe the role of temperature mixed samples containing 30 %, 50 % and 60 % chromium oxide were cured in 100 K intervals to study the intermediates formed with vibrational spectroscopies. The TGAs of these samples were also collected after drying in order to measure the temperature of any phase changes occurring. The spectra of the 50 % chromium oxide sample are shown below in Figure 3.26 and Figure 3.27 with the TGA in Figure 3.28. The collected spectra and TGAs from the other samples are in Appendix 1. Inspection of the IR spectra (Figure 3.26) shows little change in the bands present, however the relative intensities have altered, particularly between 973 and 1073 K. As the temperature increases the intensity of the bands related to chromium pyrophosphate (at 1049.3 and 1242.2 cm⁻¹) also increases until they dominate the spectrum at 1073 K. The positions of all bands observed in the spectra at 573 and 1073 K are recorded in Table 3.17 along with their assignments.

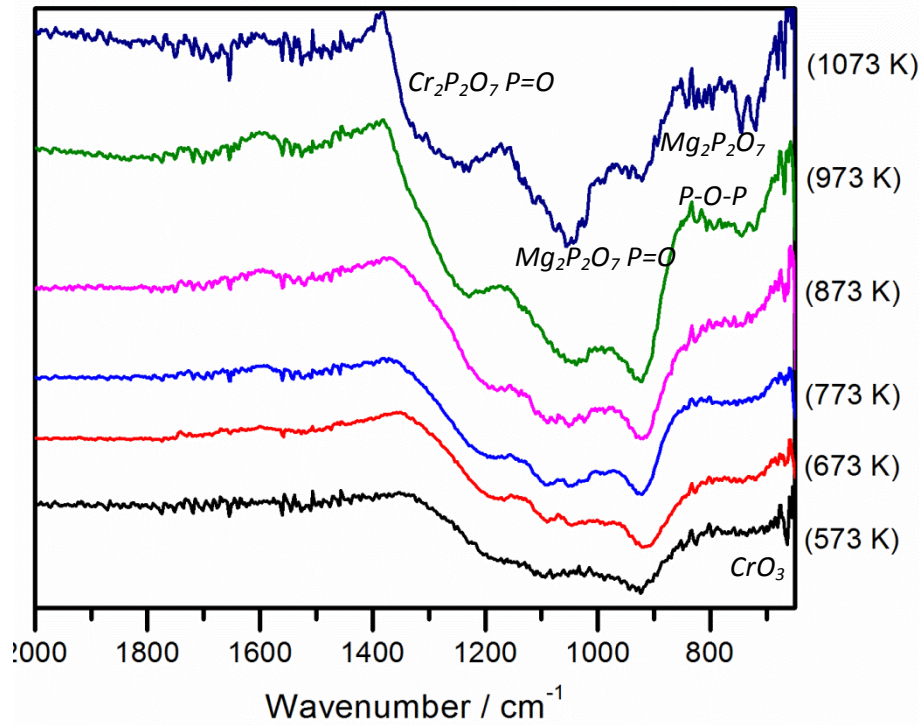


Figure 3.26 The ATR-IR spectra of a 50 % chromium oxide/magnesium phosphate mixed model coating after curing for 15 minutes in 100 K intervals.

IR Absorption		Assignment	Reference
573 K	1073 K		
665.4		Chromium Trioxide	
	719.4		
	746.5	Magnesium	
923.9	923.9	pyrophosphate P- O-P	
	1049.3	Magnesium phosphate P=O	
1082.1		MgO?	
	1242.2	Chromium Phosphate P=O	

Table 3.17 The absorption bands observed in the ATR-IR spectra of a 50 % chromium oxide/magnesium phosphate mixed model coating after drying at 573 K and curing at 1073 K for 15 minutes.

Chapter 3 The Structure and Stability Of Model Phosphate Coatings

The Raman spectra of the 50 % chromium oxide/ magnesium phosphate sample (Figure 3.27) were found to be more complicated than the ATR-IR spectra. The bands recorded in the spectra after heating at 673 K and 973 K are given in Table 3.18 along with their assignments and references. The spectrum collected at 573 K contained only two Raman bands at 905.2 and 992.1 cm^{-1} , however when the sample was heated to 673 K additional bands were resolved. These bands could be assigned to magnesium ortho- and pyrophosphate, as indicated in Table 3.18. This is in fairly good agreement with the results obtained from X-ray diffraction (see Table 3.16), however no chromium trioxide was observed in the Raman spectrum. Further heating caused the absorption bands to become less resolved until no absorption bands were observed at 873 K. A clear change in the spectrum is observed at 973 K, interpreted as the formation of magnesium orthophosphate (Table 3.18). Heating to 1073 K again caused the Raman spectrum to become less resolved, with fewer observable bands.

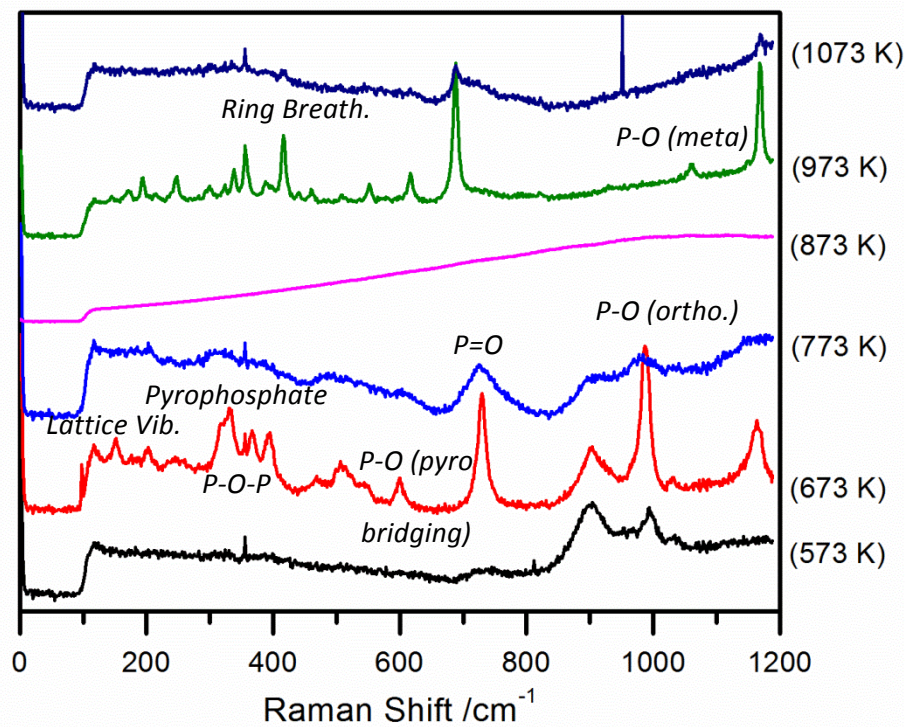


Figure 3.27 The Raman spectra of a 50 % chromium oxide/ magnesium phosphate mixed model coating after curing for 15 minutes in 100 K intervals.

Chapter 3 The Structure and Stability Of Model Phosphate Coatings

<i>Raman Shift</i>		<i>Assignment</i>	<i>Reference</i>
<i>673 K</i>	<i>973 K</i>		
118.2	116.7	<i>Lattice Vibrations</i>	
150.4	144.6	<i>Lattice Vibrations</i>	
202.9	192.7	<i>Lattice Vibrations</i>	
	246.4	<i>Lattice Vibrations</i>	
333.9	338.2	<i>Pyrophosphate P-O-P bend</i>	⁴⁷
366.7	355.3	<i>Pyrophosphate P-O-P bend</i>	⁴⁷
392.2			
	416.3	<i>Metaphosphate ring breathing</i>	⁴⁸
468.3			
507.4			
	551.9		
601.6		<i>Pyrophosphate P-O bridging stretch</i>	⁴⁶
	616.8	<i>Metaphosphate P-O-P symmetric stretch</i>	⁴⁸
	687.9	<i>Metaphosphate P-O-P asymmetric stretch</i>	⁴⁸
730.0		<i>Pyrophosphate symmetric P-O-P stretch</i>	⁴⁷
903.9		<i>Orthophosphate P-OH asymmetric stretch</i>	⁵⁰
985.5		<i>Orthophosphate P-O symmetric stretch</i>	⁴⁶
	1061.1	<i>Metaphosphate P-O symmetric stretch</i>	⁴⁸
1162.9	1168.02	<i>Orthophosphate P-O asymmetric stretch</i>	⁵⁰

Table 3.18 The absorption bands observed in the Raman spectra of a 50 % chromium oxide/magnesium phosphate mixed model coating after drying at 573 K and curing at 1073 K for 15 minutes.

Chapter 3 The Structure and Stability Of Model Phosphate Coatings

The vibrational spectra of samples containing an excess of chromium oxide and an excess of magnesium phosphate showed very similar behaviour to that observed in the 50 % sample and are shown in appendix 1.

Inspection of the TGA of the 50 % chromium oxide magnesium phosphate mixed model coating (Figure 3.28) shows that the system is very complex with at least four transitions occurring. The temperatures of the main transitions are given in Table 3.19, however the shape of the TGA indicates that many small reactions are occurring in addition to the ones reported.

The TGA indicates that a large amount of water was removed from the coating by 344.4 K (7.8 % total weight), despite the coating being dried at 573 K for 15 minutes in the furnace to produce the sample. This was not observed in the pure magnesium phosphate or chromium oxide. The phase transformation at 513.3 K could not be assigned to any transitions observed in the TGA of the previous pure samples as it at a much lower temperature than the formation of either CrO_x or Magnesium metaphosphate (607 and 636.3 K respectively). It is most likely to be some kind of interaction between the chromium oxide and phosphate or unreacted phosphoric acid to form chromium pyrophosphate, as observed in the X-ray diffraction patterns from some mixed samples. The final two transitions can be assigned to the formation of magnesium metaphosphate and chromium III oxide.

Temperature / K	Mass Loss /%	Assignment
344.4	7.8	Removal of Physisorbed water
513.3	5.1	unknown
663.6	5.0	$\text{Mg}_2\text{P}_2\text{O}_7 \rightarrow \text{Mg}_2(\text{PO}_3)$
719.6	6.1	$\text{Cr}_2\text{O}_5 \rightarrow \text{Cr}_2\text{O}_3$

Table 3.19 Transitions observed in the TGA of dried 50 % Chromium trioxide/ Magnesium phosphate model coating.

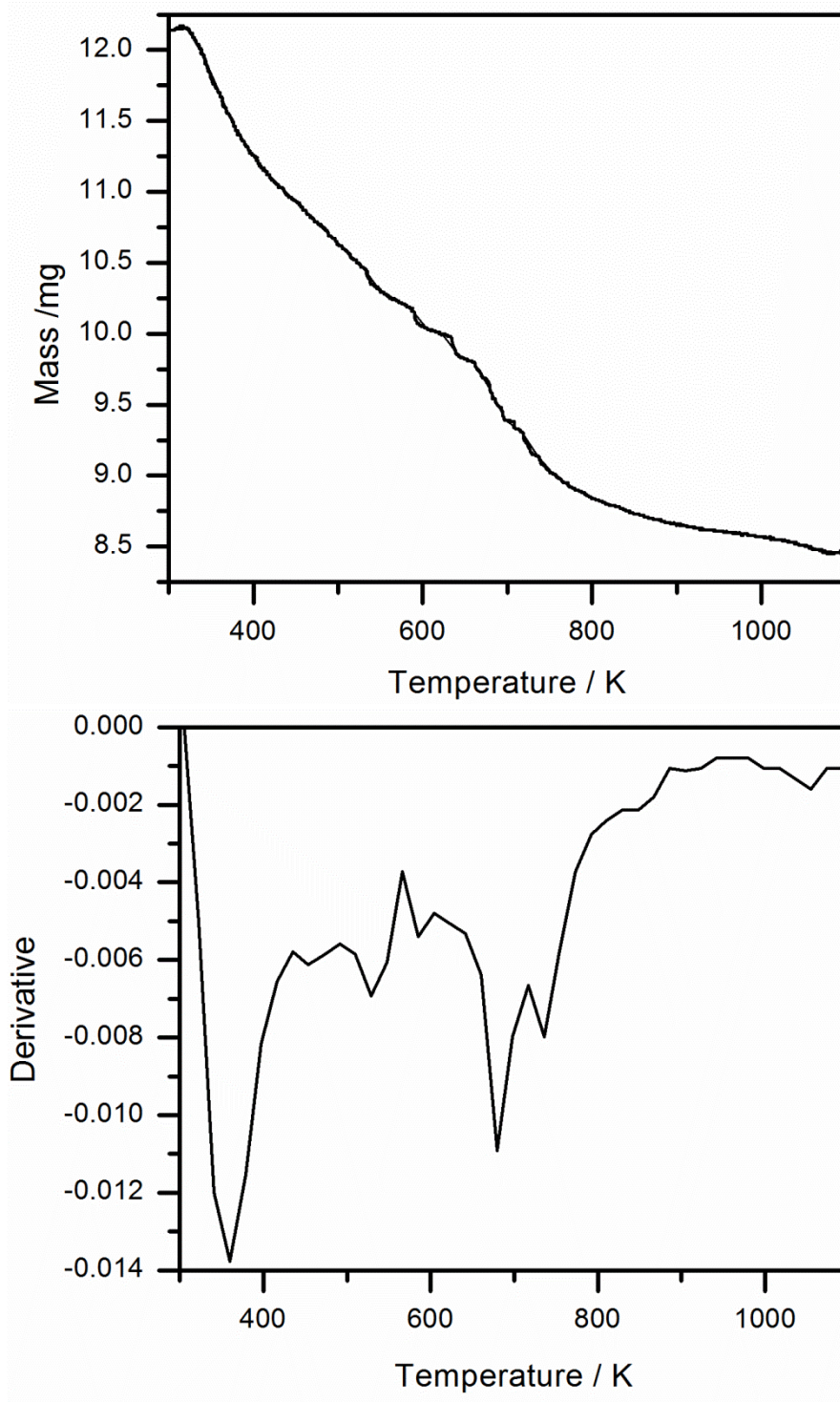


Figure 3.28 The thermo-gravimetric analysis of a dried 50 % chromium oxide/ magnesium phosphate mixed model coating.

Increasing the concentration of chromium oxide within the mixture appeared to simplify the TGA (Figure 3.29) with only four apparent transitions. These transitions have the same assignments as those in the previous TGA however there are several key differences. The mass

Chapter 3 The Structure and Stability Of Model Phosphate Coatings

loss associated with physisorbed water is at a slightly lower temperature (323.3 K) and much greater (15.9 % compared with 7.8 %). This appears to indicate that dried coatings with higher chromium oxide content are more hygroscopic and absorb more water. The transition thought to be associated with the formation of chromium pyrophosphate was at a lower temperature than in the 50 % sample and showed a much larger drop in mass. This may indicate that the reaction is easier to perform with a higher chromium oxide concentration and that much more pyrophosphate is formed.

The formation of magnesium phosphate shows a much smaller drop in mass than expected (1.7 % instead of 4.2 %). This may imply that excess phosphoric acid is required to promote the condensation reaction for the formation of the metaphosphate or that the ring formation is a reaction between the pyrophosphate and phosphoric acid. When chromium oxide is added to the coating it reacts with the excess phosphoric acid to form chromium pyrophosphate at a lower temperature, preventing (or reducing) the formation of magnesium metaphosphate. This would stabilise the mixed coatings as the presence of magnesium metaphosphate has been identified as the major cause of coating degradation.

<i>Temperature / K</i>	<i>Mass Loss /%</i>	<i>Assignment</i>
323.3	15.9	<i>Removal of Physisorbed water</i>
453.9	11.6	<i>unknown</i>
696.4	1.7	<i>Mg₂P₂O₇ → Mg₂(PO₃)</i>
771.1	6.2	<i>Cr₂O₅ → Cr₂O₃</i>

Table 3.20 Transitions observed in the TGA of dried 66 % Chromium trioxide/ Magnesium phosphate model coating.

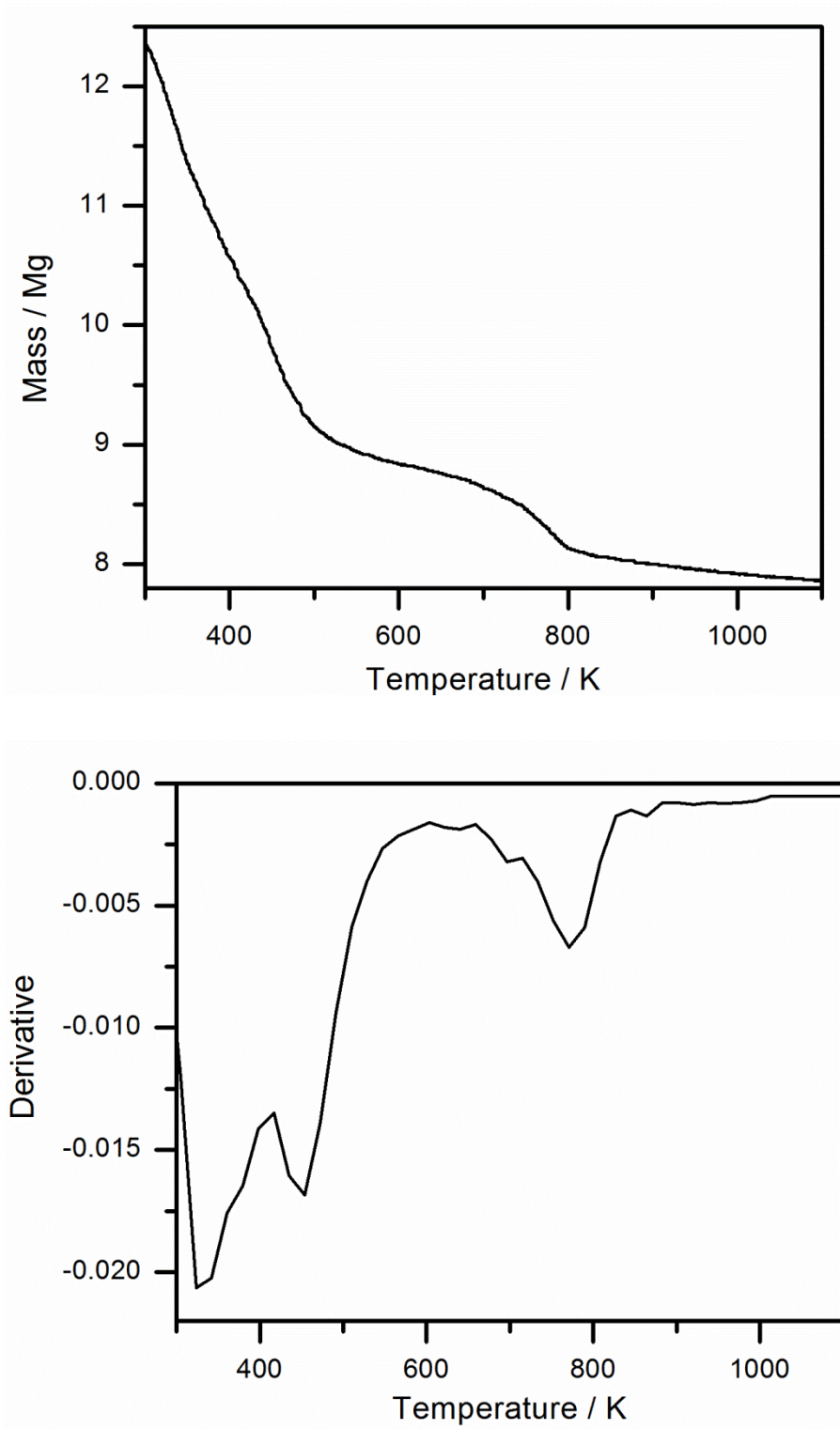


Figure 3.29 The thermo-gravimetric analysis of a dried 66 % chromium oxide/ magnesium phosphate mixed model coating.

3.5.3.3 PROBING THE ACTIVE CHROMIUM SPECIES

In order to determine the active chromium species a sample was prepared containing 50 % Cr_2O_5 (the assumed intermediate in the thermal decomposition of chromium trioxide) and magnesium phosphate. XRD (Figure 3.30) indicated that after drying the sample was amorphous and after curing consisted of chromium (III) oxide and magnesium pyrophosphate. The diffraction pattern collected from the cured sample indicated that the powder still had a large amount of amorphous material present (as indicated by the typical amorphous curve). This loss of crystallinity was observed in the samples containing chromium (VI) oxide and in the literature.⁹

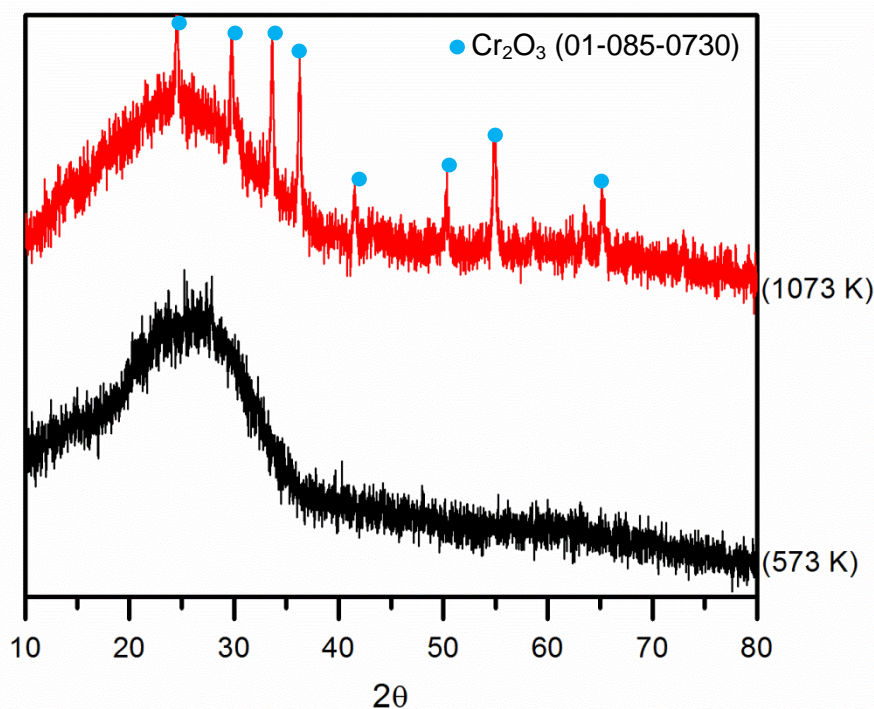


Figure 3.30 The X-ray Diffraction patterns collected from a 50 % Cr_2O_5 / magnesium phosphate mixed model coating after drying at 573 K and curing at 1073 K for 15 minutes.

The X-ray diffraction patterns appear to indicate that there is little interaction between the magnesium phosphate and chromium oxide intermediate, a conclusion which is supported by the thermogravimetric analysis (see Figure 3.31). The three main transitions observed in the TGA occur at 352.4 (1.6 %), 503.7 (7.8 %) and 705.5 K (5.1 %). These transitions can be assigned to the loss of physisorbed water, magnesium metaphosphate formation and chromium (III) oxide formation respectively. These transitions were all observed in the TGA collected from pure magnesium phosphate or pure chromium (VI) oxide, indicating that there was little interaction between the magnesium phosphate and Cr_2O_5 intermediate and the hexavalent

species is responsible for formation of chromium pyrophosphate, thought to be important in coating stability.

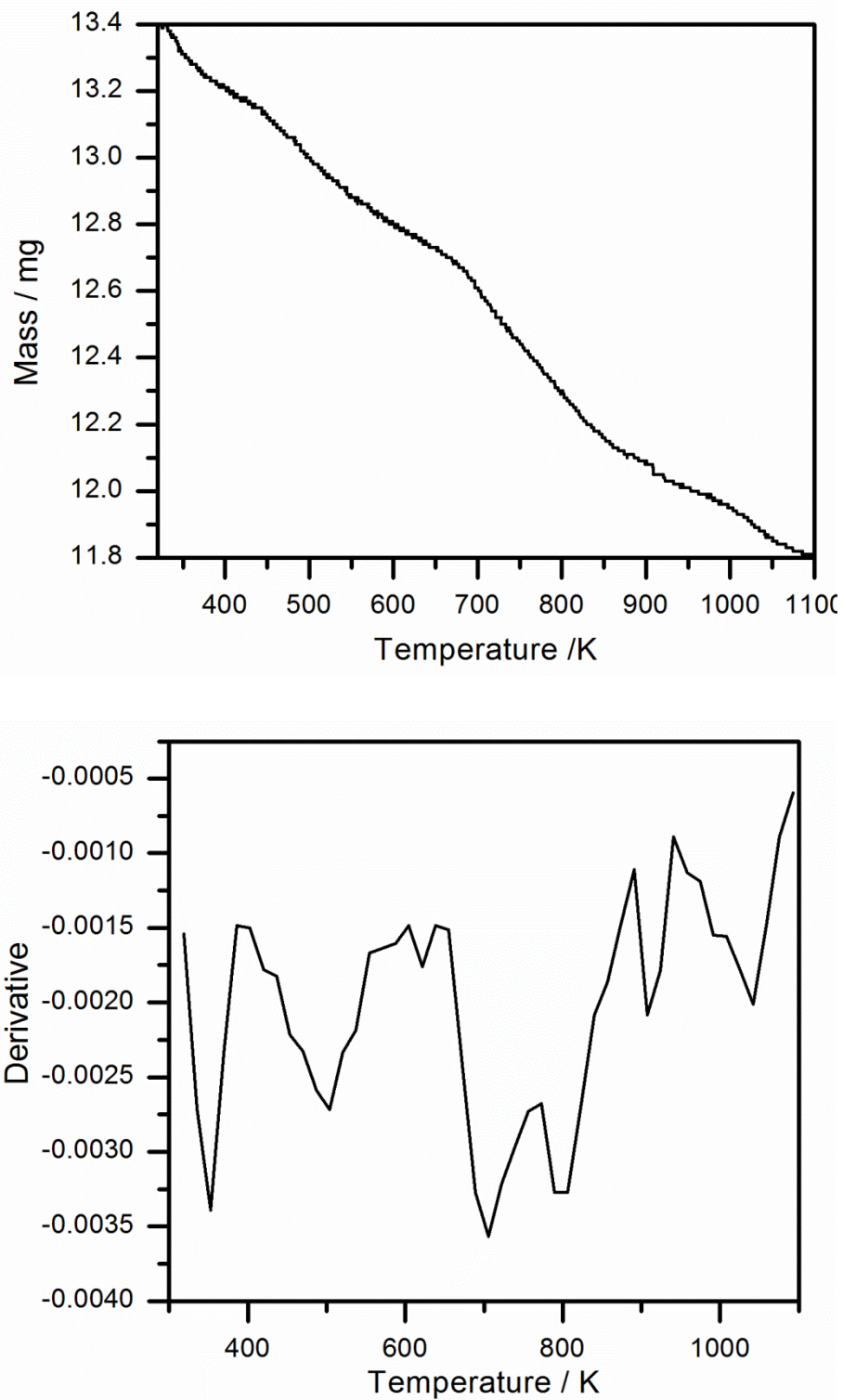


Figure 3.31 The thermogravimetric Analysis of a 50 % Cr_2O_5 / magnesium phosphate mixed model coating after drying at 573 K for 15 minutes.

Chapter 3 The Structure and Stability Of Model Phosphate Coatings

Additional small transitions were observed at higher temperatures (800 K and above), however any products formed in these reactions is unlikely to have an effect on the stability of the magnesium phosphate, as the metaphosphate has already formed by 600 K.

3.5.3 THE EFFECTS OF CHROMIUM ADDITION TO MODEL ALUMINIUM PHOSPHATE COATINGS

As with the model magnesium phosphate coatings a range of model aluminium phosphate coatings were produced with different concentrations of chromium oxide present. The ATR-IR and Raman spectra of the resulting powders before and after curing are shown in Figure 3.32, Figure 3.33, Figure 3.34 and Figure 3.35.

It is clear from Figure 3.32 the ATR-IR spectra of the mixed samples after drying at 573 K are a mixture of the spectra collected from the pure samples and the assignments of each band (chromium trioxide or aluminium phosphate) are given in Table 3.21. It is clear from the spectra that whilst the compounds are physically mixed within the coating there has been no reaction between them at this temperature, as was observed in the magnesium phosphate mixed coatings (Figure 3.19). The addition of chromium oxide to the coating has a dramatic effect on the spectra, even at low concentrations.

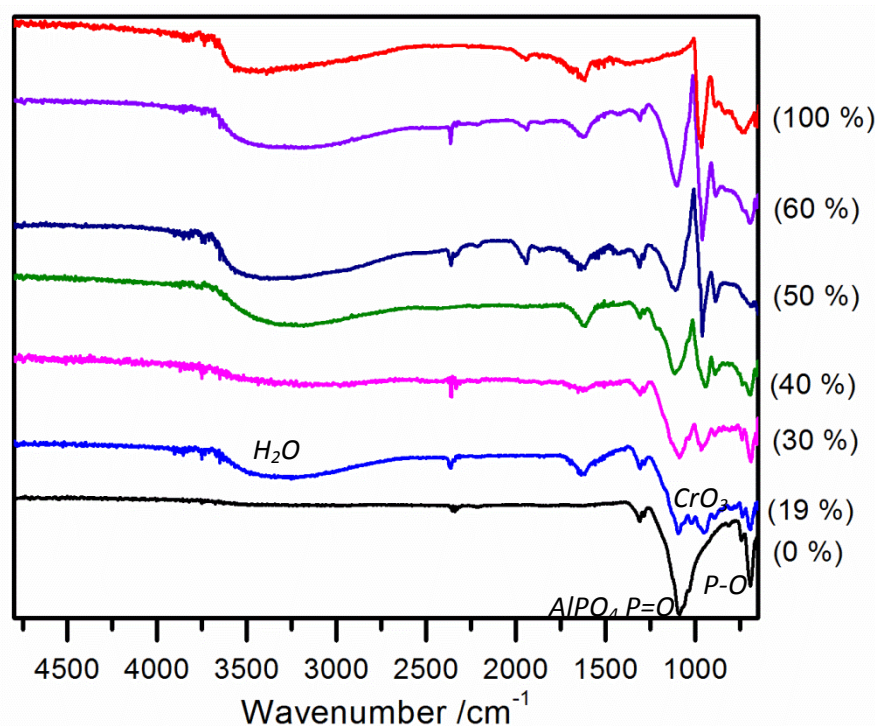


Figure 3.32 The ATR-IR spectra of aluminium phosphate/ chromium (VI) oxide model coatings after drying at 573 K. The percentage concentration of chromium (VI) oxide is given for each spectrum.

<i>Absorbance/ cm⁻¹</i>	<i>Assignment</i>
3398	Water
1940.4	Chromium Trioxide
1614.4	Chromium Trioxide
1311.6	Aluminium Orthophosphate
1286.5	Aluminium Orthophosphate
1111.0	Aluminium Orthophosphate
962.5	Chromium Trioxide
889.2	Chromium Trioxide
692.4	Aluminium Orthophosphate

Table 3.21 The absorption bands in the ATR-IR spectra of mixed aluminium phosphate/ chromium oxide samples after drying at 573 K.

Inspection of the spectra after curing at 1073 K (Figure 3.33) showed that the spectra were dominated by the aluminium orthophosphate at all chromium oxide concentrations. This is likely to be because the strongest IR absorptions by the chromium III oxide are at lower wavenumber than recorded in these spectra (as limited by the spectrometer) however the increase in transmission at 727.2 cm⁻¹ in the chromium oxide spectrum becomes more pronounced with increasing oxide concentration.

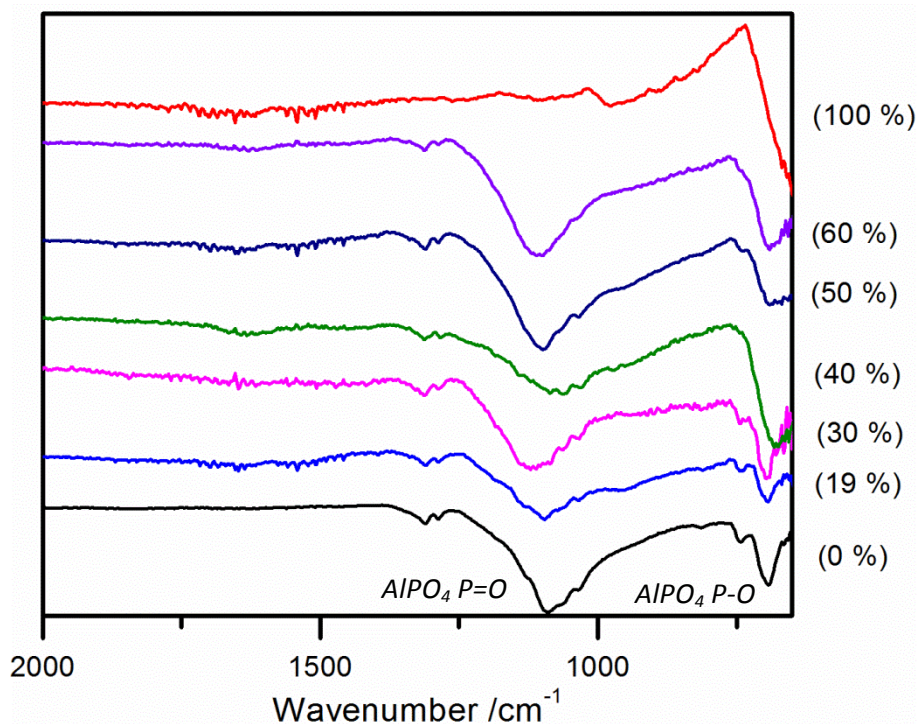


Figure 3.33 The ATR-IR spectra of aluminium phosphate/ chromium (VI) oxide model coatings after curing at 1073 K. The percentage concentration of chromium (VI) oxide is given for each spectrum.

Absorbance/ cm^{-1}	Assignment
1654.9	Chromium oxide
1541.1	Aluminium Orthophosphate
1311.6	Aluminium Orthophosphate
1288.4	Aluminium Orthophosphate
1097.5	Aluminium phosphate
1033.8	Aluminium Orthophosphate
949.0 (sh)	Chromium oxide
738.7	Chromium oxide
690.5	Aluminium Orthophosphate

Table 3.22 The absorption bands in the ATR-IR spectra of mixed aluminium phosphate/ chromium oxide samples after curing at 1073 K.

Chapter 3 The Structure and Stability Of Model Phosphate Coatings

Adding chromium oxide to the coating caused a significant shift in the energy of the absorption arising from the P-O bond from 1092 cm^{-1} to 1096 cm^{-1} . The energy increased with additional chromium oxide to 1114.9 cm^{-1} in the spectrum taken from the sample containing 60 % chromium oxide. This wavenumber is more typical of aluminium metaphosphate (for example bands have previously been recorded at 1020 , 1040 and 1145 cm^{-1} by Rojo et al⁵⁶). This has previously been rationalised as metaphosphate having shorter P-O_{ext} bond lengths and therefore absorbing light at a higher wavenumber.

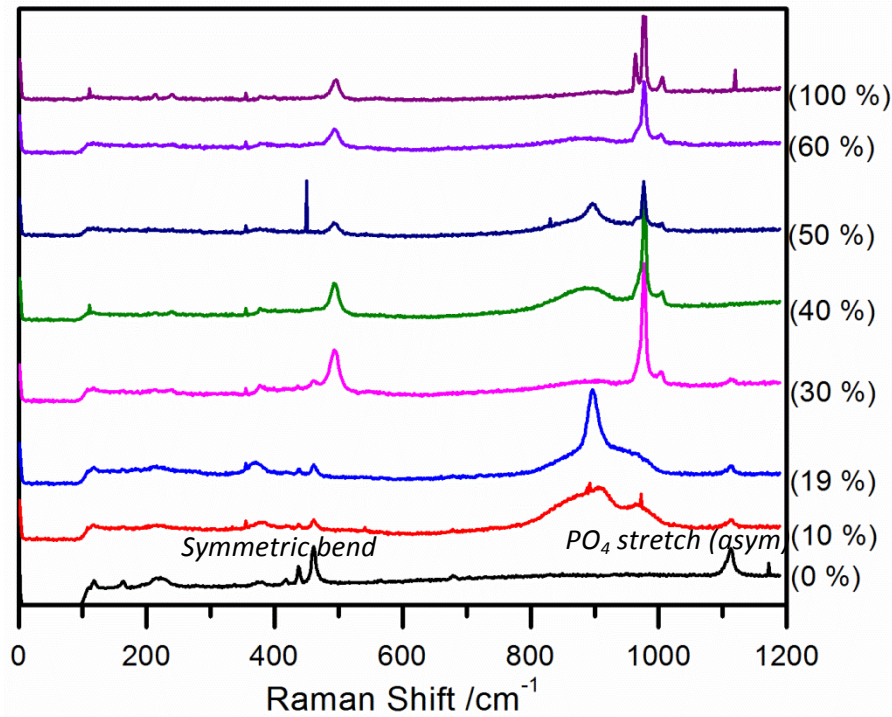


Figure 3.34 The Raman spectra of aluminium phosphate/ chromium (VI) oxide model coatings after drying at 573 K. The percentage concentration of chromium (VI) oxide is given for each spectrum.

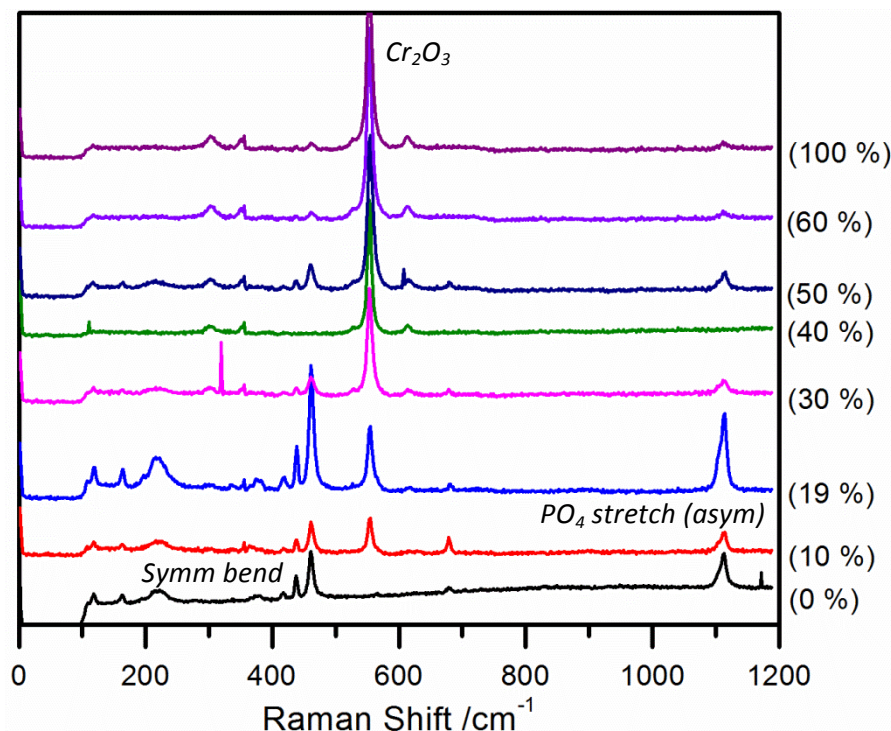


Figure 3.35 The Raman spectra of aluminium phosphate/ chromium (VI) oxide model coatings after curing at 1073 K. The percentage concentration of chromium (VI) oxide is given for each spectrum.

These data in conjunction with XRD (patterns are in Appendix 1, however the phases observed in a selection of samples indicative of all the chromium oxide/ aluminium phosphate mixtures are summarised in Table 3.23) indicate that the addition of chromium (VI) oxide to aluminium orthophosphate promotes the dehydrolytic condensation reaction previously observed in magnesium phosphate samples.

The formation of aluminium metaphosphate ($\text{Al}(\text{PO}_3)_3$) in these model coatings may explain the increased tension exerted on electrical steel sheets by the industrial 'Mix 2' trial coating. The reaction the aluminium phosphate undergoes during curing is outlined in Equation 3.11.



Equation 3.11 The formation of aluminium metaphosphate from aluminium orthophosphate during heating in the presence of chromium trioxide

The equation indicates that in addition to aluminium metaphosphate aluminium oxide is also formed. Aluminium oxide was observed in the x-ray diffraction patterns of the model coatings (Table 3.23 and appendix one). Chromium trioxide has historic uses as an oxidant in organic chemistry in reactions such as the Jones⁵⁷ and Sarett⁵⁸ oxidations, however its use has been

Chapter 3 The Structure and Stability Of Model Phosphate Coatings

reduced in favour of less toxic reagents. The results observed in this section indicate that chromium trioxide may have a role in the promotion of the reaction forming the aluminium oxide and as a side effect is causing the formation of the metaphosphate.

Sample	Pure			
	Aluminium Phosphate	19% CrO₃	50% CrO₃	75% CrO₃
Phase Before Curing	Berlinite (AlPO ₄)	Berlinite (AlPO ₄)	Berlinite (AlPO ₄) CrO ₃	Berlinite (AlPO ₄) CrO ₃
Phase after curing	Berlinite (AlPO ₄)	Berlinite (AlPO ₄), Cr ₂ O ₃ ? Al(PO ₃) ₃ , Al ₂ O ₃	Berlinite (AlPO ₄), Cr ₂ O ₃ Al(PO ₃) ₃ , Al ₂ O ₃	Berlinite (AlPO ₄), Cr ₂ O ₃ Al(PO ₃) ₃ , Al ₂ O ₃

Table 3.23 Summary of Phases observed in the X-ray diffraction patterns of model aluminium phosphate coatings

Thermogravimetric analysis was performed on a selection of the aluminium phosphate chromium oxide mixtures (50 % chromium oxide shown in Figure 3.36, and 19% chromium oxide shown in appendix one). Three weight losses were observed in both samples, one around 340 K, one around 690 K and one around 735 K (exact temperatures of point of greatest change are recorded in Table 3.24). The first of these three transitions is assigned as the loss of absorbed water from the surface of powdered coating. It was noted that the mass of water desorbed from the coating increased with chromium oxide concentration, with the exception of the 100 % chromium oxide sample, where no water was desorbed during TGA.

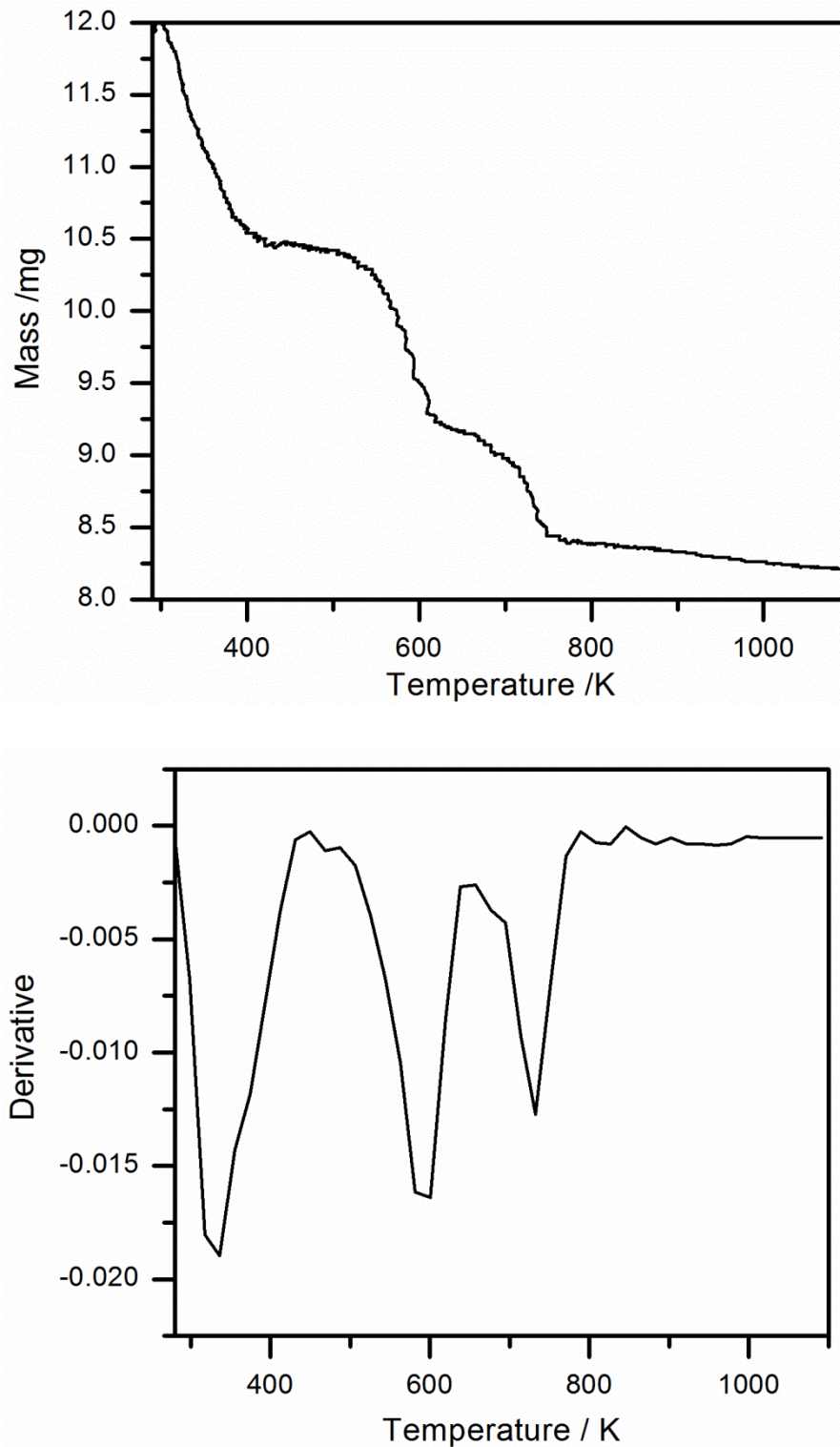


Figure 3.36 The Thermogravimetric analysis of the model aluminium phosphate coating containing 50 % chromium oxide

The second transition is at similar temperature to that seen in the TGA of chromium oxide (Figure 3.18) and is assigned to the formation of the CrO_x intermediate observed in the chromium oxide TGA. The third transition is at similar temperature to the reaction of this

Chapter 3 The Structure and Stability Of Model Phosphate Coatings

intermediate in the TGA of the pure chromium (VI) sample, and is therefore assigned to the formation of Cr_2O_3 .

% Chromium Oxide	Absorbed water		CrO_x formation		Cr_2O_3 Formation	
	Temp	Mass	Temp	Mass	Temp	Mass
	/K	/%	/K	/%	/K	/%
0	325.7	1.1	-	-	-	-
19	342.2	10.1	587.3	2.8	738.1	1.7
50	336.5	12.6	600.6	11.7	732.7	6.5
100	-	-	607	20.7	758	14.9

Table 3.24 Summary of Transitions observed during Thermo-gravimetric analysis of model aluminium phosphate coatings.

3.6 SUMMARY

This chapter has investigated model aluminium and magnesium phosphate coatings in order to probe the stability of online and trial tension coatings used at Cogent Power Ltd. It has been found that aluminium and magnesium phosphates impart tension on steel sheets via two different mechanisms, however it is unclear precisely how this occurs in aluminium phosphate coatings.

Magnesium phosphate was found to undergo a dehydrolytic condensation reaction during the curing process leading to the formation of magnesium tetrametaphosphate. This reaction did not occur in the aluminium phosphate model coating. When these observations are compared to the reports from Cogent Power Ltd of increased tension when using a magnesium phosphate coating rather than an aluminium phosphate one, it implies that the formation of a metaphosphate during curing is key to imparting a large amount of tension on the steel substrate.

Aging the magnesium phosphate model coating showed that the tetrametaphosphate was unstable in humid conditions and it decomposed back to the orthophosphate after 2 weeks, indicating that the condensation reaction was reversible. Industrial reports showed that magnesium phosphate coatings degraded in air (and much more rapidly under humid

conditions) and all positive tension effects of the coatings were lost (it was also noted that the coating became 'tacky'). This leads to the conclusion that the instability of the tetrametaphosphate and its breakdown back to the orthophosphate is the cause of the instability of the magnesium phosphate tension coatings and the observed loss of tension.

Aluminium phosphate does not form the metaphosphate as easily as the magnesium phosphate, despite literature results indicating metaphosphate formation was likely^{3,4,7}. In addition a range of magnesium phosphate samples with different initial phosphoric acid concentrations was produced and the sample containing an excess of magnesium oxide did not form the metaphosphate. It is therefore proposed that an excess of phosphoric acid is important in the formation of metaphosphate. This lack of metaphosphate in the aluminium phosphate coatings explains not only the observed reduction in tension with these coatings, but also the greater stability seen with them.

The addition of chromium (VI) oxide was found prevent the formation of magnesium metaphosphate. It is thought that this is caused by the formation of chromium pyrophosphate, most likely from a reaction between chromium (VI) oxide and phosphoric acid, removing the excess from the system (supporting the previous conclusion that an excess of acid is required to form the metaphosphate). The prevention of metaphosphate formation links in well with observations of industrial coatings by Cogent Power Ltd, which showed that the addition of chromium trioxide to the phosphates improved both the stability of the coating and the tension it imparted on the steel. The chromium pyrophosphate is presented as a cause of the increased tension exerted on steel sheets reported when these mixed coatings are used.

It was also observed that the addition of chromium (VI) oxide to aluminium phosphate coatings did cause the formation of aluminium metaphosphate. It was argued that as chromium (VI) oxide is widely used as an oxidant in organic chemistry it could be oxidising the aluminium by-products of the condensation reaction making the formation of alumina much easier therefore increasing aluminium metaphosphate formation. The presence of aluminium metaphosphate is proposed as the cause of the increase in tension when chromium trioxide is added to aluminium phosphate coatings.

3.7 REFERENCES

1. S.-S. Cho, S.-B. Kim, J.-Y. Soh and S.-O. Han, *IEEE Transactions on Magnetics*, 2009, **45**, 4165-4168.

Chapter 3 The Structure and Stability Of Model Phosphate Coatings

2. A. J. Moses, *IEEE Proceedings-a-Science Measurement and Technology*, 1990, **137**, 233-245.
3. H.-S. M. Dong-Pyo Kim, Jae-Seong Rho, Kyoo-Seung Han, Hee-Gweon Woo, Hunseung Ha, Feng Cao,, *Composites Science and Technology*, 2003, **63**, 493-499.
4. G. Tricot, D. Coillot, E. Creton and L. Montagne, *Journal of the European Ceramic Society*, 2008, **28**, 1135-1141.
5. L. Y. Hong, H. J. Han, H. Ha, J. Y. Lee and D. P. Kim, *Composites Science and Technology*, 2007, **67**, 1195-1201.
6. M. Vippola, J. Keranen, X. D. Zou, S. Hovmoller, T. Lepisto and T. Mantyla, *Journal of the American Ceramic Society*, 2000, **83**, 1834-1836.
7. J. H. Morris, P. G. Perkins, A. E. A. Rose and W. E. Smith, *Chem. Soc. Rev.*, 1977, **6**, 173-194.
8. M. N. Singh, I. Singh and J. L. Pandey, *Anti-Corrosion Methods and Materials*, 1997, **44**, 90-&.
9. H.-J. Han and D.-P. Kim, *Journal of Sol-Gel Science and Technology*, 2003, **26**, 223-228.
10. S. Ahmaniemi, M. Vippola, P. Vuoristo, T. Mantyla, M. Buchmann and R. Gadow, *Wear*, 2002, **252**, 614-623.
11. E. Cuynen, G. Goeminne, P. Van Espen and H. Terryn, *Surface and Interface Analysis*, 2000, **30**, 589-591.
12. S. Feliu and V. Barranco, *Electrochimica Acta*, 2004, **49**, 951-964.
13. B. Formanek, K. Szymanski, B. Szczucka-Lasota and A. Wlodarczyk, *Journal of Materials Processing Technology*, 2005, **164**, 850-855.
14. A. Kalendova, *Anti-Corrosion Methods and Materials*, 2003, **50**, 82-90.
15. J. H. Morris, P. G. Perkins, A. E. A. Rose and W. E. Smith, *Journal of Applied Chemistry and Biotechnology*, 1976, **26**, 385-390.
16. J. A. Cotton and G. Wilkinson, in *Advanced Inorganic Chemistry*, Wilet Interscience, 5 edn., 1988, vol. 5, pp. 424-427.
17. R. C. Geoff, in *Descriptive Inorganic Chemistry*, W. H. Freeman and Company, 1995, pp. 294-305.

Chapter 3 The Structure and Stability Of Model Phosphate Coatings

18. J. O. Nriagu and P. B. Moore, *Phosphate Minerals*, Springer-Verlag, 1984.
19. R. J. Kirkpatrick and R. K. Brow, *Solid State Nuclear Magnetic Resonance*, 1995, **5**, 9-21.
20. M. Crobu, A. Rossi, F. Mangolini and N. D. Spencer, *Tribology Letters*, 2010, **39**, 121-134.
21. I. Rashkovan, L. Kuz'minskaya and V. Kopeikin, *Neorganicheskie Materialy*, 1965, **2**, 541-549.
22. K. Kobayashi, *Journal of Materials Science Letters*, 2001, **20**, 1121-1123.
23. W. D. Kingery, *Journal of the American Ceramic Society*, 1950, **33**, 242-247.
24. J. H. Morris, P. G. Perkins, A. E. A. Rose and W. E. Smith, in *Industrial Alumina Chemistry: The Chemistry and Binding Properties of Aluminium Phosphate*, ACS Monograph, Washington DC, 1986, p. 173.
25. N. J. Kreidl and W. A. Weyl, *Journal of the American Ceramic Society*, 1941, **24**, 372-378.
26. S. W. Lai and D. D. L. Chung, *Journal of Materials Science*, 1994, **29**, 3128-3150.
27. T. Finch and J. H. Sharp, *Journal of Materials Science*, 1989, **24**, 4379-4386.
28. M. F. Morks, *Materials Letters*, 2004, **58**, 3316-3319.
29. B. E. I. Abdelrazig and J. H. Sharp, *Thermochimica Acta*, 1988, **129**, 197-215.
30. R. Dudenhoefer, G. L. Messing, P. W. Brown and G. G. Johnson Jr, *Journal of Crystal Growth*, 1992, **125**, 121-126.
31. A. Baykal, M. Kizilyalli and R. Kniep, *Turkish Journal of Chemistry*, 1997, **21**, 394-400.
32. M. a. A. Aramendía, V. Borau, C. Jiménez, J. M. a. Marinas and F. J. Romero, *Journal of Colloid and Interface Science*, 1999, **217**, 288-298.
33. B. Boonchom, *Journal of Thermal Analysis and Calorimetry*, 2009, **98**, 863-871.
34. B. Boonchom, *International Journal of Thermophysics*, 2010, **31**, 416-429.
35. S. Mousa, *Phosphorus Research Bulletin*, 2010, **24**, 16-21.
36. N. E. Hipedinger, A. N. Scian and E. F. Aglietti, *Cement and Concrete Research*, 2002, **32**, 675-682.
37. *British Pat.*, GB962182, 1964.

Chapter 3 The Structure and Stability Of Model Phosphate Coatings

38. A. G. Nord and Kierkega.P, *Acta Chemica Scandinavica*, 1968, **22**, 1466-&.
39. N. Yoshida, T. Kimura, M. Sugimoto, M. Nishida, H. Ogawa and S. Kishimoto, *Journal of Catalysis*, 1993, **139**, 568-575.
40. T. Ohno and J. Moffat, *Catal Lett*, 1991, **9**, 23-34.
41. R. L. Frost, *Spectrochimica Acta Part A: Molecular and Biomolecular Spectroscopy*, 2004, **60**, 1439-1445.
42. A. John, D. Philip, K. R. Morgan and S. Devanarayanan, *Spectrochimica Acta Part A: Molecular and Biomolecular Spectroscopy*, 2000, **56**, 2715-2723.
43. R. A. Nyquist and R. O. Kagel, *Infrared Spectra of Inorganic Compounds*, 1 edn., Academic Press, 1971.
44. T. R. Hinsch, W. Guse and H. Saalfeld, *Journal of Crystal Growth*, 1986, **79**, 205-209.
45. D. E. C. Corbridge and E. J. Lowe, *Journal of the Chemical Society (Resumed)*, 1954, **0**, 493-502.
46. L. Popovic, D. de Waal and J. C. A. Boeyens, *Journal of Raman Spectroscopy*, 2005, **36**, 2-11.
47. O. Sarr and L. Diop, *Spectrochimica Acta Part A: Molecular Spectroscopy*, 1984, **40**, 1011-1015.
48. P. Tarte, A. Rulmont, K. Sbai and M. H. Simonot-Grange, *Spectrochimica Acta Part A: Molecular Spectroscopy*, 1987, **43**, 337-343.
49. O. Miroshnichenko and V. Mombelli, *Russian Journal Of Inorganic Chemistry*, 1979, **24**, 1631.
50. H. Assaaoudi, Z. Fang, I. S. Butler, D. H. Ryan and J. A. Kozinski, *Solid State Sciences*, 2007, **9**, 385-393.
51. J. Jin, Z. Zhang, H. Ma, X. Lu, J. Chen, Q. Zhang, H. Zhang and Y. Ni, *Materials Letters*, 2009, **63**, 1514-1516.
52. W. K. Jóźwiak, W. Ignaczak, D. Dominiak and T. P. Maniecki, *Applied Catalysis A: General*, 2004, **258**, 33-45.
53. N. E. Fouad, *Journal of Thermal Analysis and Calorimetry*, 2000, **60**, 541-547.

Chapter 3 The Structure and Stability Of Model Phosphate Coatings

54. N. E. Fouad, H. Knözinger, M. I. Zaki and S. A. A. Mansour, *Zeitschrift für Physikalische Chemie*, 1991, **171**, 75-96.
55. Z.-m. Yao, Z.-h. Li and Y. Zhang, *Journal of Colloid and Interface Science*, 2003, **266**, 382-387.
56. J. M. Rojo, J. L. Mesa, L. Lezama and T. Rojo, *Journal of Materials Chemistry*, 1997, **7**, 2243-2248.
57. K. Bowden, I. M. Heilbron, E. R. H. Jones and B. C. L. Weedon, *Journal of the Chemical Society (Resumed)*, 1946, **0**, 39-45.
58. G. I. Poos, G. E. Arth, R. E. Beyler and L. H. Sarett, *Journal of the American Chemical Society*, 1953, **75**, 422-429.

CHAPTER 4 XPS STUDIES OF PHOSPHATE COATINGS

4.1 Introduction.....	115
4.2 Background.....	115
4.2.1 The use of XPS in the characterisation of phosphates.....	115
4.2.2 The use of NMR in the characterisation of phosphates	120
4.3 Determination of Phosphate Chain length using XPS.....	121
4.3.1 Sodium Phosphates.....	121
4.3.1.1 Sodium Orthophosphate	121
4.3.1.2 Sodium Hexametaphosphate.....	126
4.3.1.3 NMR Analysis	130
4.3.1.4 Summary.....	132
4.3.2 Magnesium Phosphate.....	133
4.3.2.1 Purchased Magnesium Phosphate	133
4.3.2.2 Synthesised Magnesium Phosphate	136
4.3.2.3 Summary.....	141
4.4 XPS Characterisation of Powdered Coatings.....	141
4.4.1 Model Coatings.....	141
4.4.1.1 Aluminium Phosphate	141
4.4.1.2 Model magnesium phosphate coatings and the effects of chromium addition	144
4.4.2 Industrial Coatings	159
4.4.2.1 Aluminium Phosphate Coatings	160
4.4.2.2 Aluminium Phosphate and Chromium Oxide Mixed Coatings.....	163
4.5 XPS Characterisation of Coated Steels	167

Chapter 4 XPS Studies of Phosphate Coatings

4.5.1 Preliminary Studies	168
4.5.1.1 Bare Steel	169
4.5.1.2 Forsterite Coated Steel.....	171
4.5.1.3 Fully Coated Steel.....	175
5.5.2 The Effects of Heating	177
5.5.2.1 Bare Steel	177
5.5.2.2 Forsterite Coated Steel.....	181
5.5.2.3 Fully Coated Steel	189
4.6 Summary.....	192
4.7 References.....	193

4.1 INTRODUCTION

In this chapter the XPS spectra of various phosphate compounds are probed. Previous work by others¹ has indicated that XPS can be used to measure the average length of metaphosphate chains. This theory is tested using sodium orthophosphate, sodium hexametaphosphate and magnesium orthophosphate.

XPS is then used as a method to characterise industrial model aluminium and magnesium phosphate coatings synthesised in house, both with and without the addition of chromium. The resulting XP spectra are compared to the results obtained from bulk analysis (XRD and NMR in this chapter and additional results from the previous chapter). Finally the XP spectra of industrial coatings both as powders and as coatings on steel are given.

4.2 BACKGROUND

4.2.1 THE USE OF XPS IN THE CHARACTERISATION OF PHOSPHATES

XPS has been widely used in the study of phosphates as both powders¹⁻¹⁰ and as coatings for a range of materials¹¹⁻¹⁵. Gresch¹ first investigated the application of XPS for the determination of phosphate chain length and studied a range of sodium phosphates. In the spectra generated from the metaphosphate and pyrophosphate standards (Figure 4.2) the oxygen 1s region was found to split into two components with a peak separation of approximately 1.5-2 eV. These components could be assigned to the bridging (BO) and non-bridging (NBO) oxygen atoms within the phosphate chain (α and β in Figure 4.1).

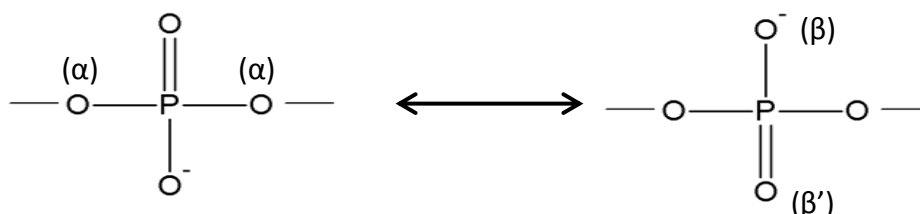


Figure 4.1 (α) bridging and (β) terminal oxygen positions in a chain metaphosphate structure
(adapted from (1))

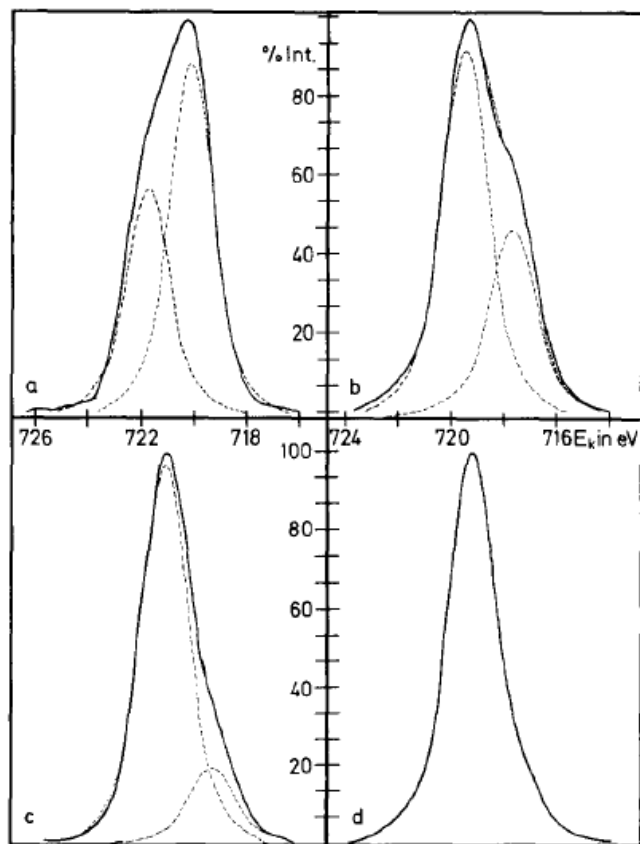


Figure 4.2 The Oxygen 1s region of the XP spectra collect from (a) P_4O_{10} (b) $(NaPO_3)_n$ (c) $Na_4P_2O_7$ and (d) Na_3PO_4 (taken from reference (1))

The ratio of the intensities as determined from the component areas (I_α/I_β) can be used as measure of the chain-length where an infinite chain will have a ratio of 0.5. The measured ratios showed good correlation with those expected for a range of sodium phosphate standards (see Table 4.1).

Compound	O 1s Binding Energy / eV		$\Delta O (1s)$ /eV	I_{α}/I_{β}	
	β	α		Measured	Theoretical
Sodium metaphosphate ((NaPO₃)_n)	531.7	533.6	1.9	0.51	0.50
Sodium pyrophosphate (Na₄P₂O₇)	531.3	533.1	1.8	0.20	0.17
Sodium orthophosphate (Na₂PO₄)	530.5	-	-	0	0

Table 4.1 binding energies, shifts and ratios of oxygen 1s components for a range of sodium phosphate standards (taken from (1))

Table 4.1 also shows that the binding energy of the O 1s components shifted to slightly higher binding energy as the number of bridging oxygen atoms within the chain increased. This was also observed for the binding energy of the phosphorous 2p and 2s transitions; however the binding energy of sodium transitions decreased as electron density was transferred from the phosphate chain to the sodium atoms. Gresch then successfully applied this method to measuring the average chain length of a range of sodium phosphate glasses.

XPS has since been used to measure the average chain length of many metaphosphate glasses, as it is one of the few techniques that are easily applied to amorphous structures. Addition of a divalent modifier to a metaphosphate glass has the effect of depolymerising it (i.e. decreasing the average chain length) by converting metaphosphate units to pyrophosphate⁴. This can be seen in XPS and the relationship between the type of oxygen bonds present and the concentration of this modifier is given in Equation 4.1.

$$\frac{BO}{NBO} = 0.5(3 - 4x)$$

Equation 4.1 the relationship between the BO/NBO ratio and the amount of modifying oxide (x) in a binary phosphate glass^{1, 4}

Since publication of this method of chain length determination, it has been successfully applied to a range of phosphates including zinc phosphates^{4, 9}, zinc borophosphates glasses⁴, zinc tribofilms^{6, 8}, iron phosphates¹⁶, vanadium phosphates⁷, iron-vanadium phosphates¹⁷ and phosphates with a range of additives^{2, 18-21}. This method of fitting the oxygen 1s spectra has been applied to vanadium phosphate glasses subjected to pulsed laser irradiation and used to follow

the variation in non-bridging oxygen atoms as a fraction of the total oxygen present²². The system has also been successfully applied to silicate glasses.^{23, 24}

XPS has previously been used to study phosphates used as protective and anti-corrosion coatings on a range of materials including aluminium^{13, 25}, magnesium alloy¹² and zinc electroplates¹¹, however literature on phosphate coatings for steel is limited^{14, 26, 27}.

The role of chromium as a post coating treatment has been investigated using XPS²⁶. Traditionally a solution of hexavalent chromium or a mixture of trivalent and hexavalent chromium was applied to steel after zinc phosphating²⁷. Using XPS Maeda and Yamato have shown that the surface of an untreated zinc phosphate coating consisted of an incomplete hydrated phosphate layer with small amounts of ferric oxide and phosphate (Fe_2O_3 and FePO_4) present over a thick ($\sim 1\mu\text{m}$) hopeite layer ($\text{Zn}_3(\text{PO}_4)_2 \cdot 4\text{H}_2\text{O}$). When the chromium rinse was applied it removed this top layer of ferric compounds and left a mainly trivalent chromium coating ($\text{CrOOH} \cdot 0.2\text{H}_2\text{O}$). However a small amount of hexavalent chromium was still present in the upper coating. A schematic of the resulting coatings is shown in Figure 4.3.

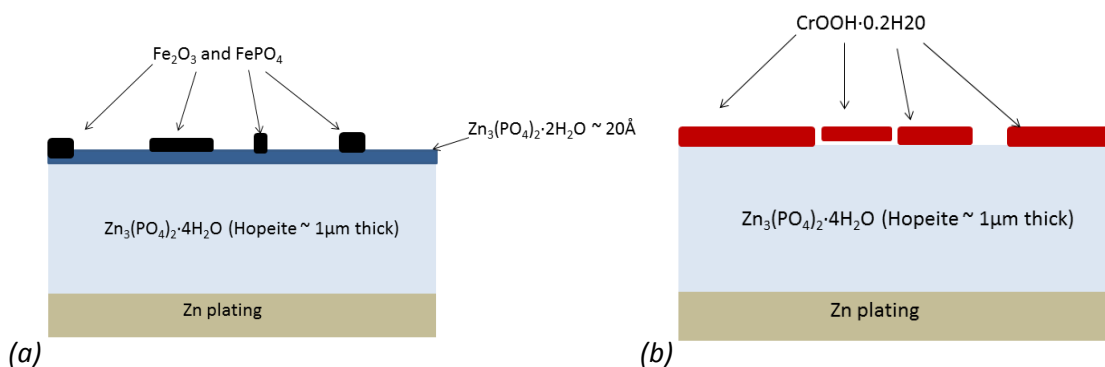


Figure 4.3 Schematics of zinc phosphate coatings (a) before and (b) after chromium rinse treatment (adapted from (26))

Due to the range of samples studied in this chapter a large number of transitions are observed. For ease, assignments of the key transitions relevant to this work are listed in Table 4.2, along with references found on the NIST XPS database.²⁸

Chapter 4 XPS Studies of Phosphate Coatings

<i>Element</i>	<i>Binding Energy / eV</i>	<i>Assignment</i>	<i>Reference</i>
Aluminium (2p)	75.0	Alumina (Al_2O_3)	(29)
Carbon (1s)	283.9	Iron Carbide (Fe_3C)	(30)
Chromium (2p)	577.3	Chromium oxide (CrO_3)	(31, 32)
	579.6	Chromium Oxide (Cr_2O_3)	(31, 33-35)
Iron (2p)	707	Iron Metal	(36, 37)
	710-712	Iron Oxide (Fe_2O_3)	(38)
	710-712	Iron Oxide (Fe_3O_4)	(31)
	708.1	Iron Carbide (Fe_3C)	(30)
Oxygen (1s)	528.5	Iron Oxide (Fe_2O_3)	(31, 38)
	529.7	Iron Oxide (Fe_3O_4)	(31, 38)
	530.0	Magnesium Oxide (MgO)	(39)
	530.5	Orthophosphate	(1)
	530.8	Chromium Oxide (CrO_3)	(40)
	530.8	Chromium Oxide (Cr_2O_3)	(41)
	531.3	Pyrophosphate (P_2O_7) NBO	(1)
	531.7	Metaphosphate (PO_3) NBO	(1)
	532.6	Silica (SiO_2)	(42-44)
	533.1	Pyrophosphate (P_2O_7) BO	(1)
533.6	Metaphosphate (PO_3) BO	(1)	
Phosphorus (2p)	132.3	Orthophosphate (PO_4)	(1)
	134.4	Metaphosphate (PO_3)	(1)
Silicon (2p)	99.6	Silicon	(45-47)
	101.8	Silicon Carbide (SiC)	(48, 49)
	103.7	Silica	(42-44)

Table 4.2 Assignments of key binding energies observed in XP spectra in this chapter.

4.2.2 THE USE OF NMR IN THE CHARACTERISATION OF PHOSPHATES

NMR has been used to characterise a wide range of phosphates including sodium^{50, 51}, aluminium^{2, 52} and magnesium⁵³⁻⁵⁵ phosphates; however the discussion here will focus on the NMR spectra of sodium phosphates as they are most relevant to this chapter. NMR spectra are normally discussed in terms of the Qⁱ nomenclature as summarised in Figure 4.4.

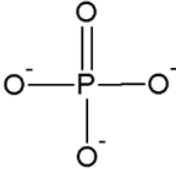
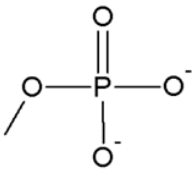
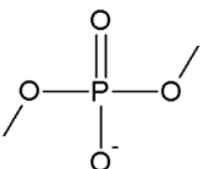
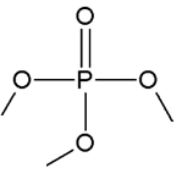
Q ⁰ Orthophosphate	Q ¹ Pyrophosphate
	
Q ² Metaphosphate	Q ³
	

Figure 4.4 Nomenclature and representations of PO₄ tetrahedra with different polymerisations

³¹P NMR is a popular technique for the characterisation of phosphates as the signals from different polymerised tetrahedra are spread over a large range of chemical shifts. They are easily distinguished from each other and NMR is easily applied to amorphous systems. Typical ranges from sodium phosphates are 12 ppm for a Q⁰ orthophosphate tetrahedron, 6 to -8 ppm for a Q¹ pyrophosphate tetrahedron, -15 to -32 ppm for a Q² metaphosphate tetrahedron and below -36 ppm for a Q³ branched chain tetrahedron as summarised in Figure 4.5.⁵¹

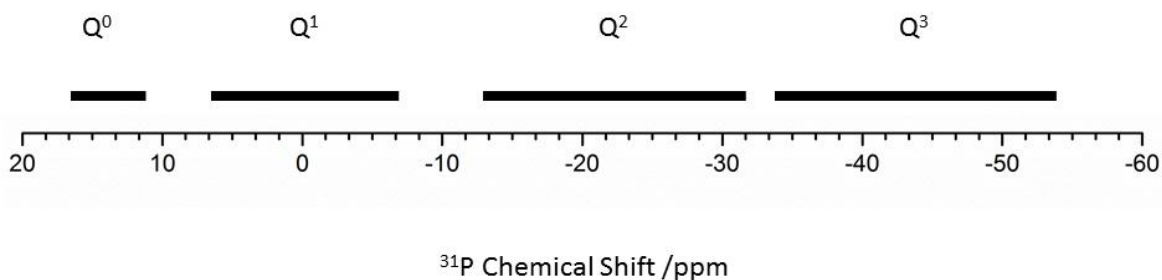


Figure 4.5 Typical ^{31}P NMR chemical shifts for sodium phosphates (adapted from (29))

^{31}P NMR is extremely sensitive to the level of protonation of a phosphate; for example in the case of pyrophosphates the anhydrous phosphate resonates a 2.1 ppm, the monohydrogen salt at -3.7 ppm and the dihydrogen salt at -8.2 ppm.⁵⁰

4.3 DETERMINATION OF PHOSPHATE CHAIN LENGTH USING XPS

In this chapter section the same phosphate standards studied by Gresch et al¹ have also been studied. The spectra of the samples were collected before any treatment in an attempt to reproduce the results seen by the previous authors. The phosphates were then heated in order to see if the metaphosphate chain formation and growth observed in chapter 3 could be monitored in XPS. Once the sodium phosphate standards have been fully characterised the same procedure was applied to magnesium orthophosphate in order to see if the method could be applied to model phosphate coatings.

For this study sodium orthophosphate (Na_3PO_4 96% pur.), sodium hexametaphosphate ($\text{Na}(\text{PO}_3)_n$ 96% pur.) and magnesium phosphate hydrate ($\text{Mg}_3(\text{PO}_4)_2 \cdot x\text{H}_2\text{O}$) were purchased from Sigma Aldrich and used as received. Portions of the phosphates were heated for 15 minutes in air before the XP spectra were collected.

4.3.1 SODIUM PHOSPHATES

4.3.1.1 SODIUM ORTHOPHOSPHATE

Before the XP spectra of the sodium phosphate samples were collected the XRD patterns of the orthophosphate were collected both before heating and after heating between 473 and 1073 K (Figure 4.6).

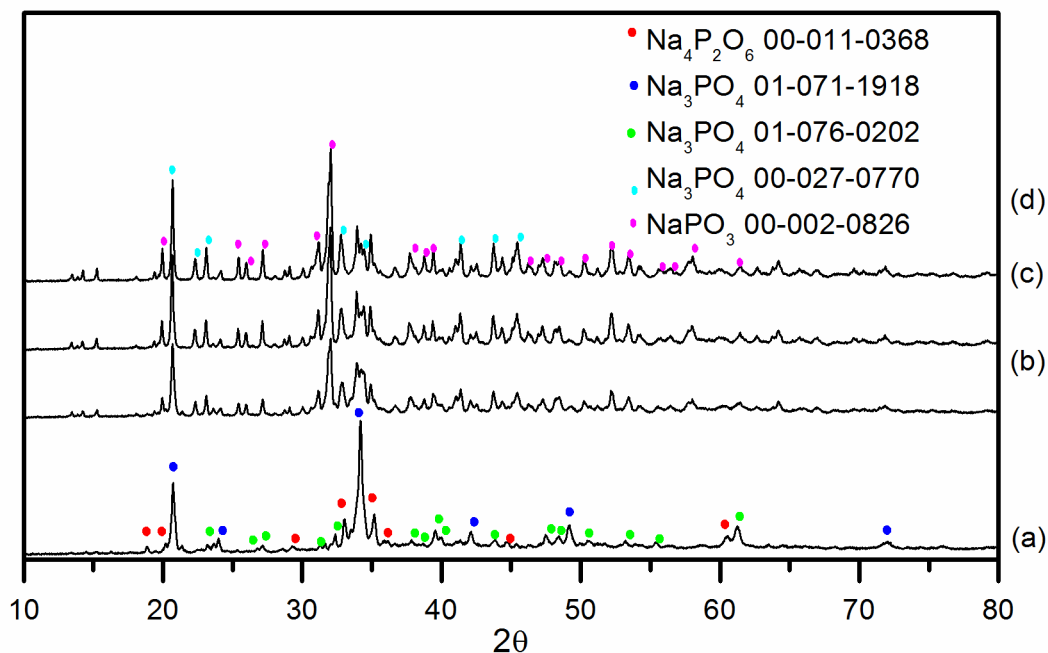


Figure 4.6 The X-ray diffraction patterns of sodium orthophosphate after (a) no heat treatment and heating to (b) 473 K (c) 673 K (d) 873 K and (e) 1073 K.

The diffraction patterns indicate that the sample was primarily sodium orthophosphate (both cubic (pattern 01-071-1918) and tetragonal (01-076-0202) but that a small ringed metaphosphate impurity ($\text{Na}_4\text{P}_2\text{O}_6$, 00-011-0368 Figure 4.7) was also present. Upon heating to 473 K the diffraction peaks related to this impurity disappeared and additional diffraction peaks are observed. These new peaks can be assigned to the formation of a metaphosphate chain. Heating the sample beyond 473 K saw little change in the diffraction patterns.

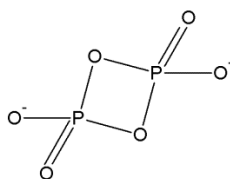


Figure 4.7 the structure of the metaphosphate impurity $\text{Na}_4\text{P}_2\text{O}_6$

Inspection of the XP spectrum of the sodium orthophosphate as received (Figure 4.8) indicates that in addition to the expected sodium, oxygen, phosphorus and carbon a small amount of chlorine was present on the surface of the sample. This was also observed with the samples originally used by Gresch.¹

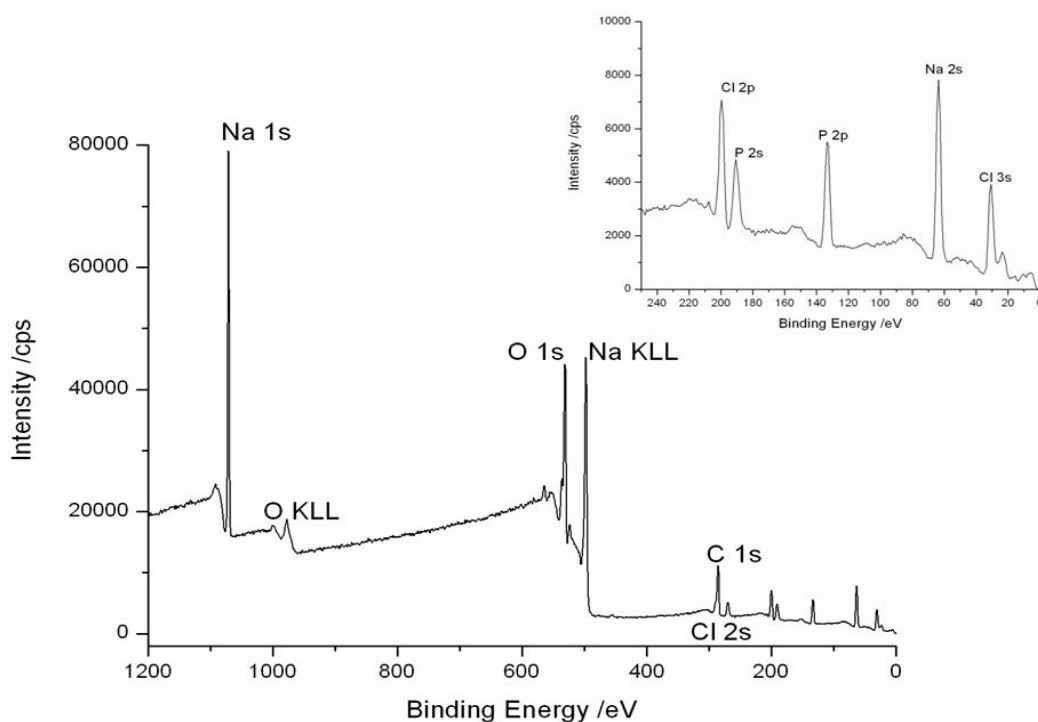


Figure 4.8 The XP spectrum of sodium orthophosphate as received. All major photoelectron and Auger transitions are labelled.

The oxygen 1s region (Figure 4.9) consists of 4 components. The components at 530.6 eV and 532.6 eV can be assigned to NBO and BO atoms of a phosphate chain respectively¹. The component at 535.3 eV is part of the sodium KLL Auger transition⁵⁶ and the component at 537.2 eV is assigned as physisorbed water.²⁸ The presence of a bridging oxygen species is in disagreement with the findings reported by Gresch and is assumed to arise from the metaphosphate impurity observed in the XRD (Figure 4.6). It is believed that the non-bridging oxygen species from this impurity would have a binding energy very close to the pure orthophosphate (see Table 4.1) and this is why the component at 530.6 eV cannot be resolved into two separate components.

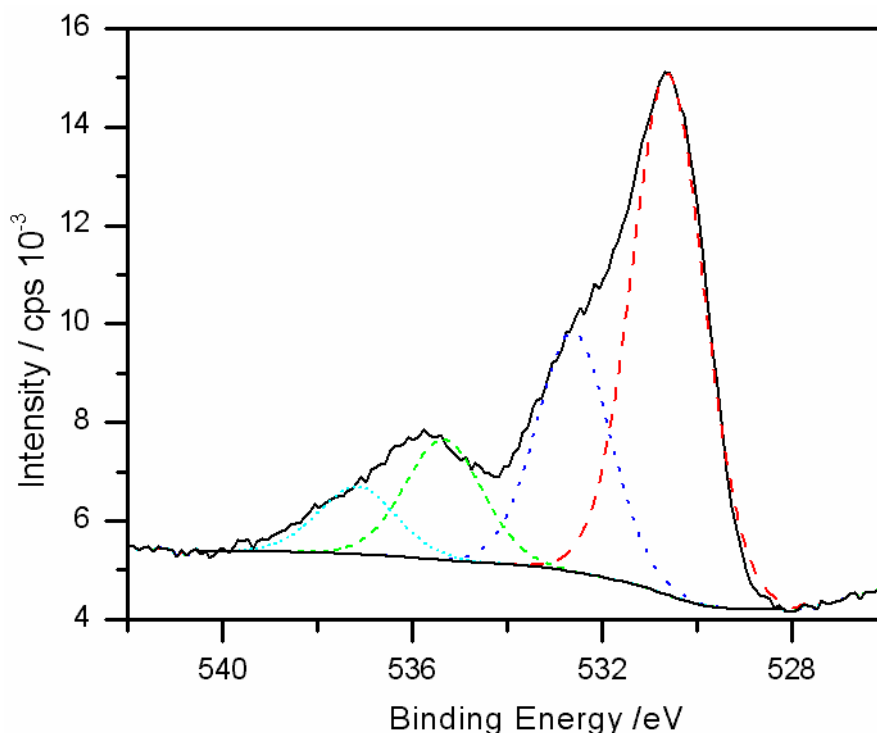


Figure 4.9 The oxygen 1s region of the XP spectrum of sodium orthophosphate as received

Heating the phosphate to 473 K caused a large reduction in the shoulder at 532.6 eV (Figure 4.10a), thought to be caused by breaking of the metaphosphate ring and the loss of the component at 537.2 eV arising from water. Water is known to stabilise phosphates, with chain growth and dehydration occurring in one step (see chapter 3) so it is thought that the loss of physisorbed water during heating aids the breakdown of the ringed impurity shown in Figure 4.7.

Inspection of the P 2p region of the XP spectra (Figure 4.10b) indicates two phosphorus species were present in the as received sample (in agreement with the oxygen 1 s assignments) as there was a main peak at 132.3 eV and with a shoulder at 134.4 eV. The binding energy of these peaks are in good agreement with those recorded by Gresch for sodium orthophosphate and sodium metaphosphate respectively. Upon heating to 473 K the shoulder at 134.4 eV arising from the metaphosphate is lost and the spectrum resolves to one component at 132.5 eV.

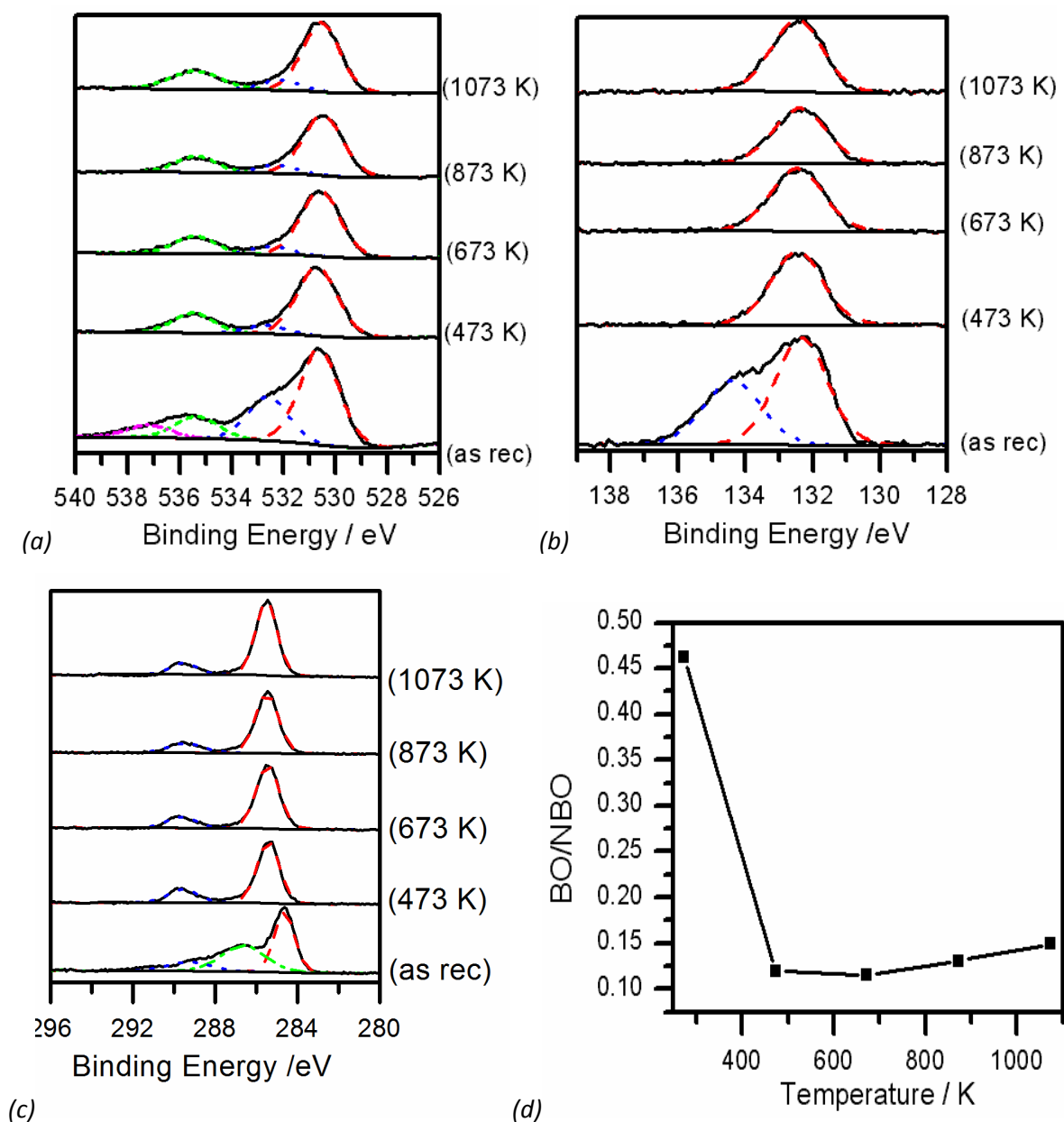


Figure 4.10 The (a) oxygen 1s, (b) phosphorous 2s and (c) carbon 1s regions of the XP spectra of sodium orthophosphate before and after heating and (d) the dependence of the BO/NBO ratio on temperature

Inspection of the carbon 1s region (Figure 4.10c) showed that it initially consisted of three components with binding energies of 284.6, 286.6 and 289.3 eV. The component at 284.6 eV can be assigned to adventitious carbon and it is clear from the figure that this component dominates the carbon spectrum. The component at 289.3 eV can be assigned to carbonate, and it is therefore likely that oxygen from the carbonate molecule is contributing to the oxygen 1s signal.

The third component cannot be readily assigned. Heating to 473 K caused the removal of the third unknown component, after which the carbon spectrum remained fairly consistent.

Figure 4.10d shows the relationship between the curing temperature and the ratio between BO and NBO environments taken from the oxygen 1s spectra (Figure 4.10a). A large drop in chain length was observed when the sample was heated to 473 K (coinciding with the large reduction in metaphosphate content observed in the P 2p spectra and the loss of the metaphosphate impurity in the XRD patterns). This is followed by a slight increase in average chain length (as indicated by the increase in BO/NBO ratio). The average chain length remains very low, with the final BO/NBO value of 0.16 indicating that the sample has an average chain length of 2 phosphate atoms i.e. pyrophosphate.

4.3.1.2 SODIUM HEXAMETAPHOSPHATE

In addition to sodium orthophosphate, sodium hexametaphosphate was studied by Gresch (and therefore repeated in this work) as an example of a long chain metaphosphate. XRD (Figure 4.11) of the samples to be studied here showed that the as received sample was largely amorphous although some very broad diffraction peaks could be seen and could be assigned to the metaphosphate.

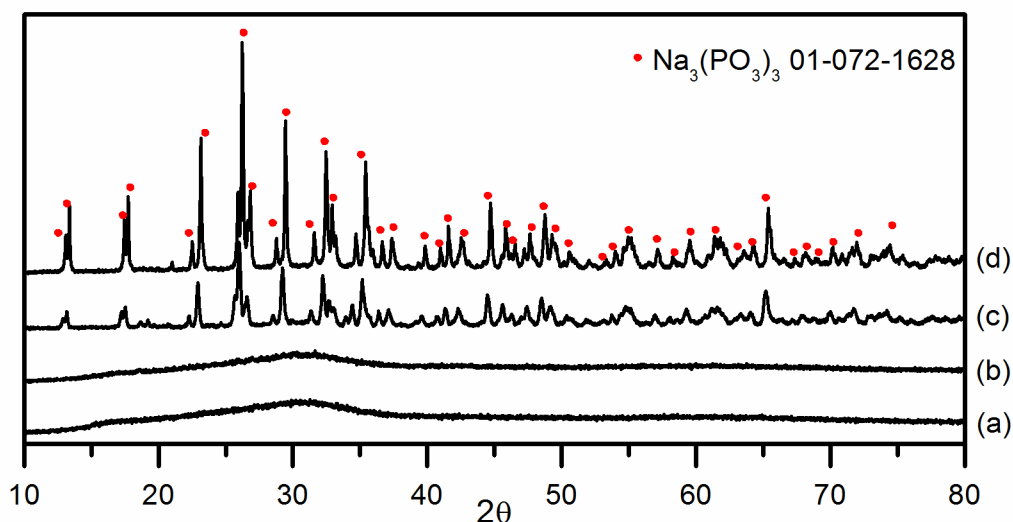


Figure 4.11 X-ray diffraction patterns from sodium hexametaphosphate (a) as received and after heating to (b) 473 K(c) 673 K and (d) 873 K

When heated above 673 K the sample became more crystalline with easily determined diffraction peaks. The diffraction patterns for the 673 and 873 K samples could both be matched

to sodium metaphosphate. Heating the sample to 1073 K saw the formation of a metaphosphate glass which when cooled could not be removed from the ceramic crucible it was heated in and therefore could not be analysed.

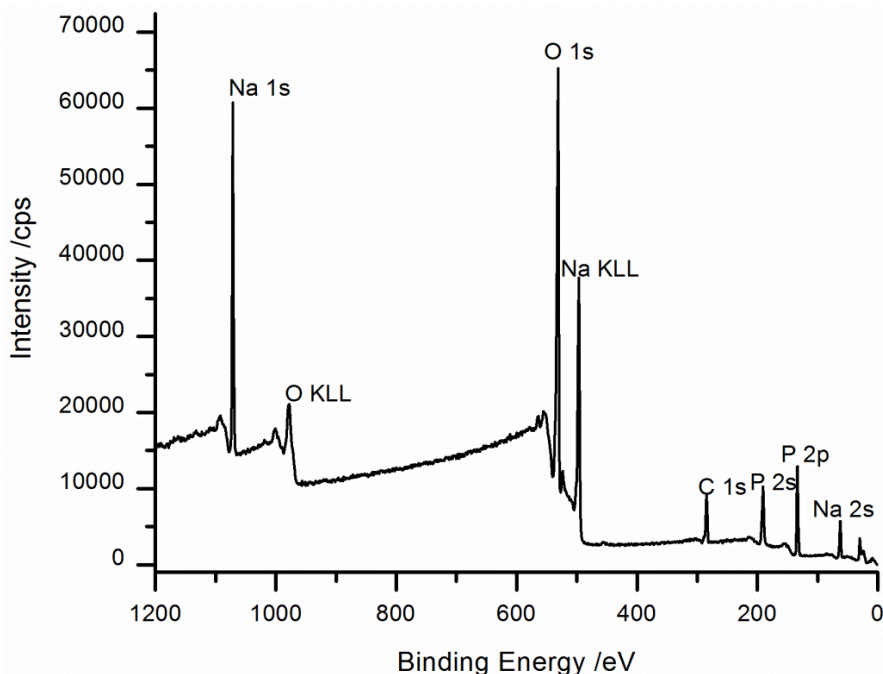
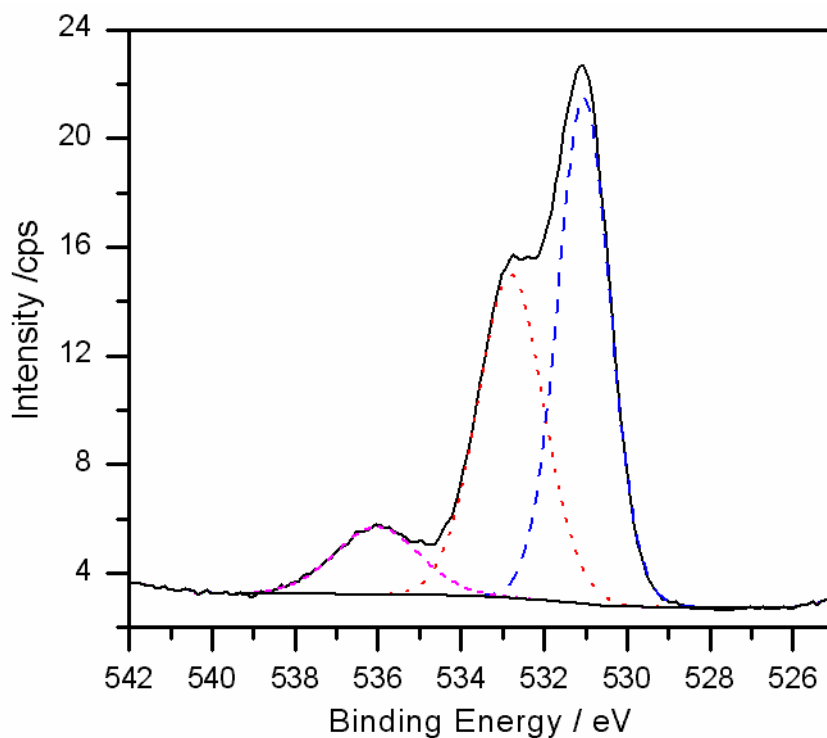


Figure 4.12 the XPS wide scan of sodium hexametaphosphate. All major photoelectron and Auger transmissions are labelled

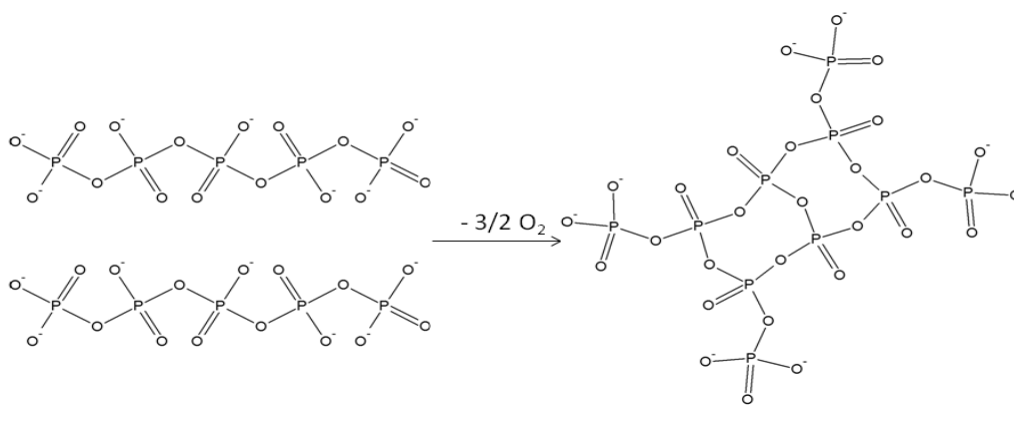
Figure 4.12 shows the XPS wide scan of the sodium hexametaphosphate before any heat treatment. Inspection of the spectrum shows the expected sodium, oxygen, phosphorus and carbon peaks, and that unlike the sodium orthophosphate there were no significant impurities present at the surface of the sample.

Inspection of the oxygen 1s region in the XP spectrum of the as received sample (Figure 4.13a) shows that the signal consists of three components. As with the sodium orthophosphate the components at 531.0 and 532.8 eV can be assigned to NBO and BO atoms respectively. Again the component at 536.0 eV is part of the sodium KLL Auger transition. Taking the ratio of the BO/NBO areas gives a value of 0.80. This is much larger than the value calculated for a theoretical infinite length metaphosphate chain (0.5) and the value recorded previously by Gresch et al (0.51). This ratio may be a sign that 'cross-linking' may be occurring between two separate phosphate chains as depicted in Figure 4.13b. This cross linking would have the effect of increasing the number of bridging oxygen atoms present whilst also decreasing the number

of non-bridging oxygen atoms present within the system, therefore producing BO/NBO values greater than 0.5. Heating the sample to 473 K caused the position of the oxygen components to shift to slightly lower binding energy (for example the bridging oxygen component moved to 532.4 eV), typical of phosphate chain growth. Further heating had no effect on the position of the components in the oxygen 1s spectrum (Figure 4.14a).



(a)



(b)

Figure 4.13 (a) The oxygen 1s region of the XP spectrum of sodium hexametaphosphate before heat treatment and (b) the proposed 'cross-linking' of metaphosphate chains

Inspection of the P 2p region (Figure 4.14b) indicates that the peaks consist of one component at 133.6 eV (consistent with literature values for sodium hexametaphosphate¹). Heating the system to 473 K caused a slight shift in the binding energy of this component to 134.2 eV. This shift in binding energy is typically associated with growth of the metaphosphate chain. Further heating caused no changes in the phosphorus 2p XPS spectrum.

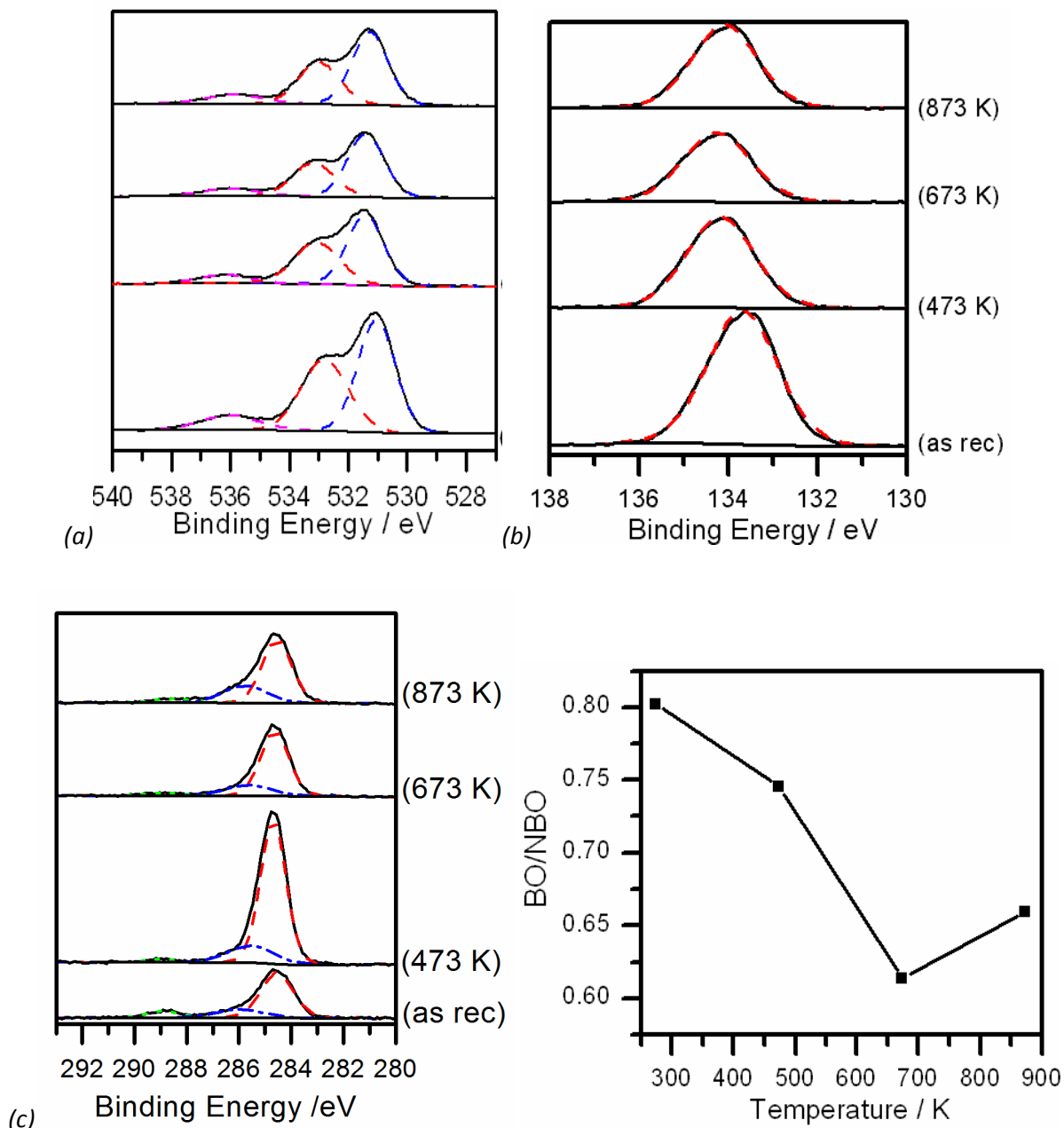


Figure 4.14 The (a) oxygen 1s, (b) phosphorous 2p regions and (c) carbon 1s of the XP spectra of sodium hexametaphosphate before and after heating and (d) effects of heating sodium hexametaphosphate on BO/NBO ratio

As with the previous sodium phosphate sample the as received sample was observed to contain three components- the binding energies of which were recorded as 284.5, 286.0 and 288.8 eV. The assignments are similar as in the sodium orthophosphate spectrum i.e. adventitious carbon at 284.5 eV, carbonate at 288.8 eV and no clear assignment for the middle component. Unlike the orthophosphate heating did not cause the removal of this third component.

Heating up to 673 K caused a slight decrease in the BO/NBO ratio which reached a minimum of 0.61 at 673 K (see Figure 4.14c). The variation in BO/NBO ratio was much less than that observed in the previous sample. All BO/NBO ratios remained above the 0.5 value calculated for a theoretical infinite length chain phosphate, indicating that either the 'cross-links' described previously (Figure 4.13) were breaking and reforming during heating, or there was some form of impurity present. This impurity would have had to consist of magnesium, oxygen or phosphorus as no other elements were detected in the XPS, and would have had to have been at very low concentrations (and mostly at the surface of the sample) as there was only one phase detected in the XRD (Figure 4.11).

4.3.1.3 NMR ANALYSIS

NMR spectra were acquired on a Chemagnetics Infinity Plus spectrometer at a ^{31}P Larmor frequency of 121.50 MHz. The samples were contained in a 4mm rotor with magic-angle spinning at 12 kHz. Dimethyl-methylphosphonate (DMMP) was used as a reference.

The ^{31}P MAS NMR spectra (Figure 4.15) of sodium orthophosphate before heating consisted of a main peak at 14.06 ppm consistent with values recorded by others for sodium orthophosphate^{50, 51}. There is a small peak present at 8.02 ppm which is consistent with a Q¹ pyrophosphate and can be assigned to the ringed impurity observed in the XRD patterns (Figure 4.6). Heating the system to 873 K saw a reduction in intensity of the peak at 14.06 ppm from the orthophosphate and a large signal at 6.82 ppm. Chemical shifts in this region typically arise from Q¹ phosphate tetrahedra (orthophosphate tetrahedron, see Figure 4.4)⁵¹, indicating that the system is primarily pyrophosphate after heating. This is in good agreement with both the XRD and XPS data.

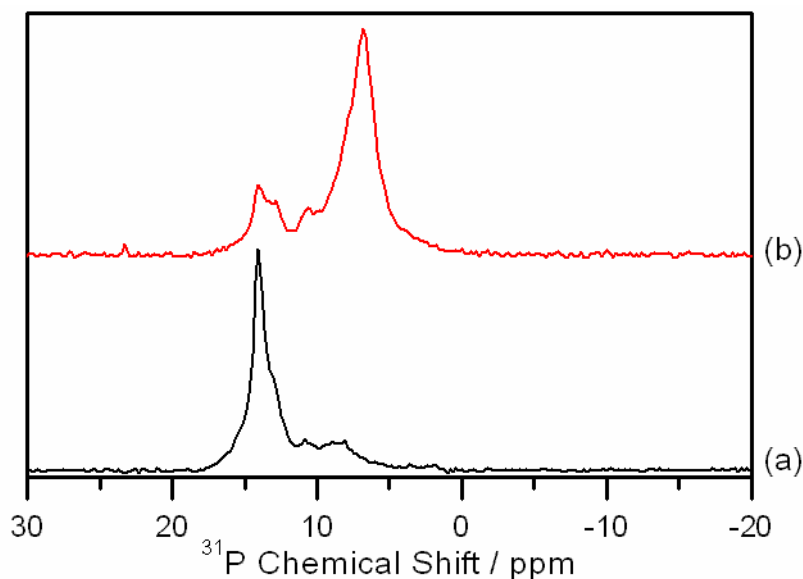


Figure 4.15 ^{31}P MAS NMR of sodium orthophosphate (a) before and (b) after heating to 873 K

The NMR spectrum of the sodium hexametaphosphate as received is shown in Figure 4.16a. The spectrum consists of three broad peaks at 1.20, -7.04 and -19.30 ppm. Upon heating to 873 K these three broad peaks resolved into 6 sharp peaks at 5.22, 1.60, -5.43, -7.04, -15.69 and -18.69 ppm (Figure 4.16b).

In the spectrum of the as received sample the peak at 1.20 ppm is assigned to the end of chain Q^1 tetrahedra, and the peaks at -7.04 and -19.30 ppm to the mid chain Q^2 tetrahedra⁵¹. The presence of these peaks indicates that the bulk of the sample is metaphosphate in good agreement with the XRD data (Figure 4.11). No Q^3 tetrahedra were observed (typical chemical shifts below -34 ppm⁵¹), indicating that the cross linking model used to explain the BO/NBO ratio is either incorrect or cross linking occurs only at the surface.

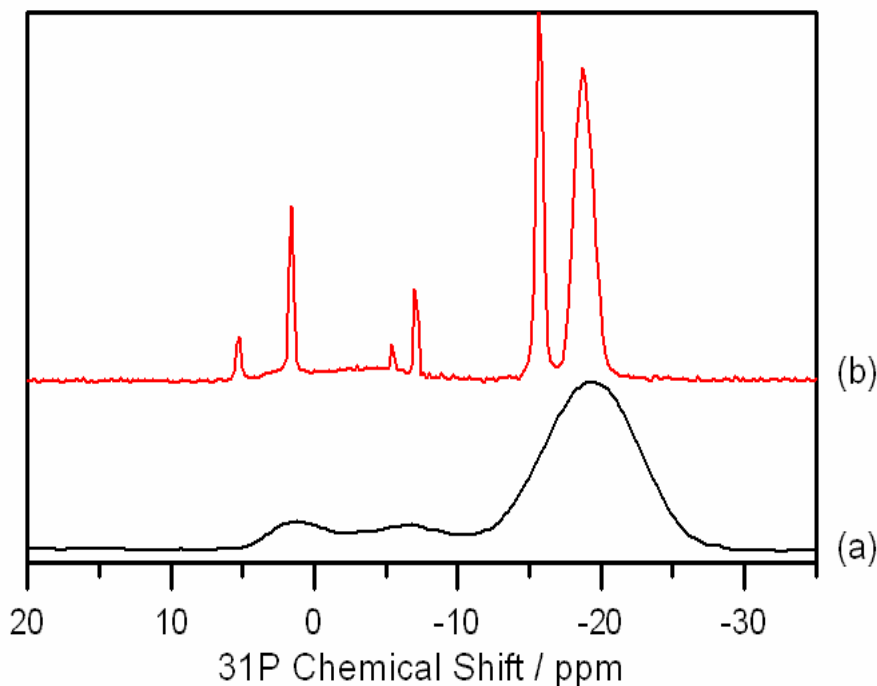


Figure 4.16 ^{31}P MAS NMR spectra of sodium hexametaphosphate (a) before and (b) after heating to 873 K

The resolved peaks in the spectrum from the sample heated to 873 K have similar chemical shifts to the broad peaks seen previously and therefore have similar assignments (5.20 and 1.60 ppm are the end of chain Q^1 tetrahedra, and the peaks at -5.43, -7.04, -15.69 ppm and -18.69 ppm to the mid chain Q^2 tetrahedra⁵¹). Again there are no peaks at chemical shifts typical of branched Q^3 tetrahedra, indicating that any metaphosphate chain cross-linking is limited to the surface of the sample and is not present in the bulk, providing a strong argument for the high BO/NBO ratios arising from an impurity.

4.3.1.4 SUMMARY

The combination of XRD, XPS and MAS-NMR has been successfully used to fully characterise sodium phosphate powders. XPS indicated that once impurities were removed from the systems (by heating sodium orthophosphate to 473 K and hexametaphosphate to 673 K) the increase in average chain length could be followed using the BO/NBO value calculated from the oxygen 1s region of a samples XP spectrum.

4.3.2 MAGNESIUM PHOSPHATE

This section of the chapter covers the XPS studies of two forms of magnesium phosphate, that purchased from Sigma Aldrich and as synthesised in house. The previous chapter showed magnesium phosphate undergoes dehydrolytic condensation at 653 K to form a metaphosphate. It is believed that this metaphosphate formation is responsible for the improved tension observed with magnesium phosphate coatings. The ability to follow metaphosphate chain formation in model steel coatings using XPS is desirable as it provides a measure of the average chain length as well as merely indicating metaphosphate bonds are present within the sample as done by other techniques such as Raman and IR spectroscopies.

4.3.2.1 PURCHASED MAGNESIUM PHOSPHATE

As with the previous sodium phosphate samples the X-Ray diffraction patterns of the purchased magnesium phosphate before and after heating (Figure 4.17) were collected to aid in interpretation of the XP Spectra. The diffraction patterns indicated that the as received sample (Figure 4.17a) consisted of trimagnesium bisphosphate $Mg_3(PO_4)_2$ in addition to magnesium pyrophosphate ($Mg_2P_2O_7$) and cyclo-tetraphosphate ($Mg_2P_4O_{12}$) impurities.

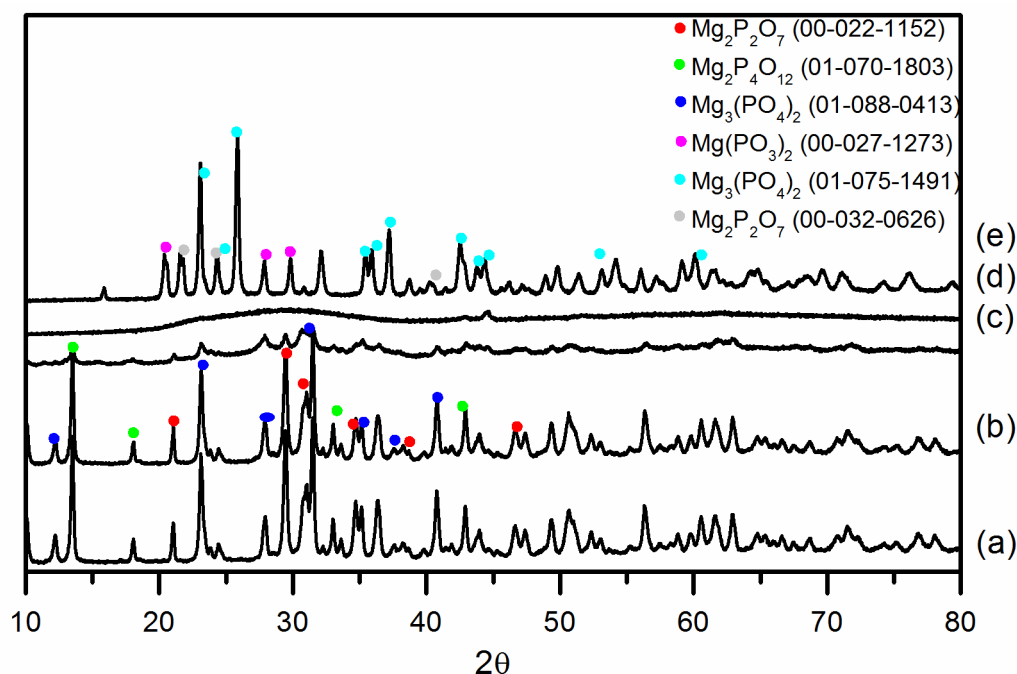


Figure 4.17 The X-ray diffraction patterns of magnesium phosphate hydrate after (a) no heat treatment and heating to (b) 473 K (c) 673 K (d) 873 K and (e) 1073 K

Heating to 673 K saw a reduction in the number of diffraction peaks, attributed to a reduction in crystallinity, however the peaks could be assigned to the same magnesium phosphates. At 873 K the sample was largely amorphous and no assignments could be made.

After heating to 1073 K the metaphosphate $\text{Mg}(\text{PO}_3)_2$ was observed in the diffraction pattern, in addition to the ortho and pyrophosphates seen previously.

Inspection of the wide scan XP spectrum (Figure 4.18) indicates that the only atoms present on the surface of the sample are the expected magnesium, phosphorous, oxygen and carbon. No significant impurities were observed.

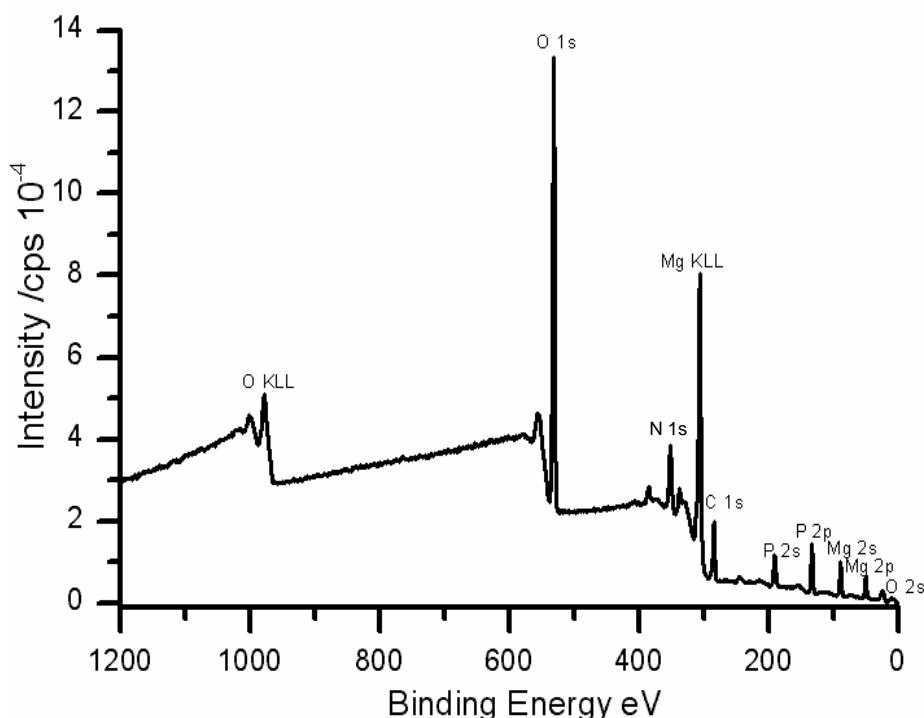


Figure 4.18 The XP spectrum of magnesium phosphate hydrate

Inspection of the oxygen 1s region of the XP spectrum (Figure 4.19a) shows that it consists of three components at 531.5, 533.1 and 534.2 eV. These components can be assigned to NBO and BO atoms, and water respectively. Heating the system caused a loss of the component at 534.2 eV due to water at 473 K, and a reduction in the signal arising from the bridging oxygen atoms. As discussed in the previous chapter other authors have stated waters of crystallization cannot usually be removed without destruction of the anion structure^{57, 58} implying a phase transformation is occurring during this water loss, and explaining why water is not lost at 373

K. The area of the component arising from bridging oxygen atoms decreased steadily with heating.

The BO/NBO ratio of magnesium phosphate starts at 0.34, which is close to the theoretical value for a 5 member chain. Heating the magnesium phosphate causes a steady decrease in BO/NBO to a minimum of 0.11 indicating a decrease in the average chain length to less than 2 phosphorus atoms. This is in direct contrast to the results published by others which state that pyrophosphate is formed when magnesium orthophosphate is heated above 523 K⁵⁹ and metaphosphate forms when heated above 723 K. It also directly contradicts the XRD data which indicated metaphosphate formation occurs by 1073 K, and results obtained in the previous chapter.

The phosphorus 2p peak (Figure 4.19b) was found to consist of one component at 133.7 eV which is consistent with binding energies reported by others for magnesium orthophosphate.⁶⁰ The spin orbit splitting of the phosphorus 2p transition is typically around 0.84 eV⁵⁶ and therefore difficult to resolve under typical experimental conditions. After heating to 873 K there is a slight shift in binding energy to 133.9 eV. This coincides with the formation of the amorphous phase observed in the XRD patterns (Figure 4.17) which resolved into a mixture of ortho and metaphosphate upon further heating. A shift to higher binding energy has been noted by others when comparing ortho and metaphosphates¹.

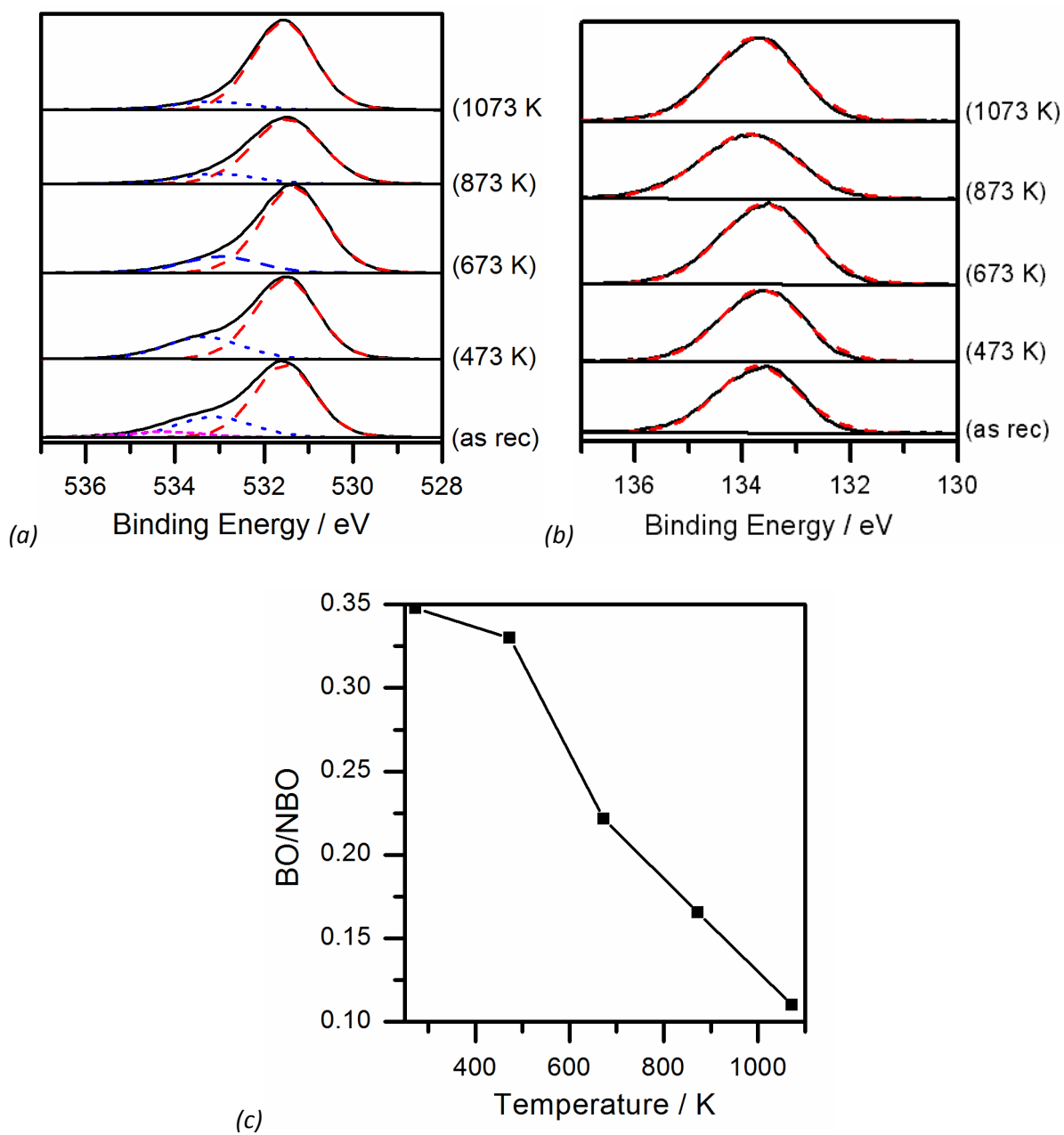


Figure 4.19 The (a) oxygen 1s and (b) phosphorous 2p regions of the XP spectra of magnesium phosphate hydrate before and after heating and (c) the effects of heating magnesium phosphate hydrate on BO/NBO ratio

4.3.2.2 SYNTHESISED MAGNESIUM PHOSPHATE

The X-Ray diffraction patterns from synthesised model magnesium phosphate coatings were previously discussed in chapter 3. The patterns indicated that after drying the sample consisted of trimagnesium orthophosphate and pyrophosphate MgHP_2O_7 (previously observed when

heating magnesium orthophosphate above 523 K.). The sample heated at 1073 K was found to be magnesium cyclo-tetraphosphate ($Mg_2(PO_3)_4$). The XPS wide scan of the dried sample (Figure 4.20) indicated that magnesium, phosphorous, oxygen and carbon were the only elements present on the surface of the sample.

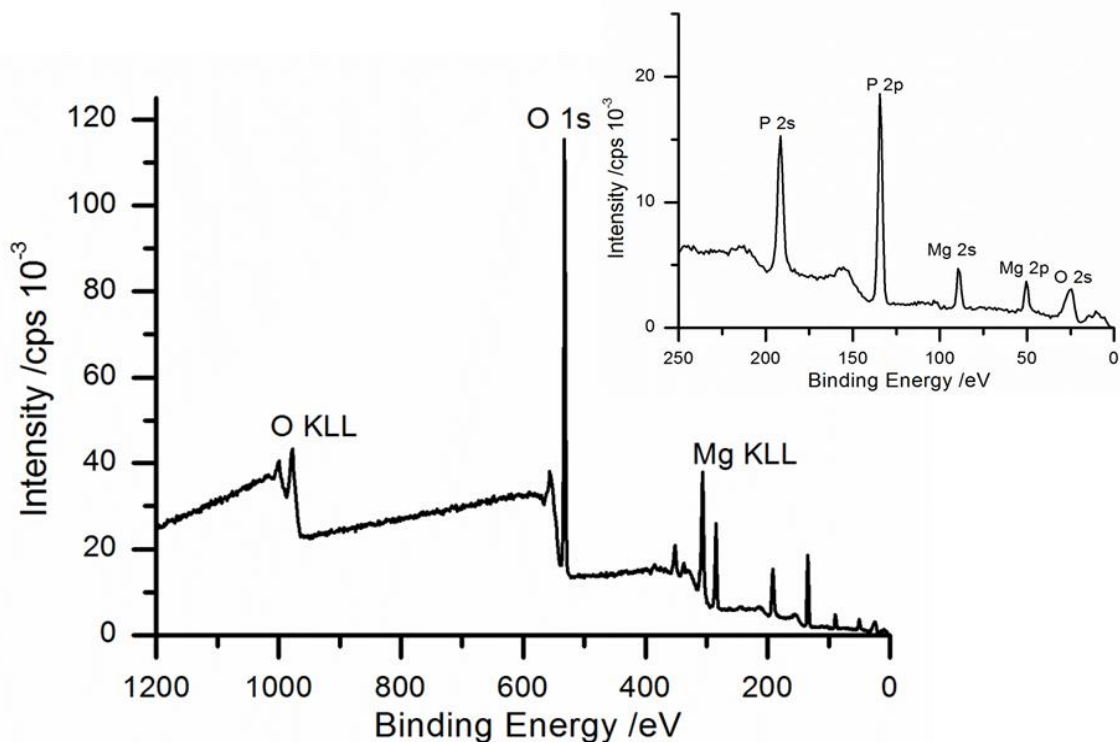


Figure 4.20 The XP spectrum of synthesised magnesium phosphate

Sample	Concentration / at %			
	Carbon	Oxygen	Phosphorus	Magnesium
Dried	26.6	52.9	14.9	5.6
Cured	44.8	40.0	11.7	3.4
Aged	52.6	34.2	10.1	3.1

Table 4.3 The concentration (in at %) of elements observed in the XP spectra collected from synthesised magnesium phosphate samples

Inspection of the oxygen 1s region after drying (Figure 4.21a) showed that the peak consisted of two components at 531.6 and 533.1 eV. These values are similar to the binding energies of the

BO and NBO atoms in sodium pyrophosphate reported by Gresch et al (see Table 4.1), however the ratio of binding energies is very different with a BO/NBO ratio of 1.35. this ratio does not allow for a meaningful estimation of

Heating the sample to 1073 K saw a shift in the binding energy of the oxygen 1s components to 532.1 and 533.6 eV. This shift to higher binding energy is typical of metaphosphate formation. Ageing the sample saw the binding energies of the oxygen components reduce slightly to 531.8 and 533.4 eV indicating that there is some breakdown of the metaphosphate occurring and there is either pyrophosphate reforming or orthophosphate formation.

Curing the sample was observed to cause a slight reduction in the BO/NBO ratio which increased again as the sample was aged (Figure 4.21b). This would imply curing caused a breakdown of the metaphosphate chain, which reformed again during ageing. This is in direct contrast to both the interpretation of the changes in binding energy and the results obtained in the previous chapter. In addition all the BO/NBO ratios recorded for this sample are larger than 1 (Figure 4.21) which would indicate that there are many more bridging oxygen atoms on the surface than non-bridging, most likely from a phosphate chain with extensive branching and cross-linking. The formation of such a chain is highly unlikely and does not explain the changes in the ratio being the inverse to what was expected.

It is more likely that there is some form of impurity present in the sample causing the unusually high BO/NBO ratios, this may be unreacted magnesium oxide or phosphoric acid as there was no purification step in the synthesis of the phosphate. As no additional phases were observed in the XRD the impurities must be in low concentrations and located mainly at the surface of the sample. Inspection of the carbon 1s region of the XP spectrum (Figure 4.21c) showed that it consisted of three components with binding energies of 284.6, 286.1 and 288.9 eV. The largest of these components was the one at 284.6 eV which was assumed to arise from adventitious carbon which is always present on the surface. The highest energy component is possible due to carbonate which has been recorded as have a binding energy 4.5 eV above adventitious carbon.²⁸ This carbonate it is likely to be the cause of the unexpectedly high BO/NBO ratio calculated from the oxygen 1s spectra.

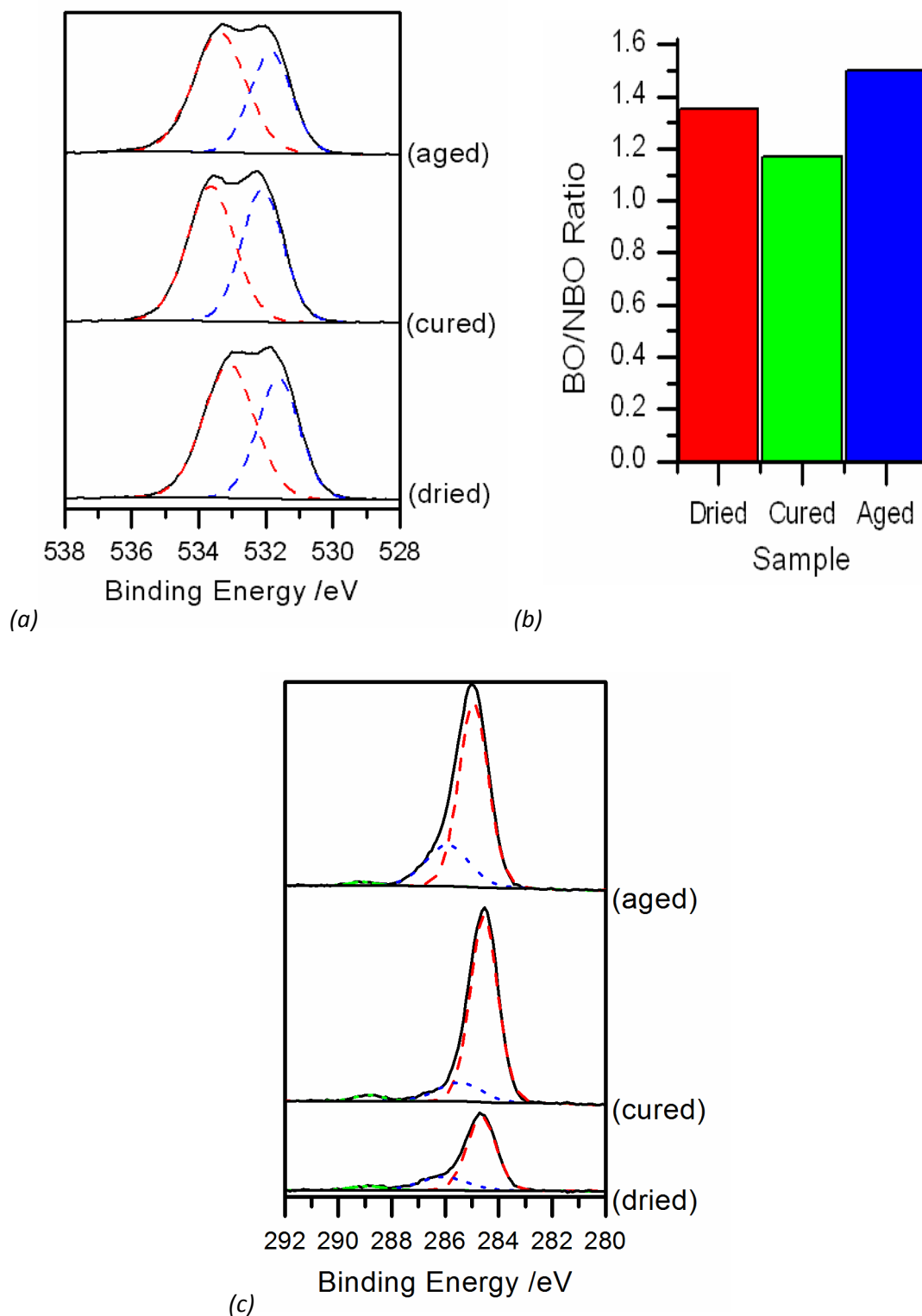


Figure 4.21 (a) the Oxygen 1s region of the XP spectra of synthesised magnesium phosphate after drying at 573 K curing at 1073 K and ageing for 3 weeks in a humidity chamber, (b) the variation of BO/NBO with sample treatment and (c) the carbon 1s spectra

Inspection of the phosphorous 2p region of the XP spectrum taken from the dried sample (Figure 4.22) showed that it consisted of one peak at 134.3 eV. This is fairly consistent with values recorded previously for metaphosphates¹, however the XP spectrum of magnesium metaphosphate and consequently the phosphorus 2p binding energy does not appear to have been previously reported.

Heating the sample to 1073 K saw a shift of around 0.5 eV in the binding energy of the phosphorus 2p signal (Figure 4.22). This change in binding energy indicates a change in the oxidation state of the phosphate and indicates that the phosphate is developing a more metaphosphate character (in good agreement with the shifts in binding energy of the oxygen 1s signal and as seen previously in chapter 3) and was also observed by Gresch in his studies on sodium phosphates. Inspection of the XP spectra collected from the aged sample showed that this shift in binding energy was reversible. This is in good agreement with data collected in the previous chapter (see section 3.2.2) which showed that the dehydrolytic condensation reaction that occurred during curing to form the metaphosphate was reversed during ageing to reform the magnesium ortho- and pyrophosphates.

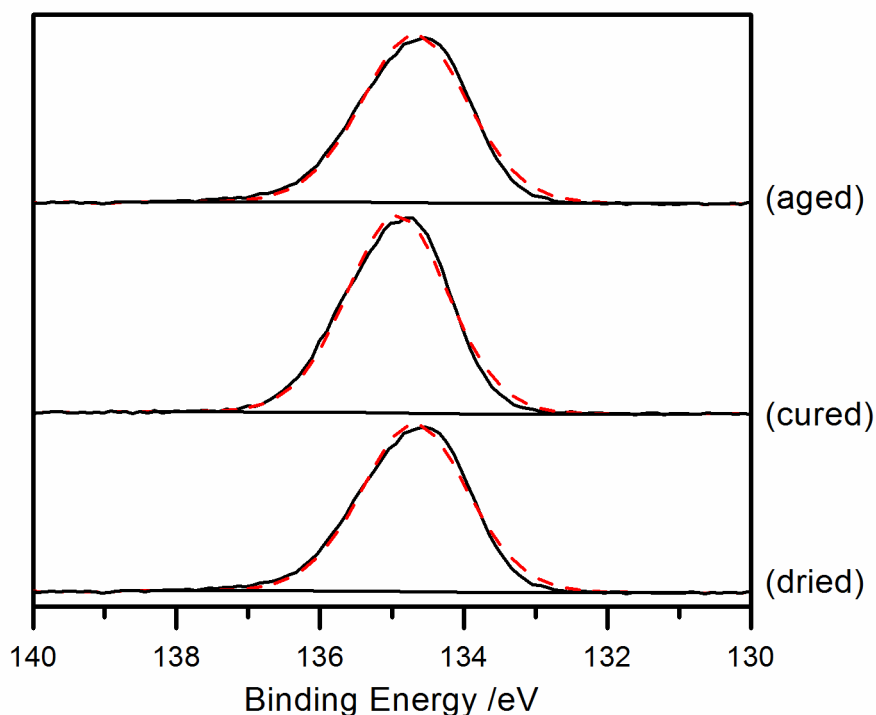


Figure 4.22 the Phosphorus 2p region of the XP spectra of synthesised magnesium phosphate after drying at 573 K, curing at 1073 K and ageing for 3 weeks in a humidity chamber.

4.3.2.3 SUMMARY

Comparison of the XP spectra of the two magnesium phosphate samples yields some significant differences. Whilst both sets of spectra indicated that the BO/NBO decreased with heating the BO/NBO ratio was significantly higher in the synthesised sample. The BO/NBO values of the synthesised magnesium phosphate were all greater than 1, indicating that there is some impurity present affecting this ratio. Inspection of the phosphorus 2p region indicates there are two phosphorus species present, whereas only one was observed in the purchased sample. The presence of impurities is highly likely as there was no purification step involved in the synthesis of the model coating material.

In both samples the changes in binding energy of the phosphorus 2p and oxygen 1s transitions when the sample is cured and aged followed the expected patterns, despite the issues surrounding the calculated BO/NBO values. This indicates that whilst XPS can be used to follow the changes in the phosphate chain it cannot be used to give an accurate measure of the average chain length.

4.4 XPS CHARACTERISATION OF POWDERED COATINGS

The previous work has shown that XPS cannot be used to measure average chain length of phosphates in model coatings due to impurities and multiple phosphate species complicating the oxygen 1s spectrum, however XPS still has uses in the full characterisation of the surface of both model and real systems, in particular when studying the phosphorus 2p region. In this section XPS is applied to model aluminium and magnesium phosphate samples, with particular attention on the phosphorus spectra.

4.4.1 MODEL COATINGS

4.4.1.1 ALUMINIUM PHOSPHATE

The wide scan of aluminium orthophosphate (Figure 4.23) showed that in addition to aluminium, phosphorous, oxygen and carbon a small amount of silicon was also present at the surface (approximately 1 %). The concentration of the silicon remained at 1 % after curing but increased to around 2 % after ageing.

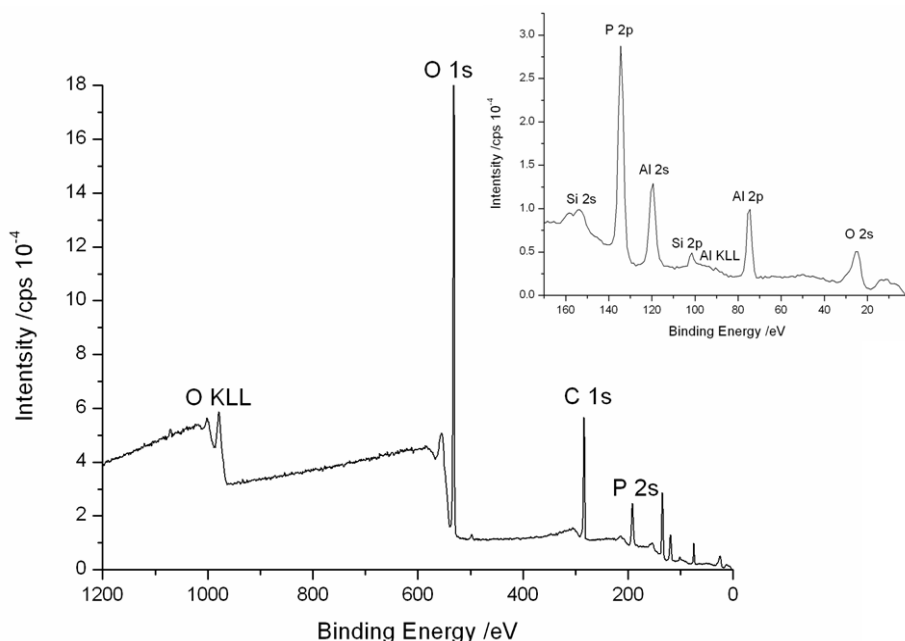


Figure 4.23 The XP spectrum of aluminium orthophosphate as received

Inspection of the oxygen region in the XP spectra of aluminium phosphate as received (Figure 4.24) shows the signal consists of two components at 532.3 and 533.7 eV. These binding energies are consistent with the values for NBO and BO atoms reported in previous samples. Heating the system to 1073 K (as a mimic of on-line curing in industry) caused a shift in the binding energy of the bridging oxygen component to 534.0 eV and an increase in the area relative to the non-bridging component (Figure 4.24b). Both of these observations indicate that the surface of the aluminium orthophosphate is developing a more metaphosphate character as it is heated, unlike the bulk of the model coating, which was shown to be unaffected by the curing process in the previous chapter.

The spectrum of the aged sample was largely unchanged from the cured spectrum. This indicates that the ageing process had little effect on any metaphosphate formed. This is in good agreement with the results in the previous chapter and observations made by Cogent Power Ltd with regards to their coating trials which both indicated that aluminium phosphate is more stable towards hydration than magnesium phosphate.

Following the changes in the BO/NBO ratios from the spectra taken from the aluminium phosphate samples after each treatment (Figure 4.24b) shows the expected pattern of increasing during heating and then decreasing after ageing. The BO/NBO ratio from the as received sample is very low at 0.018, indicating that the surface contains a large amount of

orthophosphate, with an average chain length of 1.07 phosphorus atoms. When the sample is cured the ratio increases to 0.1, indicating an average chain length of 1.5 phosphorus atoms (i.e. a 1:1 ratio of ortho- to pyrophosphate). This ratio is much lower than any recorded for any of the previous heated samples, indicating that metaphosphate formation is much less favourable in aluminium phosphate (this is supported by the work on the bulk studies of the samples in the previous chapter). Ageing the sample caused a slight decrease in the BO/NBO ratio, indicating that some dehydrolytic condensation is occurring at the surface; however it is happening very slowly, especially in comparison to magnesium phosphate.

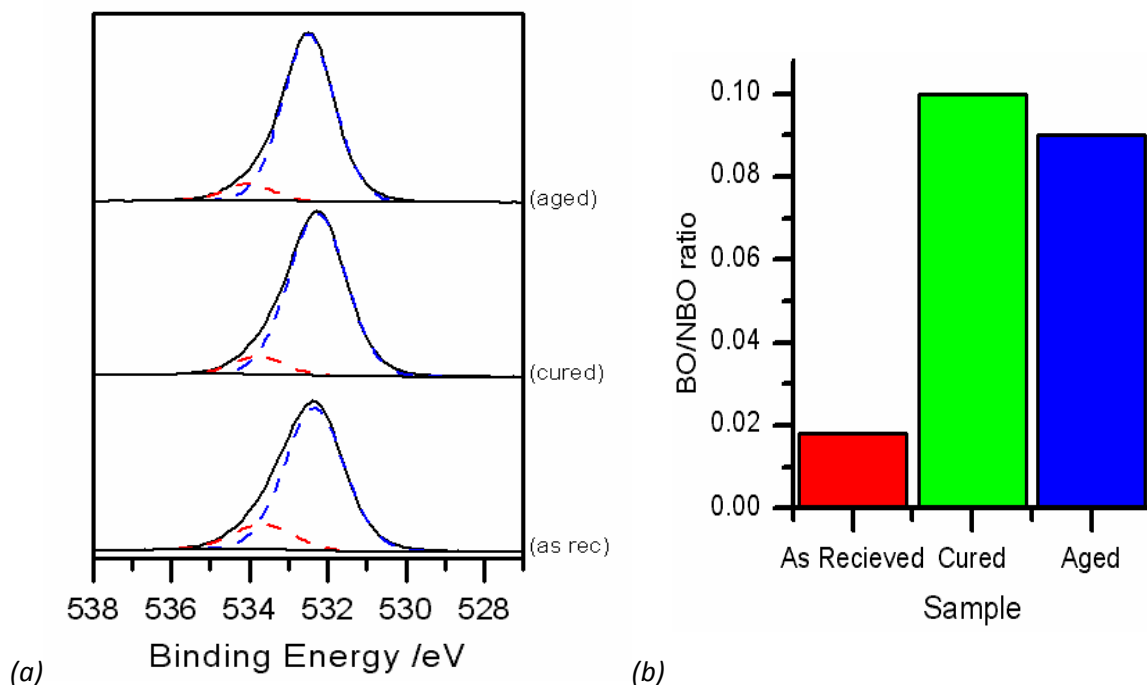


Figure 4.24 (a) the Oxygen 1s region of the XP spectra of model aluminium phosphate coating and (b) the variation of BO/NBO ratio with sample treatment of aluminium phosphate model coating

Inspection of the phosphorus 2p region showed that each peak consisted of one component. Fixing the relative areas of the components to the expected 2:1 ratio gave a peak splitting of 1.04 eV, close to the typical values reported in literature (0.86 +/- 0.05 eV)⁵⁶. The binding energy of the 2p transition is measured as 134.6 eV which is generally much more typical of metaphosphates,²⁸ however the 2p binding energy of aluminium orthophosphate has previously been recorded at this binding energy by others. When this information is combined with the ratio of the areas of the oxygen 1s and phosphorus 2p peak areas (4.1: 1) and XRD and vibration

spectroscopies in the previous chapter, it is clear that the surface is formed primarily of aluminium orthophosphate.

Curing and ageing caused little change in the phosphorus 2p spectrum of the model aluminium phosphate coating, with the binding energy remaining constant at 134.6 eV. In addition the relative surface concentrations of oxygen and phosphorus remained constant at 3.9:1 in the cured sample and 4:1 in the aged sample. This supports the conclusions drawn in the previous chapter that aluminium orthophosphate does not react upon curing to form aluminium metaphosphate, and that it is stable when aged in a humidity chamber.

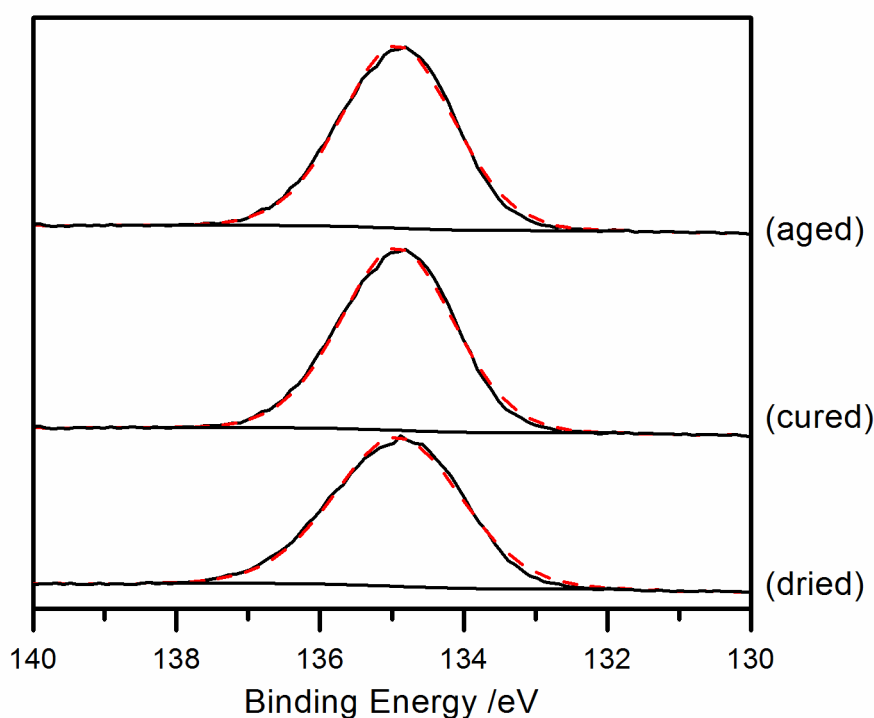


Figure 4.25 The phosphorus 2p region of the XP spectra of model aluminium phosphate coating.

The relative areas of the components has been fixed

4.4.1.2 MODEL MAGNESIUM PHOSPHATE COATINGS AND THE EFFECTS OF CHROMIUM ADDITION

In addition to the 40 % magnesium oxide phosphate discussed previously in section 4.3.2.2 XPS data has been collected for samples synthesised from 50 and 75 % magnesium oxide, and a sample synthesised from 40 % magnesium oxide with chromium oxide added. For reference the phases previously observed in the XRD patterns of the magnesium phosphates in Chapter 3 are given in Table 4.4.

Chapter 4 XPS Studies of Phosphate Coatings

<i>Sample</i>	<i>40 % Magnesium oxide</i>	<i>50 % Magnesium oxide</i>	<i>75 % Magnesium oxide</i>	<i>40 % Magnesium oxide + Chromium Oxide</i>
<i>Dried</i>	$Mg_3(PO_4)_2 \cdot xH_2O$	$Mg_3(PO_4)_2$, $MgH_2P_2O_7$	MgO , $Mg_2P_2O_7$	MgO , $Mg_2P_2O_7$, CrO_3 , $Cr_2P_2O_7$
<i>Cured</i>	$Mg_2P_4O_{12}$	$Mg_2P_4O_{12}$	$Mg(PO_3)_2$, MgO , $Mg_2P_2O_7$	$Cr_2O_3 + Mg_2P_2O_7$

Table 4.4 The phases observed in the X-ray Diffraction patterns of magnesium phosphates

Inspection of the wide scans of the 50 and 75 % magnesium oxide samples indicated that the only elements present on the surface of the samples were magnesium, phosphorous, oxygen and carbon.

4.4.1.2.1 50 % MAGNESIUM OXIDE

	<i>Relative Concentration / at %</i>			
	<i>Oxygen (O 1s)</i>	<i>Phosphorus (P 2p)</i>	<i>Magnesium (Mg 2p)</i>	<i>Carbon (C 1s)</i>
<i>Dried</i>	61.5	14.4	5.7	18.4
<i>Cured</i>	50.6	13.3	5.6	30.4
<i>Aged</i>	17.1	4.3	2.0	76.6

Table 4.5 The relative atomic concentrations of elements at the surface of 50 % magnesium oxide model phosphate coatings

Inspection of the areas of the oxygen 1s, magnesium 2p and phosphorus 2p transitions in the spectrum taken from the dried 50 % magnesium oxide sample showed a ratio of 1 magnesium: 2.5 phosphorus: 11 oxygen atoms. There is a slightly higher concentration of phosphorus and oxygen than predicted by the XRD data (Table 4.4) but the ratio between the number of

phosphorus and magnesium atoms implies the surface is mainly comprised of the pyrophosphate $\text{MgH}_2\text{P}_2\text{O}_7$.

The oxygen 1s region of the XP spectrum of the 50 % magnesium phosphate after drying (Figure 4.26a) showed that as with previous samples it consists of two components at 531.7 and 533.2 eV. These components are assigned to the NBO and BO atoms respectively. The BO/NBO ratio was found to be 1.28. These values are comparable to the dried 40 % magnesium oxide sample (binding energies of 531.6 and 533.1 eV and BO/NBO = 1.35, see Figure 4.21a). Ortho and pyrophosphates have previously been shown to have very similar binding energies (average binding energies of 531.0 and 531.1 eV respectively)^{1,28}.

Inspection of the phosphorus 2p region showed that it consisted of one component. As with the oxygen 1s region the binding energies of ortho- and pyro phosphate are very similar making assignment of the XP spectra based on binding energies impossible. The binding energy of the P 2p peak in this sample is 134.2 eV, which as noted when discussing the aluminium phosphate data is high for an ortho or pyrophosphate, however the ratio between elements and position of the oxygen 1s peak indicates that pyrophosphate is the most reasonable assignment.

Heating the system to 1073 K saw a large decrease in the overall area of the oxygen region (Figure 4.26b). This is accompanied by a shift to approximately 0.5 eV higher binding energies, generally associated with a reduction in the oxidation state of the phosphate (i.e. ortho to pyro or metaphosphate). The BO/NBO ratio dramatically reduces to 0.64 indicating a decrease in the chain length, which directly contradicts the observed shift in binding energy.

Heating the system also caused a shift in the phosphorus 2p binding energy to 134.5 eV, in good agreement with literature binding energies with an average of 134.6 eV for metaphosphate²⁸. If the areas of the magnesium 2p, phosphorus 2p and oxygen 1s transitions are compared the resulting ratio is 1: 2.3: 9. As with the dried sample the XPS results indicate that the surface is more oxidised than predicted by XRD; however the ratio between magnesium and phosphorus atoms is close to 1:2, confirming the identity of the sample as $\text{Mg}_2\text{P}_4\text{O}_{12}$.

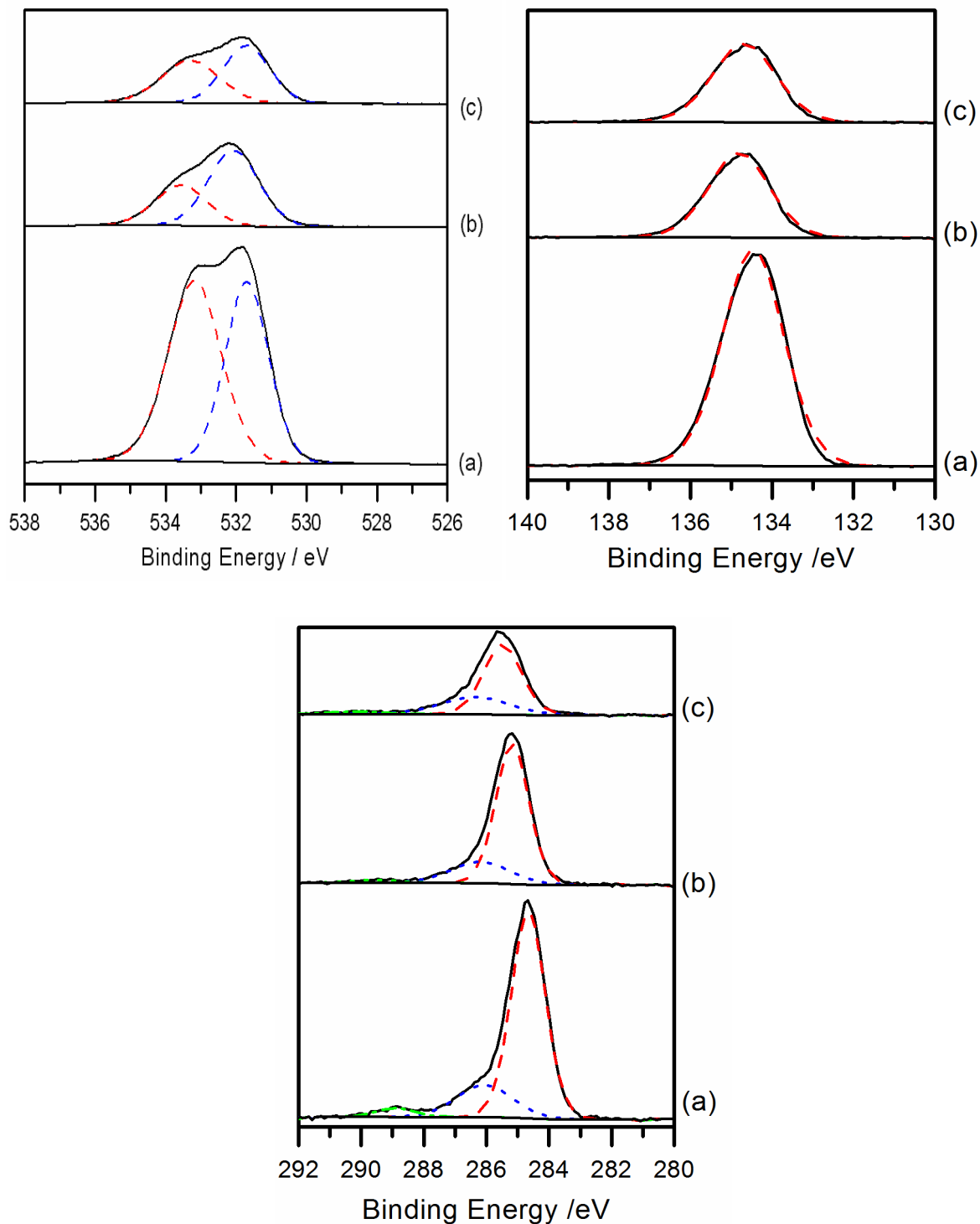


Figure 4.26 The oxygen 1s, phosphorus 2p regions and carbon 1s regions of the XP spectra of model 50 % magnesium phosphate coating (a) after drying at 573 K (b) after heating to 1073 K and (c) after ageing in a humidity chamber for 3 weeks.

Ageing the sample (Figure 4.26c) saw the binding energies of the oxygen 1s components shift back to 531.7 and 533.3 eV, indicating that ageing was causing the reversal of the curing reaction via breakage of the P-O-P bonds, as observed in the previous chapter. The binding energy of the phosphorus 2p transition was also found to shift back to its original binding energy of 134.4 eV, indicating that the observed transformation in the cured sample is reversible. The relative concentration of the elements was found to be 1 Mg: 2.4 P: 8 O, similar to the starting material $\text{MgH}_2\text{P}_2\text{O}_7$. The BO/NBO ratio increases again to 1.00, implying an increase in metaphosphate character in contrast to all other results.

In all instances the BO/NBO ratios for the 50 % magnesium phosphate sample (Figure 4.27) were lower than the ones recorded for the 40 % sample (Figure 4.21 **Error! Reference source not found.**); however they all remained above the expected maximum of 0.5. In addition both samples showed the same pattern of decreased BO/NBO when cured which increased again upon ageing. This is in strong disagreement with other features in the XP spectra- namely the observed shifts in binding energies and the variation of the relative concentrations of the elements present at the surface of the sample. This result supports the conclusion presented earlier that the oxygen 1s spectra cannot be used to reliably follow the changes in average phosphate chain length in model coatings.

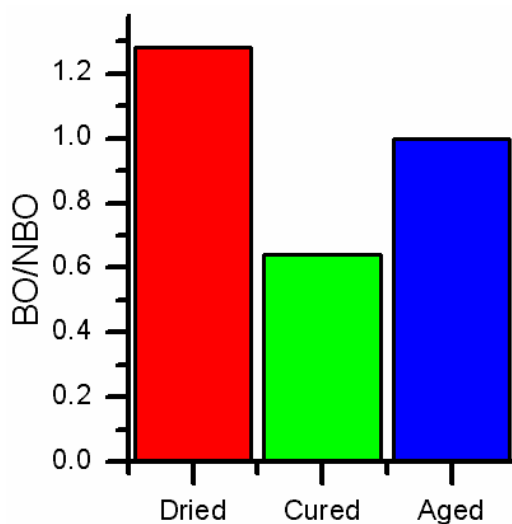
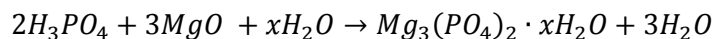


Figure 4.27 The effect of sample treatment on the BO/NBO ratio in 50 % magnesium phosphate

The carbon 1s region (Figure 4.26) was observed to contain 3 regions prior to curing with binding energies of 284.6, 286.0 and 288.9 eV. As with previous samples the largest component at 284.6 eV was assigned to adventitious carbon and the component at 288.9 eV to carbide. This

carbide was observed to decrease dramatically upon curing and could be used as an explanation for the unexpected decrease in BO/NBO ratio (with the oxygen of the carbide contributing to the component in the oxygen 1s spectrum attributed to bridging oxygen atoms within the phosphate chain).

Equation 4.2 shows the proposed reaction between phosphoric acid and magnesium oxide to form magnesium orthophosphate during production of steel coatings (see previous chapter). It is clear that the reaction requires a 2:3 mixture of phosphoric acid to magnesium oxide. In both the 40 and 50 % magnesium oxide samples phosphoric acid is present in excess and may be altering the BO/NBO ratio. This could also be the cause of the unexpectedly high concentration of oxygen at the surface and the dried samples phosphorus 2p binding energies being higher than previously recorded orthophosphates.



Equation 4.2 The proposed reaction for the formation of magnesium orthophosphate in the synthesis of model coatings

4.4.1.2.2 75 % MAGNESIUM OXIDE

Comparison of the areas of the magnesium 2p, phosphorus 2p and oxygen 1s transitions in the XP spectrum of the dried 75 % magnesium phosphate sample gave a ratio 1:1.4:5.9. This indicates that the surface is mostly MgP_2O_7 as observed in the X-Ray diffraction patterns (Table 4.4) but that there is also a small amount of unreacted magnesium oxide present on the surface (due to the higher than expected magnesium concentration). This was expected as magnesium oxide was present in excess during the synthesis of the model coating.

Chapter 4 XPS Studies of Phosphate Coatings

	<i>Relative Concentration / at %</i>			
	<i>Oxygen (O 1s)</i>	<i>Phosphorus (P 2p)</i>	<i>Magnesium (Mg 2p)</i>	<i>Carbon (C 1s)</i>
<i>Dried</i>	47.0	11.3	8.0	33.8
<i>Cured</i>	50.4	14.5	7.9	27.3
<i>Aged</i>	34.3	10.7	6.5	48.5

Table 4.6 The relative atomic concentrations of elements at the surface of 75 % magnesium oxide model phosphate coatings

Closer inspection of the oxygen 1s region (Figure 4.28a) shows that it consists of the expected two components at 532.3 and 533.9 eV. As with previous samples these components can be assigned to NBO and BO atoms of the pyrophosphate, however the binding energies of these components is significantly higher than those recorded in the previous samples. Figure 4.29 shows that there is a linear relationship between the amount of magnesium oxide present during the synthesis of the model coating and the binding energies of both oxygen 1s components in the XP spectra of the dried samples. The BO/NBO ratio of this sample was calculated as 0.64, again much higher than what is expected for a pyrophosphate. It is possible that excess magnesium oxide is contributing to the bridging oxygen signal, producing an artificially high BO/NBO ratio (binding energies for oxygen 1s in magnesium oxide typically lie between 530.0- 531.0 eV²⁸).

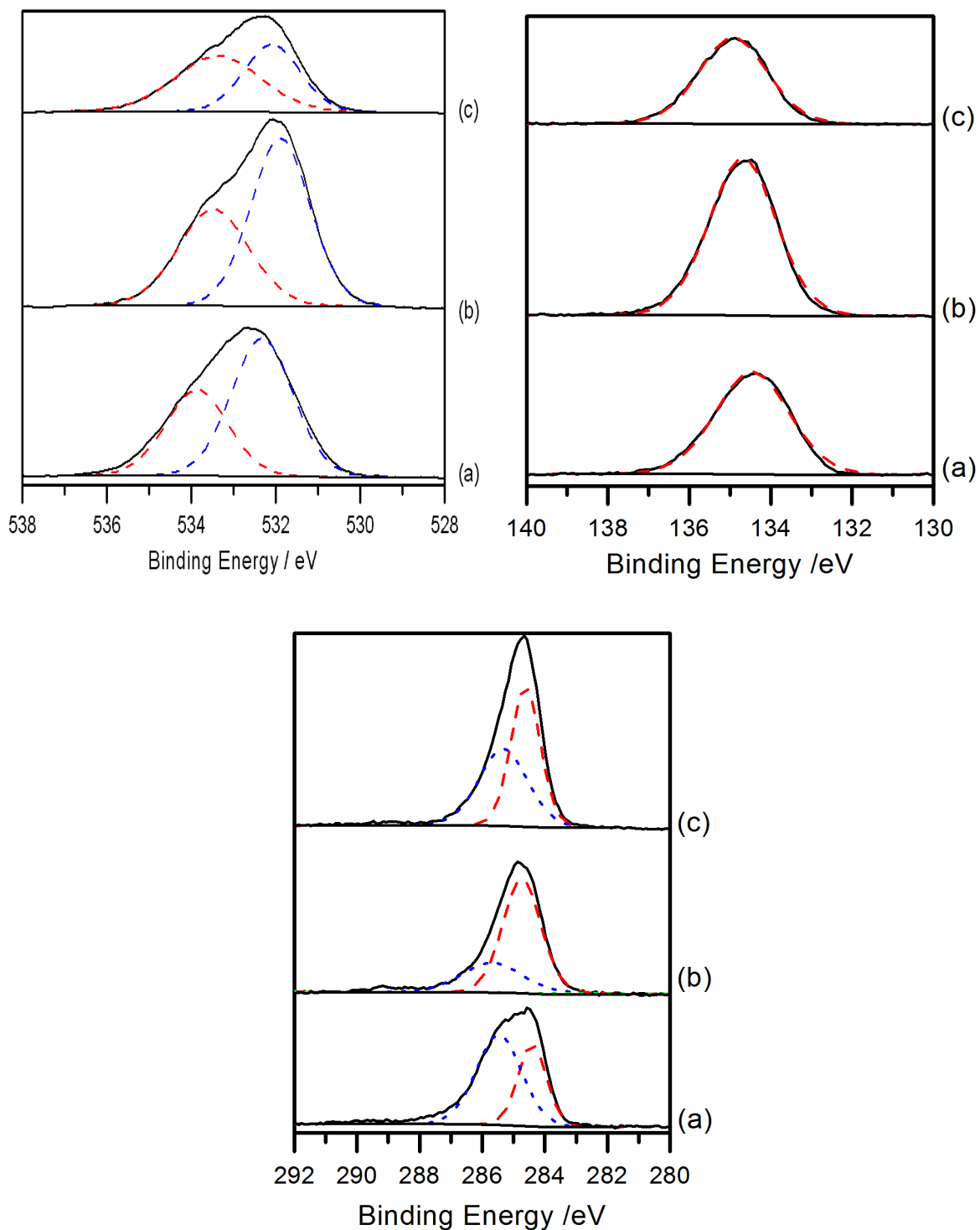


Figure 4.28 The oxygen 1s, phosphorus 2p and carbon 1s regions of the XP spectra of model 75 % magnesium phosphate coating (a) after drying at 573 K (b) after heating to 1073 K and (c) after ageing in a humidity chamber for 3 weeks.

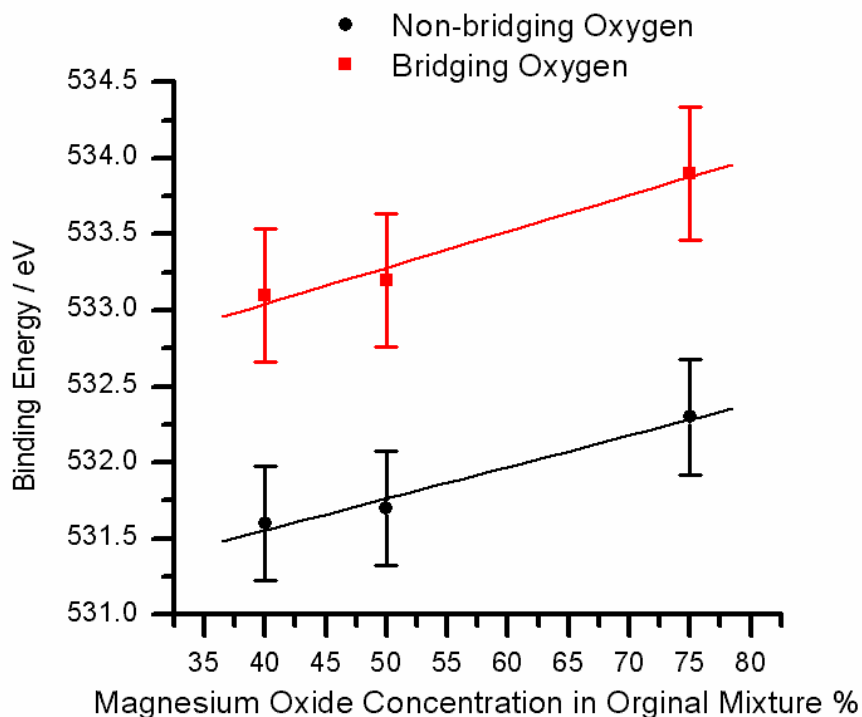


Figure 4.29 The effect of magnesium oxide concentration in reaction on the position of peaks in the oxygen 1s XP spectra of the resulting dried model coating

The phosphorus 2p signal consisted of the expected two components arising from the $\frac{1}{2}$ and $\frac{3}{2}$ transitions. The binding energy was recorded as 134.1 eV which is higher than previously recorded binding energies for pyrophosphates (averaging at 133.2 eV), however is consistent with binding energies recorded for other magnesium pyrophosphates within this study. Unlike previous samples no carbonate was observed in the carbon 1s spectrum.

Heating the sample to 1073 K altered the ratio of magnesium: phosphorus: oxygen to 1:2:3.5 (see Table 4.6) indicating there has been a reduction in the concentration of oxygen at the surface of the sample, implying there may have been a slight increase in average chain length. The ratio does not match the $\text{Mg}(\text{PO}_3)_2$ observed in the XRD, most likely because of the unreacted magnesium oxide also observed in the XRD.

Within the oxygen 1s region the component at 532.1 eV shifts to a slightly lower binding energy of 531.9 eV and the component at 533.1 eV shifts to 533.5 eV (Figure 4.28b). The shift in binding energy of the BO atom is typical of metaphosphate formation; however a shift to a lower binding energy as observed in the component arising from non-bridging oxygen atoms is typical of orthophosphate reforming via the breakdown of metaphosphate. The data in the previous

chapter and results from the previous samples indicate that metaphosphate formation occurs during curing, indicating that the shift in the bridging oxygen binding energy must occur by some other means- possibly some reaction involving the magnesium oxide (which has a typical oxygen 1s binding energy of 530.8-532.1 eV which is similar to the BO atoms in the phosphate chain).

The ratio of BO and NBO atoms was calculated as 0.69. When this small change is coupled with the lack of change in the phosphorus 2p spectrum it is unlikely to be meaningful.

Ageing the sample caused a change in the ratio of elements to approximately 2:3:11. This implies that the surface is likely to be made up of a mixture of magnesium pyro and orthophosphates (MgP_2O_7 and MgPO_4). This increase in the relative concentration of oxygen at the surface provides good evidence for the breakdown of metaphosphate chains.

Close inspection of the oxygen 1s region (Figure 4.28c) saw that the region still consisted of two components. The lower energy component arising from NBO atoms shifted closer to its original binding energy at 532.1 eV, and the higher energy component (BO) remained at 533.4 eV. This result indicates that the possible reaction involving magnesium oxide is reversible. The BO/NBO ratio was observed to decrease to 0.6, indicating some breakdown of metaphosphate chains at the surface. The phosphorus 2p region again remained largely unchanged with two components observed and the 2p 3/2 binding energy was fairly consistent at 134.6 eV.

If all three BO/NBO ratios from the 75 % sample are compared the expected pattern of increasing upon heating followed by decreasing when the sample is aged is observed (Figure 4.30). This implies that the average metaphosphate chain length increases when the sample is heated and the chain breaks down upon ageing. This observation is in good agreement with the relative concentrations of atoms on the surface and the observed changes in binding energies, however the ratios are much higher than expected after all treatments. This is likely to be because of excess magnesium oxide present from the coating synthesis causing an increase in the observed signal from bridging oxygen atoms.

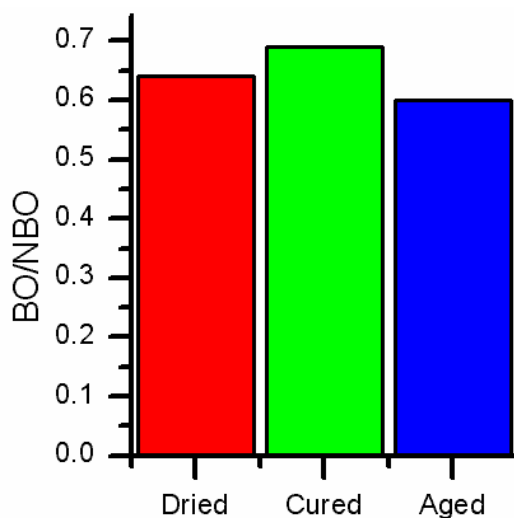


Figure 4.30 The effect of sample treatment on the BO/NBO ratio in 75 % magnesium phosphate

4.4.1.2.3 THE ROLE OF CHROMIUM

In order to probe the effects of chromium addition on the surface of model coatings a sample containing equal amounts of chromium (III) oxide and magnesium phosphate was produced and dried at 573 K. A portion of this sample was cured at 1073 K in order to probe the effects of curing on the sample composition. The sample heated to 573 K was calibrated using adventitious carbon to 284.7 eV, however it was assumed heating to 1073 K altered the carbon and the magnesium 2p peak was used for calibration of this sample.

Table 4.7 shows the relative concentrations of chromium, magnesium, phosphorus and oxygen at the surface of the sample after both heat treatments. The relative concentrations of the elements in the surface of the dried (heated to 573 K) sample consists of equal amounts of chromium (VI) oxide (CrO_3) and magnesium pyrophosphate ($\text{Mg}_2\text{P}_2\text{O}_7$) as observed in the XRD patterns (Table 4.4). Heating the sample to 1073 K caused a notable decrease in the surface concentration of chromium from 7.6 to 3 %, indicating that the surface ratio of chromium oxide to magnesium phosphate was no longer 1:1. The concentration of phosphorus atoms were higher than expected from the XRD patterns.

Sample	Concentration / Atomic %					
	Temp /K	Cr 2p	O 1s	P 2p	Mg 2p	C 1s
573		5.3	49.6	10.3	4.0	30.8
1073		2.6	59.7	16.2	5.5	15.9

Table 4.7 the relative concentrations of surface atoms in chromium containing model phosphate coatings

Inspection of the chromium 2p spectrum of the dried sample (Figure 4.31a) showed the spectrum consisted of two components- a narrow peak at 579.6 eV and a broader peak at 577.3 eV. The peak at 579.6 eV can be assigned to trivalent chromium(Cr^{3+})^{31, 33-35} and the broader peak to hexavalent chromium (Cr^{6+})^{31, 32}. The broadening of the hexavalent chromium peak is caused by multiplet splitting (not shown) due to unpaired electrons in the 3d sub-shell³¹.

The presence of trivalent chromium was unexpected as it had not been observed in other techniques used to characterise dried samples (see chapter three), however it was also observed in the chromium 3p spectrum which overlapped the magnesium 2p (around 45 eV see Figure 4.31). The photo-reduction of hexavalent chromium during XPS experiments has been noted by others;^{33, 61, 62} however there has been some controversy over whether Cr(IV)⁶¹ or Cr(III)⁶² is formed during this process. Based on the binding energies observed in the current set of spectra it appears that this sample is reduced to Cr(III).

Heating the sample to 1073 K (Figure 4.31b) caused the loss of the peak at 579.6 eV and the chromium 2p 3/2 spectrum simplified to 1 broad peak (FWHM = 3.07 eV) at 577.9 eV arising from the trivalent chromium species Cr_2O_3 . This simplification of the chromium spectrum is also observed in the Cr 3p spectrum. This indicates the surface of the sample is completely reduced during the curing process as no Cr (VI) was observed.

The main difference in the magnesium 2p region of the XP spectrum is the shift from three peaks to two. As mentioned previously the chromium 3p transition is very close in energy to the magnesium 2p peak, and therefore additional peaks are observed (at 47 and 44 eV, pink and

blue in the figure). One chromium 3p peak is removed upon heating due to the removal of Cr (VI) from the sample as previously discussed.

In both samples the magnesium 2p spectrum is one component with a binding energy of 49.9 eV. The 2p 3/2 and 1/2 peaks could not be resolved due to a small peak splitting.

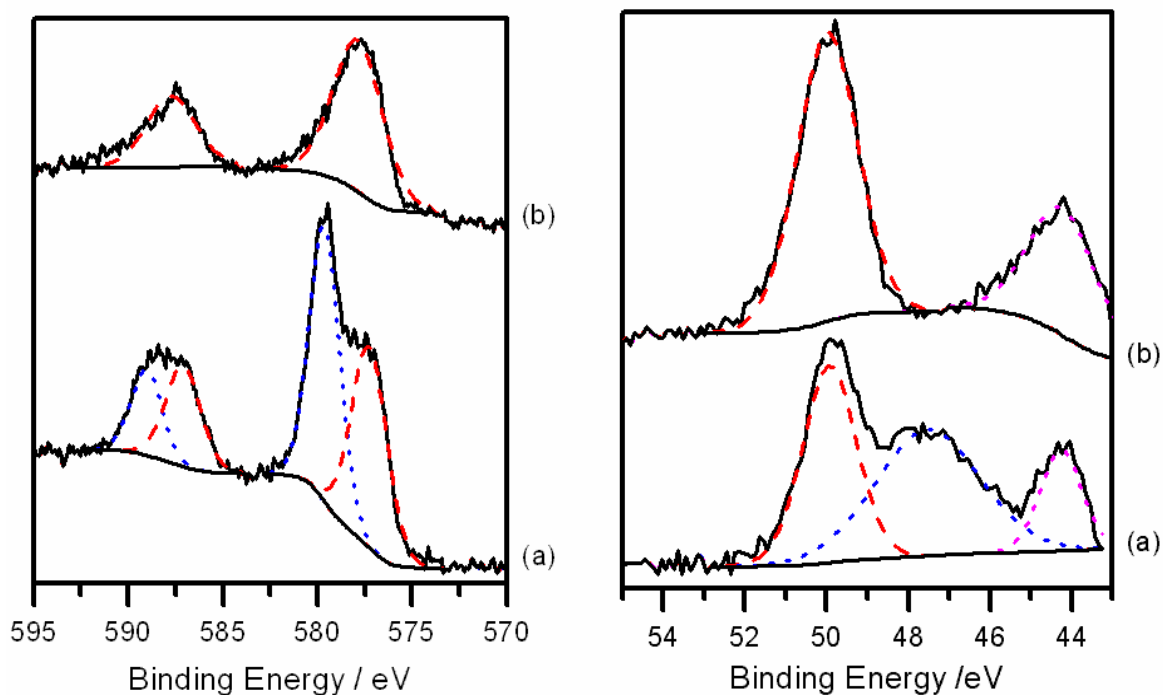


Figure 4.31 the chromium 2p and magnesium 2p regions of the XP spectra of chromium oxide / magnesium phosphate after heating to (a) 573 and (b) 1073 K.

Inspection of the oxygen 1s region of the dried sample (Figure 4.32) showed that it consists of three components with binding energies of 530.8, 531.4 and 532.6 eV. The components at 531.4 and 532.6 eV are similar in binding energy to those observed in the chromium free sample (binding energies 531.7 and 533.2 eV, Figure 4.21) and therefore can be assigned to the NBO and BO atoms within the phosphate chain. The BO/NBO ratio taken from these components is 0.90, significantly lower than the ratio recorded for the chromium free sample (1.35). The component at 530.8 eV can be assigned to chromium oxide; however it is unclear if it arises from the hexavalent or trivalent species. The binding energies of oxygen atoms in both chromium oxide species are similar (both have an average binding energy of 530.3 eV from the NIST database²⁸) and binding energies of 530.8 eV have been recorded for both species^{40, 41}.

Heating the sample to 1073 K (Figure 4.32b) saw a shift in the binding energies of the oxygen components related to the phosphate chain (532.3 and 534.0 eV). This shift in binding energy is typical of metaphosphate chain formation and is a strong sign dehydrolytic condensation is occurring at the surface of the sample. In contrast the BO/NBO ratio calculated from this spectrum is 0.15, signifying a dramatic decrease in the amount of bridging oxygen present at the surface. The chromium oxide component remains constant at 530.8 eV; however the relative concentration of this component increases relative to the phosphate components. This is in good agreement with the reduced chromium signal (Table 4.7) and the proposed reduction to Cr_2O_3 .

Inspection of the phosphorus 2p region of both spectra (Figure 4.32) showed it consisted of one component. The binding energy in the dried spectrum was recorded as 133.2 eV, lower than those recorded for chromium free samples but matching the average value recorded in the literature for both ortho and pyrophosphates.²⁸ Heating the sample caused no change in the phosphorus 2p spectrum, indicating that any dehydrolytic condensation occurring is most likely to be an ortho to pyrophosphate transition.

Inspection of the carbon 1s region indicated that carbonate was also present on the surface of the sample after heating to both 573 and 1073 K as with many of the previous samples.

From the XP spectra it is clear that the presence of hexavalent chromium in the coating reduces the amount of condensation occurring in the phosphate chain as it is reduced during heating. It is also clear that the surface layer of the model coating after curing is formed mainly of the magnesium phosphate as the chromium concentration is much lower than in the bulk.

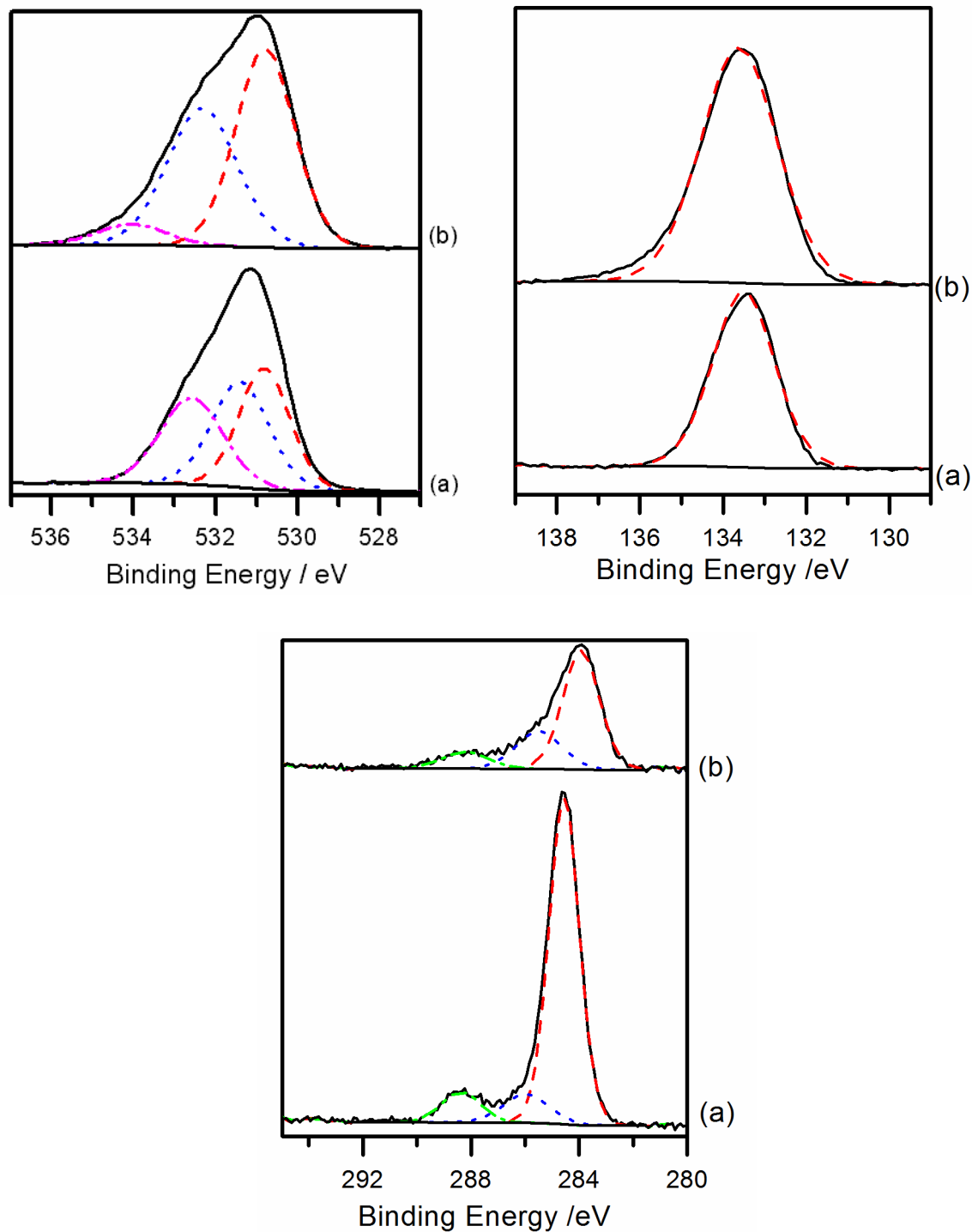


Figure 4.32 the Oxygen 1s, phosphorus 2p regions and carbon 1s of the XP spectra of chromium oxide / magnesium phosphate after heating to (a) 573 and (b) 1073 K.

4.4.2 INDUSTRIAL COATINGS

As a thorough understanding of the model coating materials had been developed it was decided to apply this understanding to powdered industrial coatings. These coatings are more complex due to the presence of colloidal silica which produces additional transitions in the XP spectra (particularly in the oxygen 1s region). Two coatings were studied- an aluminium phosphate coating currently used online at Cogent Power Ltd known as Mix 4 and a mixed aluminium phosphate and chromium oxide test coating known as Mix 2. Both coatings have been shown to have excellent degradation properties in trials at Cogent, and Mix 2 was shown to have enhanced tension properties when compared to Mix 4. Table 4.8 shows the expected atomic concentrations in the coatings and those measured using XPS after drying at 373 K and curing at 1073 K. The concentration of aluminium is notably lower than predicted by the coating formulation for all samples; it is also much lower than the concentration of phosphorus when the formulation predicted they would be equal. The ratio of aluminium to phosphorus atoms was approximately 1:3 in the dried mix 4 sample and decreased further upon curing to 1:4. The ratio in the Mix 2 coating remained constant at 1:4.

It is clear from the table that in all spectra the concentration of silicon at the surface was much higher than would be predicted from the coating formulation. The concentration of silicon at the surface is reduced after curing; however it is still significantly higher than expected. The presence of chromium within the coating appears to have the effect of increasing the silicon concentration at the surface.

The concentration of oxygen atoms is slightly higher than predicted from the coating formulas, however is generally in good agreement with the concentrations of phosphorus, silicon and chromium for the formulas of the expected compounds (AlPO_4 and SiO_2 in the Mix 4 coating, AlPO_4 , SiO_2 and CrO_3 in the dried Mix 2 coating and AlPO_4 , SiO_2 and Cr_2O_3 in the cured Mix 2 coating).

Sample		Concentration / Atomic %				
		<i>Al</i>	<i>P</i>	<i>O</i>	<i>Si</i>	<i>Cr</i>
Aluminium Phosphate Coating (Mix 4)	<i>Dried</i>	1.5	4.4	70.4	23.8	0
	<i>Cured</i>	2.1	7.9	70.4	19.8	0
	<i>From Formulation</i>	10.0	10.0	66.7	13.3	0
Aluminium Phosphate Coating with chromium oxide (Mix 2)	<i>Dried</i>	0.8	3.4	69.8	25.1	1.0
	<i>Cured</i>	1.9	8.2	70.7	17.6	1.6
	<i>From Formulation</i>	8.4	8.4	68.1	11.1	4.2

Table 4.8 The Concentration of elements present in coatings obtained from Cogent Power Ltd as determined from XP spectra and the expected concentrations based on coating formulations. All concentrations are given in atomic per cent.

From the data presented in Table 4.8 it is clear that the surface of the powdered coatings is dominated by the colloidal silica added to the coating, rather than the phosphates thought to be responsible for the main tension properties. In the next sections a more detailed analysis of the XP spectra of the coating materials is presented.

4.4.2.1 ALUMINIUM PHOSPHATE COATINGS

Inspection of the wide scan of the XP spectrum of the dried mix 4 coating indicated that the surface comprised only of the expected aluminium, oxygen, carbon, phosphorus and silicon. The wide scan of the cured sample indicated that sodium was also present on the surface of the sample, which is added to the colloidal silica solution by the supplier as a stabilising counter ion.

Inspection of the oxygen 1s region of the dried sample (Figure 4.33a) showed that it consists of two components at 532.6 and 534.2 eV. These components can be assigned to silica^{28, 42-44} and aluminium phosphate (consistent with binding energies recorded previously in section 4.4.1.1) respectively. The relative areas of these two components are 1:32, which gives 1 molecule of

AlPO_4 to 64 SiO_2 molecules. This is much higher concentration of silica than implied by the ratio of silicon atoms to either aluminium or phosphorus ones. Heating the sample to 1073 K (Figure 4.33b) caused the component arising from the phosphate to shift to a higher binding energy (535.0 eV), as typically seen during metaphosphate chain formation; however 535.0 eV is significantly higher than energies recorded previously²⁸. The area of this component has also increased relative to the area of the silica component (the binding energy of which remained fairly consistent (532.9 eV)) to 1:11.4, or 1 molecule of AlPO_4 to 23 of SiO_2 . This increase in aluminium phosphate is observed in the concentration of aluminium and phosphorus atoms (see Table 4.8), however again the relative areas of the oxygen components implies a much higher concentration of silica than the ratio of the other elements present would suggest.

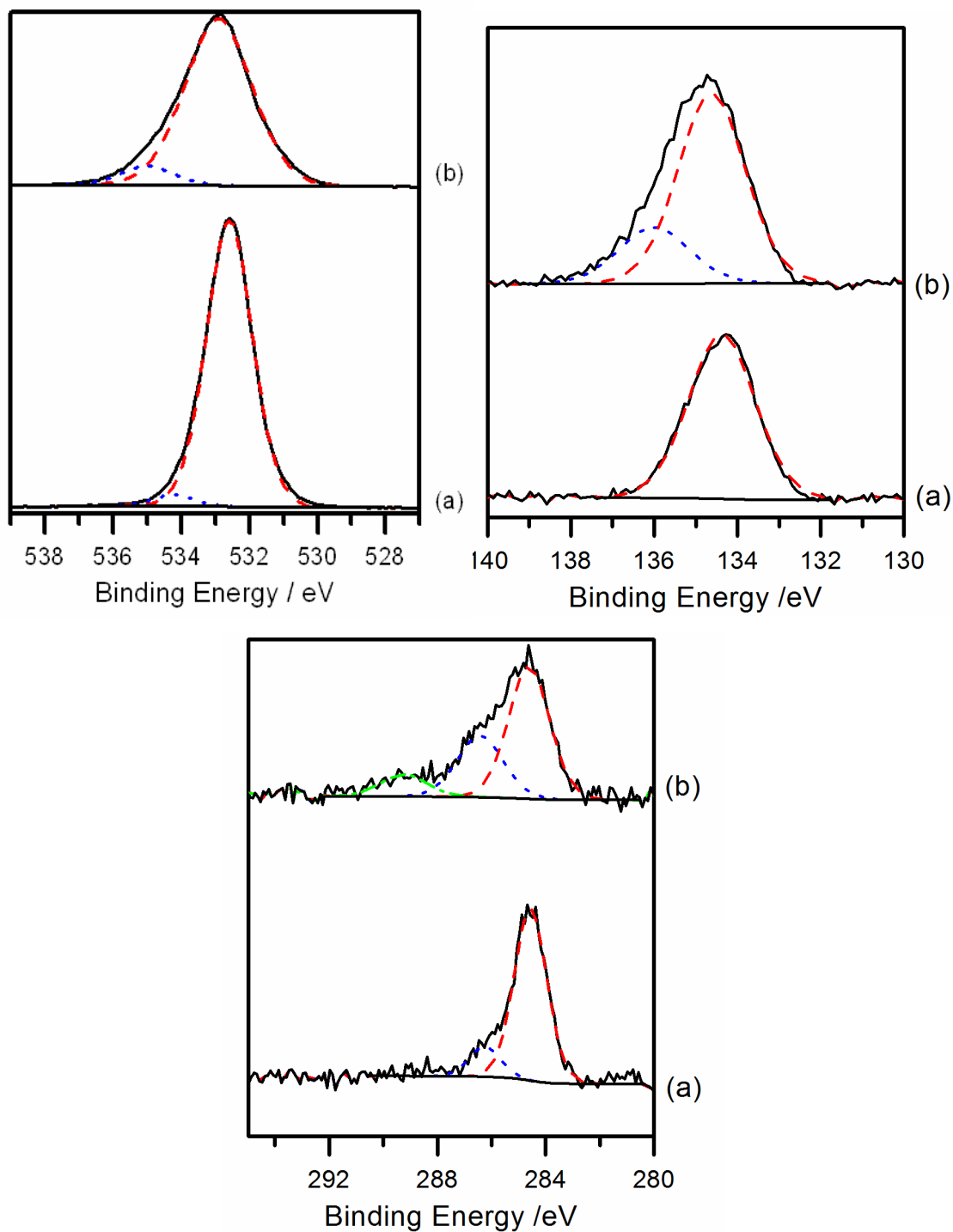


Figure 4.33 the oxygen 1s, phosphorus 2p and carbon 1s of the XP spectra of Mix 4 industrial coating after (a) drying at 373 K and (b) curing at 1073 K.

Inspection of the dried phosphorus 2p spectrum shows that it consists of one component. The binding energy was recorded as 134.1 eV, slightly lower than values recorded in the previous section for pure aluminium phosphate model coatings (134.6 eV), however in keeping with

binding energies recorded by others for various orthophosphate species. Further heating of the system to 1073 K (spectrum b) caused a shift in the binding energy to 134.5 eV and the formation of a new component the binding energy of which was recorded as 136.9 eV. The binding energy of 134.5 eV is closer to the binding energy previously measured for the pure aluminium orthophosphate. The high binding energy species may be some form of phosphoric acid, for which a typical binding energy is 135.2 eV²⁸. This high energy component comprises of approximately 5 % of the phosphorus 2p signal. The presence of phosphoric acid on the surface could explain the lower than predicted aluminium concentration.

The aluminium 2p region (Figure 4.34) was observed to comprise of one component in both sets of spectra, with a binding energy of 74.8 eV which remained constant during heating. The silicon 2p transition was also visible in this region and was observed to have a fairly constant binding energy of 103.7 eV, typical of silica^{28, 42-44}. The area of the silicon 2p peak was observed to decrease relative to the aluminium 2p transition.

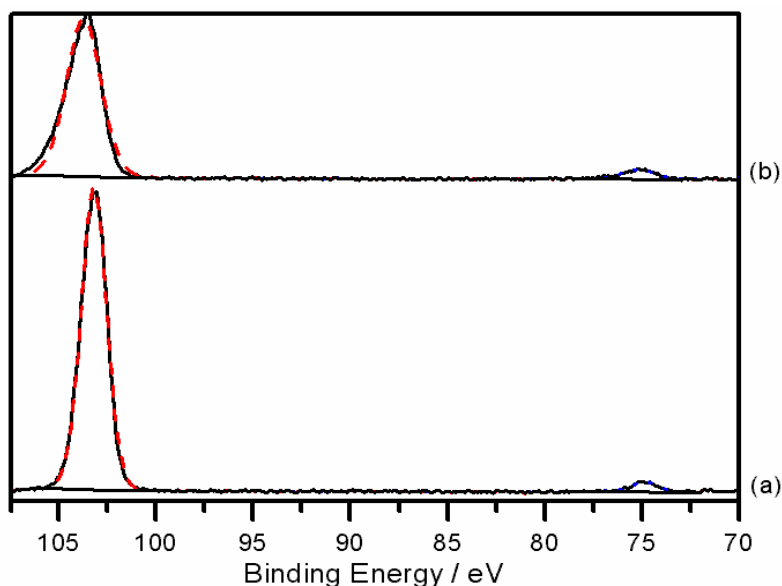


Figure 4.34 the aluminium 2p region of the XP spectra of Mix 4 industrial coating after (a) drying at 373 K and (b) curing at 1073 K.

4.4.2.2 ALUMINIUM PHOSPHATE AND CHROMIUM OXIDE MIXED COATINGS

As with the mix 4 samples the XPS wide scan showed that the surface of the Mix 2 coatings consisted only of the expected elements, which in this case were aluminium, oxygen, carbon, phosphorus, silicon and chromium. As with the mix 4 sample sodium for the colloidal silica solution was observed in the wide scan of the sample heated to 1073 K.

Inspection of the oxygen 1s region of the XP spectrum of the dried sample (Figure 4.35a) showed that it consists of three components at 530.8, 532.2 and 533.3 eV. The two higher binding energy components are similar in energy to those observed in the mix 4 spectrum (Figure 4.33a) and therefore can be assigned to oxygen in silicon and aluminium orthophosphate respectively. The component at 530.8 eV can be assigned to the chromium oxide present in the coating, and is at the same binding energy as observed in the model coating contain chromium (Figure 4.32a). The ratio of the areas of these components implies the surface is approximately 90 % silica, 3 % aluminium phosphate and 7 % chromium. This is in fairly good agreement with the relative concentrations of the silicon, aluminium and chromium atoms which gives a surface of 93 % silica, 3% aluminium phosphate and 4 % chromium oxide.

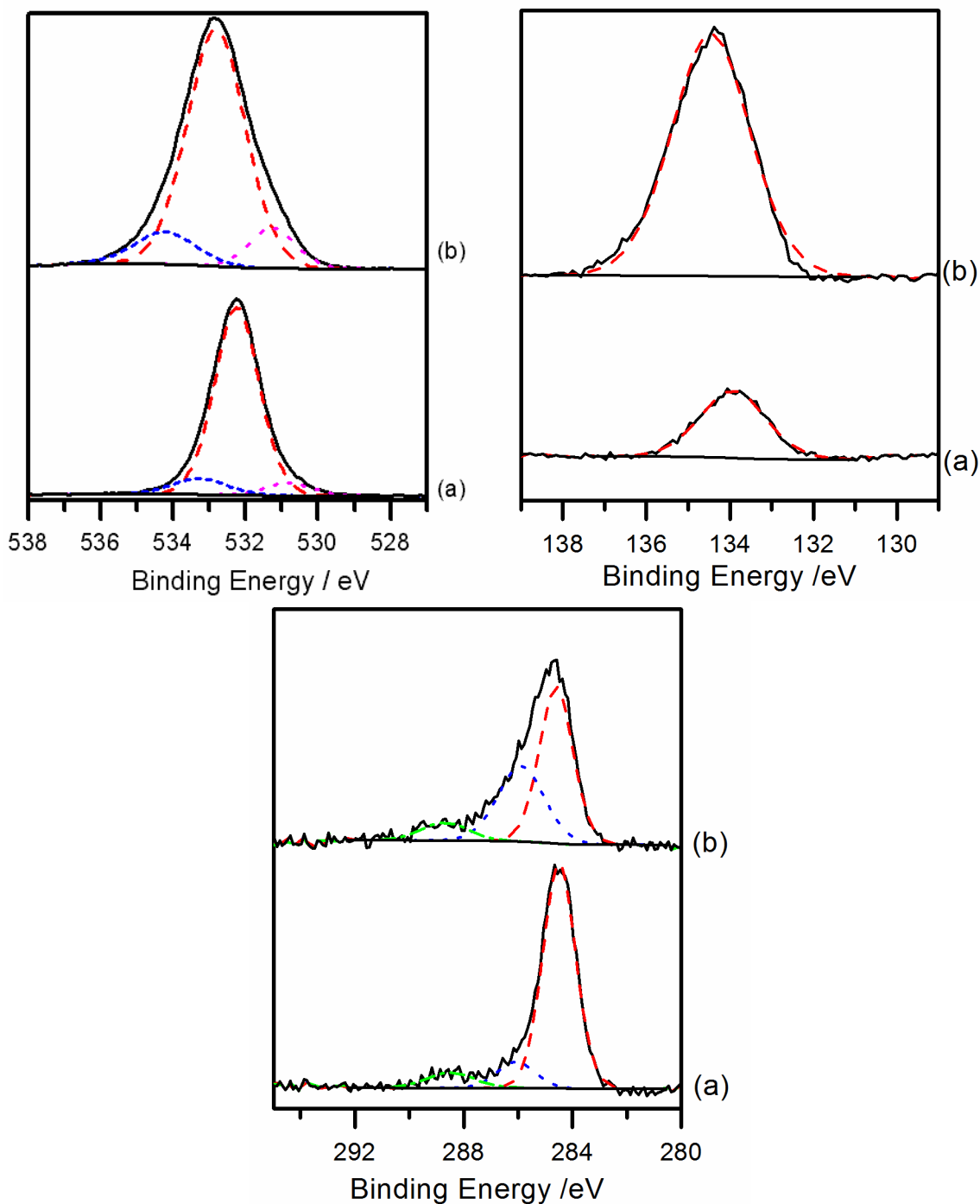


Figure 4.35 the oxygen 1s, phosphorus 2p regions and carbon 1s of the XP spectra of Mix 4 industrial coating after (a) drying at 373 K and (b) curing at 1073 K.

Heating the sample to 1073 K (Figure 4.35b) caused all three components within the oxygen 1s spectrum to shift to 0.5-1 eV higher binding energy. The largest shift was observed in the highest energy component associated with the aluminium orthophosphate. This may be associated with a change in the phosphate chain; however no new component was observed

related to BO atoms. The areas of the three components implies the surface is 86 % silica, 6 % aluminium orthophosphate and 8 % chromium oxide. These values are in fairly good agreement with the relative concentrations of the silicon, aluminium and chromium atoms, which imply that the surface is 86 % silica, 9 % aluminium orthophosphate and 4 % chromium oxide (assumed to be Chromium (III) oxide (Cr_2O_3)). Both sets of concentrations show that curing decreases the amount of silica present on the surface of the powdered coating, as observed in the mix 4 samples. The chromium 2p region of the spectrum of the dried Mix 2 coating was found to consist of two sets of 2p 3/2 and 1/2 transitions imply the system is a mixture of Cr^{3+} and Cr^{6+} ions. This was observed in the model coating containing chromium oxide (see Figure 4.31a) and is thought to be caused by the photo-reduction of hexavalent chromium during XPS experiments, as discussed previously. Heating the system to 1073 K saw the spectrum change to one set of peaks associated with the chromium (III) species.

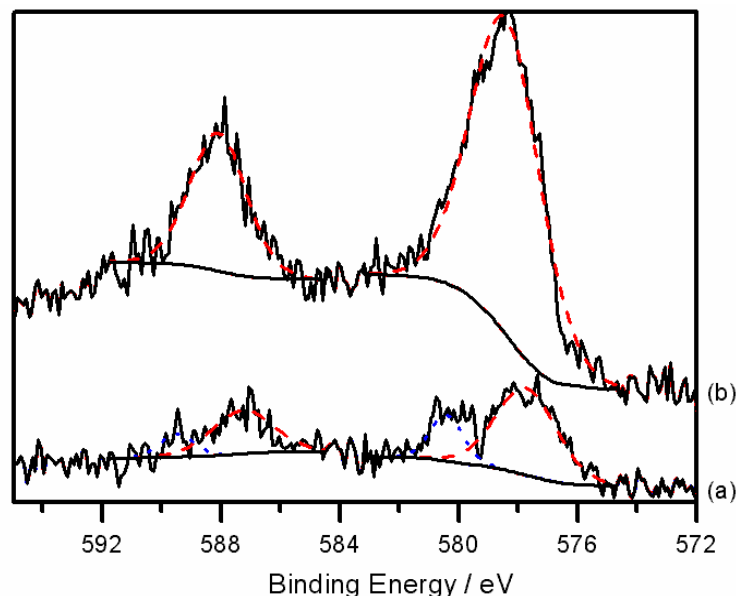


Figure 4.36 the chromium 2p region of the XP spectra of Mix 2 industrial coating after (a) drying at 373 K and (b) curing at 1073 K.

The aluminium 2p spectrum (Figure 4.37) was very similar to the spectrum for the chromium free industrial coating (Figure 4.34). It comprised of one component in both sets of spectra, with an initial binding energy of 74.3 eV, however unlike the chromium free coating the binding energy increased upon heating to 75.3 eV. Again the silicon 2p transition was also visible in this region and was observed to have a fairly constant binding energy of 102.9 eV; however this binding energy is much more difficult to assign as it lies almost directly between silica (103.7

eV⁴²⁻⁴⁴) and silicon carbide (101.8 eV^{48,49}). As with the previous sample the area of the silicon 2p peak was observed to decrease relative to the aluminium 2p transition upon heating.

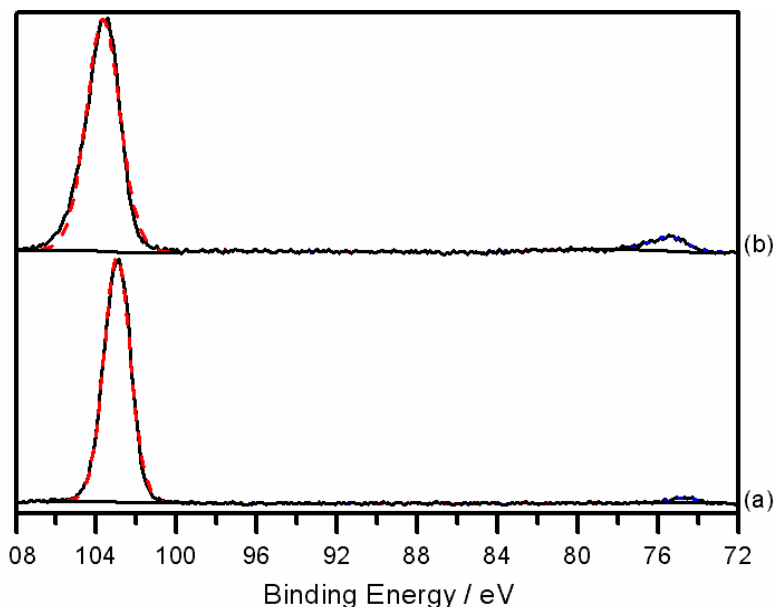


Figure 4.37 the aluminium 2p region of the XP spectra of Mix 2 industrial coating after (a) drying at 373 K and (b) curing at 1073 K.

4.5 XPS CHARACTERISATION OF COATED STEELS

Following from the work on the powdered phosphate coatings the final step of analysis is of the coatings when on sheet steel samples. In order to build a thorough understanding of the behaviour of coatings when applied to steel both the bare steel and the first Forsterite based coating have been studied using XPS, in addition to the fully coated sample. The Forsterite coating is important as it will affect the behaviour of the phosphate coating as it is applied directly to it.

All preliminary studies were done in the Kratos Axis DLD Ultra on samples 1 cm x 1cm square cut from standard Epstein strips and used as received with no further treatment. The more in depth heating studies were performed on similar samples in the UHV chamber described in chapter 2; however samples for the heating studies were placed in methanol in an ultra-sonic bath for 20 minutes and dried under helium before insertion into the UHV chamber in order to remove any grease or other contaminants present on the surface. The samples were also sputtered briefly with Ar⁺ before heating work began in order to remove further contaminants.

4.5.1 PRELIMINARY STUDIES

The relative concentrations of the elements observed on the surface of the steel samples are given in Table 4.9. Sample a (the bare steel sample) consisted of the expected iron, silicon, oxygen and carbon but that there were also small amounts of aluminium and sulphur present at the surface. The aluminium is likely to arise from the aluminium nitride added to the steel to inhibit the growth of grains not on the Goss orientation. As the steel was collected after the decarburisation anneal it is likely that the sulphur has segregated from the bulk of the steel. The concentration of silicon relative to the iron was much higher than expected as the sample is 3 % silicon steel.

The Forsterite coated sample (sample b) was found to have tin and calcium contaminants present on the surface of the sample. It has been noted that the magnesia slurry precursor to the Forsterite coating is not produced using deionised water, so this is the likely source of the calcium.

Sample c was observed to have an unexpectedly high concentration of phosphorus on the surface when compared to sample b. This implies that the pickling process used at Cogent Power Ltd to remove the phosphate coating was not completely effective, leaving some of the top coating behind. The concentration of silicon and magnesium are much higher in sample c than in sample b. When sample b was produced excess magnesium oxide was removed using a wire brush, which may have damaged the Forsterite coating, reducing the relative concentration of these atoms. This is also supported by sample b having a much higher concentration of iron than sample c. The Forsterite coating is known to be several microns thick, meaning that the XPS is detecting iron in the Forsterite coating, not from the steel underneath.

The chemical formulation of Forsterite is Mg_2SiO_4 and therefore a 1:2 ratio of silicon to magnesium atoms is expected in samples b and c. The ratios observed (1: 1.3 and 1:2.4) are fairly close to this, however sample c was observed to have a significantly higher concentration of magnesium than expected.

The fully coated sample was found to have a small amount of sodium present at the surface; it is unclear where this contaminant came from. The concentrations of oxygen, silicon, aluminium and phosphorus were found to be in a similar ratio to those in the powdered coating (see Table 4.8). The concentration of silicon was significantly higher than predicted from the coating

Chapter 4 XPS Studies of Phosphate Coatings

formulation and there was some discrepancy between the concentrations of aluminium and phosphorus.

Sample		Surface Concentration / Atomic %										Notes
		Fe	O	C	Si	Al	P	Mg	S	Sn	Na	
(a) Bare Steel	A	3.3	32.2	55.9	2.3	5.8	0	0	0.6	0	0	
	P*	39.0	59.8	-	1.2	-	-	-	-	-	-	
(b) Forsterite Coated	A	7.8	43.2	43.1	1.4	0	0.5	2.2	0	1.9	0	Ca observed in wide scan
	P	-	57.1	-	14.3	-	-	28.6	-	-	-	
(c) Fully Coated then pickled	A	0.7	38.5	40.8	4.8	0	3.3	11.9	0	0	0	
	P	-	57.1	-	14.3	-	-	28.6	-	-	-	
(d) Fully Coated	A	0	55.0	20.3	19.3	0.9	3.4	0.6	0	0	0.6	
	P	-	66.7	-	13.3	10	10	-	-	-	-	

Table 4.9 The actual (a) and predicted from coating formations (p) relative concentrations of elements on the surface of steel samples as determined from their XPS spectra.

4.5.1.1 BARE STEEL

Figure 4.38a shows the silicon 2p region of the XP spectrum of the bare steel sample. The binding energies of the iron 3s and 3p transitions are also in this region, however more in depth analysis will be performed on the 2p peaks as this is the strongest transition for iron. The silicon 2p transition could only be resolved into one component with a binding energy of 101.6 eV, which is typical of silicon carbide, The aluminium 2p transition was also visible in this region, and the binding energy was recorded as 74.7 eV, which is similar in binding energies reported for oxygen containing aluminium compounds such as alumina by others.^{28, 29} As discussed previously this aluminium is most likely to arise from the aluminium nitride used to inhibit grain growth within the steel.

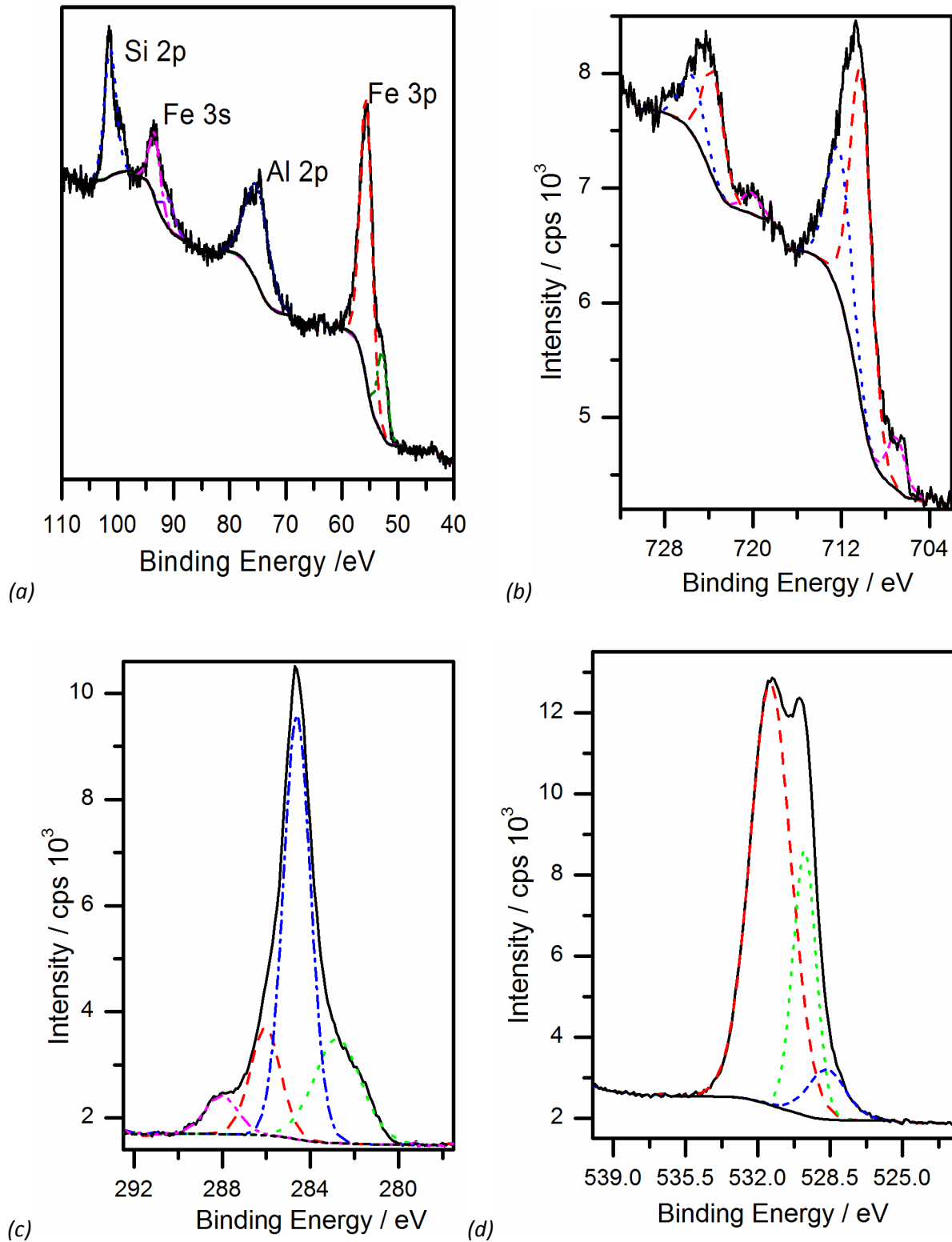


Figure 4.38 (a) silicon 2p (b) iron 2p (c) carbon 1s and (d) oxygen 1s regions of the XP spectrum of bare steel obtained from Cogent Power Ltd.

Inspection of the iron 2p region (Figure 4.38b) indicates that the 3/2 and 1/2 transitions were at 710.5 and 723.9 eV respectively. The transitions were both very broad and consisted of three components, with 3/2 binding energies of 707.0, 710.3 and 712.4 eV. The component at 707.0 eV can be assigned to metallic iron^{28, 36, 37, 56} and the other two components to the cations Fe²⁺ and Fe³⁺. There are two cationic components are present in the spectrum it is safe to assign the component at 710.3 eV to the Fe²⁺ and 712.4 eV to Fe³⁺.

The presence of both cations at the surface should indicate that the oxide formed is Fe₃O₄, however if this is the case the ratio of the 2+:3+ areas should be close to 1:2. Instead the ratio of the components is 2:1, indicating that an excess of 2+ ions are present on the surface. The most likely explanation for this is the formation of either another iron oxide (such as FeO) or iron carbide (Fe₃C). Comparing the areas of the three components in the 3/2 spectrum indicates that around 90 % of the iron at the surface of the sample is oxidised.

The carbon 1s spectrum was observed to consist of four components at 282.8, 284.6, 286.0 and 288.1 eV, indicating that a range of carbon species were present on the surface of the steel. The binding energy of the main component of the spectrum was fixed to 284.6 eV as part of the XPS calibration process. The component at 282.8 eV is likely to arise from some form of carbide, most likely iron, in good agreement with the above interpretation of the iron 2p spectrum. The higher energy components are likely to arise from functional groups such as surface carbonyls, and such contamination of the surface after air exposure is usual for most samples.

Inspection of the oxygen 1s region showed that it consists of three components at 528.5, 529.7 and 531.4 eV. These can be assigned to silica (SiO₂) and the iron oxides Fe₃O₄⁶³ and Fe₂O₃³⁹ respectively. It is clear that the iron oxides are much more abundant than silica based on the areas of the components (only 7.5 % of the oxygen signal arises from the silica component), in good agreement with the conclusions taken from the element concentrations summarized in Table 4.9.

4.5.1.2 FORSTERITE COATED STEEL

Two Forsterite samples have been prepared- one which was removed from the end of the High Coil temperature anneal line and had excess magnesium oxide removed by brushing with a wire brush and another which was taken from the end of the M2 coating line. This sample was coated with the final phosphate coating which had been annealed and was removed by pickling in

sodium hydroxide. It is hoped that by comparing these samples the effects of the phosphate coating on the Forsterite layer underneath can be probed.

Figure 4.39a shows the silicon 2p region of the XP spectrum of the Forsterite coated samples. The region also contains peaks related to magnesium, aluminium and iron photoelectrons. From this spectrum alone there are clear differences between the brushed (i) and pickled (ii) samples. As discussed previously the presence of iron on the surface of the sheet in the brushed sample (the 3s and 3p transitions are visible in this region of the spectrum) indicate that brushing damages the thick coating. The concentration of silicon is much higher in the pickled sample than in the brushed sample; however this is likely to be from the phosphate coating not being completely removed as aluminium is also present. The binding energy of the silicon 2p signal is 104.7 eV in the brushed sample and 105.6 eV in the pickled sample, indicating that the silicon present at the surface is most likely to be silica; however the binding energy is much higher than values recorded both by others and early in this study.

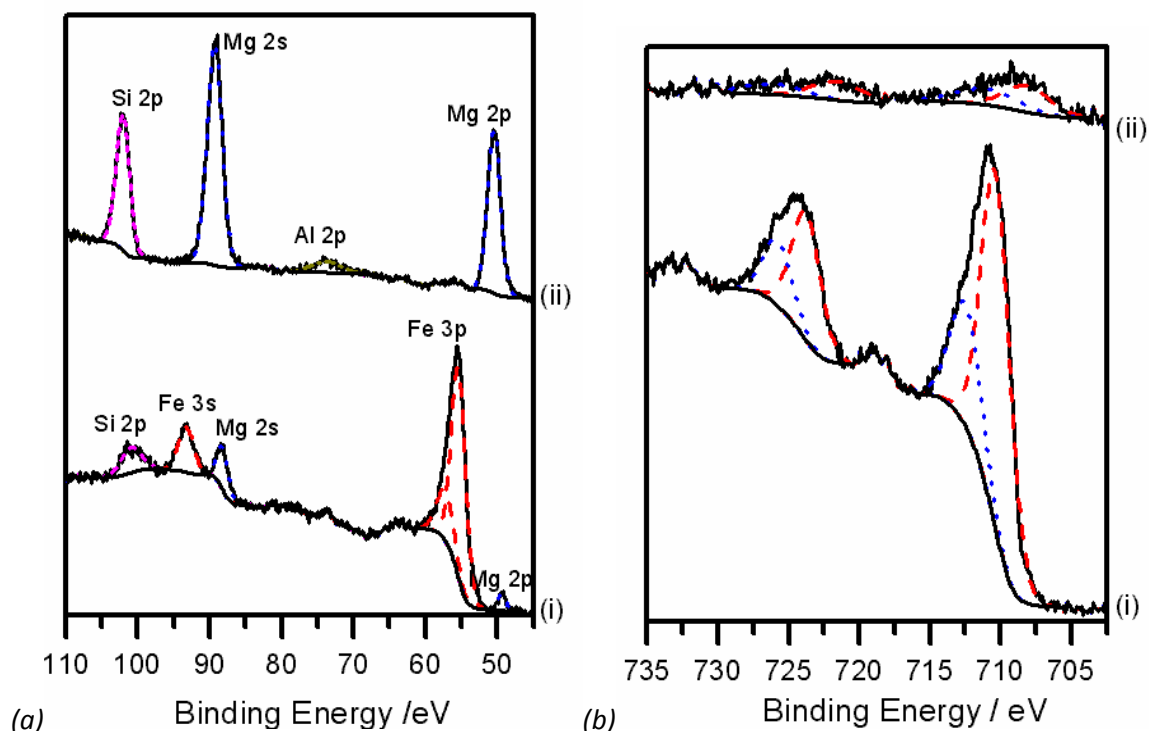


Figure 4.39 The (a) silicon 2p and (b) iron 2p regions of the XP spectrum of (i) brushed Forsterite coated and (ii) pickled forsterite coated steel samples obtained from Cogent Power Ltd.

Inspection of the iron 2p region in the brushed forsterite sample (Figure 4.39bi) shows that two components are present in the 3/2 transition with binding energies of 710.3 and 712.5 eV.

These are similar to the binding energies of the iron oxide components in the bare steel sample and have the same assignments of Fe^{2+} and Fe^{3+} respectively. The iron metal peak observed at 707.0 eV in the previous sample is not observed in this spectrum. The iron signal is greatly reduced in the spectrum from the pickled sample (spectrum ii) indicating that the coating is much thicker and more continuous than the damaged brushed coating.

The unexpected phosphorus observed in the XP spectrum (Figure 4.40a) is likely to arise from the phosphorus coating in the pickled sample; however the most likely source of phosphorus in the brushed sample is cross-contamination, most likely in the lab at Cogent Power Ltd. The position of the peak in both spectra (133.4 eV in the brushed spectrum and 133.9 eV in the pickled one) is consistent with those previously recorded for phosphate coatings.

The carbon 1s spectrum of the brushed sample spectrum (Figure 4.40bi) was very similar to the carbon 1s spectrum of the bare steel sample (Figure 4.38c), as it consisted of 4 components at 282.7, 284.7, 286.0 and 288.3 eV. These components have the same assignments as the components in the previous spectrum, i.e. carbide, adventitious carbon, and functional groups. The component arising from the carbide was missing from the spectrum taken from the pickled sample; however the three other components were present and at very similar binding energies to those recorded in the previous samples (284.6, 285.6 and 287.8 eV) and therefore will have the same assignments.

The oxygen 1s regions of both samples were observed to consist of two components (Figure 4.40c). Within the spectrum from the brushed sample (spectrum i) the two components have binding energies of 529.7 and 531.1 eV and can be assigned to Forsterite and iron oxide respectively. The areas of the components are approximately 2:3, which is in good agreement with the ratio between the iron and magnesium/silicon atoms taken from Table 4.9. The binding energies of the components in the pickled sample (spectrum ii) had shifted to the higher binding energies of 531.2 and 532.2 eV. These components can be assigned to Forsterite and silica from the phosphate coating which had not been completely removed. The ratio between the areas of these components is 2:1, indicating that most of the phosphate coating had successfully been removed and the surface was mainly Forsterite.

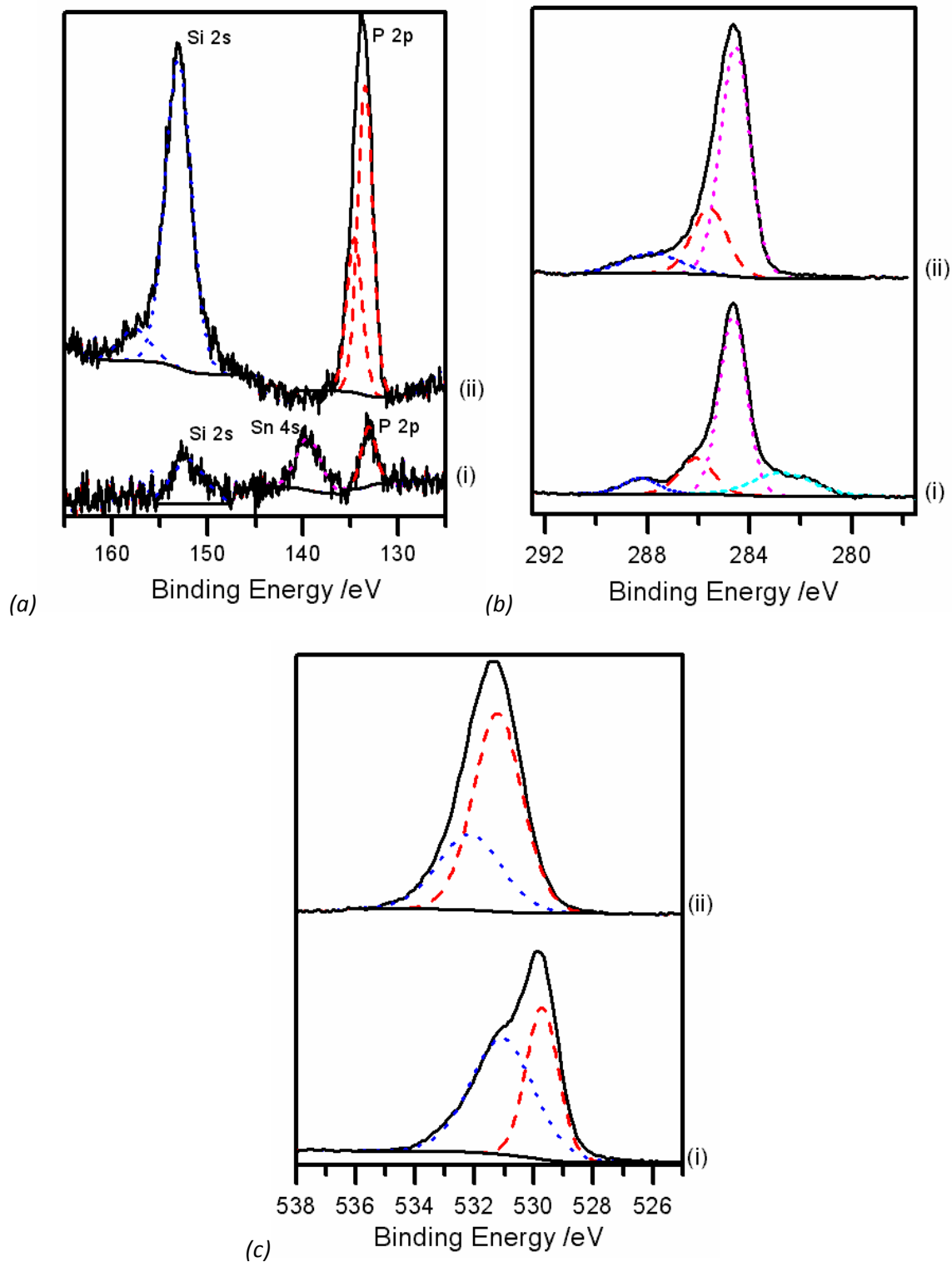


Figure 4.40 The (a) phosphorus 2p (b) carbon 1s and (c) oxygen 1s regions of the XP spectrum of (i) brushed Forsterite coated and (ii) pickled Forsterite coated steel samples obtained from Cogent Power Ltd.

4.5.1.3 FULLY COATED STEEL

Inspection of the silicon 2p region of the XP spectrum taken from the fully coated sample (Figure 4.41a) showed that the sample was mainly silicon but small amounts of magnesium, aluminium and sodium were also present. The aluminium arises from the aluminium phosphate which forms part of the coating mixture; however it is at a much lower concentration than expected from the formulation. This was also observed in the XP spectra obtained from powdered coating mixture. The presence of the magnesium may be caused by unreacted magnesia from the bottom coating mixing into the top phosphate coating, or by contamination from the previous forsterite coated samples. The presence of sodium on the sample is unexplained.

The binding energy of the silicon 2p peak was measured as 103.4 eV, which as with the previous samples is consistent with silica. The binding energy of the aluminium 2p peak was measured as 74.9 eV, in good agreement with the measurements made on powdered aluminium phosphate based coatings in this study.

The phosphorus 2p transition (Figure 4.41b) was observed to have a binding energy of 134.2 eV, which as with the aluminium was consistent with the binding energies recorded previously for aluminium phosphate. From these data it is clear that the colloidal silica has no chemical effect on the aluminium phosphate in the coating, either as a powder or when applied to the steel.

Inspection of the carbon 1s region (Figure 4.41c) showed that it consisted of one main component which was assumed to arise from adventitious carbon and therefore its binding energy was fixed to 284.7 eV as part of the calibration process. Additional components were observed at 286.0, 288.5 and 292.8 eV and are thought to arise from functional groups present on the surface. No carbide was observed on the surface of the fully coated sample, due to the absence of iron.

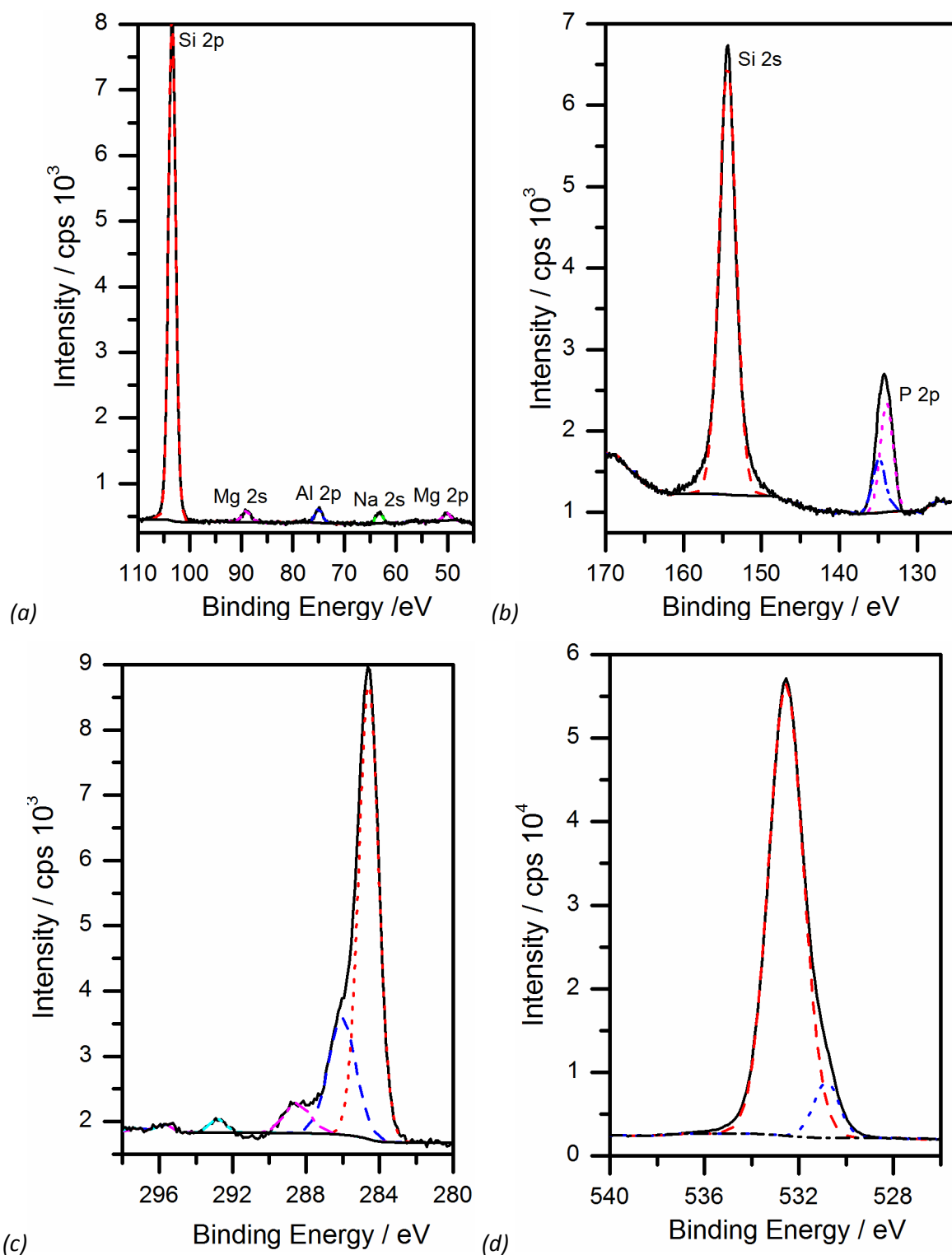


Figure 4.41 The (a) silicon 2p (b) phosphorus 2p (c) carbon 1s and (d) oxygen 1s regions of the XP spectrum of fully coated steel samples obtained from Cogent Power Ltd.

The oxygen 1s region (Figure 4.41d) was observed to consist of two components at 530.8 and 532.5 eV. Based on the relative areas of the components the higher energy component can be assigned to the silica within the coating, as the relative concentrations of aluminium and silicon indicate the silica is much more abundant. This interpretation implies the component at 530.8 eV arises from the aluminium orthophosphate, which although is consistent with literature values for orthophosphate^{1, 28} is much lower than those recorded from aluminium orthophosphate earlier in these studies.

5.5.2 THE EFFECTS OF HEATING

5.5.2.1 BARE STEEL

Before studying the effects of heating on the bare steel surface the sample was sputtered for 90 minutes with argon ions (Ar^+) in an effort to reduce the surface concentration of carbon. After sputtering the carbon concentration was reduced from ~56 % (Table 4.9) to around 23.5 % (assumed to be from the bulk of the samples, see Figure 4.45). Inspection of the carbon 1s region (Figure 4.42b) showed that it consisted of two components, with the lower energy component dominating. Based on the interpretation of the iron 2p spectrum in the preliminary studies, this lower energy component was assumed to arise from iron carbide (Fe_3C) and was calibrated to 282.8 eV based on previous work. It is clear from Figure 4.42b that carbide dominates the carbon 1s signal across the range of temperatures studied.

Inspection of the iron 2p XP spectrum (Figure 4.42a) after this process showed the surface was still heavily oxidised and the metallic iron component at around 707 eV could not be observed in the spectrum. Two sets of components were observed in the spectrum with binding energies of 707.8 and 721.0 eV in one set and 710.8 and 723.9 eV in the other. The binding energies recorded in the spectra are lower than those recorded in the preliminary work, however can still be assigned to Fe^{2+} and Fe^{3+} respectively. The iron spectrum is dominated by the components arising from the 2+ oxidation state at all temperatures, however heating the sample was shown to cause a steady decrease in the average oxidation state of the iron (as shown in Figure 4.43, where the percentage of iron $^{2+}$ atoms is shown to increase with temperature). The initial ratio of 2+:3+ irons is 2.5:1, indicating that whilst some iron oxide is present on the surface (either as Fe_3O_4 or Fe_2O_3) there is an excess of 2+ ions present, most likely as iron carbide. This assignment is also supported by the binding energy of the 2+ component, which at 707.8 eV is very similar to the literature value of 708.1 eV³⁰.

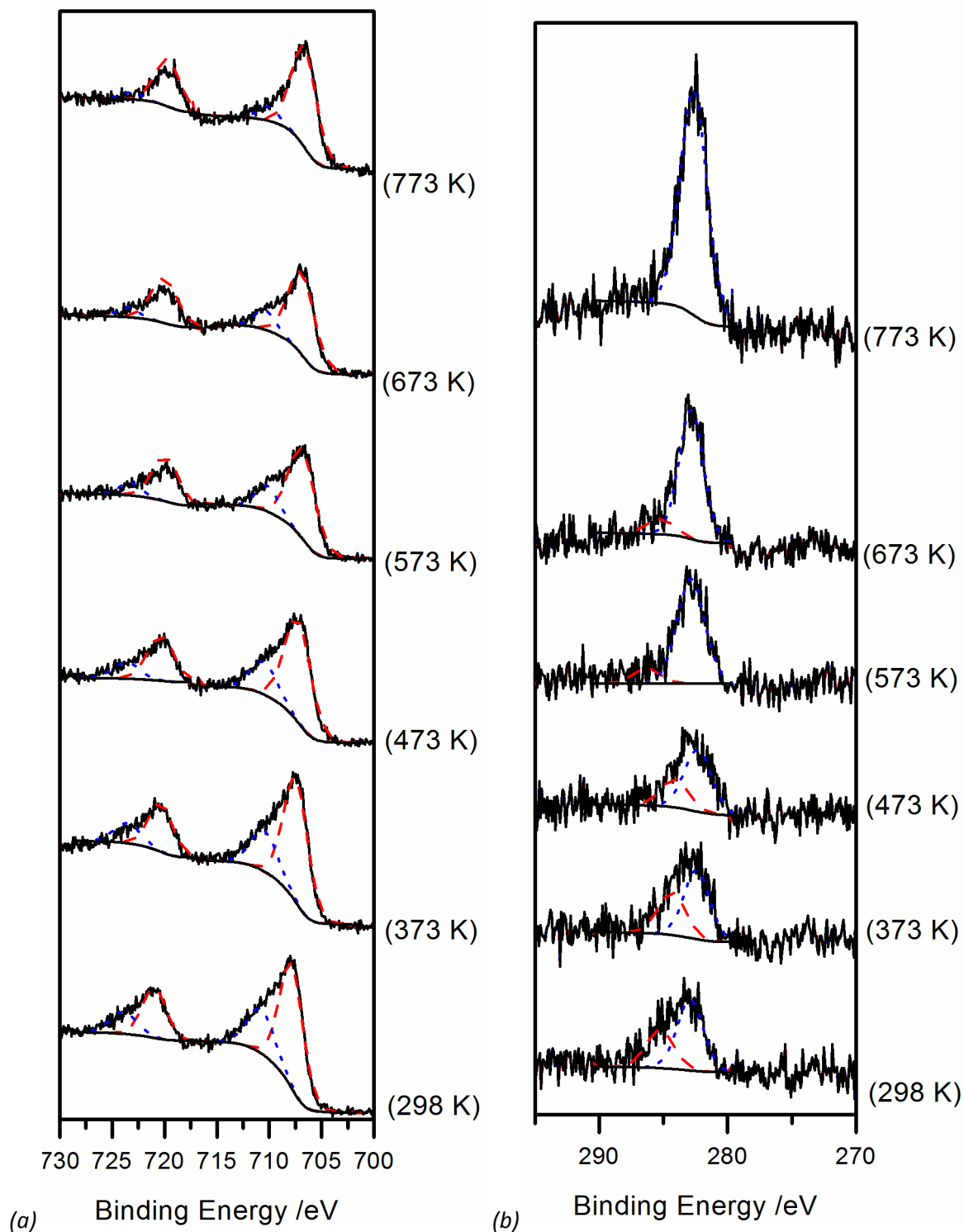


Figure 4.42 The effects of heating on the (a) Fe 2p and (b) C 1s regions of the XP spectrum of bare steel

The decrease in iron oxidation state is accompanied by an increase in the concentration of silicon on the surface (Figure 4.44b). Silicon is first observed on the surface after heating to 673 K and after this point increases steadily until it reaches a maximum concentration of 25 % at 823 K (spectrum not shown). The segregation of silicon in iron silicon single crystals has been well studied,⁶⁴⁻⁶⁶ and is known to be affected by the presence of carbon on the surface. An increase in Fe²⁺ concentration as silicon segregates would appear to indicate that carbon concentration also increases (due to the increase in carbide) concentration, in disagreement with results observed on single crystals by others, however their studies involved carbon atoms desorbed from the bulk, rather than carbide as present here which may behave differently.

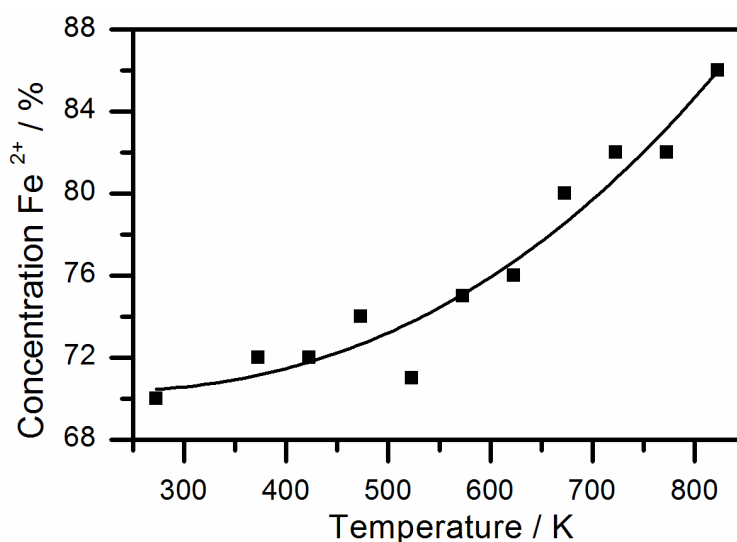


Figure 4.43 The effects of heating on the percentage of iron present as Fe²⁺ at the surface of bare steel. The remainder of the iron was in the 3⁺ oxidation state.

Inspection of the oxygen 1s region of the XP spectrum (Figure 4.44) showed that the spectrum could only be resolved into two components after sputtering as opposed to the three observed in the as received sample (Figure 4.38d). This is assumed to be due to the use of lower resolution instrumentation for this section of work. The two components had binding energies of 530.5 and 532.5 eV. The lower energy component is similar in energy to that recorded for the iron oxides in the preliminary studies; however the higher energy component does not have a clear match from the preliminary work. The lower energy component accounts for 68 % of the oxygen 1s signal. The concentration of the lower energy component remains fairly consistent until the sample reaches 723 K, at which point it drops to 35 % of the signal. The surface

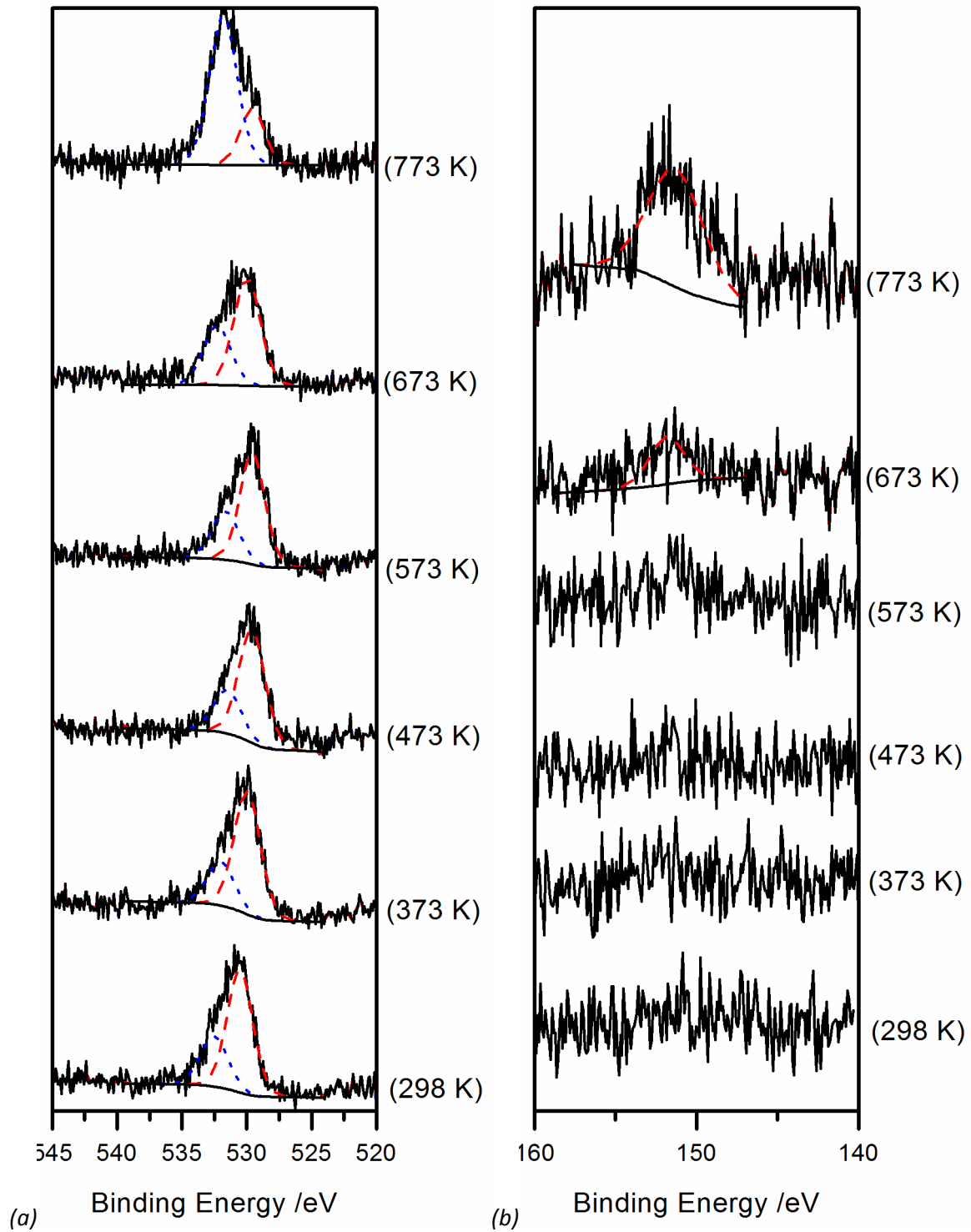


Figure 4.44 The effects of heating on (a) the O 1s and (b) Si 2s regions of the XP spectrum of bare steel

segregation of silicon was first observed at 673 K, so it is therefore likely that the higher energy component arises from the silica.

Figure 4.45 shows the changes in the surface composition as the sample is heated under vacuum. Initially iron is the most abundant element on the surface making up nearly 45 % of the surface. The concentration of iron atoms steadily reduces as the sample is heated until it reaches a minimum of 25 % at 773 K. Silicon is first observed at the surface at 673 K, and the concentration is observed to increase rapidly with further heating.

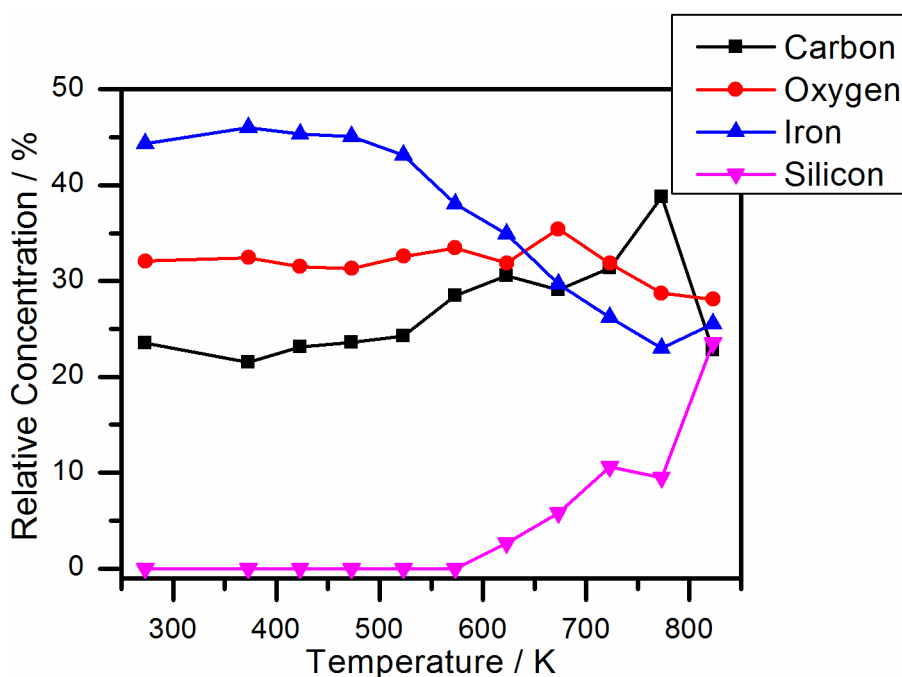


Figure 4.45 The effect of heating on the relative surface concentrations of elements on bare steel

5.5.2.2 FORSTERITE COATED STEEL

5.5.2.2.1 BRUSHED FORSTERITE SAMPLE

XPS analysis of the brushed sample was performed after the sample had been sonicated in methanol, however no sputtering was performed before heating work began. Inspection of the iron 2p region (Figure 4.46a) showed that iron was present on the surface, as observed in the preliminary work; however due to the weak signal only one component could be fitted within the 2p 3/2 spectrum. The binding energy of this component was measured as 711.0 eV indicating that the iron on the surface is oxidised. As the sample was heated the iron signal became strong and two components could be fitted to the 2p 3/2 spectrum after heating to 473

K. These components had binding energies of 709.9 and 713.1 eV, which is in good agreement to the binding energies recorded in the bare steel sample. Further heating caused continued increase in the iron 2p signal until the 2p $\frac{1}{2}$ spectrum could also be peak fitted (673 K). During heating the binding energies of the 3/2 components remained fairly consistent, as did the ratio of the areas of the two components (with the Fe 2⁺ signal comprising 65-75 % of the total signal).

Inspection of the silicon 2p region (Figure 4.46b) showed a small peak was visible with a binding energy of 100.9 eV, which is more consistent with silicon⁶⁷ or silicon carbide^{48, 49} than silica. Heating the system caused a reduction in the silicon signal and a shift in binding energy when heated to 573 K. The new binding energy was recorded as 101.8 eV, which is still more readily associated with silicon carbide than silica. Heating beyond 573 K saw a further reduction in the silicon signal until it was no longer recorded.

Inspection of the oxygen 1s region (Figure 4.47) showed that two components were present in the spectrum. These components had binding energies of 529.4 eV and 532.3 eV and can be assigned to iron oxide and silica respectively. The signal arising from iron oxide accounts for 21 % of the oxygen signal and steadily increased as the sample was heated (see Figure 4.48) until it dominates the oxygen spectrum.

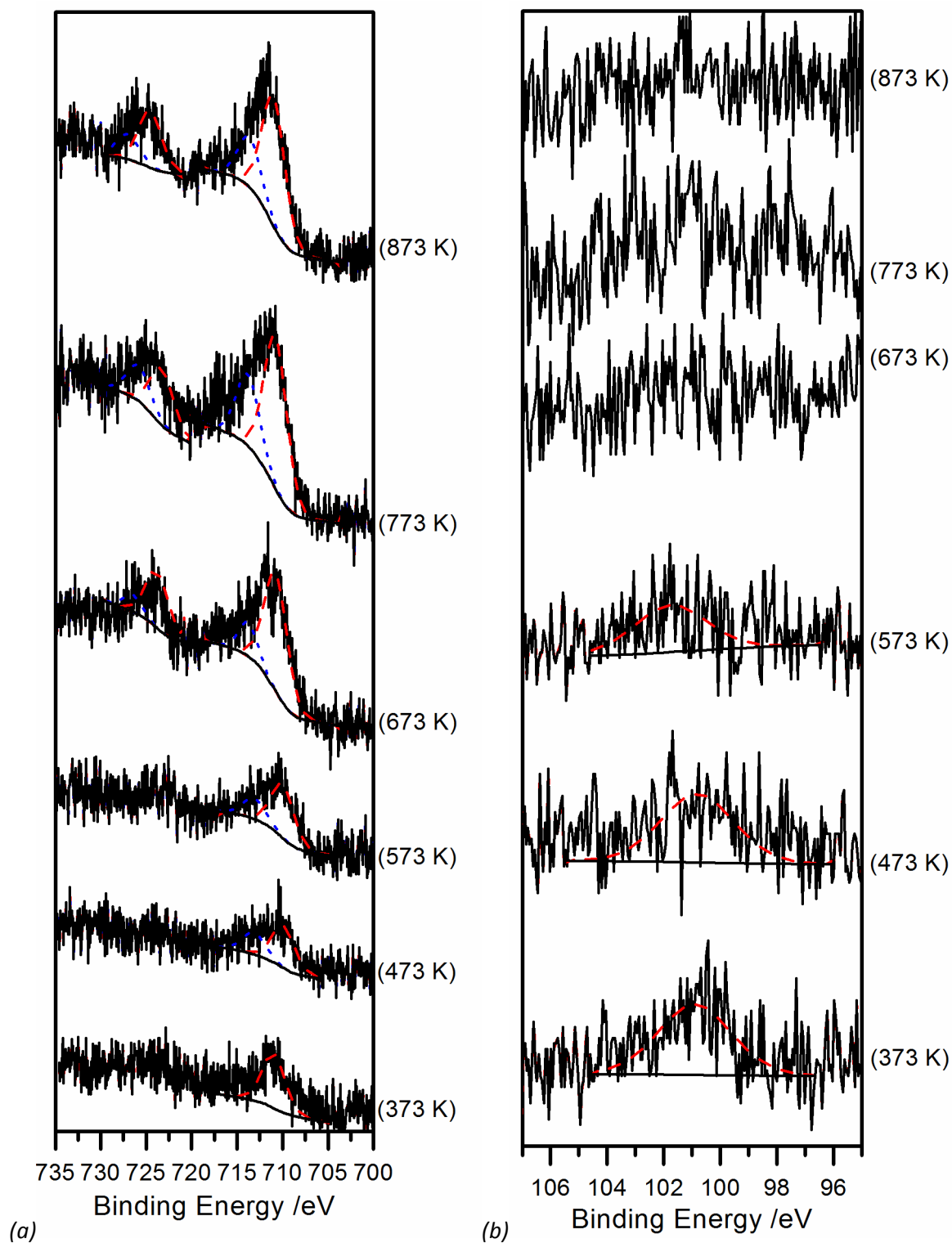


Figure 4.46 The effects of heating on the (a) Fe 2p and (b) Si 2p regions of the XP spectrum of brushed Forsterite coated steel

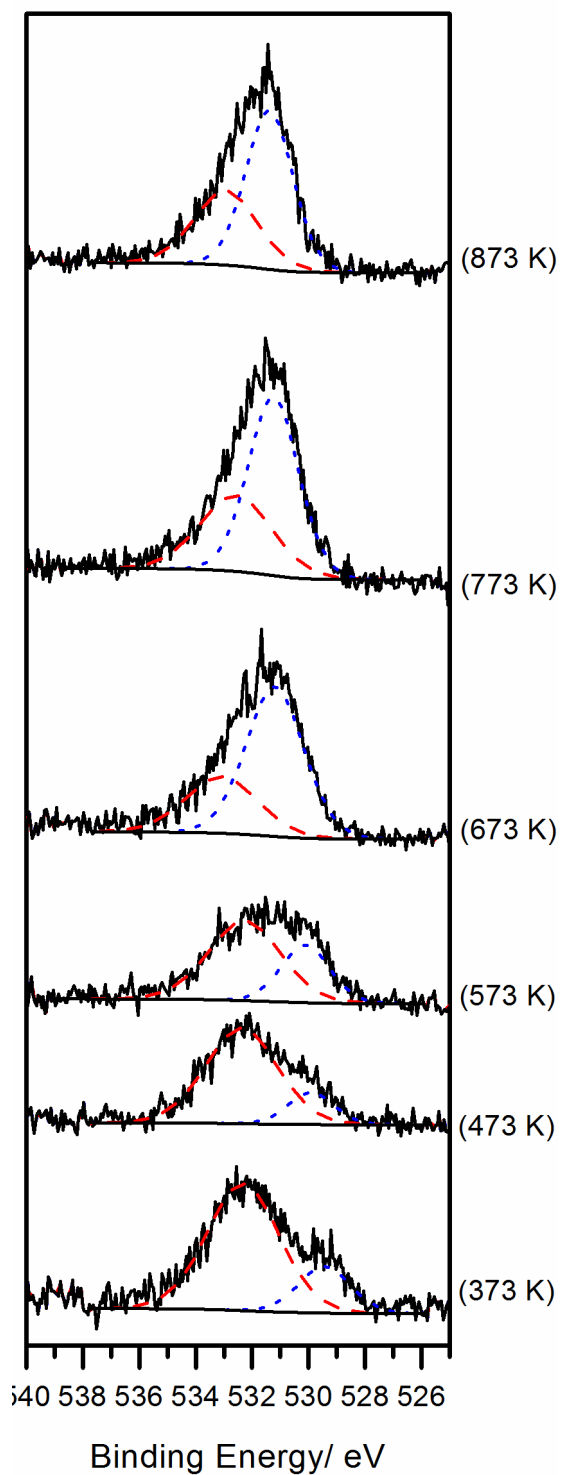


Figure 4.47 The effects of heating on the oxygen 1s region of the XP spectrum of brushed Forsterite coated steel

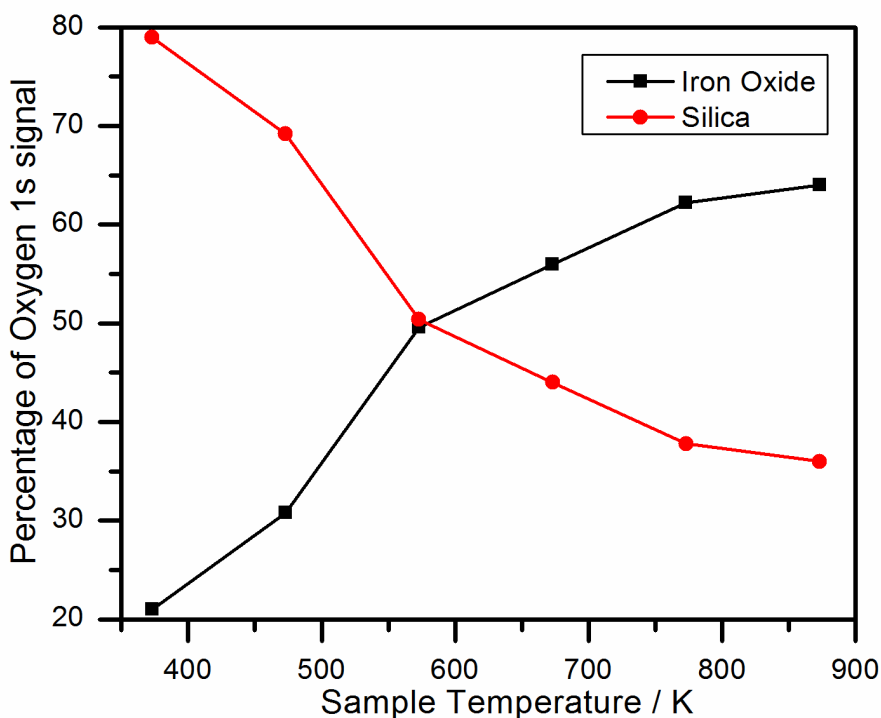


Figure 4.48 The change in intensity of the components of the oxygen 1s signal in the XP spectra of Forsterite coated steel when heated.

The overall changes in surface composition as the sample was heated are shown in Figure 4.49. It is clear from the figure that the surface was dominated by carbon and that the work should have been repeated after sputtering the surface, however there was no time available for this to be done. The concentration of carbon on the surface decreased significantly when the sample was heated to 673 K. This was accompanied by a large increase in the concentration of oxygen on the surface and iron oxide becoming the more dominant component of the oxygen 1s spectrum (see Figure 4.47). Iron and silicon both remained at low concentrations throughout the experiments (both below 15 % at all times). The concentration of iron increased significantly at 673 K, coinciding with the changes just discussed.

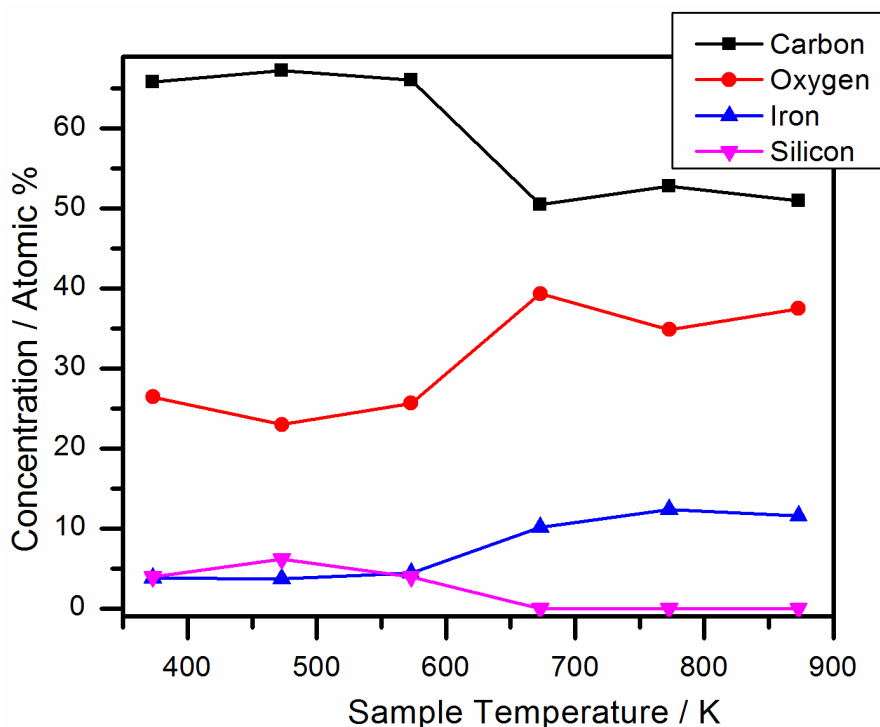


Figure 4.49 The effect of heating on the relative surface concentrations of elements on brushed Forsterite coated steel

5.5.2.2.2 PICKLED FORSTERITE SAMPLE

The results obtained from the brushed sample indicated that the surface was dominated by carbon contamination. Due to this the pickled Forsterite sample was lightly sputtered before analysis to remove the contaminants and allow for a better analysis of the surface. The magnesium 2s spectrum is shown in Figure 4.50a. The magnesium 2p and silicon 2s spectra were chosen for interpretation as the magnesium 2s and silicon 2p spectra (the stronger transitions) occur at similar binding energies and overlapped in spectra collected from certain samples. After heating at every temperature the magnesium 2p spectrum consisted of one component with a binding energy of 49.5 eV, assumed to arise from Forsterite. Inspection of the silicon 2s spectrum (Figure 4.50b) showed that it also consisted of one component which remained consistent at all temperatures. The binding energy of the component was recorded as 152.6 eV. The oxygen 1s spectrum (Figure 4.51a) showed similar behaviour (i.e. one component unchanged by heating) and the binding energy was measured as 532.0 eV.

Inspection of the iron 2p region (Figure 4.51b) showed that a small signal could be seen (mainly as the sharp drop in background associated with the iron 2p peaks), however only one small

component in the $2p\ 3/2$ transition could be resolved (the $1/2$ transition could not be determined from the noise). The binding energy was recorded as 710.9 eV, indicating that the small amount of iron present at the surface was oxidised. The weak iron signal indicates this coating is less damaged than the previous brushed Forsterite sample.

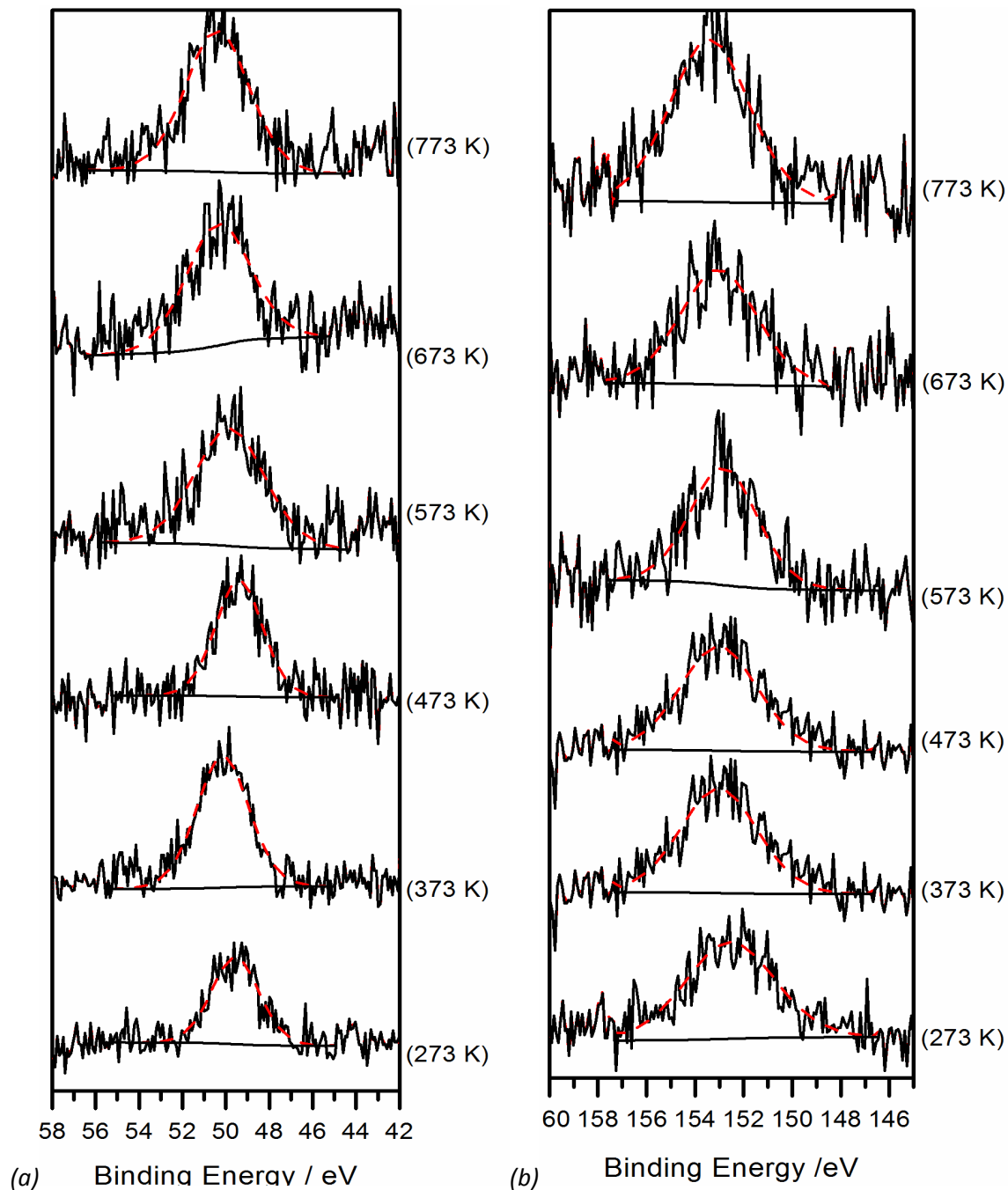


Figure 4.50 The effects of heating on the (a) Mg 2s and (b) Si 2s regions of the XP spectrum of pickled Forsterite coated steel

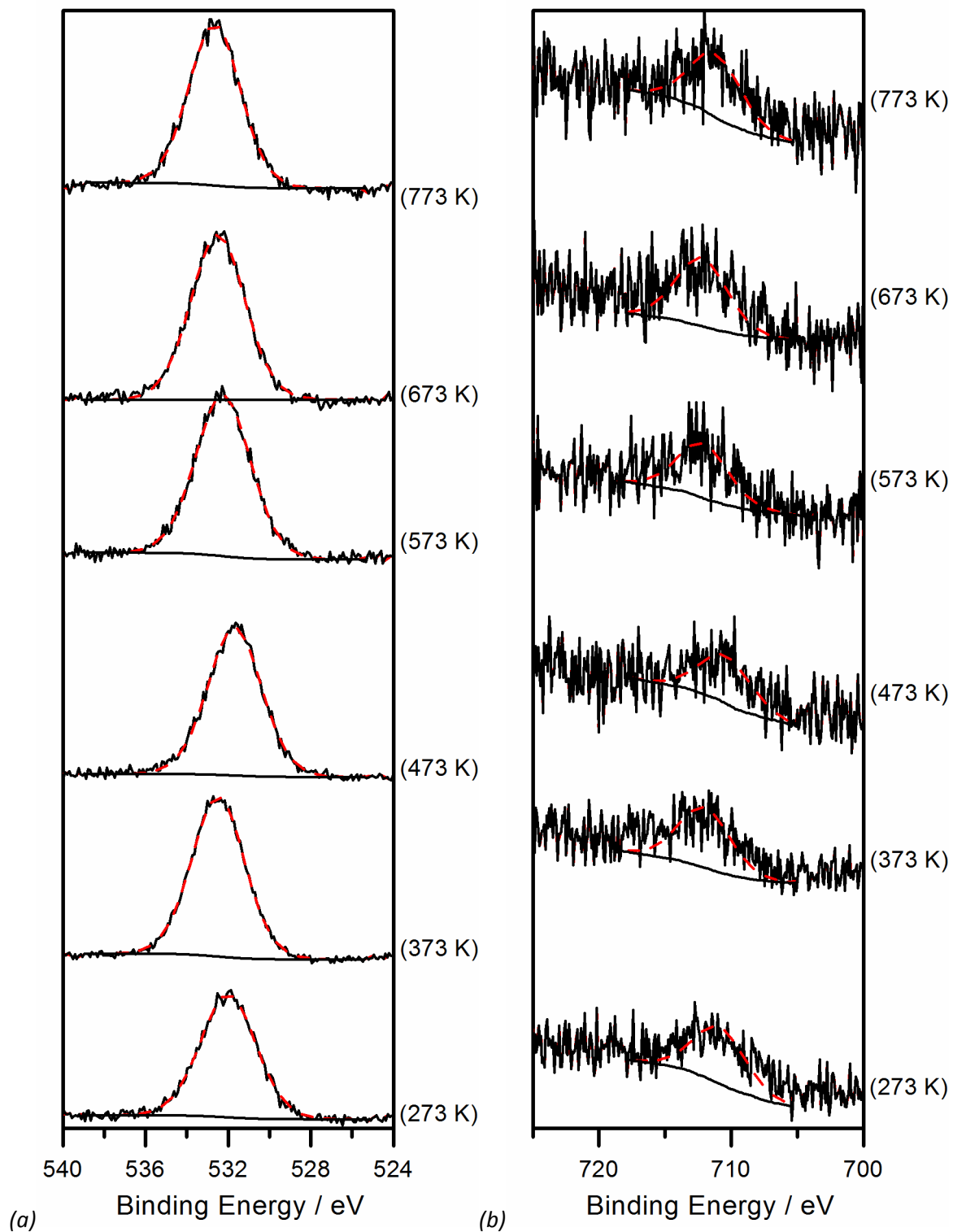


Figure 4.51 The effects of heating on the (a) O 1s and (b) Fe 2p regions of the XP spectrum of brushed Forsterite coated steel

The changes in surface composition when the sample is heated are summarised in Figure 4.52. It is clear from the figure that oxygen is the most abundant element on the surface accounting for up to 78 % of the surface. The concentration of carbon, silicon and magnesium were similar at all temperatures and stayed around 10-15 %. The relative concentration of iron at the surface remained around 5 % at all temperatures. The relative concentration of all elements remained fairly consistent throughout the heating experiments, indicating that the sample was unchanged and the forsterite coating is stable up to 823 K.

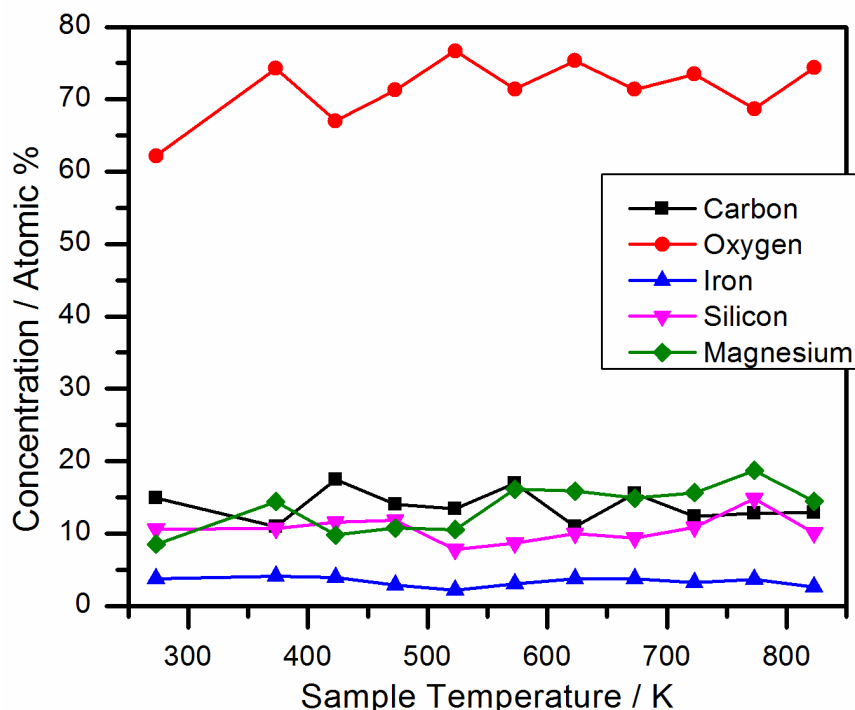


Figure 4.52 The effect of heating on the relative surface concentrations of elements on pickled Forsterite coated steel

5.5.2.3 FULLY COATED STEEL

From Figure 4.53 it is clear that heating has very little effect on the composition of the final coating. This is likely to be because this sample was taken from the line after the sheet has been cured, therefore any reactions in the coating would have already occurred. It is clear from the figure that the surface is dominated by oxygen (typically making up around 70 % of the surface composition). Aluminium was not observed in the wide scan of the sample and therefore scans were not performed in this region.

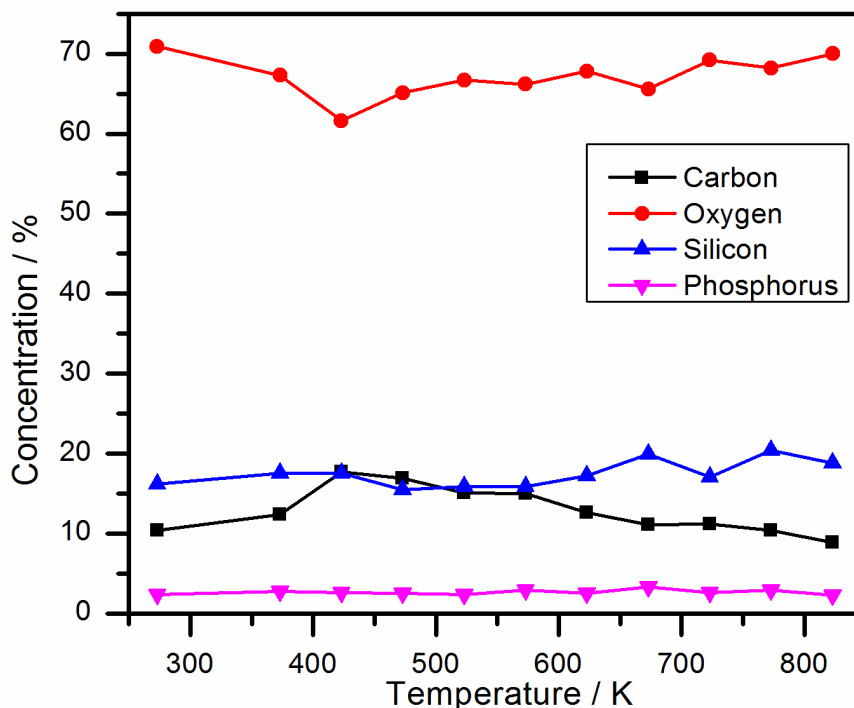


Figure 4.53 The effect of heating on the concentrations of selected elements on the surface of fully coated steel.

Figure 4.54a shows the effects of heating on the oxygen 1s region. After sputtering the region was observed to consist of two components at 528.3 and 533.6 eV compared to the two observed in the preliminary work. The two higher energy components are similar in energy to two observed previously on the fully coated steel and may be assigned to the phosphate and silica respectively. The ratio of the areas of these two components implies the surface is 92 % silica and 8 % phosphate compared to the concentration of silicon and phosphorous atoms which gives 86 % silica and 13% phosphate. The additional component at 522.8 eV is assumed to arise from part of the copper LMM Auger transition due to the copper rods of the sample holder (copper was observed in the wide scans of all samples for this reason).

Inspection of the silicon 2p region of the XP spectrum showed that it consisted of one component at 102.8 eV. This binding energy is difficult to assign as it lies directly between literature values for silicon carbide (101.8 eV^{48,49}) and silica (103.7 eV⁴²⁻⁴⁴). Heating had little effect on the XPS of the silicon, which is a similar observation to the powdered coating. This was expected as the primary role of the silica within the coating is as a bulking agent. The phosphorus 2p signal was also observed in this XPS region scan and was observed to remain

fairly constant at 134.4 eV, which is in good agreement with previous data obtained from model and industrial aluminium orthophosphate coatings.

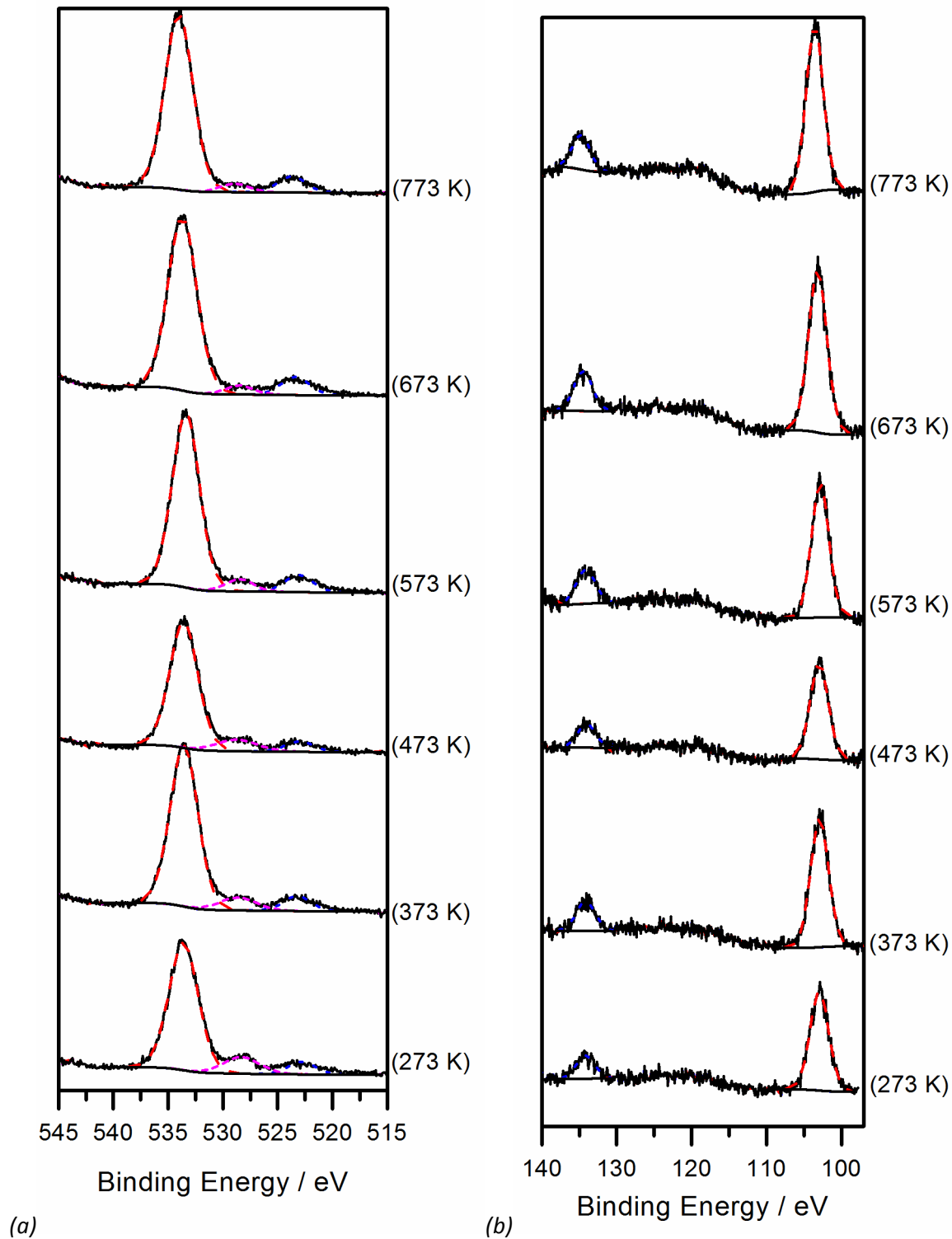


Figure 4.54 The effects of heating under vacuum on the (a) oxygen 1s and (b) silicon 2p regions of the XP spectrum of fully coated steel obtained from cogent power Ltd.

4.6 SUMMARY

This chapter has probed the uses of X-ray photoelectron spectroscopy in the study of phosphate coatings. The results indicate that whilst the oxygen 1s region of the XP spectrum can be used to follow changes in the average chain length it is of little use in model phosphate coatings, however changes from ortho to metaphosphate can be observed by following changes in the binding energies of the oxygen 1s and phosphorus 2p transitions. The XP spectra of the pure samples purchased from sigma Aldrich showed good agreement with bulk analysis techniques such as XRD and MAS-NMR.

XPS indicated that dehydrolytic condensation occurred during curing in all model coatings, however it was much more prevalent in the magnesium phosphates than aluminium ones. During ageing the reverse reaction occurred, causing reformation of the orthophosphates (as observed in the changes in binding energy). The magnesium phosphate chains were found to be much more susceptible to breakage than the aluminium ones.

The XP spectra of the chromium containing samples indicated that hexavalent chromium was fully reduced to the trivalent species upon heating. The presence of chromium oxide appeared to reduce the number of bridging oxygen atoms present on the surface, and this may be the cause of the increased stability in these coatings.

XPS of industrial coatings (both as powders and applied to sheet steel samples) showed a higher than predicted concentration of silica at the surface. The concentration of aluminium was much lower than phosphorus, presenting some evidence for the presence of phosphoric acid at the surface. A brushed forsterite sample was shown to have a large concentration of iron at the surface, indicating that the wire brushes used to clean the sample have also damaged the coating. The pickled forsterite coating was shown to have a high concentration of phosphorus indicating that the upper phosphate coating had not been completely removed before analysis.

Finally the effects of heating the samples on the XP spectra were also studied. Silicon segregation from the bulk to the surface was observed (to be discussed in more detail in the next chapter), whilst the pickled forsterite and fully coated steel samples were observed to be largely unaltered by the heating.

4.7 REFERENCES

1. R. Gresch, W. Mullerwarmuth and H. Dutz, *Journal of Non-Crystalline Solids*, 1979, **34**, 127.
2. R. K. Brow, R. J. Kirkpatrick and G. L. Turner, *J. Am. Ceram. Soc.*, 1990, **73**, 2293.
3. R. K. Brow, D. R. Tallant, J. J. Hudgens, S. W. Martin and A. D. Irwin, *Journal of Non-Crystalline Solids*, 1994, **177**, 221.
4. R. K. Brow, *Journal of Non-Crystalline Solids*, 1996, **194**, 267.
5. R. Bruckner, H. U. Chun, H. Goretzki and M. Sammet, *Journal of Non-Crystalline Solids*, 1980, **42**, 49.
6. M. Crobu, A. Rossi, F. Mangolini and N. Spencer, *Tribology Letters*, 2010, **39**, 121.
7. G. D. Khattak, A. Mekki and L. E. Wenger, *Journal of Non-Crystalline Solids*, 2009, **355**, 2148.
8. J. M. Martin, C. Grossiord, T. Le Mogne, S. Bec and A. Tonck, *Tribology International*, 2001, **34**, 523.
9. E. C. Onyiriuka, *Journal of Non-Crystalline Solids*, 1993, **163**, 268.
10. G. Tricot, D. Coillot, E. Creton and L. Montagne, *Journal of the European Ceramic Society*, 2008, **28**, 1135.
11. F. X. Perrin, M. P. Gigandet, M. Wery and J. Pagetti, *Surface and Coatings Technology*, 1998, **105**, 135.
12. Z. Yong, J. Zhu, C. Qiu and Y. Liu, *Applied Surface Science*, 2008, **255**, 1672.
13. V. Burokas, A. Martushene, A. Ruchinskene, A. Sudavichyus and G. Bikul'chyus, *Protection of Metals*, 2006, **42**, 339.
14. M. Wolpers and J. Angeli, *Applied Surface Science*, 2001, **179**, 281.
15. S. Feliu Jr and V. Barranco, *Electrochimica Acta*, 2004, **49**, 951.
16. R. K. Brow, C. M. Arens, X. Yu and E. Day, *Phys. Chem. Glasses*, 1994, **35**, 132.

17. M. A. Salim, G. D. Khattak, P. S. Fodor and L. E. Wenger, *Journal of Non-Crystalline Solids*, 2001, **289**, 185.
18. A. Mogus-Milankovic, A. Gajovic, A. Santic and D. E. Day, *Journal of Non-Crystalline Solids*, 2001, **289**, 204.
19. L. Koudelka, J. Subcik, P. Mosner, L. Montagne and L. Delevoye, *Journal of Non-Crystalline Solids*, 2007, **353**, 1828.
20. J. J. Videau, A. El Hadrami, C. Labrugere, M. Couzi, L. Montagne, M. Mesnaoui and M. Maazaz, *Physics and Chemistry of Glasses-European Journal of Glass Science and Technology Part B*, 2007, **48**, 363.
21. M. Karabulut, G. K. Marasinghe, C. S. Ray, D. E. Day, O. Ozturk and G. D. Waddill, *Journal of Non-Crystalline Solids*, 1999, **249**, 106.
22. G. D. Khattak, A. Mekki and M. A. Gondal, *Journal of Physics and Chemistry of Solids*, 2013, **74**, 13.
23. A. Mekki, G. D. Khattak, D. Holland, M. Chinkhota and L. E. Wenger, *Journal of Non-Crystalline Solids*, 2003, **318**, 193.
24. H. W. Nesbitt, G. M. Bancroft, G. S. Henderson, R. Ho, K. N. Dalby, Y. Huang and Z. Yan, *Journal of Non-Crystalline Solids*, 2011, **357**, 170.
25. X. Sun, D. Susac, R. Li, K. C. Wong, T. Foster and K. A. R. Mitchell, *Surface and Coatings Technology*, 2002, **155**, 46.
26. S. Maeda and M. Yamamoto, *Progress in Organic Coatings*, 1998, **33**, 83.
27. T. Narayanan, *Reviews on Advanced Materials Science*, 2005, **9**, 130.
28. A. V. Naumkin, A. Kraut-Vass, J. W. Allison, S. W. Gaarenstroom and C. J. Powell, *NIST X-Ray Photoelectron Spectroscopy Database*, <http://srdata.nist.gov/xps/Default.aspx>,
29. V. Di Castro, G. Polzonetti, G. Contini, C. Cozza and B. Paponetti, *Surface and Interface Analysis*, 1990, **16**, 571.
30. I. N. Shabanova and V. A. Trapeznikov, *Journal of Electron Spectroscopy and Related Phenomena*, 1975, **6**, 297.

31. M. C. Biesinger, B. P. Payne, A. P. Grosvenor, L. W. M. Lau, A. R. Gerson and R. S. C. Smart, *Applied Surface Science*, 2011, **257**, 2717.
32. W. Jianjun and X. Qunji, *Wear*, 1994, **176**, 213.
33. S. V. Kagwade, C. R. Clayton and G. P. Halada, *Surface and Interface Analysis*, 2001, **31**, 442.
34. C. Sleight, A. P. Pijpers, A. Jaspers, B. Coussens and R. J. Meier, *Journal of Electron Spectroscopy and Related Phenomena*, 1996, **77**, 41.
35. A. Rahman, M. H. Mohamed, M. Ahmed and A. M. Aitani, *Applied Catalysis A: General*, 1995, **121**, 203.
36. S. L. T. Andersson and R. F. Howe, *The Journal of Physical Chemistry*, 1989, **93**, 4913.
37. A. G. Sault, *Applied Surface Science*, 1994, **74**, 249.
38. T. Fujii, F. M. F. de Groot, G. A. Sawatzky, F. C. Voogt, T. Hibma and K. Okada, *Physical Review B*, 1999, **59**, 3195.
39. V. I. Nefedov, Y. V. Salyn, G. Leonhardt and R. Scheibe, *Journal of Electron Spectroscopy and Related Phenomena*, 1977, **10**, 121.
40. D. Shuttleworth, *The Journal of Physical Chemistry*, 1980, **84**, 1629.
41. I. Ikemoto, K. Ishii, S. Kinoshita, H. Kuroda, M. A. Alario Franco and J. M. Thomas, *Journal of Solid State Chemistry*, 1976, **17**, 425.
42. T. Gross, M. Ramm, H. Sonntag, W. Unger, H. M. Weijers and E. H. Adem, *Surface and Interface Analysis*, 1992, **18**, 59.
43. M. L. Miller and R. W. Linton, *Analytical Chemistry*, 1985, **57**, 2314.
44. H. Seyama and M. Soma, *Journal of the Chemical Society, Faraday Transactions 1: Physical Chemistry in Condensed Phases*, 1985, **81**, 485.
45. I. Montero, L. Galán, E. de la Cal, J. M. Albella and J. C. Pivin, *Thin Solid Films*, 1990, **193-194, Part 1**, 325.

46. M. Jeske, K. G. Jung, J. W. Schultze, M. Thönissen and H. Münder, *Surface and Interface Analysis*, 1994, **22**, 363.
47. R. Baptist, A. Pellissier and G. Chauvet, *Solid State Communications*, 1988, **68**, 555.
48. A. A. Galuska, J. C. Uht and N. Marquez, *Journal of Vacuum Science & Technology A: Vacuum, Surfaces, and Films*, 1988, **6**, 110.
49. T. M. Parrill and Y. W. Chung, *Surface Science*, 1991, **243**, 96.
50. L. Griffiths, A. Root, R. K. Harris, K. J. Packer, A. M. Chippendale and F. R. Tromans, *Journal of the Chemical Society, Dalton Transactions*, 1986, 2247.
51. R. J. Kirkpatrick and R. K. Brow, *Solid State Nuclear Magnetic Resonance*, 1995, **5**, 9.
52. R. K. Brow, *J. Am. Ceram. Soc.*, 1993, **76**, 913.
53. D. Laurencin, C. Gervais, H. Stork, S. Kraemer, D. Massiot and F. Fayon, *Journal of Physical Chemistry C*, 2012, **116**, 19984.
54. M. A. Aramendia, V. Borau, C. Jimenez, J. M. Marinas, F. J. Romero and J. R. Ruiz, *Journal of Solid State Chemistry*, 1998, **135**, 96.
55. J. Zhu and Y. Huang, *Canadian Journal of Chemistry-Revue Canadienne De Chimie*, 2011, **89**, 803.
56. J. F. Moulder, W. F. Stickle, P. E. Sobol and K. D. Bomben, *Handbook of X-Ray Photoelectron Spectroscopy*, Perkin Elmer Corporation, 1992.
57. B. Boonchom, *Int J Thermophys*, 2010, **31**, 416.
58. B. Boonchom, *J Therm Anal Calorim*, 2009, **98**, 863.
59. T. R. Hinsch, W. Guse and H. Saalfield, *Journal of Crystal Growth*, 1986, **79**, 205.
60. J. C. Fuggle, *Surface Science*, 1977, **69**, 581.
61. G. P. Halada, C. R. Clayton and D. H. Lindsley, *Materials Science and Engineering: A*, 1988, **103**, L5.
62. S. Contarini, S. Aduru and J. W. Rabalais, *The Journal of Physical Chemistry*, 1986, **90**, 3202.

63. N. S. McIntyre and D. G. Zetaruk, *Analytical Chemistry*, 1977, **49**, 1521.
64. H. D. Rugsy and H. Viefhaus, *Surface Science*, 1986, **173**, 418.
65. M. Es-Souni and A. Mosser, *Surface Science*, 1988, **199**, 439.
66. F. Bezuidenhout, J. Du Plessis and P. E. Viljoen, *Applications of Surface Science*, 1984, **17**, 374.
67. S. A. Chambers and V. A. Loeb, *Physical Review B*, 1993, **47**, 9513.

CHAPTER 5 CONCLUSIONS AND FUTURE WORK

5.1 Introduction.....	199
5.2 Summary and Conclusions	199
5.2.1 Model Phosphate Coatings.....	199
5.2.2 XPS studies of Phosphate Coatings.....	200
5.3 Future Work.....	201
5.4 References.....	202

5.1 INTRODUCTION

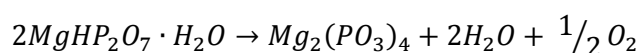
The main aim of this work has been to explore the fundamental chemical properties of phosphate coatings used on electrical steels produced at Cogent Power Ltd. It is known that magnesium phosphate coatings impart a greater tension on steel substrates than aluminum phosphate ones however they are less stable towards hydration. It is also known that the addition of chromium trioxide to both coatings improves the stability and tension of the coatings. This thesis has aimed to determine a chemical model for these observations, with a view towards developing new improved steel coatings. Chapter 3 has explored these themes using model coatings and a range of characterisation techniques. The results have been used to develop a thorough chemical understanding of the phosphate coatings. Chapter 4 continued the theme of coating analysis from chapter 3, however focused solely on the use of XPS with a view to developing a quantitative understanding of the coatings.

The main findings of each chapter will be summarized in this final chapter along with future work that could be performed based on these results.

5.2 SUMMARY AND CONCLUSIONS

5.2.1 MODEL PHOSPHATE COATINGS

The work in chapter 3 was focused on the synthesis and analysis of model phosphate coatings in order to develop a complete understanding of the industrial coatings developed at Cogent Power Ltd. Magnesium phosphate was found to undergo a dehydrolytic condensation reaction to form magnesium metaphosphate (see Equation 5.1). It was also noted that this reaction did not occur with aluminium phosphate model coatings and thus a hypothesis was developed that the formation of metaphosphate plays a key role in of the increased tension imparted on steel sheets coated with the magnesium phosphate coatings. No changes were observed during the curing of aluminium phosphate, suggesting that it imparts tension on the steel via some other mechanism.



Equation 5.1 The dehydrolytic condensation of magnesium phosphate in electrical steel coatings

The metaphosphate formed during curing was found to be unstable in humid atmospheres and degraded back to the orthophosphate within two weeks, consistent with the ‘tackiness’

associated with magnesium phosphate coatings in humid atmospheres. Aluminium phosphate was found to be stable in humid conditions with the IR spectra remaining constant throughout the trial, supporting this conclusion.

Producing magnesium phosphates using a range of phosphoric acid concentrations aided in developing the conclusion that excess phosphoric acid is required to form the metaphosphate during curing. This is supported by the behaviour of the aluminium phosphate samples, as literature results (from samples cured without being purified, therefore retaining an excess of acid, unlike the purified commercial product used here and at Cogent Power Ltd.) indicate that aluminium orthophosphate should undergo the same dehydrolytic condensation as magnesium metaphosphate.¹⁻³

When chromium trioxide was added to magnesium phosphate chromium pyrophosphate was formed instead of magnesium metaphosphate. This led to the conclusion that the oxide reacts with excess phosphoric acid in the system to prevent magnesium metaphosphate formation and increases the stability of the coating as the pyrophosphates do not degrade. The chromium pyrophosphate is presented as a cause of the increased tension exerted on steel sheets reported when these mixed coatings are used. The addition of the Cr_2O_3 to magnesium phosphate did not yield the same chromium pyrophosphate, leading to the conclusion that the trioxide is the active species in this reaction.

In direct contrast the addition of chromium trioxide to the aluminium phosphate coatings did cause the formation of aluminium metaphosphate. Chromium trioxide is widely used as an oxidant in organic chemistry,^{4, 5} leading to the conclusion that it is oxidising the by-products of the condensation reaction and aiding the formation of alumina.

The combined results strongly support the hypothesis that the metaphosphate is central to the ability of the phosphate film to impart tension onto the steel substrate.

5.2.2 XPS STUDIES OF PHOSPHATE COATINGS

X-ray photoelectron spectroscopy was also used to study phosphate coatings and the results were presented in chapter 4. Work by Gresch⁶ indicated that the oxygen 1s region of the XP spectrum could be used to determine the average length of metaphosphate chains, and this was successfully applied to the same samples he studied. The condensation of these samples could be followed using XPS and the results showed good agreement with the results obtained from the bulk techniques used (XRD and MAS-NMR), however the ratio of oxygen 1s components was of little use for model phosphate coatings, possibly due to the presence of other phases and by-

products. Changes from ortho to metaphosphate can be observed by following changes in the binding energies of the oxygen 1s and phosphorus 2p transitions.

XPS indicated that dehydrolytic condensation occurred at the surface during curing in all model coatings; however it was much more prevalent in the magnesium phosphates than the aluminium phosphates. During aging the reverse reaction occurred, causing reformation of the orthophosphates (as observed in the changes in binding energy). The magnesium phosphate chains were found to be much more susceptible to hydrolysis than the aluminium chains, supporting the observation that the aluminium phosphate samples were more stable than the magnesium phosphates. These results are in good agreement with the results obtained in the bulk analysis of model coatings (chapter 3), supporting the use of XPS for the analysis of phosphate coatings.

The XP spectra of the chromium containing samples indicated that oxide completely reduced upon heating to a trivalent species and the presence of chromium oxide appeared to reduce the number of bridging oxygen atoms present on the surface. This is in good agreement with results in the previous chapter, which indicated the formation of chromium pyrophosphate in preference to magnesium metaphosphate.

XPS of industrial coatings showed the concentration of aluminium was much lower than phosphorus, presenting some evidence for the presence of phosphoric acid at the surface of the sheet. A brushed forsterite sample was shown to have a large concentration of iron at the surface, indicating that the wire brushes used to clean the sample have also damaged the coating. XPS also showed that 'pickling' did not fully remove the upper phosphate coating as phosphorus was still present at the surface. Finally the effects of heating the samples on the XP spectra were also studied. Silicon segregation from the bulk to the surface was observed for the bare steel sample, whilst the pickled forsterite and fully coated steel samples were largely unaltered by heating.

The results from both chapters show that the interchange between ortho and metaphosphate is vital to the stability of the steel coatings.

5.3 FUTURE WORK

At the beginning of this project the initial aims were much broader, with developing an understanding of the phosphate coatings only part of the overall project. It was also hoped that once an understanding was developed new coating materials could be suggested and possibly

trialled, however the coating systems were much more complex than initially thought, giving scope for a wide range of future works.

One key future experimental aim is the production of aluminium metaphosphate via the dehydrolytic condensation of aluminium orthophosphate. There are two possible routes through which this could be attempted; the first is to mix purchased aluminium orthophosphate with phosphoric acid. This would also test the conclusion reached in chapter 3 that excess phosphoric acid is required for the condensation reaction to occur. The second possible route for aluminium metaphosphate which could be trialled is the synthesis from aluminium orthophosphate precursors and an excess of phosphoric acid. Possible precursors include aluminium chloride, aluminium nitrate and aluminium oxide.

Once aluminium metaphosphate has successfully been produced, nontoxic replacements to chromium trioxide for the addition to either magnesium or aluminium phosphates could be investigated. In the case of magnesium phosphates the additive would most likely be some form of metal oxide which readily forms a phosphate. Commonly studied phosphates that could be studied include zinc phosphates, which are already widely used as coating materials.⁷⁻⁹

5.4 REFERENCES

1. H.-S. M. Dong-Pyo Kim, Jae-Seong Rho, Kyoo-Seung Han, Hee-Gweon Woo, Hunseung Ha, Feng Cao,, *Composites Science and Technology*, 2003, **63**, 493-499.
2. G. Tricot, D. Coillot, E. Creton and L. Montagne, *Journal of the European Ceramic Society*, 2008, **28**, 1135-1141.
3. J. H. Morris, P. G. Perkins, A. E. A. Rose and W. E. Smith, *Chem. Soc. Rev.*, 1977, **6**, 173-194.
4. K. Bowden, I. M. Heilbron, E. R. H. Jones and B. C. L. Weedon, *Journal of the Chemical Society (Resumed)*, 1946, **0**, 39-45.
5. G. I. Poos, G. E. Arth, R. E. Beyler and L. H. Sarett, *Journal of the American Chemical Society*, 1953, **75**, 422-429.
6. R. Gresch, W. Mullerwarmuth and H. Dutz, *Journal of Non-Crystalline Solids*, 1979, **34**, 127-136.
7. S. Jegannathan, T. Narayanan, K. Ravichandran and S. Rajeswari, *Surface & Coatings Technology*, 2006, **200**, 4117-4126.

8. P. Nguyen Van, S. Moon, D. Chang and K. H. Lee, *Applied Surface Science*, 2013, **264**, 70-78.
9. L. Y. Niu, Z. H. Jiang, G. Y. Li, C. D. Gu and J. S. Lian, *Surface & Coatings Technology*, 2006, **200**, 3021-3026.

APPENDIX 1 ADDITIONAL CHARACTERISATION DATA FROM MODEL PHOSPHATE COATINGS

Introduction.....	205
Phosphate 1 (Aluminium Orthophosphate)	207
Phosphate 2 (Magnesium Phosphate, Cogent Power Ratio)	208
Phosphate 3 (Magnesium Phosphate, 25 % Magnesium Oxide).....	208
Phosphate 4 (Magnesium Phosphate, 50 % Magnesium Oxide).....	209
Phosphate 5 (Magnesium Phosphate 75 % Magnesium Oxide).....	210
Aging of Aluminium Phosphate	211
Aging of Magnesium Phosphate.....	211
Chromium Oxide	211
Chromium Oxide Magnesium Phosphate Mixtures- The role of chromium concentration.....	211
Chromium Oxide Magnesium Phosphate mixture- 50 % Chromium Oxide.....	211
Chromium Oxide Magnesium Phosphate mixture- 66 % Chromium Oxide.....	212
Cr ₂ O ₅ Magnesium Phosphate mixture.....	212
Chromium Oxide Aluminium Phosphate Mixtures- The role of chromium concentration.....	213

INTRODUCTION

Appendix 1 contains all additional characterisation data collected from model phosphate coating materials that was not included in chapter 3 (generally to aid the flow of the chapter or save space, see Table 1 for the page numbers of data included within the chapter). All spectra are collected by sample and any additional information such as sample labels and additional information on the conditions the spectra were collect under is given in notes below the spectra. A full analysis of the samples is given in chapter 3.

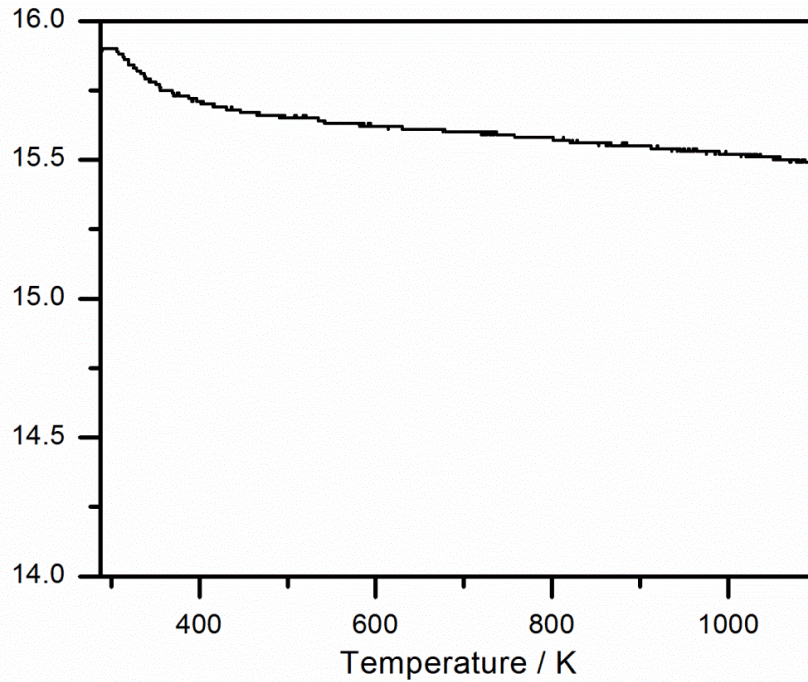
Appendix 1 Additional Characterisation Data from Model Phosphate Coatings

<i>Sample</i>	<i>Technique</i>	<i>Page</i>
<i>Phosphate 1 (Aluminium Orthophosphate)</i>	<i>ATR-IR</i>	<i>57</i>
	<i>Raman</i>	<i>57</i>
	<i>ATR-IR</i>	<i>60</i>
<i>Phosphate 2 (Magnesium Phosphate, Cogent Power Ltd Ratio)</i>	<i>Raman</i>	<i>61</i>
	<i>XRD</i>	<i>62</i>
	<i>TGA</i>	<i>63</i>
<i>Phosphate 3 (Magnesium Phosphate, 25 % Magnesium Oxide)</i>	<i>Raman</i>	<i>64</i>
<i>Phosphate 4 (Magnesium Phosphate, 50 % Magnesium Oxide)</i>	<i>Raman</i>	<i>67</i>
<i>Phosphate 5 (Magnesium Phosphate, 75 % Magnesium Oxide)</i>	<i>Raman</i>	<i>69</i>
<i>Aging Of Aluminium Phosphate</i>	<i>ATR-IR</i>	<i>73</i>
<i>Aging Of Magnesium Phosphate</i>	<i>ATR-IR</i>	<i>74</i>
	<i>ATR-IR</i>	<i>77</i>
<i>Chromium Trioxide (CrO₃)</i>	<i>TGA</i>	<i>78</i>
<i>Chromium Oxide Magnesium</i>	<i>ATR-IR</i>	<i>80</i>
<i>Phosphate Mixtures- The role of Chromium concentration</i>	<i>Raman</i>	<i>81</i>
	<i>XRD</i>	<i>86</i>
<i>Chromium Oxide Magnesium</i>	<i>ATR-IR</i>	<i>89</i>
<i>Phosphate mixture- 50 % Chromium Oxide</i>	<i>Raman</i>	<i>90</i>
	<i>TGA</i>	<i>93</i>
<i>Chromium Oxide Magnesium</i>		
<i>Phosphate mixture- 66 % Chromium Oxide</i>	<i>TGA</i>	<i>95</i>
	<i>XRD</i>	<i>96</i>
<i>Cr₂O₅ Magnesium Phosphate Mixture</i>	<i>TGA</i>	<i>97</i>
<i>Chromium Oxide Aluminium</i>	<i>ATR-IR</i>	<i>98</i>
<i>Phosphate Mixtures- The role of Chromium concentration</i>	<i>Raman</i>	<i>102</i>
	<i>TGA</i>	<i>104</i>

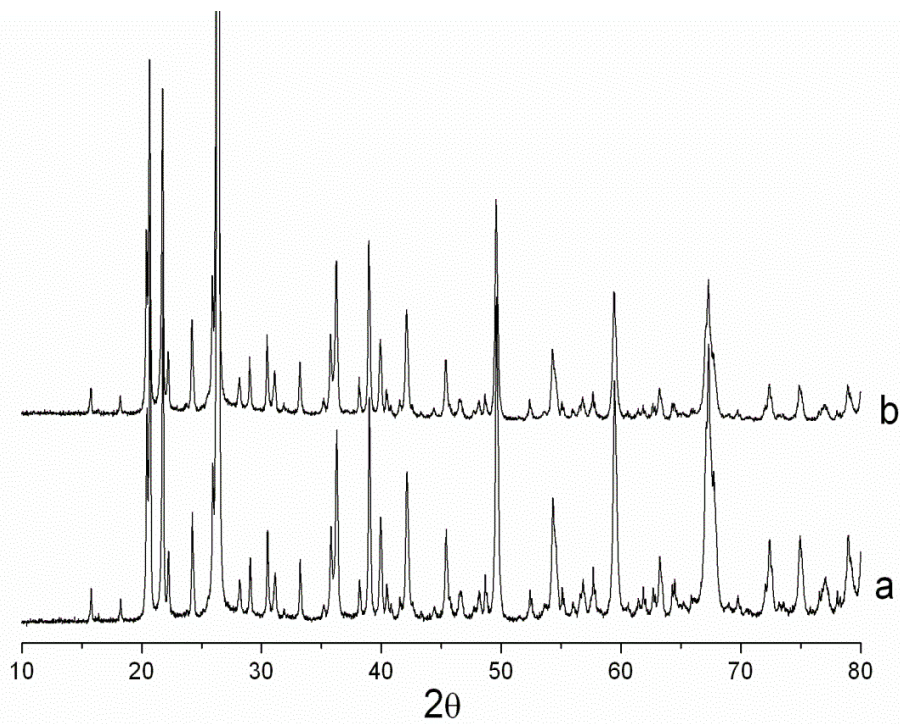
Table 1 Additional data not included in this appendix.

PHOSPHATE 1 (ALUMINIUM ORTHOPHOSPHATE)

TGA



XRD



a) As received and b) after heating to 1073 K for 15 minutes in air. Both samples were matched to aluminium phosphate (AlPO_4 , berlinite). No other phases were identified.

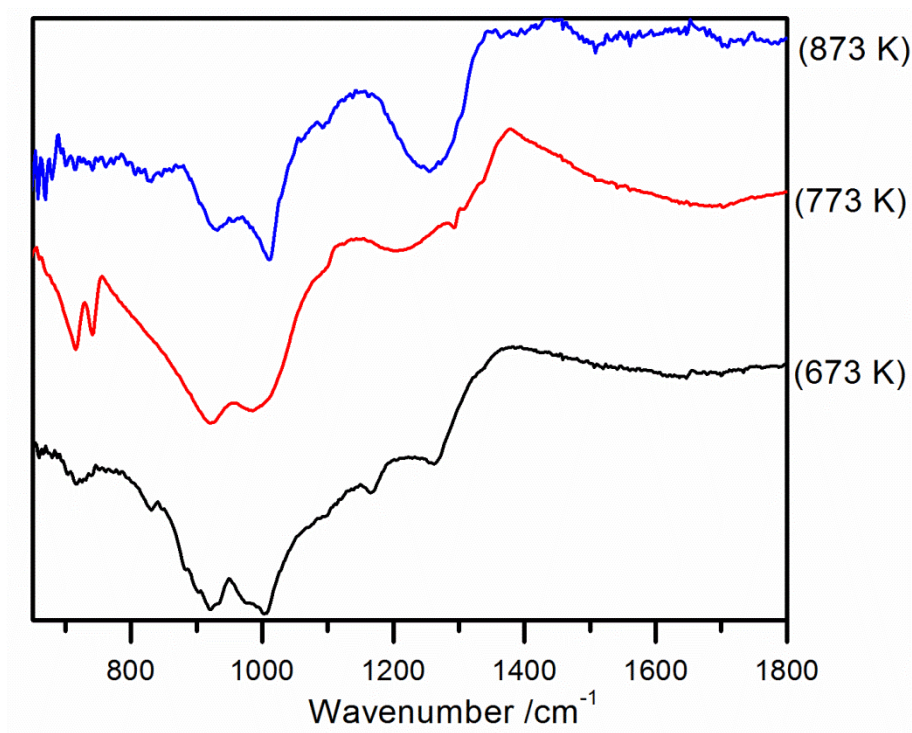
Appendix 1 Additional Characterisation Data from Model Phosphate Coatings

PHOSPHATE 2 (MAGNESIUM PHOSPHATE, COGENT POWER RATIO)

All characterisation data for this sample is presented in chapter 3.

PHOSPHATE 3 (MAGNESIUM PHOSPHATE, 25 % MAGNESIUM OXIDE)

ATR-IR

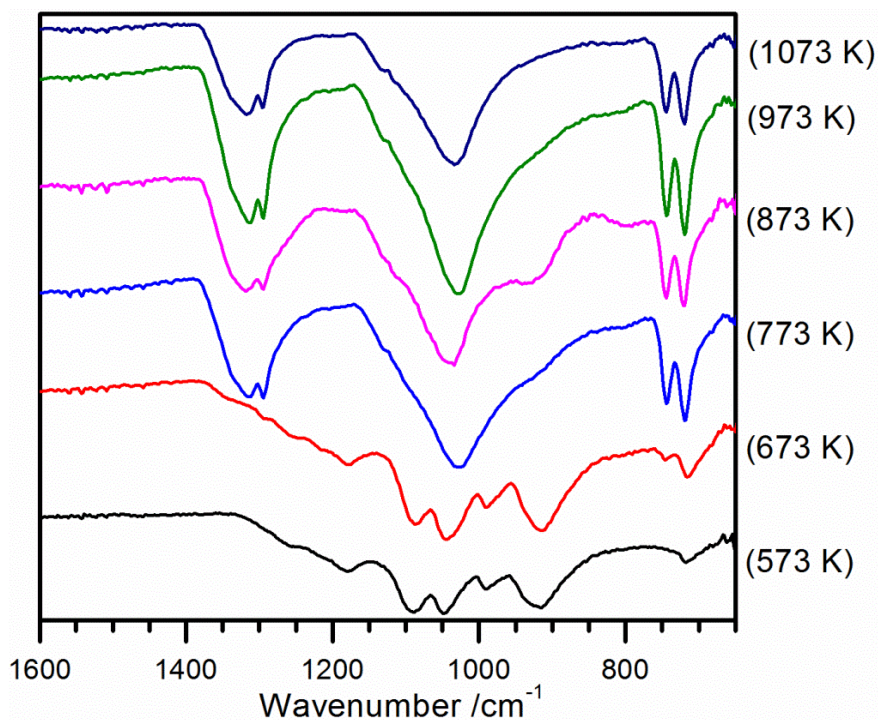


The IR spectra of the phosphate 3 could not be collected when the sample was heated about 873 K as the resulting powder was too hard to achieve a good contact between the sample and the germanium crystal of the ATR system.

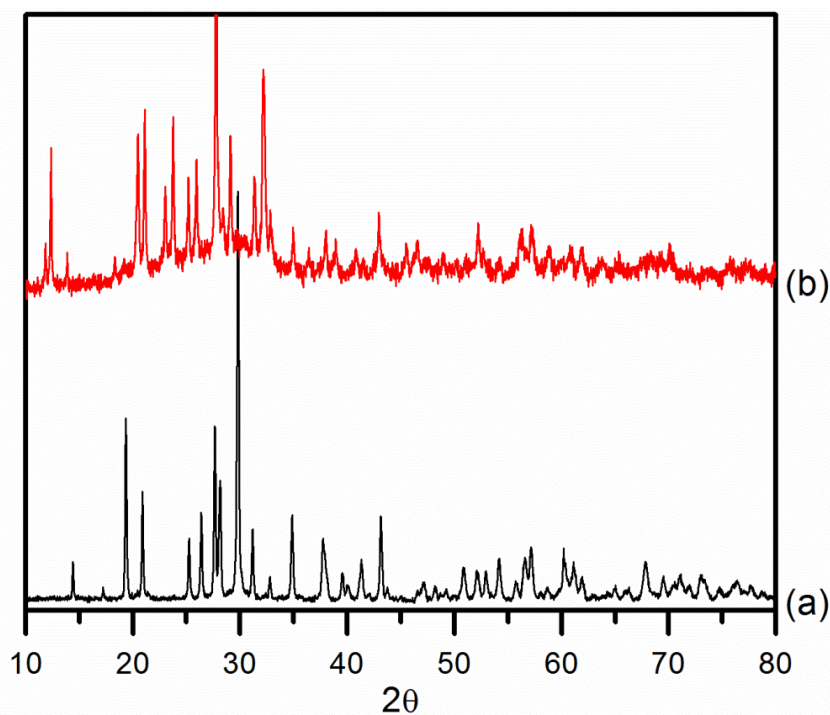
Appendix 1 Additional Characterisation Data from Model Phosphate Coatings

PHOSPHATE 4 (MAGNESIUM PHOSPHATE, 50 % MAGNESIUM OXIDE)

ATR-IR



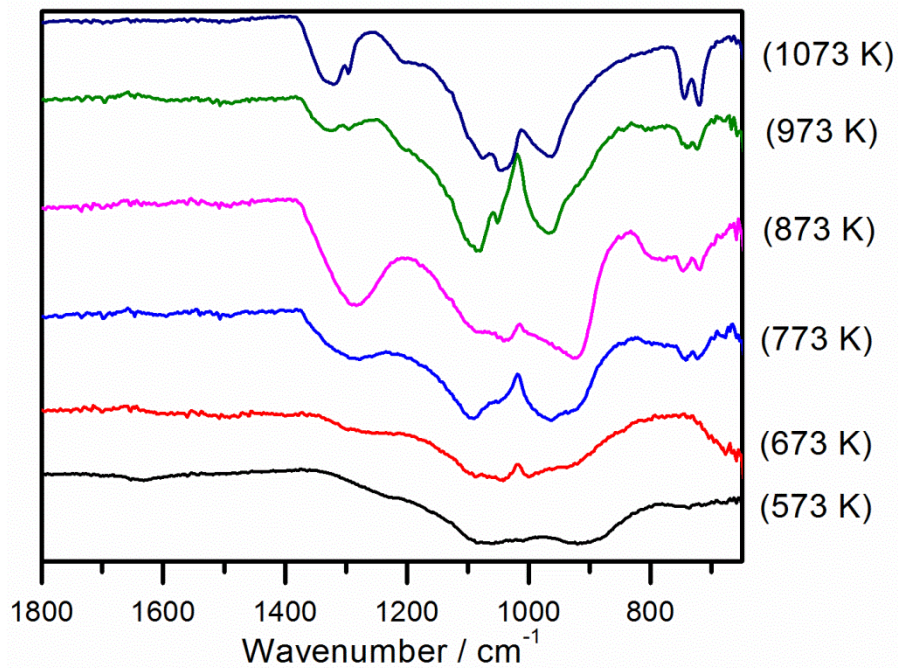
XRD



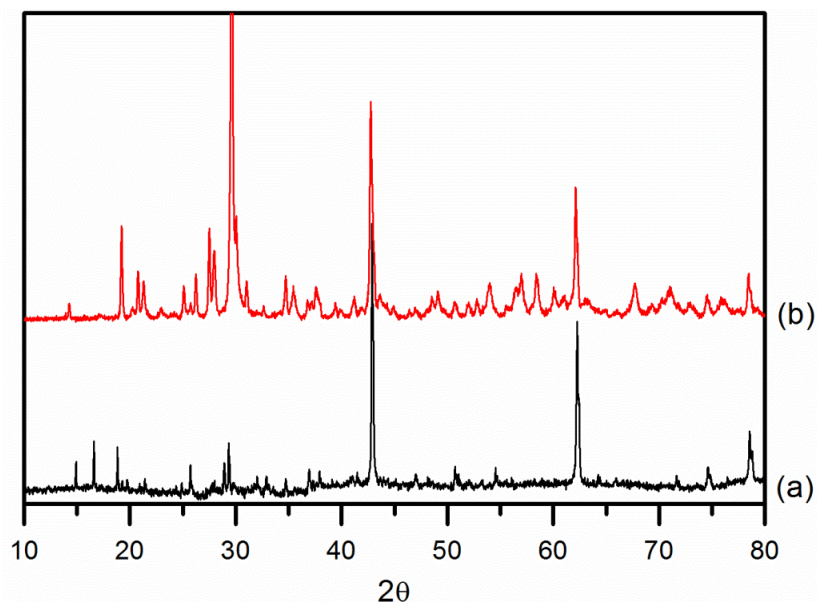
a) Dried at 573 K (matched to Mg₃(PO₄)₂, MgH₂P₂O₇) and (b) cured at 1073 K (matched to Mg₂P₄O₁₂)

PHOSPHATE 5 (MAGNESIUM PHOSPHATE 75 % MAGNESIUM OXIDE)

ATR-IR



XRD



a) Dried at 573 K (matched to MgO , $\text{Mg}_2\text{P}_2\text{O}_7$) and (b) cured at 1073 K (matched to $\text{Mg}(\text{PO}_3)_2$, MgO , $\text{Mg}_2\text{P}_2\text{O}_7$)

AGING OF ALUMINIUM PHOSPHATE

All characterisation data for this sample is presented in chapter 3.

AGING OF MAGNESIUM PHOSPHATE

All characterisation data for this sample is presented in chapter 3.

CHROMIUM OXIDE

All characterisation data for this sample is presented in chapter 3.

CHROMIUM OXIDE MAGNESIUM PHOSPHATE MIXTURES- THE ROLE OF CHROMIUM CONCENTRATION

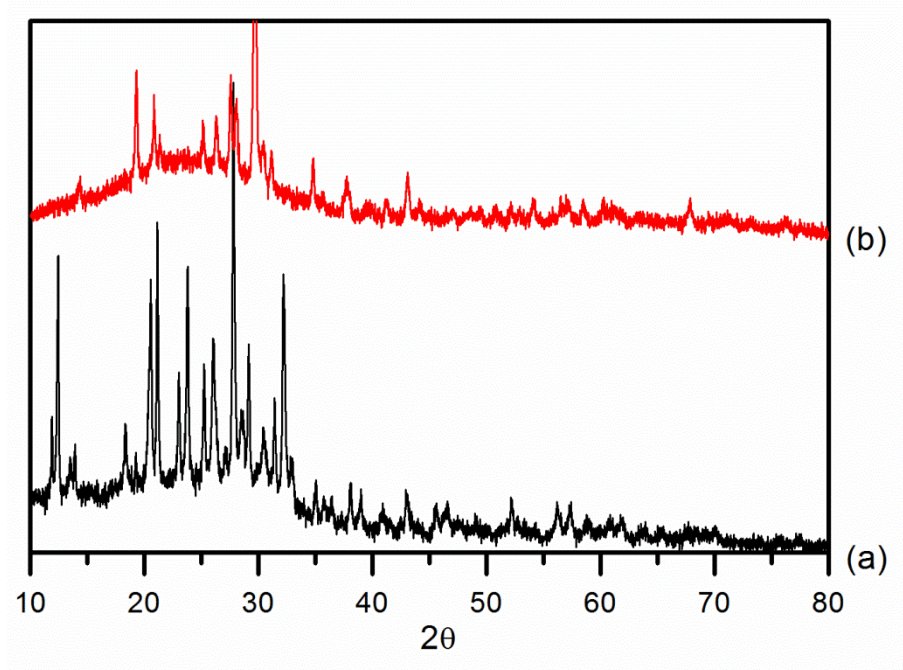
All characterisation data for this sample is presented in chapter 3.

CHROMIUM OXIDE MAGNESIUM PHOSPHATE MIXTURE- 50 % CHROMIUM OXIDE

All data collected from this sample is presented in chapter 3.

CHROMIUM OXIDE MAGNESIUM PHOSPHATE MIXTURE- 66 %
CHROMIUM OXIDE

XRD



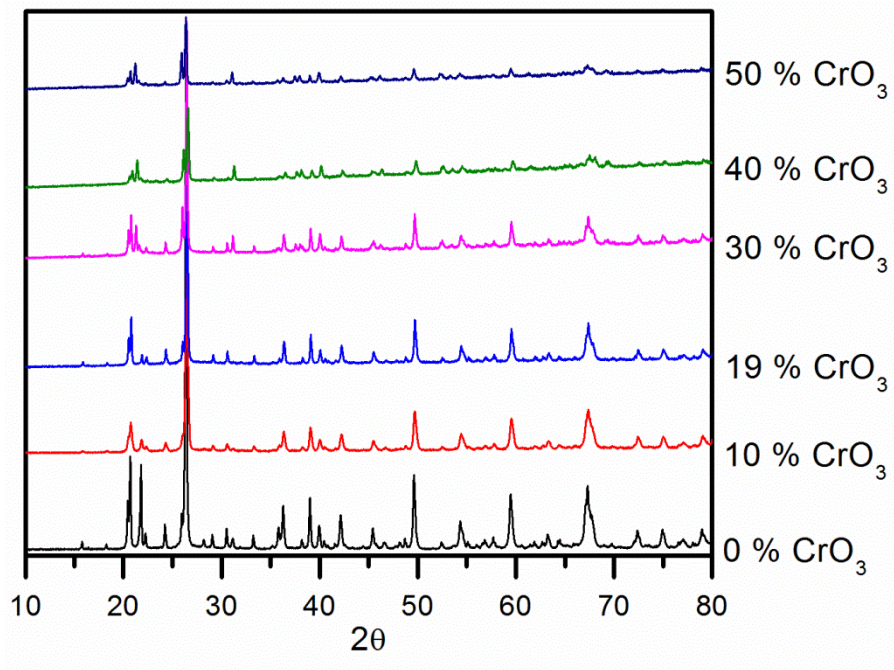
Cr_2O_5 MAGNESIUM PHOSPHATE MIXTURE

All data collected from this sample is present in chapter 3.

CHROMIUM OXIDE ALUMINIUM PHOSPHATE MIXTURES- THE ROLE OF CHROMIUM CONCENTRATION

XRD

Dried



Cured

